Inférence statistique de la population de défauts pour l'étude et la simulation de la fatigue oligocyclique d'un alliage d'aluminium de fonderie

Pablo Wilson

ParisTech
INSTITUT DES SCIENCES ET TECHNOLOGIES
PARIS INSTITUTE OF TECHNOLOGY

ARTS ET MÉTIERS ParisTech

2017-ENAM-0001

École doctorale n° 432 : Sciences des Métiers de l'Ingénieur

Doctorat ParisTech

THÈSE

pour obtenir le grade de docteur délivré par

L'École Nationale Supérieure d'Arts et Métiers

Spécialité "Mécanique-Matériaux"

Présentée et soutenue publiquement par

Pablo WILSON

le 17 janvier 2017

Statistical Inference of Defect population for the Study and Simulation of the Low-Cycle Fatigue of a Cast Aluminium Alloy

Inférence statistique de la population de défauts pour l'étude et la simulation de la fatigue oligocyclique d'un alliage d'aluminium de fonderie

Directeur de thèse : **Nicolas Saintier**
Co-directeur de thèse : **Thierry Palin-Luc**

Jury

M. Jean-Yves Buffière, Professeur, MATEIS, INSA Lyon	Président
M. Karl-Heinz Lang, Docteur Ingénieur, IAM, Karlsruher Institut für Technologie (KIT), Allemagne	Rapporteur
M. Habibou Maitournam, Professeur, UME, ENSTA ParisTech	Rapporteur
M. Vincent Maurel, Maître de Recherche, Centre des Matériaux, MINES ParisTech	Examinateur
M. Thierry Palin-Luc, Professeur, I2M, Arts et Métiers ParisTech, Bordeaux	Examinateur
M. Nicolas Saintier, Professeur, I2M, Arts et Métiers ParisTech, Bordeaux	Examinateur
M. Sébastien Bergamo, Ingénieur, Renault, Technocentre Guyancourt	Invité

Arts et Métiers ParisTech - Centre de Bordeaux - Talence
Département Durabilité des Matériaux, des Assemblages et des Structures
Institut de Mécanique et d'Ingénierie

THESE

Pour Fafa.
Pour Maman et pour Fieu.
Mam et Michel.
Les autres, je vous aime bien aussi.

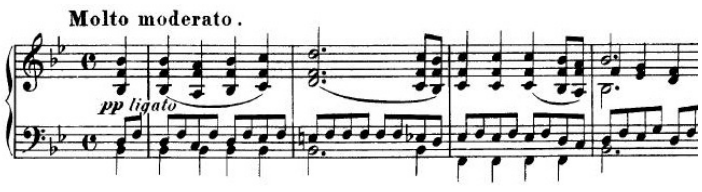

Remerciements

Je tiens à remercier Nicolas Saintier, mon directeur de thèse, et Thierry Palin-Luc, mon co-directeur. Nicolas, merci pour ces réunions de travail plus ou moins formelles, même si j'en ressortais souvent avec plus de questions que de réponses (voire avec un nouveau sujet de thèse). Ton soutien pendant la rédaction m'a été d'une grande aide. Thierry, merci pour tes conseils précieux, ta rigueur scientifique et ta disponibilité expérimentale. C'était toujours un plaisir de te voir et d'échanger avec toi en salle d'essai. Si je retiens une seule chose de la démarche de thèse, c'est la possibilité qu'elle m'a donnée d'avoir des échanges scientifiques avec vous. Quelle ne fut pas ma fierté quand, pour la première fois, j'ai pu ne pas être d'accord avec vous et défendre un point de vue scientifique.

Merci à Sébastien Bergamo et David Hamel de m'avoir donné ma chance chez Renault. Conjuguer recherche scientifique et contraintes industrielles n'est pas facile mais fut passionnant. Je tiens à vous remercier pour la liberté que vous m'avez donnée d'orienter les recherches qui ont pu rester scientifiques. Outre la recherche scientifique, j'ai pu découvrir les rouages, tout aussi subtils, du monde de l'entreprise.

Je tiens également à remercier les membres du jury. Vous exposer mon travail a été pour moi un honneur. Danke M. Karl-Heinz Lang for reading my manuscript and the following debate. Having a point of view from abroad opened new prospects for me. Merci à M. Habibou Maitournam de m'avoir enseigné la fatigue à l'ENSTA, d'avoir suivi mon stage de recherche et accepté de rapporter ma thèse. Merci à M. Jean-Yves Buffière d'avoir présidé mon jury de thèse. Toutes vos publications m'ont été d'une grande aide. Enfin merci à M. Vincent Maurel pour son modèle de propagation, mais aussi pour les corrections, remarques et questions sur mon manuscrit.

Je souhaite remercier toutes les personnes que j'ai pu rencontrer au laboratoire I2M. Merci à ceux qui m'ont aidé à faire des essais (Jonathan, Charles, Christophe, David, Helmi, Momo), des observations (Jérémie), des calculs (Sondes, Jean-Luc, Mathieu), des démarches administratives (Annie, Marinette, Sonia), des hors-jeu (Jean-Benoit, Jérémie, Kévin, Moubarak, Nicolas, Pablo), des sorties piscine (Arthur). Merci aussi à tous les enseignants-chercheurs.

Merci aussi à toutes les personnes que j'ai pu rencontrer chez Renault. Merci de m'avoir aidé à mettre en place les essais (Yassin, Reynald), pour les tomographies (Patrick, Jean-Baptiste), pour les calculs sur culasses (Mathieu), et surtout pour la bonne ambiance dans l'équipe (Jean-Baptiste, Christophe, Amélie, Nadia)

Merci Héloïse pour les débats hautement scientifiques et les potins. Dans cet ordre ?

Merci à tous ceux que j'ai pu oublier.

Enfin, un grand big-up à Salut et à BGU. Merci d'avoir arrêté de me demander "Ça finit quand ta thèse ?". C'est fini.

Table des matières

Liste des Figures / Figure List

Liste des tables / Table List

Liste des symboles / Symbol List

In order to use identical symbols to the ones used in the original papers, the symbols used in the literature survey are not presented here.

Latin symbols

Symbol	Units	Description
a		Power law criterion exponent
a_{Kuma}		First shape parameter of Kumaraswamy distribution
A	m^2	Area
a_0	µm	Initial crack length
a_f	µm	Final crack length
$A0$	mm^2	Specimen cross section
a_{median}	µm	Median defect size
B		Power law criterion constant value
B_{sub}		Subset of observation window W
b_{Kuma}		Second shape parameter of Kumaraswamy distribution
c		Individual Parent (in a spatial point process)
$\bar{c}$		Poisson distribution parameter for children points
C		Copula
C_k		First kinematic hardening parameter
$C^{\mathcal{A}}$		Archimedean copula
$C^{\mathcal{N}}$		Gaussian copula
C_p		Circularity of a particle
d	µm	Feret diameter (for chapter from 1-5)
d	mm	Displacement value (only used in chapter 6)
$D(.)$		Contrast function
$\mathbf{d}$	µm	Feret diameter sample
$\mathcal{D}_D$	µm	Upper bound of Feret diameter distribution support
d_{2D}	µm	2D Feret Diameter
d_{3D}	µm	3D Feret Diameter
d_{ij}		Distance matrix
d_R		Dimension of considered real space (2 or 3D)
$\mathcal{D}_S$		Upper bound of Sphericity distribution support
e	mm	Displacement
E	GPa	Young modulus
$\mathbb{E}$		Statistical expected value

e_n		Global error
F	kN	Force
$f_X(.)$		Probability density function (PDF) of $\mathbf{X}$
$F_X(.)$		Cumulative distribution function of $\mathbf{X}$
$\hat{f}_X(.)$		Function estimate of f_X
f_D		Marginal PDF of Feret diameter
f_{DS}		Joint PDF of Feret diameter and sphericity
F_{DS}		Joint cumulative distribution of Feret diameter and sphericity
$f_{gev}(x)$		Generalized extreme value distribution PDF
$f_{gpd}(x)$		Generalized Pareto distribution PDF
$f_{logn}(x)$		Log-normal distribution PDF
$f_{logit}(x)$		Logit-normal distribution PDF
$f_M(.)$		PDF of marks
$F_M(.)$		Cumulative distribution of marks
f_S		Marginal PDF of Sphericity
F_{scd}		Scpherical contact distribution function
G		Nearest neighbour distribution
h	mm	Sample height
h_{opt}	length unit	Optimal kernel bandwidth
J		J-function used in spatial statistics
K		Ripley's function
$\hat{K}_{bias}(.)$		Biased estimate of Ripley's function
$K^{cluster}(.)$		Clustered point process K Ripley function
$\hat{K}_{edge}(.)$		Edge corrected estimate of Ripley's function
$\hat{K}_{exp}(.)$		Experimental estimate of Ripley's function
$K^{grid}(.)$		Grid point process K Ripley function
$\hat{K}_{iso}(.)$		Isotropic correction estimate of Ripley's function
$K_k(.)$		Kernel function
$K_{mm}(.)$		Weighted K-Ripley function
$K^{PPP}(.)$		Poisson point process K Ripley function
$K^{regular}(.)$		Regular point process K Ripley function
$\hat{K}_{trans}(.)$		Translation correction estimate of Ripley's function
$K_\theta(.)$		Analytical Ripley's function
L	µm	Profile line
L_0	mm	Gauge length
$L_B(.)$		Besag function
l_{gev}		log-likelihood of Generalized extreme value distribution
l_{gpd}		log-likelihood of Generalized Pareto distribution
$l_{lh}(.)$		Log-Likelihood function
l_{logn}		log-likelihood of lognormal distribution
$L_{lh}(.)$		Likelihood function
$L_{mm}(.)$		Weighted l-Besag function
logit(.)		Logit function
m		Mark

M		Random variable mark
m_0		Fixed mark
m_e		Crack growth model parameter
m_p		Crack growth model parameter
n		Size of statistical sample
n_1		Nearest neighbour mean
N_c		Number of concordant observations
N_{ch}		Number of children points
N_d		Number of discordant observations
N_f	cycles	Number of cycles to failure
N_{init}	cycles	Number of cycles to crack initiation
n_{mm}		Mean mark product
N_{repl}		Number of replications
$n_{\mathbb{X}}$		Number of points in set of points
$\mathcal{N}$		Multivariate gaussian distribution
n_γ		Variographic mark index
nei(.)		Nearest neighbour function
p		Cumulative plastic strain
$\bar{p}$		Poisson distribution parameter for parent points
P	m	Perimeter
q_1		First exponent for the contrast function D
q_2		Second exponent for the contrast function D
Q		Number of sub processes
R	mm	Specimen radius
R_0	mm	Radius of ball for Matern Point Process
r_d		Ranks of Feret diameter sample
R_{min}	mm	Inside radius of tube specimen
r_s		Ranks of Sphericity diameter sample
R_ε		Strain ratio
S		Sphericity
S_{sub}		Subset of $\mathbb{R}^d$
$\mathbf{S}$		Sphericity sample
T	°C	Temperature
T_g		Thresholding value
T_m	°C	Temperature measured in useful section
T_{sp}	°C	Temperature set point
$\mathcal{U}$		Uniform distribution
u_ε		Strain uncertainty
u_σ	MPa	Stress uncertainty
u_d	mm	Diameter uncertainty
u_{A0}	mm^2	Uncertainty of specimen cross section
u_e	mm	Uncertainty of displacement
V	m^3	Volume
V_{d_R}	$mm^{(d_R)}$	Volume of a sphere in d_R dimensions
W		Window of observation
$W_{\ominus r}$		Reduced observation window
$w^{trans}(.,.)$		Translation correction factor
$W_{\boldsymbol{x}^*}$		Translated window W

$\mathbb{X}$		Set of spatial points
$\mathbb{X}_{\text{।}}$		Parent point process
x_f	µm	Filtering level of size
$\mathbf{X_n}$		Size n univariate sample
Ys	MPa	Yield strength
$Z(.,.)$		Random continuous field
z_i	length unit	height signed distance in cylindrical coordinates
$\mathbb{Z}$		Child point process

Greek symbols

Symbol	Units	Description
α		Equivalent energy material parameter
α_{beta}		First shape parameter of beta distribution
β_{beta}		Second shape parameter of beta distribution
β_e		Crack growth model parameter
β_p		Crack growth model parameter
γ_e		Crack growth model parameter
γ_k		First kinematic hardening parameter
γ_p		Crack growth model parameter
$\Delta\varepsilon$		Strain range
$\Delta\varepsilon/2$		Strain amplitude
$\Delta\varepsilon_p$		Plastic Strain range
$\Delta\varepsilon_p/2$		Plastic Strain amplitude
ε_{macro}		Macroscopic strain
ΔT	°C	Temperature variation
ΔW_e	MJ/m^3	Elastic strain energy
ΔW_p	MJ/m^3	Plastic strain energy dissipated
ΔW_T	MJ/m^3	Total equivalent energy
ε		Strain
$\dot{\varepsilon}$	s^{-1}	Strain rate
$\underline{\dot{\varepsilon}}_p$	s^{-1}	Strain rate tensor
$\boldsymbol{\theta}$		Vector parameter
$\hat{\boldsymbol{\theta}}$		Vector parameter estimate
$\boldsymbol{\theta}^*$		Best Vector parameter estimate
$\boldsymbol{\theta}_0$		True Vector parameter
θ_{corr}		Correlation coefficient
θ_i	radians	angle in cylindrical coorinates
θ_C		Clayton copula correlation coefficient
θ_F		Frank copula correlation coefficient
θ_G		Gumbel copula correlation coefficient
θ_N		Gaussian copula correlation coefficient
λ		Point process intensity
λ_p		Parent point process intensity
λ_{N_f}		Expected fatigue life
μ_e	length unit	Excess threshold

μ_{gev}	length unit	Location parameter of generalized extreme value distribution
μ_{gpd}	length unit	Location parameter of generalized Pareto distribution
μ_{logn}	length unit	Location parameter of log-normal distribution
μ_{logit}	length unit	Location parameter of logit-normal distribution
μ_M	mark unit	Mark mean
ρ_i	length unit	radial distance in cylindrical coordinates
ρ_P		Linear coefficient of Bravais Pearson
ρ_{sp}		Spearman rank coefficient
ξ_{gev}		Shape parameter of generalized extreme value distribution
ξ_{gpd}		Shape parameter of generalized Pareto distribution
σ	MPa	Stress
$\underline{\underline{\sigma}}$	MPa	Stress tensor
σ_c		Standard deviation of Poisson distribution of number of children
σ_{exp}	MPa	Experimentally measured stress
$\sigma_f(.)$		Deterministic function representing standard deviation of expected fatigue life
σ_{gev}	length unit	Scale parameter of generalized extreme value distribution
σ_{gpd}	length unit	Scale parameter of generalized Pareto distribution
$\tilde{\sigma}_k$		Deviation factor
σ_{logn}	length unit	Scale parameter of log-normal distribution
σ_{logit}	length unit	Scale parameter of logit-normal distribution
σ_M	mark unit	Mark variance
σ_n		Standard deviation of total number of points for a point process
σ_{n_p}		Standard deviation of Poisson distribution of number of parents
σ_{sim}	MPa	Simulated stress
σ_T		Standard deviation of the covariant matrix of modified Thomas Point process
σ_y	MPa	Elastic limit
τ		Kendall rank coefficient
$\varphi(.)$		Standard Normal PDF
Φ^{-1}		Inverse cumulative distribution function of the normal distribution
Φ_2		Bivariate normal distribution
φ_C		Clayton copula Generator function

φ_C	Frank copula Generator function
φ_g	Copula generator function
φ_G	Gumbel copula Generator function

Introduction

The present study is a Phd collaboration between Renault (DEA-TC, Guyancourt, France), and I2M (Institut de Mécanique et d'Ingénierie, CNRS UMR 5295, Bordeaux, France). Prof. Bruno Sudret (BS Conseil) has also taken part and collaborated on various statistical studies.

Cast aluminium alloys have been widely used in automotive industry for many years. They present good specific mechanical strength along with excellent castability and thermal conductivity, making them a suitable choice for engine parts such as cylinder heads. Indeed, these mass production parts are submitted to severe loading conditions: fastening screws, temperature (up to 250 °C), pressure, environment. Moreover, aluminium low specific mass makes for an excellent choice regarding reduction of energy consumption, a paramount criterion in the development of new products. Combined with a global availability, a contained cost and good recyclability, aluminium alloys are, to date, the best solution for cylinder heads.

When used in cylinder head components, aluminium alloy can undergo temperatures up to 250°C. These high temperatures, associated with the constraints caused by the structure, submit the intervalve section to thermo-mechanical fatigue (TMF) and low-cycle fatigue (LCF). While TMF tests are considered more representative of the loading conditions, the test-setup, as well as the results interpretation, remain complex. This study will focus on isothermal LCF tests, as a first step to understand the influence of defects on fatigue mechanisms. Secondary dendrite arm spacing, Iron content, heat treatment, are some of the main microstructural aspects classically studied to provide alloys for different requirements. Except for costly alloys treated by hot isostatic pressing process which exhibit extremely low porosity content, porosities are considered as the main crack initiating cause in low cycle fatigue. Therefore, it is of the utmost importance to describe the porosity contents by means of statistical distributions (especially when considering heterogeneous stress distributions): the size distribution, as well as the location of these defects. This can be done by analysing the porosity population in 2D (see Murakami [1993]), or more recently in 3D by using tomography (see Buffière et al. [2002]). This statistical distribution can then be used as an input parameter to account for the variability of fatigue lifetime.

In order to better understand the fatigue lifetime of cast aluminium, and provide suitable fatigue criteria, the main objectives of the present work are:

— Apply statistical tools to study the defect population (size and location);

— Observe the different fatigue damage mechanisms, notably with respect to the defects and the crack/defect interactions;

— Evaluate the impact of the statistical volume size used for defect generation (numerically and with notched specimens) on the extreme values statistics of defect size, and propose a method to take the defect size into account for the

simulation of the fatigue life.

The study is organized in six chapters.

In the first chapter, the literature review details the material used in this study, and the different alloy elements used. Ambient temperature fatigue mechanisms are detailed, as well as the impact of porosities on the fatigue life. The influence of temperature is then studied, and several fatigue criteria are presented. Particularly, criteria using energy quantities seem well suited to study high temperature low cycle fatigue.

Seeing as porosity plays a critical part on the fatigue mechanisms, the second chapter focuses on the statistical (size and position) description of defects. This is thoroughly investigated by means of robust statistical inference using 3D tomography. It is shown the size distribution can be inferred by analysing a single specimen which constitutes a representative volume of the defect population. Then, using point process, the location of the defects are analysed and show the defects aggregate in clusters.

In the third chapter, a series of low-cycle fatigue tests is conducted on classical smooth cylindrical specimens. After showing the problems that arise from using the classical Coffin-Manson law, a first empirical energy based fatigue criterion is applied. It allows for an accurate prediction of the fatigue life, yet remains usable in an industrial context (easiness of use and robustness).

In the fourth chapter, the fatigue damage mechanisms are observed by various techniques (Tomography, SEM and Digital Camera) and show the critical importance of porosities on crack initiation and propagation, as well as the temperature effect on the different mechanisms.

In the fifth chapter, fatigue results and observations are combined with the statistical description of porosities, and the Statistical Representative Volume Element of the specimen discussed. It is shown the location of defects is crucial for a correct simulation of the extreme value statistics of defects (i.e. the largest defect per specimen). These information are then used as an input for a crack propagation model which takes into account the defect size.

Lastly, the sixth chapter focuses on notched specimens. Tests are conducted and the different criteria applied. Using the extremely small volume highly mechanically loaded, the interaction of spatial distribution of defects with the mechanical fields is studied.

Chapitre 1

Étude bibliographique

Dans un premier temps, l'étude bibliographique présente des généralités sur la métallurgie des alliages d'aluminium, ainsi que l'influence des principaux éléments d'alliage. Des résultats sur la fatigue à température ambiante permettent de positionner le problème de l'influence de la microstructure sur la fatigue. Par la suite, les critères énergétiques sont comparés: ils permettent d'unifier les résultats en fatigue oligocyclique pour plusieurs températures. Enfin, l'effet d'entaille est présenté. L'hétérogénéité des contraintes nécessite des méthodes et des critères spécifiques, tout particulièrement pour la fatigue oligocyclique.

1.1 L'aluminium et ses alliages

1.1.1 L'aluminium pur

L'aluminium est de plus en plus utilisé dans l'industrie, même si à l'état pur, il ne présente que de médiocres performances mécaniques. L'aluminium pur possède une structure cubique à faces centrées (CFC). Les propriétés suivantes sont tirées de Mondolfo [1976] :

- paramètre de maille (cubique à faces centrées) : 0.405nm à 298K;
- masse volumique à 25 °C : 2698.7kg/m^3;
- point de fusion : 660 °C;
- coefficient de dilatation thermique moyen entre 20 et 300 °C : $2,55 \times 10^{-5}$K^{-1};
- retrait volumique : 5,6% en cours de solidification;
- capacité thermique massique à 20 °C : $c = 950$ J.kg^{-1}.K^{-1};
- conductivité thermique à 20 °C : $\lambda = 217.6$ W.m^{-1}.K^{-1};
- résistivité électrique à 20 °C : $\rho = 2.63\mu\Omega$.cm.

Le tableau 1.1 suivant présente certaines propriétés mécaniques courantes:

Table 1.1 – Propriétés de l'aluminium pur à température ambiante

Module d'élasticité (MPa)	Résistance à rupture (MPa)	Limite d'élasticité à 0.2% (MPa)	Allongement à rupture (%)
68000	80 à 100	30 à 40	25 à 30

Bien plus que l'aluminium pur, ce sont les alliages à base de ce dernier qui présentent des propriétés intéressantes comme nous allons le voir ci-après.

1.1.2 Les alliages au Silicium

Les alliages d'aluminium à base de silicium (Si) sont parmi les plus utilisés dans l'industrie. En plus d'améliorer les propriétés mécaniques, le silicium améliore grandement la coulabilité de l'alliage, et rend son utilisation possible pour des pièces de géométrie complexe.

Lors du moulage d'une pièce, la solidification débute sur les parois plus froides du moule. Des cristaux d'aluminium pur se forment et croissent vers l'intérieur de la pièce. La solubilité du Si étant plus faible à basse température, ces cristaux rejettent le Si à leur surface. Il se forme alors une zone dite de surfusion qui va donner naissance à un autre germe de solidification. L'aluminium cristallisant en structure cubique à faces centrées, des dendrites aux directions perpendiculaires apparaissent (cf. figure 1.1). Le paramètre clé de leur caractérisation est l'espacement des bras de dendrites ou DAS (*Dendrite Arm Spacing*) et l'espacement des bras de dendrites secondaires ou SDAS (*Secondary Dendrite Arm Spacing*). Bien que ces deux notions soient différentes, la bibliographie utilise parfois les deux termes de manière identique par abus de langage.

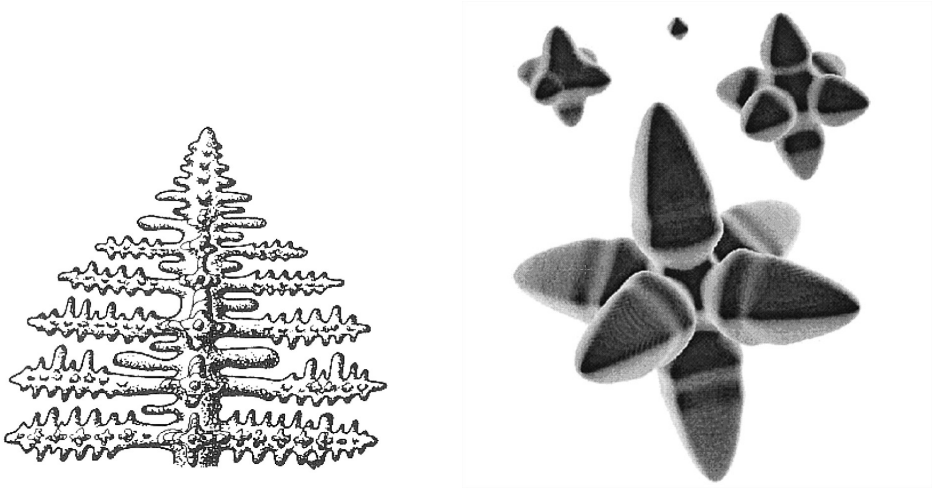

FIGURE 1.1 – (a) Schéma d'une dendrite (b) modélisation tridimensionnelle de la solidification dendritique, d'après Boettinger et al. [2002]

Suite à la formation des dendrites, la phase liquide à l'avant du front de solidification est riche en silicium (la formation des dendrites ayant drainé l'aluminium). Selon Shankar et al. [2004], la nucléation d'aiguilles de silicium eutectique débute alors sur des impuretés à la surface des dendrites (cf figure 1.2a). La phase liquide environnante s'appauvrie alors en silicium jusqu'à une valeur critique. Il se forme donc ensuite une phase d'aluminium eutectique. Si les sites de nucléations sont assez espacés, la solidification de l'aluminium eutectique fait baisser la concentration en aluminium dans la phase liquide, et, de manière analogue, il se forme une nouvelle phase de silicium eutectique (illustré par la figure 1.2b). De proche en proche il se forme des lamelles caractéristiques d'une eutectique lamellaire par croissance compétitive.

1.1.3 Influence du cuivre et du magnésium

Le cuivre

L'addition de cuivre permet un durcissement structural de l'alliage après traitement thermique. Le cuivre augmente généralement la limite d'élasticité sur une grande plage

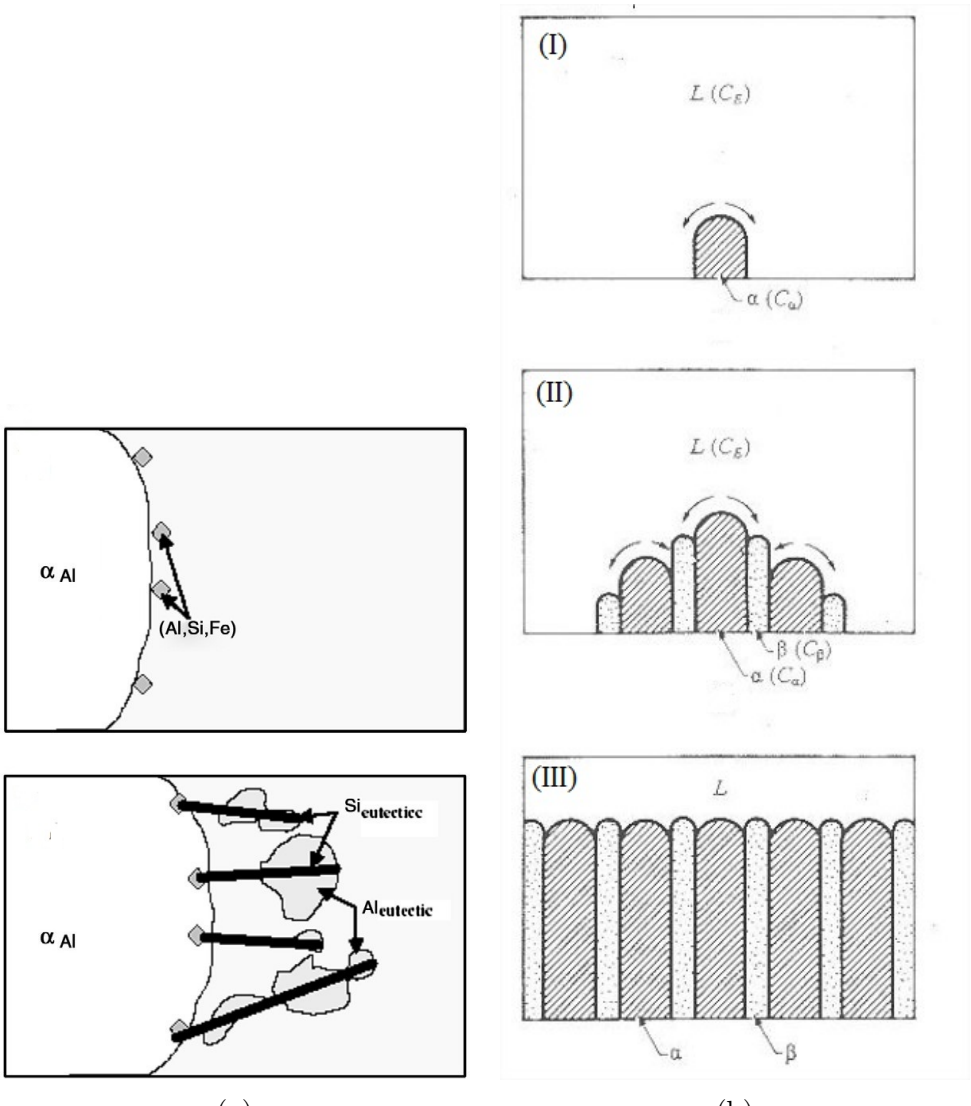

(a) (b)

FIGURE 1.2 – (a) nucléation de la phase eutectique lamellaire, la phase α_{Al} correspond à la dendrite récemment solidifiée, Shankar et al. [2004], (b) principe de la croissance eutectique lamellaire. Le silicium eutectique est ici noté $\alpha(C_\alpha)$ et l'aluminium eutectique $\beta(C_\beta)$, d'après Barralis and Maeder [1997]

de température et améliore l'usinabilité. Cependant, il diminue la résistance à la corrosion de l'aluminium et de ses alliages par la formation de piles galvaniques locales. De plus le diagramme Al-Cu couvre une large plage de température ($T_{liq} - T_{sol}$) (cf. figure 1.3(a)) qui diminue la coulabilité de l'alliage.

Dans le cas d'alliages au Si avec ajout de Cu, le pourcentage de cuivre peut atteindre 7 à 8%, la concentration en cuivre peut même parfois être supérieure à celle du silicium. Cependant, il n'est pas intéressant d'utiliser des concentrations supérieures à 4-5% car la solubilité du cuivre dans l'aluminium décroit avec la baisse de la température : elle vaut 4,1% à la température de mise en solution (environ 500 °C). Pour les alliages Al-Si-Cu avec de faibles quantités de fer et de magnésium, le diagramme ternaire (cf. figure 1.3(b)) permet d'estimer *a priori* la composition de l'alliage, et ne présente que 3 phases distinctes (Al, Si et Al_2Cu).

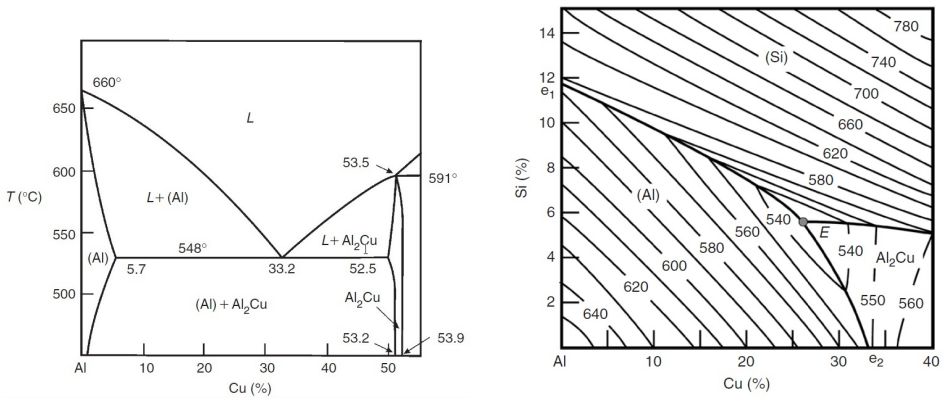

FIGURE 1.3 – (a) Diagramme de Phases du système Al-Cu (b) Diagramme de Phases du système Al-Si-Cu, d'après Zolotorevsky et al. [2007]

Le magnésium

Le rayon atomique du magnésium étant le plus éloigné de celui de l'aluminium parmi les éléments d'alliages (le rayon atomique du magnésium est 11,7% plus grand que celui de l'aluminium), il permet un durcissement par solution solide avec la formation de précipités Mg_2Si (cf. figure 1.4). Néanmoins pour les alliages d'aluminium considérés, le magnésium est présent en faibles quantités, et son influence sur le durcissement est négligeable.

1.1.4 Les impuretés dans les alliages d'aluminium

Les impuretés dans les alliages d'aluminium, voulues ou non, peuvent fortement modifier leurs propriétés mécaniques. Les principaux éléments dont la concentration est limitée sont (Mondolfo [1976])

- *l'antimoine* : il peut servir à neutraliser le phosphore mais n'est pas compatible avec le strontium ;
- *l'étain* : diminue les propriétés mécaniques et augmente le taux de porosités ;
- *le lithium* : très oxydable, il réagit fortement avec l'aluminium et entraîne une augmentation de la porosité ;

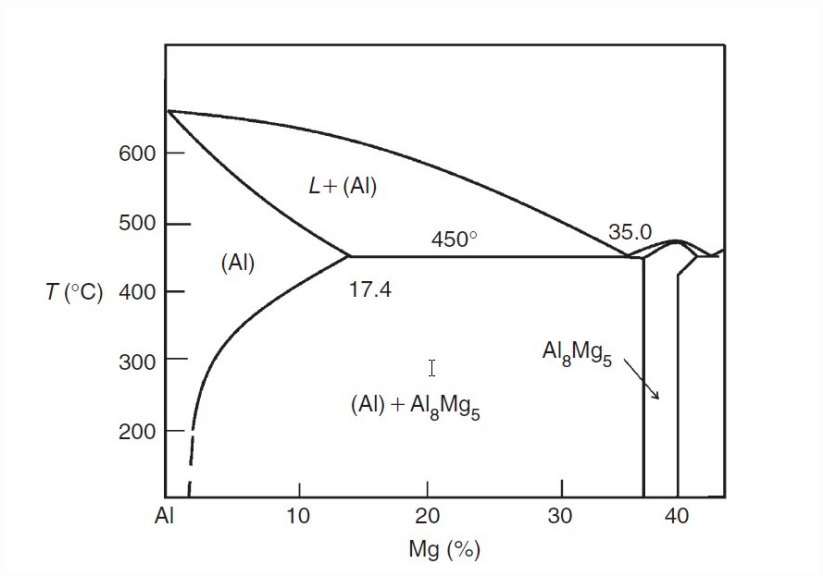

FIGURE 1.4 – Diagramme de Phases du système Al-Mg Zolotorevsky et al. [2007]

— *le nickel* : utilisé à haute température, améliore les propriétés mécaniques, mais coûte relativement cher ;

— *le fer* : il s'agit de la principale impureté étudiée dans les alliages d'aluminium de fonderie. Celle-ci forme de larges intermétalliques aux formes variées (cf. figure 1.5). De nombreuses études sont consacrées à l'étude des microstructures et morphologies de ces intermétalliques (Phragmen [1950], Mondolfo [1976], ou plus récemment avec l'apport de la tomographie Dinnis et al. [2006]). La fragilité de ces intermétalliques est le plus souvent néfaste pour les propriétés mécaniques (notamment pour l'allongement et rupture), et aussi pour la durée de vie en fatigue (Gall et al. [2000]).

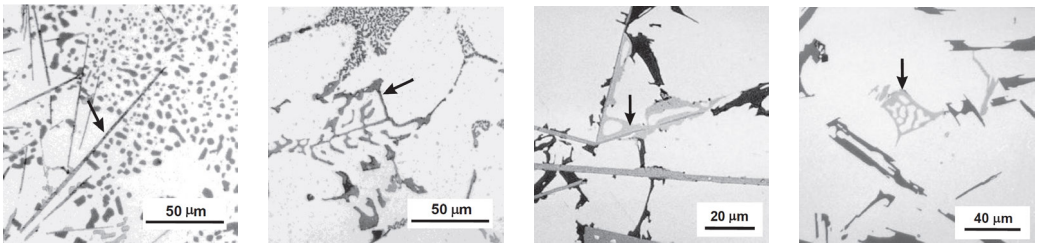

(a) (b) (c) (d)

FIGURE 1.5 – Exemples d'intermetalliques dans un alliage AS5U1G (Taylor [2012]) (a) plaquettes β-Al_5FeSi; (b) écritures chinoises α-$Al_8FeMg_3Si_6$; (c) phase π-$Al_8FeMg_3Si_6$; (d) phase π en écriture chinoises

1.1.5 Procédé d'élaboration

Méthodes de fonderie

La coulée du métal est la première étape dans la réalisation d'une pièce. Le moule peut être unique (méthode de la cire perdue), notamment pour la réalisation de prototypes, ou réutilisable pour la réalisation en série. Une liste des principales méthodes de coulée est ici présentée.

— *moulage à la cire perdue* : à partir d'un original en cire, un moule est fabriqué en ciment réfractaire. Cette solution permet de réaliser des pièces de géométrie complexe en un temps court;

— *moulage en coquille par gravité* : le métal fondu est coulé par gravité dans un moule métallique formé de deux parties. Une fois la pièce refroidie, le moule est ouvert et la pièce retirée. Cette technique présente l'avantage de permettre un meilleur contrôle du refroidissement grâce à la bonne conduction thermique du moule, et d'être réutilisable pour de moyennes ou grandes séries. Néanmoins, les pièces de géométrie complexe sont plus difficiles à réaliser avec cette méthode.

— *moulage au sable* : la pièce est coulée par gravité dans un moule destructible. Ce procédé permet la production de pièces de géométrie complexe de plus grande taille, au détriment de la qualité de surface.

Traitement thermique

(Les données numériques de température et de temps des différents traitements thermiques sont données à titre indicatif, et ne correspondent pas aux données exactes.)

Une fois sorties du moule, les pièces peuvent être soumises à un traitement thermique en vue de leur conférer des performances mécaniques adaptées. Selon le traitement, le matériau pourra être adouci ou durci, la résistance à la corrosion et/ou à la fatigue améliorée.

Les traitements thermiques suivants sont les plus courants et peuvent être appliqués en série ou indépendamment :

— l'homogénéisation : l'alliage est porté à une température élevée permettant la mise en solution des éléments durcissants;

— la trempe : l'alliage est refroidi subitement (par eau ou par air) afin de figer la microstructure. S'en suit généralement un revenu;

— le détentionnement par revenu : à la suite de la trempe, des contraintes résiduelles peuvent apparaître. Le détentionnement par revenu permet une relaxation de ces contraintes, et également la formation de phases durcissantes.

Les trois principaux états de culasse utilisés chez Renault sont l'état brut (aucun traitement thermique), le traitement thermique partiel (traitement de stabilisation T5) et le traitement thermique complet (traitement de type T7).

L'état brut F présente des caractéristiques mécaniques faibles et des contraintes résiduelles importantes. Il est utilisé lorsque la puissance spécifique du moteur, et par conséquence les contraintes mécaniques, sont relativement faibles.

Le traitement T5 consiste en un refroidissement contrôlé par brumisation ou air forcé suivi d'un vieillissement artificiel ou sur-revenu. La matière est ainsi portée à 200 °C pendant environ 5h. Les fours industriels présentant une certaine dispersion, il faut veiller à ne pas dépasser les 250 °C sous peine de dispersions mécaniques élevées.

Le traitement complet T7 comprend une mise en solution (10h à 500 °C), suivie d'une trempe à l'eau puis d'un sur-revenu (5h à 250 °C). La bibliographie montre que ce traitement est souvent utilisé pour augmenter la limite d'élasticité (par exemple dans Caton et al. [2001], la limite d'élasticité d'un alliage W319 augmente de 31%, dans González et al. [2011] de 22% pour un alliage A319). Cependant, il génère des contraintes résiduelles importantes, et son utilisation pour les culasses est surtout à

mettre en relation avec le manque de propreté des culasses en sortie de moule. Pour des géométries du noyau d'eau complexe, l'évacuation du sable peut-être rendue difficile et le traitement peut pallier ces difficultés et permettre un meilleur débourrage (extraction du sable après coulée de la pièce).

1.2 Endommagement en fatigue à température ambiante

Les précédentes parties ont permis d'avoir une compréhension globale de la métallurgie des alliages d'aluminium et des défauts de fonderie induits par les procédés de fonderie. Cette partie présente les liens avec leur endommagement et leur durée de vie ou résistance en fatigue.

1.2.1 Influence de la microstructure

Protocole expérimental

Pour étudier l'influence de la microstructure sur la durée de vie en fatigue, l'étude de Wang et al. [2001b] porte sur deux alliages AS7G de concentration 0,4% (alliage A 356) et 0,7% (A357) en Mg. Afin d'isoler l'influence de la microstructure, les alliages ont subi un traitement thermique de compaction isostatique à chaud (CIC, ou en anglais HIP pour *Hot Isostatic Pressing*) à une température de 520 °C et une pression de 100MPa, permettant de réduire fortement le taux de porosités. Les échantillons sont ensuite soumis à un traitement T6 légèrement sous vieilli (6h à 170 °C alors que le pic de dureté se situe vers 8h). Dans la suite, la notation *Sr* signifie que l'alliage est modifié (ajout de 0,0143% de strontium) et *um* signifie non-modifié ("*un-modified*").

Les échantillons sont alors testés en fatigue à une fréquence de sollicitation de 55 Hz à température ambiante. Les contraintes sont d'amplitudes et de rapports variables (σ_a : 70 et 100MPa, R : 0,1 et 0,2).

Examens microstructuraux, Wang et al. [2001b]

En prélevant les échantillons à différentes hauteurs dans le lingot, divers SDAS sont obtenus en fonction du refroidissement. Les résultats (cf. figure 1.6) sont en adéquation avec l'équation $SDAS = 39,4 V_c^{-0,317}$ décrite au paragraphe 1.1.2.

La structure eutectique (cf. figure 1.7) est composée de Si eutectique (représentés en noir), d'intermetalliques $\beta - Al_5FeSi$ et d'écritures chinoises $\pi - Al_9FeMgSi_5$ (en gris clair), et de la matrice en aluminium (en blanc). La modification au Strontium modifie ainsi les particules de silicium eutectique qui s'affinent et se transforment de larges lamelles en fines fibres. Les intermetalliques β sont prédominantes à 0,4% de Mg alors que ce sont les phases π qui prédominent dans l'alliage à 0,7% de Mg.

Résistance en fatigue

Les résultats de Wang et al. [2001b] en endurance montrent deux types de ruptures. Celles dues aux oxydes (cf figure 1.8 (a)) et celles dues aux bandes de glissement (cf. figure 1.8 (b)). D'après Wang et al. [2001a], le matériau suit la loi de Weibull, la

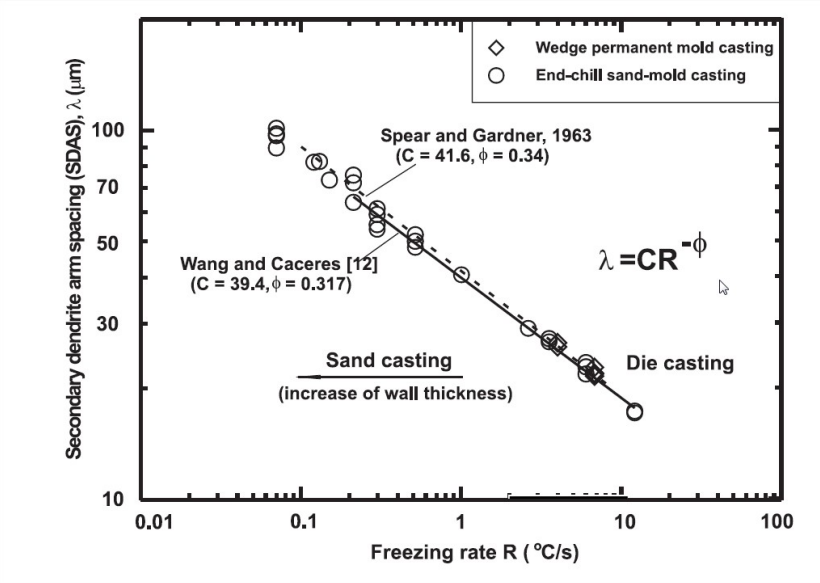

FIGURE 1.6 – Espacement des bras de dendrites secondaires (SDAS) en fonction de la vitesse de refroidissement d'un alliage d'aluminium A356/A357 Wang et al. [2001b]

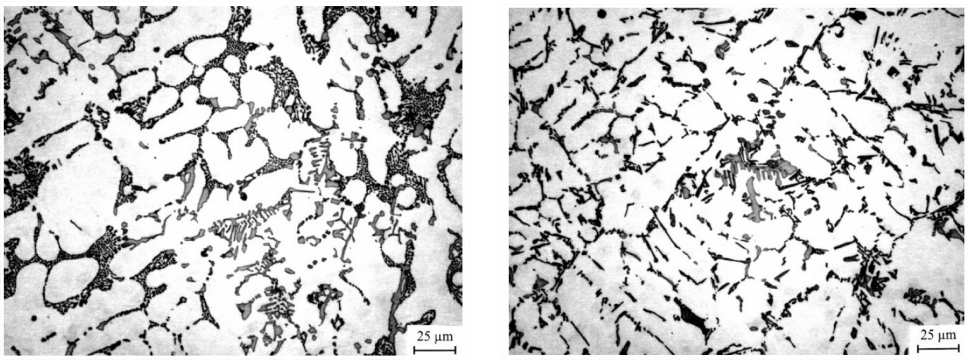

FIGURE 1.7 – Microstructure des alliages A356 (a) avec modification Sr, (b) sans modification Wang et al. [2001b]

probabilité de rupture $F_w(N_f)$ avant N_f cycles s'écrit alors :

$$F_w(N_p) = 1 - \exp\left[\left(\frac{N_f}{N_c}\right)^{\beta}\right] \tag{1.1}$$

où N_c est la durée de vie caractéristique à laquelle 63% des éprouvettes rompent et β le facteur de forme, traduisant la dispersion de la durée de vie. Les données N_f en fatigue sont classées de la plus courte à la plus longue durée de vie, en attribuant à chaque essai une probabilité de rupture en fonction de son rang j, sur le nombre total de tests n tel que :

$$F_w = \frac{j - 0.5}{n} \tag{1.2}$$

La probabilité de rupture F_w et la durée de vie en fatigue (N_f) sont converties en $lnln[1/(1 - F_w(N_f))]$ et $ln(N_f)$ permettant d'estimer les paramètres de la loi de Weibull. À première vue, la figure 1.9 (a) laisse penser que le matériau ne suit pas la loi de Weibull et montre un faible niveau de corrélation : $R = 0,931$. Cependant, en distinguant les ruptures dues aux oxydes de celles provoquées par des bandes de glissement, les résultats se divisent en deux droites de Weibull possédant de meilleurs coefficients de corrélation : $R_{oxide} = 0,971$ et $R_{glissement} = 0,982$ (cf. figure 1.9 (b)). Le nombre de cycles à rupture en fonction du SDAS (cf. figure 1.10) montre que pour des alliages où la rupture n'est pas contrôlée par les pores, la durée de vie en fatigue est minimisée pour un SDAS d'environ $60\mu m$.

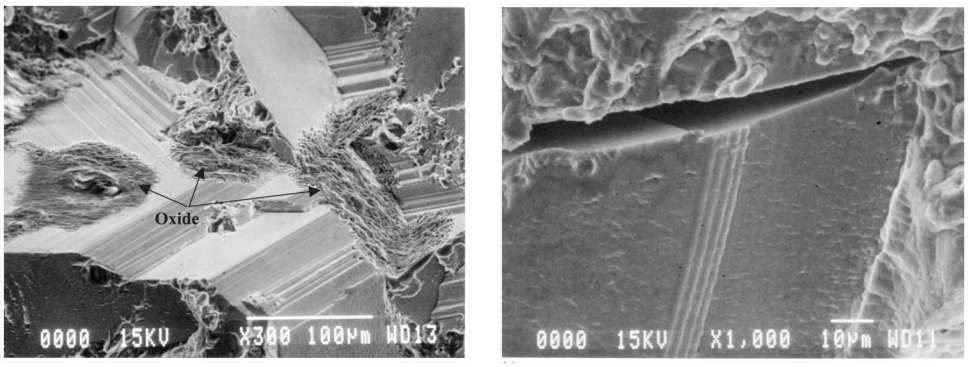

FIGURE 1.8 – Rupture en fatigue d'un alliage A356-T6 CIC due : (a) aux oxydes, (b) aux bandes de glissement Wang et al. [2001b]

Cette dépendance au SDAS peut-être expliquée par la théorie des dislocations sous chargement cyclique : l'application de contraintes, même inférieures à la limite d'élasticité, entraîne le développement de microplasticité locale au sein du matériau. Pour de faibles valeur de SDAS, les dendrites sont interconnectées dans le grain. Les dislocations peuvent alors se déplacer de manière inter-dendritiques, provoquant une diminution de l'influence du durcissement structural. Pour des SDAS plus importants, la taille de grain avoisine celle des dendrites. Les dislocations s'accumulent en bord de dendrites, où les précipités eutectiques sont concentrés, induisant une augmentation des contraintes locales en bordure de grain. Les contraintes images induites en bordure de grain par les dislocations peuvent être quantifiées par la formule suivante proposée par Wang et al. [2001b] :

$$\sigma_{forest} = C\mu_m\sqrt{b\varepsilon\left(\frac{C_1}{L} + \frac{C_2}{\lambda}\right)} \tag{1.3}$$

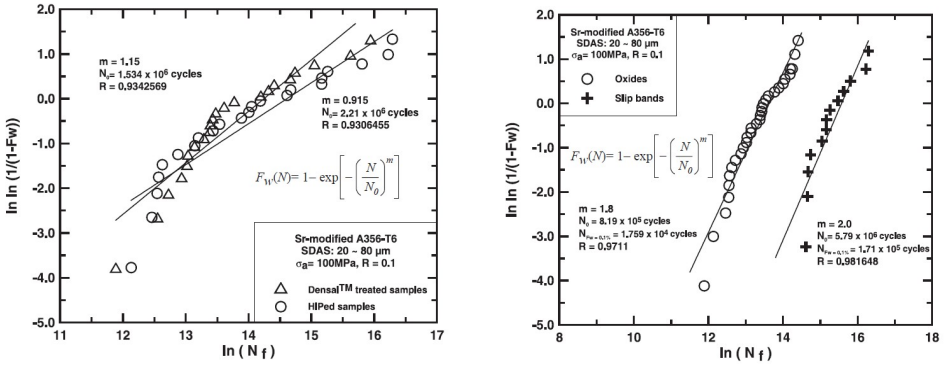

FIGURE 1.9 – Données en fatigue classées selon la loi de Weibull : (a) sans distinction de la cause de rupture, (b) après classement selon l'origine de la rupture, Wang et al. [2001b]

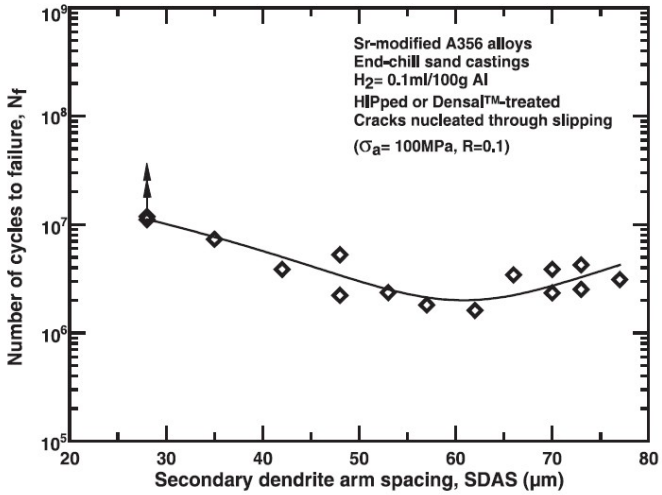

FIGURE 1.10 – Nombre de cycles à rupture en fonction du SDAS pour l'alliage modifié Sr Wang and Cáceres [1998]

L étant la distance moyenne de glissement, μ_m le module de cisaillement de la matrice d'aluminium, ε la déformation locale de relaxation, b le vecteur de Burgers, et C, C_1 et C_2 des constantes. Le SDAS est pris en compte par le paramètre λ. Ainsi pour des SDAS>60μm, λ est égal à la taille de dendrite (considéré comme l'échelle représentatif du mécanisme), alors que pour des SDAS plus faibles (SDAS<60μm) λ est égal la taille de grain.

La contribution des dislocations peut alors être décomposée en deux parties :

— les dislocations statistiquement stockées (SSD) : elles s'accumulent lors de la déformation uniforme de la matrice et interviennent dans le terme (C_1/L);

— les dislocations géométriquement nécessaires (GND) : ces dislocations sont nécessaires lors de déformations pour éviter le chevauchement ou la création de pores entre les différentes interfaces (interfaces de grains ou interface matrice/particules eutectiques). Elles correspondent au terme (C_2/λ).

Dans l'alliage modifié au Sr, un SDAS de 60μm correspond à la transition entre structure fine (SDAS<60μm) et structure grossière (SDAS>60μm). Pour la structure grossière, plus la taille de grain augmente, plus λ augmente, diminuant de fait la contrainte image. Pour la structure fine, les dislocations statistiquement stockées sont prédominantes. Plus le SDAS diminue, plus les dislocations peuvent se déplacer de manière inter-dendritiques. La distance moyenne de glissement L augmente alors, faisant baisser la contrainte image.

La microstructure, avec le SDAS, est donc un facteur d'ordre 1 dans la fatigue à température ambiante. Cette influence peut être interprétée comme la relation entre le SDAS et les contraintes induites en bord de grain par les dislocations. Les études font également ressortir l'importance de la nature du phénomène de fatigue à l'origine de la rupture. Sans distinctions, la modélisation ne reflète pas la réalité, alors qu'en prenant en compte la différence : rupture due aux oxydes / rupture due aux bandes de glissement, le matériau suit la loi de Weibull (plus précisément : 2 lois de Weibull).

1.2.2 Influence des porosités

Les porosités ont un effet catastrophique sur la durée de vie en fatigue. Par exemple, pour un alliage A356, un taux de porosités de 1% en volume peut diminuer la durée de vie en endurance de moitié (Odegard and Pedersen [1994]).

Méthodes de mesure

Les pores étant par nature en 3 dimensions, la mesure et le classement de ceux-ci peut s'avérer complexe. De-Feng et al. [2010] utilisent le paramètre de Murakami Murakami [1993] $\sqrt{A_M}$, A_M étant l'aire projetée et observée sur le faciès de rupture. Dans Buffière et al. [2002], grâce à la microtomographie, les pores ont pu être caractérisés en 3 dimensions, permettant d'établir un classement par sphéricité et taille équivalente.

La projection du pore tridimensionnel sur la surface normale à la direction de sollicitation Gao et al. [2004], semblable à celle de Li et al. [2009] (cf. figure 1.11) a été utilisé par ces mêmes auteurs pour modifier une loi de type Basquin et établir une relation entre la géométrie du pore et la durée de vie en fatigue.

Localisation des pores

L'influence de la position des pores sur la résistance en fatigue montre que les pores où s'amorcent les fissures sont principalement situés proche de la surface des éprouvettes

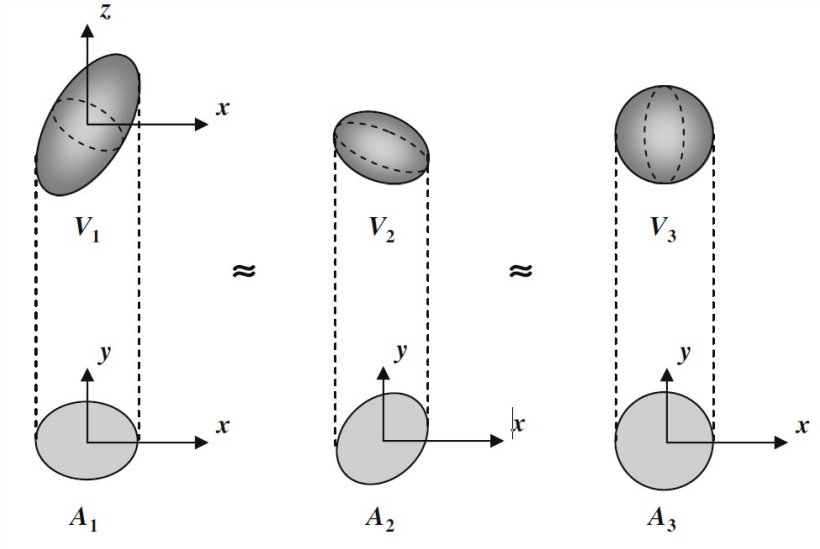

FIGURE 1.11 – Les contraintes moyennes induites sont équivalentes pour des pores de différentes formes, la direction de sollicitation étant z (Li et al. [2009])

(cf. tableau 1.2). En effet, la proximité de la surface augmente la concentration de contraintes autour du pore Pineau et al. [1986], provoquant l'apparition de fissures. L'étude plus récente de Gao et al. [2004] utilise la simulation par éléments finis pour quantifier l'influence de la distance du pore à la surface sur la fatigue (cf. tableau 1.3).

D'après Buffière et al. [2002], la plupart des pores proches de la surface provoquent l'amorçage de fissures.

La première difficulté dans l'étude de l'influence de la porosité sur la fatigue est la caractérisation de les porosités. Les pores étant par nature tri-dimensionnel, la mesure par imagerie 2-D (que ce soit par coupe micrographique ou par observation sur les surfaces de ruptures) nécessite des facteurs de correction.

Table 1.2 – Rupture en fatigue d'un alliage A319 avec différentes amplitudes de déformation De-Feng et al. [2010]

Échantillon	Amplitude de déformation (%)	Durée de vie en fatigue(cycles)	Aire du pore (mm^2)	Distance du pore à la surface (μm)
1	0.2	24806	0.0930	10
2	0.2	78322	0.0237	25
3	0.2	51244	0.0256 0.0272	Coalescence de deux pores
4	0.2	38542	0.0841	10
5	0.2	51668	0.0441	0
6	0.25	11734	0.0247	80
7	0.25	13269	0.0437	0
8	0.25	8567	0.0600	30
9	0.25	6701	0.1521	0
10	0.3	3119	0.0812	0
11	0.3	4503	0.0635	50
12	0.3	1119	0.1406	0

Table 1.3 – Facteur de concentration de contrainte en fonction du diamètre équivalent d_e et de la distance à la surface s. La valeur $s = \infty$ correspondant au centre de l'éprouvette et celle $s = -20\mu m$ à un pore intersectant la surface Gao et al. [2004]

	$s(\mu m)$						
$d_e(\mu m)$	∞	1000	500	100	50	10	-20
100	2,06	2,06	2,07	2,10	2,14	2,42	2,94
200	2,09	2,07	2,07	2,11	2,15	2,54	3,80
400	2,07	2,10	2,09	2,26	2,3	3,02	4,75
600	2,10	2,11	2,11	2,42	2,70	3,61	5,23
800	2,11	2,11	2,15	2,65	3,05	4,07	6,79
1000	2,13	2,13	2,28	2,94	3,40	4,63	7,22

Critères de fatigue avec prise en compte de défauts

Afin de prévoir la durée de vie en tenant compte des défauts présents dans le matériau, de nombreuses études se sont intéressées à la limite de fatigue. Par exemple, l'utilisation du diagramme de Kitagawa (Kitagawa H [1976], illustré figure 1.12) permet de représenter la limite en fatigue en fonction de la taille de fissure (qui pourra, sous certaines hypothèses, être assimilée à une taille de défaut). Ainsi, la figure 1.12 illustre la séparation du domaine de sécurité (*no fatigue failure*, pas de rupture en fatigue) et du domaine de danger (*fatigue failure*, rupture en fatigue). En particulier, le diagramme fait apparaître une longueur de fissure caractéristique, notée a_{crit}, en dessous de laquelle la la limite de fatigue ne dépend plus de la taille de fissure.

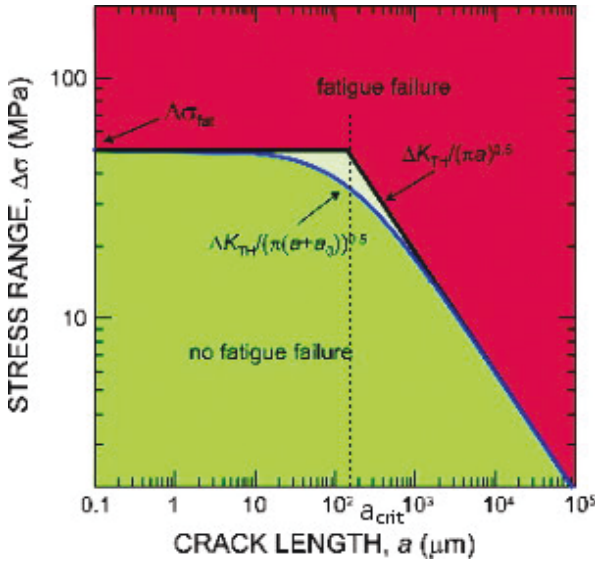

FIGURE 1.12 – Représentation du diagramme de Kitagawa-Takahashi, l'abscisse a_{crit} a été rajoutée (Kruzic and Ritchie [2006])

De manière similaire, Murakami et al. (dans Murakami [1993]) propose un critère empirique basé sur l'aire équivalente A_M (définie par la méthode de mesure décrite précédemment dans la partie 1.2.2) pour calculer la limite en fatigue σ_D. À l'aide d'une base de données contenant de nombreux matériaux métalliques, ils proposent d'utiliser cette aire en combinaison de la dureté Vickers (HV) :

$$\sigma_D = \frac{C(HV + 120))}{\sqrt{A_M}^{1/6}} \times \left(\frac{1-R}{2}\right)^{\alpha} \quad \text{avec : } \alpha = 0,226 + HV.10^{-4} \tag{1.4}$$

sachant que R représente le rapport de charge, et C un paramètre dépendant de la nature du défaut ($C = 1,43$ pour un défaut surfacique et $C = 1,56$ pour un défaut interne). Cette relation s'applique à de nombreux matériaux (ceux ayant servis à l'identification), mais nécessite plusieurs vérifications pour être appliquée à d'autres matériaux.

Afin de prendre en compte les défauts, il est également possible d'appliquer des critères locaux. Ainsi, les approches décrites pour les éprouvettes entaillées dans la partie 1.4.2 peuvent également s'appliquer aux défauts, qui agissent comme des entailles et provoquent des concentrations de contraintes.

D'autres approches présentes dans littérature plus récente permettent d'étendre ce concept à la prise en compte de chargements multiaxiaux (voir Le et al. [2016]) ou de considérer explicitement la compétition entre la microstructure (plus particulièrement la taille de grain) et les défauts (voir Guerchais et al. [2014]).

1.2.3 Mécanismes de fissuration

Amorçage de fissure

L'amorçage de fissure n'est pas nécessairement le critère dimensionnant pour la durée de vie. Dans Buffière et al. [2002], les auteurs observent des fissures ne conduisant pas systématiquement à la rupture sur un alliage A356-T6. La figure 1.13 montre un site propice à l'apparition d'une fissure. La zone convexe accompagnant le joint de grain (indiqué par une flèche blanche), ainsi que la direction de sollicitation (indiquée par σ) provoque un amorçage de fissure après un faible nombre de cycles par rapport à la durée de vie. Quelle que soit la contrainte cyclique appliquée (avec un rapport de charge R=0.1, pour des contraintes maximales σ_{max} comprises entre 130 et 240 MPa correspondant à des durées de vie entre 5×10^4 et 10^7 cycles), la phase d'initiation de fissure représente toujours moins de 2% de la durée de vie. Cependant, il faut noter que pour les durées de vie les plus élevées, des arrêts de fissures sont observés.

Modélisation de la propagation de fissure

Dans les cas où la phase de propagation est plus importante que la phase d'amorçage (cette proportion d'amorçage par rapport à la propagation est conditionnée par le matériau, mais surtout par le régime de fatigue étudié), il semble judicieux de tenter d'estimer la durée de vie par une loi similaire à la loi de Paris (voir Schwarmann [1986]). La croissance da/dN d'une fissure suivant alors :

$$\frac{da}{dN} = C\frac{\Delta K^m}{(1-R)K_f - \Delta K} \tag{1.5}$$

Ce modèle a été utilisé dans Buffière et al. [2002] sur un AS7G, avec les paramètres suivants :

- le rapport de contrainte $R = \sigma_{min}/\sigma_{max}$ est égal à R=0.1;
- m et C sont deux constantes matériaux, ici m=2.94 et C=2.9 $\times$ 10^{-9} ();
- K_f le facteur critique d'intensité de contraintes, K_f=41.5 MPa $m^{1/2}$;
- ΔK l'étendue du facteur d'intensité de contraintes.

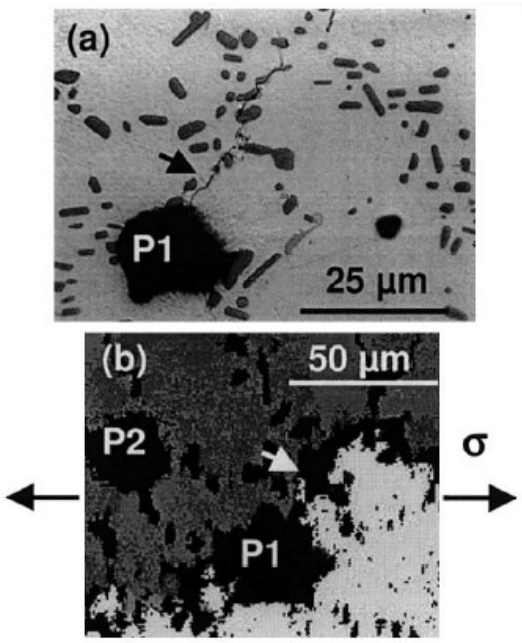

FIGURE 1.13 – (a) micrographie optique d'une fissure apparue en bordure d'une porosité P1 d'un alliage A356 T6, (b) analyse EBSD correspondante, Buffière et al. [2002]

Les résultats (cf. figure 1.14) montrent une bonne corrélation pour les contraintes élevées (correspondantes au faible durées de vie) où la propagation de fissure ne dépend que faiblement de la microstrucure. En revanche, pour les contraintes plus faibles, la modélisation sous-estime la durée de vie. Une modélisation plus récente décrite par McEvily and Ishihara [2001] propose une modélisation plus détaillée ajoutant 3 hypothèses :

1. Le comportement est élasto-plastique au lieu d'élastique, et il est introduit une longueur de fissure modifiée a_{mod} égale à la longueur réelle a à laquelle s'ajoute la moitié de la zone plastique en pointe de fissure :

$$a_{mod} = \frac{a}{2}\left(sec\frac{\pi\sigma_{max}}{2\sigma_Y} + 1\right) \tag{1.6}$$

   où σ_{max} est la contrainte maximale appliquée au cours du cycle et σ_Y la limite d'élasticité (en traction monotone) du matériau;

2. Le comportement des microfissures (moins de $100\mu m$) est gouverné par la limite d'endurance et non la loi de propagation macroscopique, conduisant à l'expression de la variation du facteur d'intensité des contraintes :

$$\Delta K = \left[\sqrt{\pi r_e\left(sec\frac{\pi\sigma_{max}}{2\sigma_Y} + 1\right)} + Y\sqrt{\frac{\pi}{2}a\left(sec\frac{\pi\sigma_{max}}{2\sigma_Y} + 1\right)}\right]\Delta\sigma \tag{1.7}$$

   où Y est le facteur de forme (par exemple Y est égal à 0,73 dans le cas d'un défaut semi-circulaire) et r_e une constante définie de manière empirique. Cette dernière permet de faire le lien entre comportement en endurance et propagation de fissure macroscopique. En première approximation, elle peut être définie physiquement comme une taille de fissure qui serait présente initialement dans le matériau.

3. La fermeture de fissure dans le cas d'une fissure nouvellement formée est prise en compte par :

$$\Delta K_{op} = (1 - \mathrm{e}^{-k\lambda})(K_{op,max} - K_{min}) \tag{1.8}$$

où ΔK_{op} est égal à $K_{op} - K_{min}$, K_{min} étant égal à $Y\sigma_{min}\sqrt{\pi a}$. La constante k représente le taux de fermeture de fissure avec l'augmentation de la taille de fissure (notée λ). Enfin, $K_{op,max}$ est le niveau d'ouverture de fissure dans le cas d'une fissure macroscopique.

Avec ces hypothèses, McEvily and Ishihara [2001] propose une nouvelle expression du taux d'accroissement de fissure :

$$\frac{da}{dN} = AM^2 \tag{1.9}$$

où M représente la quantité :

$$M = \left[\sqrt{\pi r_e\left(sec\frac{\pi\sigma_{max}}{2\sigma_Y}+1\right)} + Y\sqrt{\frac{\pi}{2}a\left(sec\frac{\pi\sigma_{max}}{2\sigma_Y}+1\right)}\right]\Delta\sigma$$
$$-(1-\mathrm{e}^{-k\lambda})(K_{op,max}-K_{min}) - \Delta K_{eff,th}$$

Cette nouvelle modélisation (cf. équation 1.9) présente les mêmes tendances que la première : une bonne corrélation pour des contraintes élevées, des écarts beaucoup plus importants à contraintes faibles. Néanmoins pour des niveaux de contraintes intermédiaires (cf. $\Delta\sigma = 200$Mpa et 160Mpa figure 1.14) la nouvelle loi présente toujours une meilleure corrélation que la loi de Paris.

Pour les contraintes plus faibles ($\Delta\sigma = 160$Mpa), les auteurs de Buffière et al. [2002] estiment que pour améliorer la modélisation, il est nécessaire de prendre en compte le blocage de la propagation de fissures aux barrières microstructurales.

Pour les matériaux concernés, et ce à température ambiante, la propagation de fissure est prédominante sur l'amorçage. Les études tendent à montrer que de nombreux défauts amorcent des fissures, mais très peu croissent jusqu'à une fissure macroscopique. La propagation de fissure est souvent modélisée par une loi de Paris (avec ou sans améliorations). Cette approche ne donne des résultats probants que pour des contraintes importantes (et donc de faibles durées de vie).

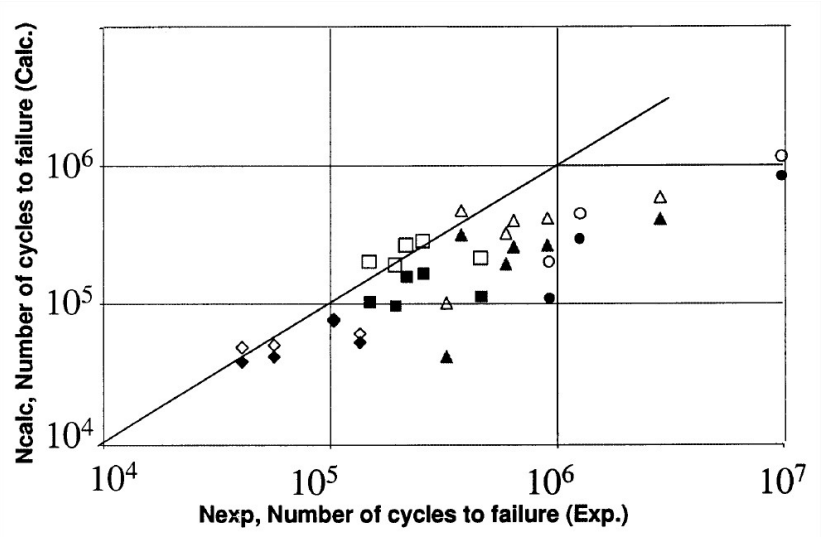

FIGURE 1.14 – Comparaison du nombre de cycles à rupture expérimental (Nexp) et calculé (Ncalc) par différentes méthodes (⋄, $\Delta\sigma$=240 MPa; □, $\Delta\sigma$=200 MPa; △, $\Delta\sigma$=160 MPa; O, $\Delta\sigma$=130 MPa). Les symboles pleins correspondent à l'application de la loi de Paris (1.5), et ceux creux à l'application de l'équation (1.9), d'après Buffière et al. [2002]

1.3 Étude de la fatigue oligocyclique à chaud

Dans la fatigue oligocyclique de l'aluminium, à chaud comme à température ambiante, les déformations plastiques sont prépondérantes. Pour caractériser l'endommagement résultant, la loi de Manson-Coffin (ici ne prenant en compte que la partie plastique de la déformation) est une des plus simples à utiliser :

$$N_F = \left(\frac{C_{MC}}{\Delta\varepsilon_p}\right)^{\gamma_{MC}} \tag{1.10}$$

Cependant, cette relation présuppose un cumul linéaire de l'endommagement qui la rend inefficace dans le cas de chargements thermomécaniques ou à température variable. Étant indépendante de la température, elle n'est applicable ni aux essais en fatigue thermomécanique, dont la température peut varier en cours d'essai, ni aux essais à températures différentes (le critère nécessite un jeu de paramètres par température, comme montré partie 3.3.1). Ce chapitre se concentrera donc sur les différentes modélisations de la littérature pouvant être utilisées comme critère de dimensionnement en fatigue oligocyclique à chaud.

1.3.1 Critère énergétique

Par la suite, les paramètres des critères seront notés Φ_i, i correspondant aux différentes modélisations. Ces critères présupposent l'utilisation d'une loi puissance du type :

$$\Phi_i = A \cdot (N_f)^B \tag{1.11}$$

A et B étant des paramètres matériaux dépendant éventuellement de la température. Le critère énergétique le plus simple s'écrit alors en calculant l'énergie dissipée sur un cycle stabilisé :

$$\Phi_{\Delta W_p} = \Delta W_p = \int_{cycle} \underline{\underline{\sigma}} : \underline{\underline{\dot{\varepsilon}}}_p dt \tag{1.12}$$

Par rapport au critère de Manson-Coffin, ce critère présente l'avantage d'être multiaxial et applicable à des configurations anisothermes. De plus, en comparaison de l'amplitude de déformation plastique, l'énergie plastique dissipée par cycle est peu sensible au durcissement et à l'adoucissement du matériau permettant d'estimer rapidement le critère de rupture, Skelton et al. [1996]. Charkaluk et al. [2004], utilisant certains des résultats de l'étude de Constantinescu et al. [2004], ont appliqué ce critère pour estimer la durée de vie d'un alliage A356 avec un traitement thermique T7, ainsi qu'un acier Silicium Molybdenum (SiMo) utilisé dans les collecteurs d'échappement. Ces matériaux ont été soumis à 3 types d'essais :

— essais LCF (*low cycle fatigue*) : essais entre 100°C et 700°C pour l'acier et 100-300°C pour l'alliage d'aluminium, pour des déformations de ±0.2% et ±1%;

— essais TMF (*thermo-mechanical fatigue*) : réalisés sur des éprouvettes de fatigue pour les mêmes températures.

— simulation sur banc : des essais sur banc d'essai d'organe sont comparés à des simulations numériques. La durée de vie correspond à l'apparition d'une fissure macroscopique (fissure pouvant être par ailleurs difficile à localisée lors des essais)

La figure 1.15 montre une bonne corrélation sur les essais faits sur éprouvettes comme sur les essais sur pièces. De plus, selon les auteurs, la cartographie de l'endommagement permet une prévision correcte des zones d'apparition de fissures.

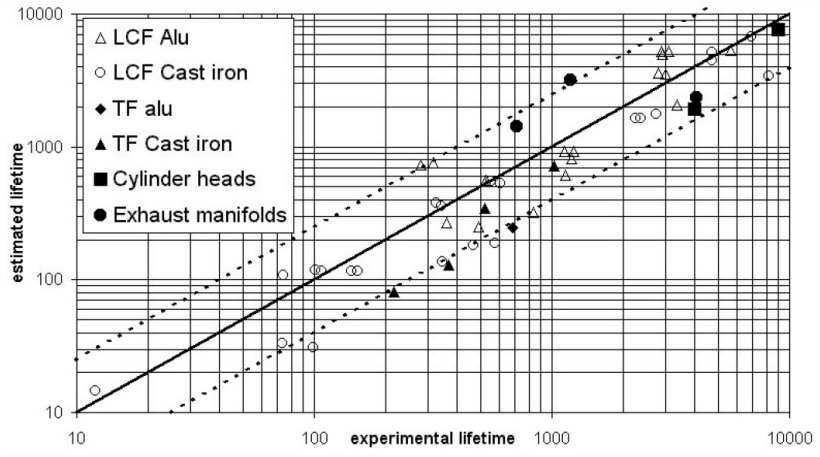

FIGURE 1.15 – Comparaison des durées de vie expérimentales et calculées d'un A356 et d'un acier SiMo, Charkaluk et al. [2004]

1.3.2 Critère de Koh

Dans Koh [2002], Koh utilise le même type d'approche pour un acier 2.2Ni-1Cr-0.5Mo-0.1V à température ambiante. L'utilisation du paramètre $\Phi_{\Delta W_p}$ montre des résultats satisfaisants uniquement pour des énergies de déformations plastiques supérieures à $1MJ/m^3$, et donc pour un nombre de cycles à rupture inférieur à 5000 cycles (cf. figure 1.16 (b)). De plus, pour les résultats d'essais de rapport de charge différents de (-1), $\Phi_{\Delta W_p}$ ne permet pas de rendre compte de l'influence de la contrainte moyenne. Pour remédier à ce défaut, une première approche consiste à utiliser l'énergie de déformation totale (se référer à la figure 1.16 (a) pour une représentation graphique des différentes énergies) :

$$\Phi_{Koh,Tot} = \Delta W_p + \Delta W_e = \Delta W_p + \frac{\Delta\sigma\Delta\varepsilon}{2} \tag{1.13}$$

Les résultats présentés en figure 1.16 (c), montrent de meilleurs résultats pour les essais à plus de 5000 cycles. Cependant, l'influence de la contrainte moyenne n'est toujours pas présente dans le critère. D'où l'introduction du critère de Koh, noté $\Phi_{Koh,e+}$, utilisant l'énergie élastique positive W_e^+ :

$$\Delta W_e^+ = \begin{cases} \dfrac{1}{2E}\left(\dfrac{\Delta\sigma}{2} + \sigma_m\right)^2 = \dfrac{\sigma_{max}^2}{2E}, & \text{pour } \sigma_{min} \leq 0 \\ \dfrac{(\sigma_{max} - \sigma_{min})^2}{2E}, & \text{pour} \sigma_{min} > 0 \end{cases} \tag{1.14}$$

ΔW_e^+ correspond à la densité d'énergie élastique par cycle en traction. Le critère de Koh s'écrit alors :

$$\Phi_{Koh,e+} = \Delta W_p + \Delta W_e^+ \tag{1.15}$$

Les résultats, présentés en figure 1.16 (d), montre de nouveau une amélioration des résultats. De plus, la droite en trait plein correspond à la droite obtenue par la méthode

des moindres carrés uniquement sur les essais à contrainte moyenne nulle (donc pour un rapport de charge R=-1). Les paramètres identifiés sont réutilisés sans recalage dans les essais à contrainte moyenne non-nulle, montrant que l'utilisation de ce critère est performante pour l'estimation de la durée de vie pour des conditions diverses.

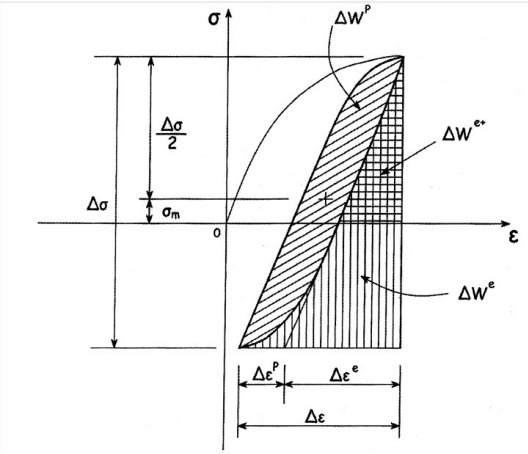

(a) Energies mises en jeu dans un cycle stabilisé

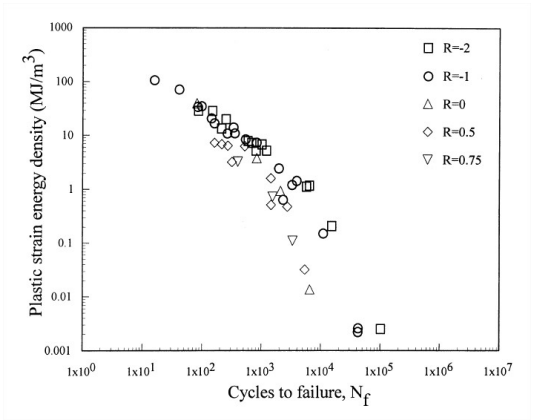

(b) nombre de cycles à rupture en fonction de l'énergie plastique $\Phi_{\Delta W_p}$

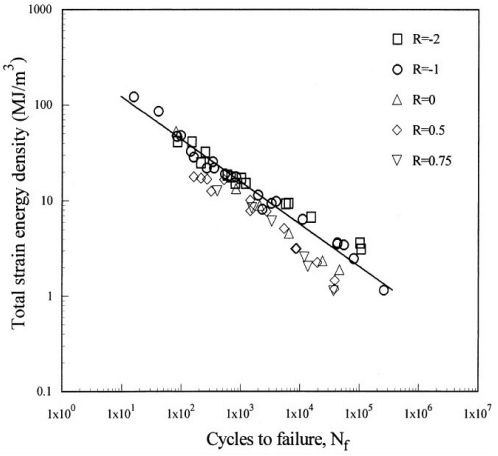

(c) en fonction de l'énergie totale $\Phi_{Koh,Tot}$

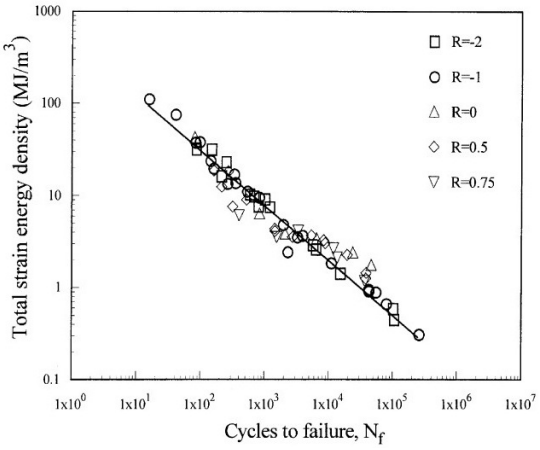

(d) en fonction du critère de Koh $\Phi_{Koh,e+}$

FIGURE 1.16 – Essai de fatigue oligocyclique sur un acier à température ambiante, Koh [2002]

1.3.3 Critère en propagation

Par une approche en fissuration, Maurel et al. [2009] introduit également un critère énergétique de fatigue oligocyclique pour un acier inoxydable. Les essais étant effectués à chaud (300 °C), le nombre de cycles à rupture est gouverné par la propagation, et non par l'amorçage de fissure. Les auteurs de Maurel et al. [2009] introduisent une longueur caractéristique λ telle que λ=3d$_g$, d$_g$ étant le diamètre moyen des grains. Cette longueur permet de rationaliser l'accroissement de fissure par cycle (da/dN) et de le relier à l'accroissement de l'endommagement par cycle (dD/dN). Le critère d'évolution de l'endommagement s'écrit alors :

$$\frac{dD}{dN} = \frac{1}{\lambda}\frac{da}{dN} = \left[\left(\beta_e \frac{W_e^{open}}{\gamma_e} a\right)^{m_e} + \left(\beta_p \frac{W_p^{dist}}{\gamma_p} a\right)^{m_p}\right] \tag{1.16}$$

avec D le paramètre d'endommagement, N le nombre de cycles, a la longueur de fissure, γ_i les énergies de surface (avec $i = p$ pour la partie plastique et $i = e$ pour la partie élastique), m_i les exposants des lois puissance et β_i les facteurs de forme. L'énergie élastique d'ouverture de fissure W_e^{open} et l'énergie plastique de distorsion W_p^{dist} sont définies par :

$$W_e^{open} = \int_{cycle} dW_e^{open} = \frac{1}{3}\int_{cycle} < tr(\underline{\underline{\sigma}}) > tr(d\underline{\underline{\varepsilon}}) \tag{1.17}$$

$$W_p^{dist} = \int_{cycle} dW_p^{dist} = \int_{cycle} \underline{\underline{s}} : d\underline{\underline{\varepsilon}}_p, \qquad \text{avec } \underline{\underline{s}} = \underline{\underline{\sigma}} - \frac{1}{3}tr(\underline{\underline{\sigma}})\underline{\underline{1}} \tag{1.18}$$

$\underline{\underline{s}}$ étant le déviateur des contraintes, : le produit doublement contracté et $< \bullet >$ la partie positive. L'énergie de déformation élastique peut être définie indépendamment en utilisant ε ou ε_e, la déformation plastique étant incompressible (ie. tr($\underline{\underline{\varepsilon}}_p$)=0).

Cette modélisation permet la comparaison simulation/expérience de la propagation de fissure (cf. figure 1.17 (a)). Il est à noter que dans ce modèle, la définition de la longueur de fissure initiale a_{ini} nécessaire à l'intégration numérique est définie comme la profondeur d'entaille pour les éprouvettes entaillées, et $a_{ini}=d_g/2$ pour une éprouvette non-entaillée. La durée de vie en fatigue oligocyclique coïncide alors avec une longueur de fissure jugée critique, ici a_f=2mm. La figure 1.17(b) montre de bons résultats au dessus de 1000 cycles. En dessous, les écarts du modèle élasto-visoplastique à la mesure sont trop importants et conduisent à une sous-évaluation des contraintes.

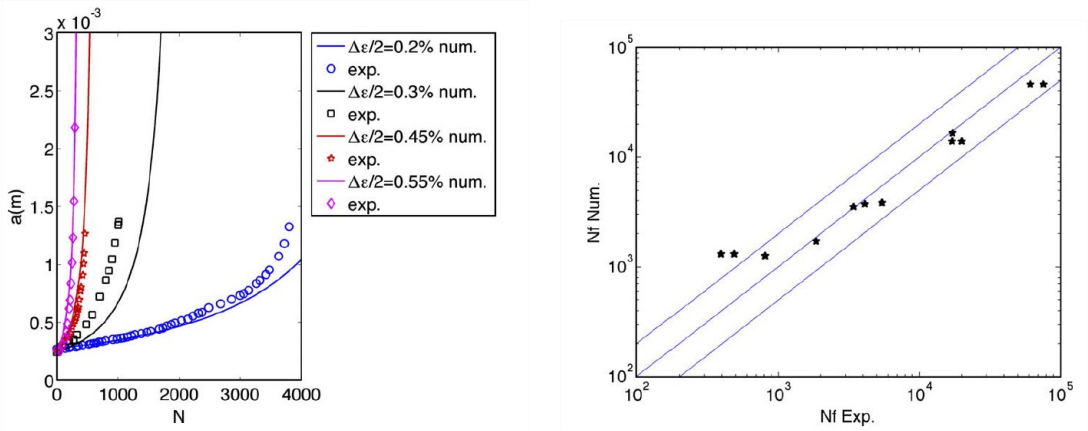

(a) Comparaison entre la longueur de fissure simulée et la longueur mesurée expérimentalement pour différentes amplitudes de déformation

(b) Durée de vie en fatigue simulée en fonction des valeurs expérimentales

FIGURE 1.17 – Cas d'un acier F17TNb en fatigue oligocyclique à 300 °C, Maurel et al. [2009]

1.3.4 Comparaison des critères

Les paragraphes précédents ont permis d'introduire différents critères. Tabibian et al. [2010] utilise ces 3 critères pour évaluer la durée de vie d'un alliage A319 (AS7U3G) moulé par modèle perdu et sans traitement thermique. Avec ce procédé, l'alliage obtenu a une structure plus grossière que par coulée par gravité, le DAS résultant étant aux alentours de 85μm. Les critères ont été simplifiés de par la nature

cyclique et uniaxiale des essais. Dans les trois cas, l'énergie est reliée au nombre de cycles à rupture par une loi puissance :

$$\Phi_i = AN^{-c} \tag{1.19}$$

Pour le critère de déformation plastique cumulé, l'énergie sur un cycle stabilisé se calcule par :

$$\Phi_{\Delta W_p} = \int_{cycle} \sigma \dot{\epsilon}_p dt \tag{1.20}$$

Pour le critère de Haddar (Haddar [2003]) :

$$\Phi_{Haddar} = \Delta W_p + \Delta W_e = \frac{\Delta\sigma^2}{E} + \Delta\sigma \cdot \Delta\epsilon \tag{1.21}$$

Enfin, pour le critère de Koh :

$$\Phi_{Koh} = \Delta W_p + \Delta W_e^+ \tag{1.22}$$

$$\Delta W_e^+ = \begin{cases} \frac{{\sigma_{max}}^2}{2E}, & \text{pour } \sigma_{min} \leq 0 \\ \frac{(\sigma_{max} - \sigma_{min})^2}{2E}, & \text{pour} \sigma_{min} > 0 \end{cases} \tag{1.23}$$

Les résultats (issus de Tabibian et al. [2010]) sont présentés dans la figure 1.18. Les différentes modélisations donnent toutes de bons résultats, avec une légère amélioration pour les critères de Haddar et de Koh (donc en utilisant une combinaison de l'énergie de déformation plastique et une énergie de déformation élastique).

En conclusion, le modèle classique de Manson-Coffin est encore très utilisé dans le domaine de la fatigue oligocyclique, car simple d'utilisation. Des critères énergétiques ont récemment été développés et présentent des résultats prometteurs, ils sont utilisables dans un cadre industriel. Ces critères peuvent en effet être appliqués aux essais de fatigue oligocycliques à partir des seules courbes de comportement mécanique contrainte-déformation.

1.3.5 Influence des porosités

De manière similaire à la fatigue à température ambiante (voir la partie 1.2.2), les porosités ont une influence négative sur la durée de vie. Plusieurs études (voir Charkaluk et al. [2014], Dezecot et al. [2016] ou encore Dahdah et al. [2016]) s'intéressent à la fatigue oligocyclique à chaud et à la fatigue thermomécanique d'alliages d'aluminium moulés par modèle perdu. Ce procédé de fabrication permet des coûts réduits, mais n'autorise pas des vitesses de refroidissement élevées (de l'ordre de 0,8°C/s à comparer à 30°C pour les modèles permanent, Albonetti [2000]). Ces vitesses plus faibles donnent lieu à des microstructures plus grossières, ainsi que des porosités de tailles importantes.

En utilisant un four spécialement conçu pour la réalisation d'essais *in-situ* de fatigue oligocyclique à chaud, les auteurs de Dezecot et al. [2016] observent la propagation de fissures dans un alliage réalisé par modèle perdu. La figure 1.19 montre ainsi un amorçage de fissure sur une porosité située proche du bord libre. Le moyen *in-situ* permet notamment de remarquer que l'amorçage de la fissure a lieu sur la partie la plus à cœur de la porosité.

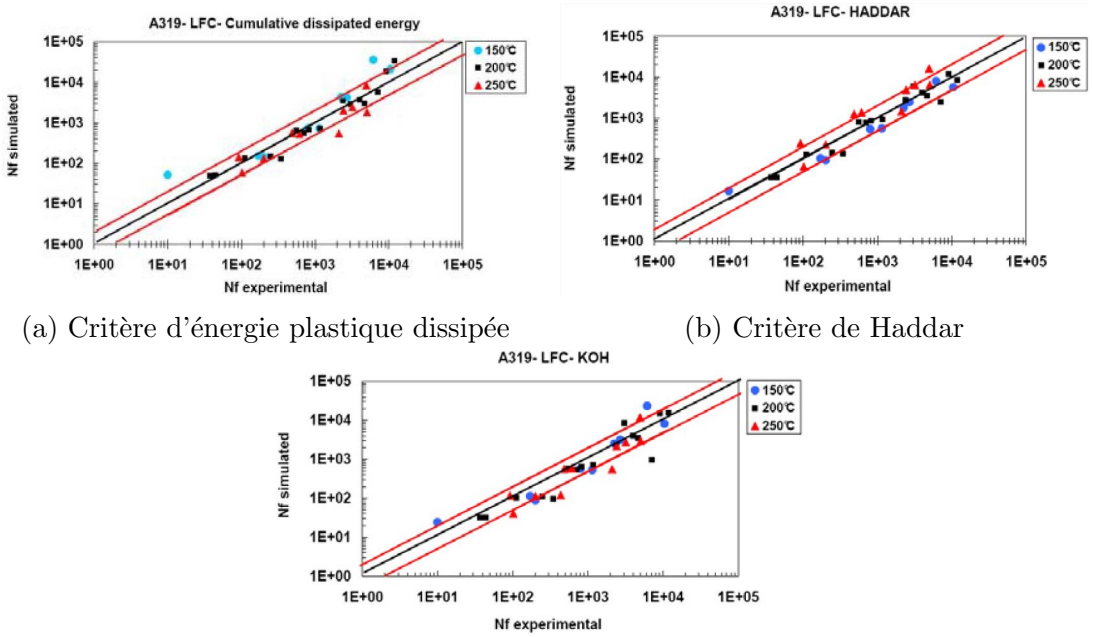

(a) Critère d'énergie plastique dissipée

(b) Critère de Haddar

(c) Critére de Koh

FIGURE 1.18 – Simulation des durées de vie en fatigue d'un alliage A319 en fatigue oligocyclique à chaud (T=150, 200 et 250 °C), Tabibian et al. [2010].

Dans un premier temps dans Wang et al. [2016], les auteurs utilisent les techniques de corrélation d'images numériques sur des observations réalisées en tomographie au synchrotron pour des essais à température ambiante. La figure 1.20 démontre les avantages de cette technique : elle permet non-seulement de confirmer l'amorçage de la fissure sur les concentrations de contraintes en bord de porosités, mais également de faire ressortir les micro-fissures grâce à la déformation plus hétérogène dans le voisinage des fissures.

En utilisant la même méthode par corrélation d'images numériques, les auteurs de Dahdah et al. [2016] observent le même alliage d'aluminium à plus haute température. Par exemple, la figure 1.21 montre la comparaison entre les calculs par la méthode des éléments finis (faits sur un maillage basé sur la microstructure observée par tomographie) et le résultat de la corrélation d'images numériques. Cette comparaison permet de montrer que les calculs ne font apparaître que les concentration de contraintes dues aux défauts de type porosité, alors que les inclusions (comme les intermétalliques) provoquent également l'amorçage de micro-fissures (entourés en rouge dans la figure 1.21).

Toujours pour le même alliage d'aluminium réalisé par modèle perdu, les auteurs de Charkaluk et al. [2014] modélisent la durée de vie en fatigue et surtout sa dispersion, en se basant sur la distribution de défauts observée en 2D. En faisant l'hypothèse que les défauts sont équivalents à des fissures, un modèle de propagation de fissure permet alors d'estimer la durée de vie N_f pour une taille de défaut donnée :

$$N_f = \left(\frac{\Phi}{k}\right)^m (a_0^{1-m} - a_f^{1-m}) \tag{1.24}$$

avec a_0 la taille de défaut (considérée comme la taille de fissure initiale), a_f la taille de fissure finale, k et m deux paramètres matériaux. La paramètre de fatigue Φ utilisé dans cette étude s'exprime en fonction de l'énergie de déformation plastique ΔW et de la pression hydrostatique maximale au cours d'un cycle σ_H^{max}:

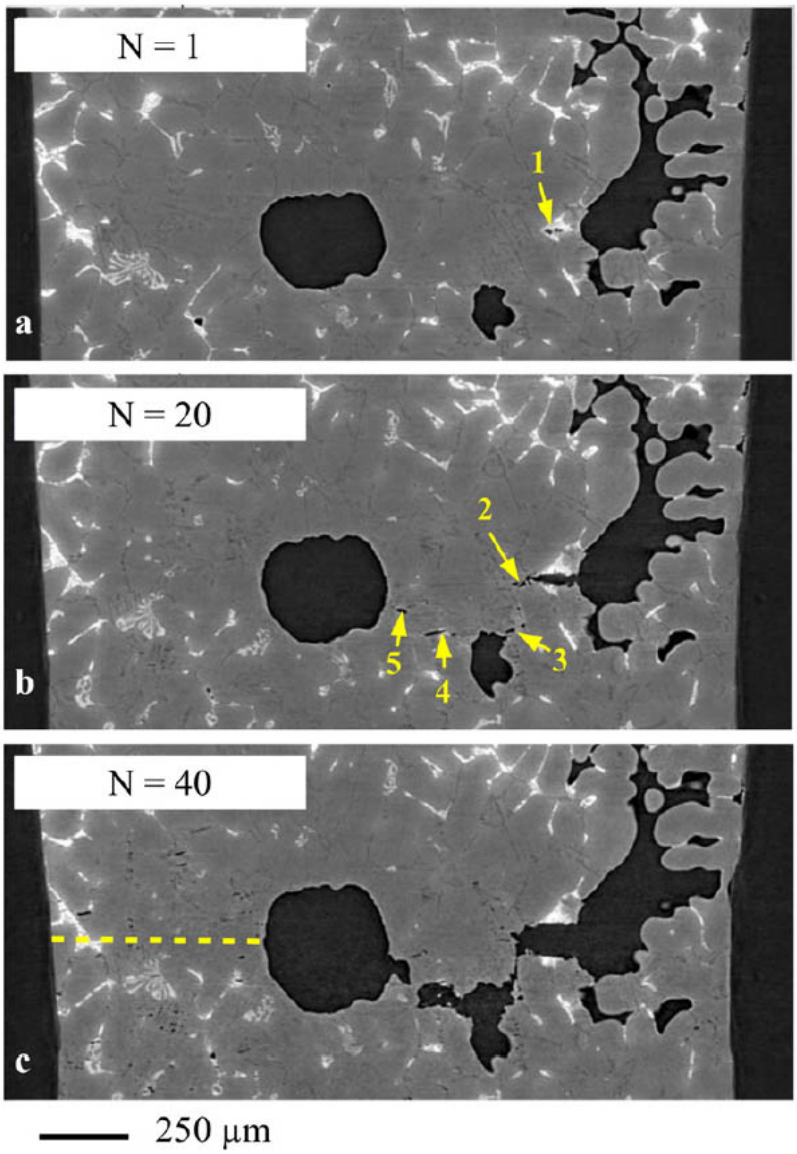

FIGURE 1.19 – Tomographie réalisée au synchrotron montrant la propagation de fissure amorcée sur une porosité en fonction du nombre de cycles N pour un essai à 250 °C. La sollicitation en fatigue est dans le sens verticale. (Dezecot et al. [2016])

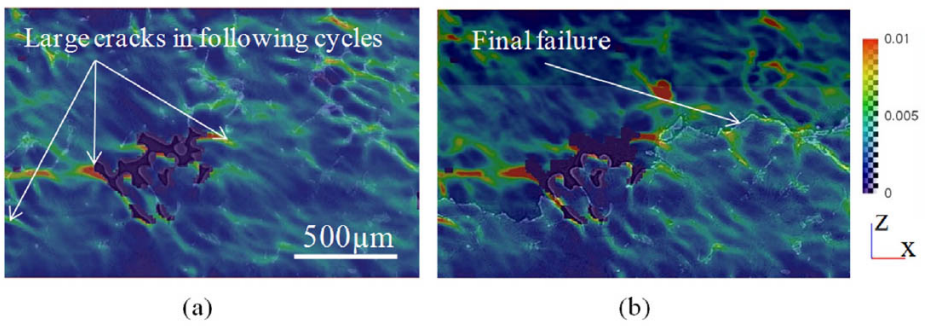

FIGURE 1.20 – Mesure de l'équivalent de von Mises de la déformation par corrélation d'images numériques entre la charge minimale atteinte au premier cycle et (a) le maximum du deuxième cycle, (b) le maximum du vingtième cycle, (Wang et al. [2016])

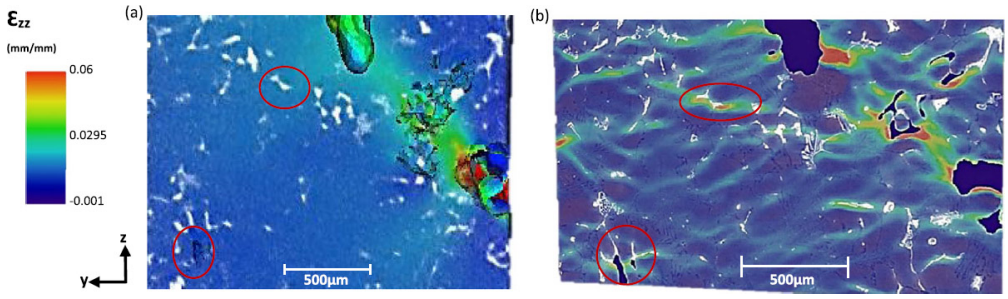

FIGURE 1.21 – Champ de déformation ε_{zz} à 250 °C au premier cycle :(a) Champ calculé par la méthode des éléments finis, (b) Champ observé par corrélation d'images numériques, (Dahdah et al. [2016])

$$\Phi = \Delta W + \alpha \sigma_H^{max} \tag{1.25}$$

où α est un paramètre matériau et avec l'énergie de déformation plastique :

$$\Delta W = \int_{cycle} \underline{\underline{\sigma}} : \dot{\underline{\underline{\varepsilon}}}_p dt \tag{1.26}$$

et la pression hydrostatique maximale :

$$\sigma_H^{max} = \max_{cycle} \frac{1}{3} \mathrm{tr} \underline{\underline{\sigma}} \tag{1.27}$$

Ainsi, il est possible d'avoir la distribution de durées de vie pour chaque condition expérimentale (voir par exemple la figure 1.22). Ce type d'approche en propagation de fissure semble la plus appropriée pour la prise en compte des défauts dans la fatigue oligocyclique.

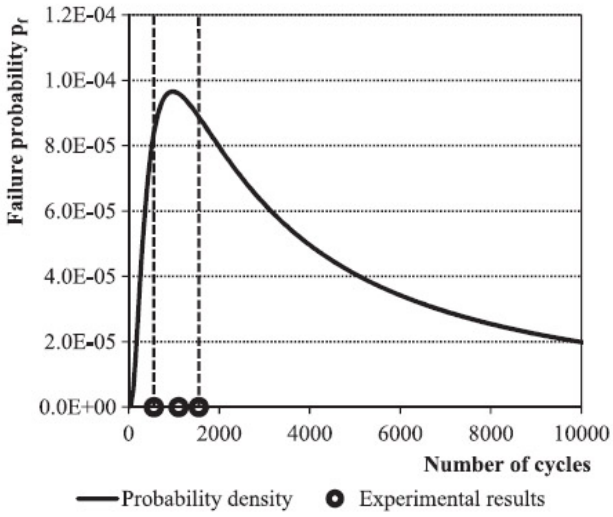

FIGURE 1.22 – Fonction densité de probabilité de durée de vie calculée à partir de la distribution de défauts, Charkaluk et al. [2014].

1.4 Concentration de contraintes sur éprouvette entaillée

Dans le cas de structures réelles, l'état de contrainte peut rarement être considéré comme homogène dans son ensemble. En particulier, la présence de concentrations de contraintes est souvent propice à l'apparition de fissures en fatigue. Ces concentrations locales peuvent être imposées par la géométrie de la structure (cas d'un trou pour le passage d'une vis) ou liées au procédé (par exemple un pore débouchant). L'étude sur éprouvette entaillée permet de quantifier l'influence des concentrations de contraintes, et en particulier de connaître la sensibilité d'un matériau à l'effet d'entaille.

1.4.1 Généralités sur les géométries entaillées

Bien que sortant du cadre de notre étude, la fatigue en endurance, donc principalement en élasticité linéaire, est à l'origine de l'introduction du coefficient théorique de concentration de contraintes K_t. Cette partie vise à introduire les concepts généraux qui pourront être étendus à la fatigue à faible nombre de cycles.

Coefficient théorique de concentration de contrainte

Dans le cadre d'un milieu plan infini soumis à un champ de contraintes homogènes, la définition du coefficient théorique de concentration de contraintes s'écrit :

$$K_t = \frac{\sigma^t_{max}}{|\sigma^t_{nom}|} \tag{1.28}$$

σ^t_{max} étant la contrainte élastique théorique maximale, ici atteinte en fond d'entaille, et σ^t_{nom} la contrainte élastique théorique nominale (c.f. figure 1.23).

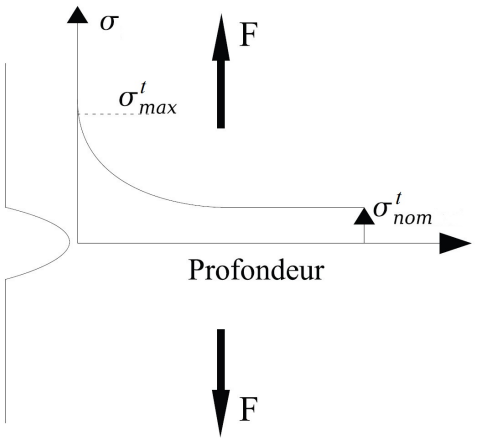

FIGURE 1.23 – Illustration d'un milieu plan infini soumis à un champ de contraintes homogènes Bidouard [2009]

La relation 1.28 est valable uniquement en régime élastique. Par extension, le coefficient théorique de contrainte $K_{t\sigma}$ est défini par :

$$K_{t\sigma} = \frac{\sigma_{max}}{|\sigma_{nom}|} \tag{1.29}$$

σ_{nom} étant la contrainte nominale réelle et σ_{max} la contrainte réelle maximale atteinte dans la structure. De manière analogue, le coefficient théorique de concentration de déformation $K_{t\varepsilon}$ est :

$$K_{t\varepsilon} = \frac{\varepsilon_{max}}{|\varepsilon_{nom}|} \tag{1.30}$$

où ε_{nom} est la déformation nominale et ε_{max} la déformation réelle maximale atteinte dans la structure. Il convient de noter que les coefficients $K_{t\sigma}$ et $K_{t\varepsilon}$ peuvent être calculés pour une structure quelconque.

Relation entre K_t et durée de vie

L'approche directe, dite du "point chaud", consiste à considérer que la limite d'endurance est un paramètre matériau indépendant de la structure. Ainsi, pour une éprouvette entaillée, sa limite d'endurance correspondra à la contrainte nominale à appliquer de manière à obtenir une contrainte maximale égale à la limite d'endurance classique (c'est-à-dire la limite d'endurance d'une éprouvette lisse). La figure 1.24 illustre ce raisonnement dans le cas d'une limite d'endurance valant 250MPa.

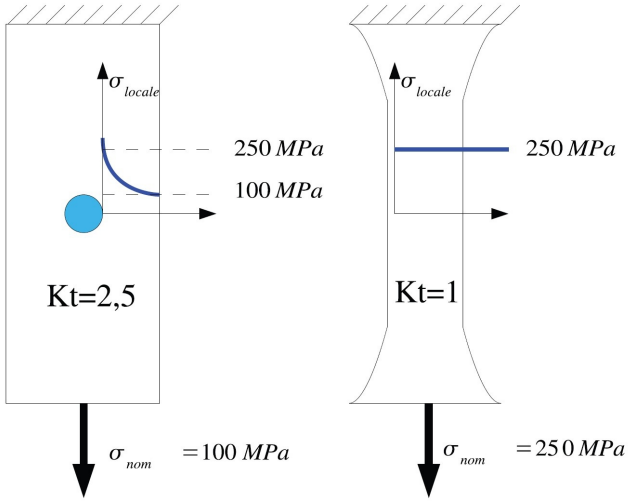

$$\Delta\sigma_{(K_t=2.5)} = \Delta\sigma_{(K_t=1)} \times 2,5$$

FIGURE 1.24 – Illustration de la limite d'endurance par la méthode du "point chaud" Bidouard [2009]

Les essais tendent à prouver que la relation n'est pas si directe. L'approche "point chaud" conduit à sous-estimer la durée de vie des éprouvettes entaillées, d'où l'introduction d'un coefficient effectif d'entaille K_f :

$$K_f = \frac{\sigma_0^{lis}}{\sigma_0^{ent}} \tag{1.31}$$

σ_0^{lis} étant la limite d'endurance d'une éprouvette lisse et σ_0^{ent} celle d'une éprouvette entaillée (en contrainte nominale).

L'indice de sensibilité q permet d'évaluer la dépendance de la durée de vie à l'entaille pour un essai :

$$q = \frac{K_f - 1}{K_t - 1} \tag{1.32}$$

ce dernier varie entre 0, dans le cas d'un essai insensible à l'effet d'entaille, à 1, valeur qui correspond à l'approche "point chaud". L'indice q est défini pour un essai et non pour un matériau. En effet, Peterson and Wahl [1936] ont montré que l'indice variait avec le matériau considéré, mais également avec la géométrie de la pièce et de l'entaille.

1.4.2 Éprouvettes entaillées en élasticité linéaire

Approches classiques

Dans Neuber [1958], l'auteur fait remarquer que l'approche "point chaud" considère uniquement le point de contrainte maximale pour évaluer la durée de vie, plutôt qu'une zone représentative. Il définit alors cette dernière comme une zone non infinitésimale dans laquelle la contrainte est moyennée sur plusieurs distances de références (taille de grains ou tout autre élément unitaire de base). Cette méthode est illustrée par la figure 1.25 (a) où D_{LM} (LM : *Line Method*) est la distance critique telle que l'intervalle $[0,D_{LM}]$ soit représentatif du comportement du matériau. Son pendant simplifié établi par Peterson dans Peterson [1959], et illustré par la figure 1.25 (b), suggère qu'il existe une distance critique D_{PM} (PM : *Point Method*) définissant un point où la contrainte est représentative du phénomène d'endommagement. Les deux méthodes LM et PM peuvent alors se simplifier en :

$$K_f = 1 + \frac{K_t - 1}{1 + \sqrt{\frac{a^*}{r_n}}} \tag{1.33}$$

$$K_f = 1 + \frac{K_t - 1}{1 + \frac{a^*}{r_n}} \tag{1.34}$$

a^* étant la constante matériau de la méthode de Neuber et a' celle de Peterson. La difficulté réside alors dans la relation entre la distances a^* et D_{LM} (ou a' et D_{PM}). À titre d'exemple, pour un chargement en flexion ou en traction/compression, la méthode PM utilise :

$$a' = D_{PM}\frac{2.5 \cdot K_t}{K_t - 1} \tag{1.35}$$

le facteur 2.5 étant le résultat d'un ajustement.

Théorie de la distance critique (TCD, *theory of critical distance*)

Les récentes avancées du calcul par éléments finis ont permis de reprendre le calcul initialement proposé par Neuber, afin d'évaluer numériquement la distance critique. Les méthodes LM de Neuber et PM de Peterson étant des cas particuliers de la théorie de la distance critique (TCD, *theory of critical distance*). Celles-ci sont à mettre en parallèle de la méthode de distance critique L issue de la mécanique de la rupture élastique (LEFM :*Linear Elastic Fracture Mechanics*) donnée par El Haddad et al. [1979] :

$$L = \frac{1}{\pi}\left(\frac{\Delta K_{th}}{\Delta \sigma_0}\right)^2 \tag{1.36}$$

ΔK_{th} étant le seuil de propagation des fissures longues et $\Delta\sigma_0$ la limite d'endurance, ces deux valeurs étant calculées pour un rapport de charge R identique.

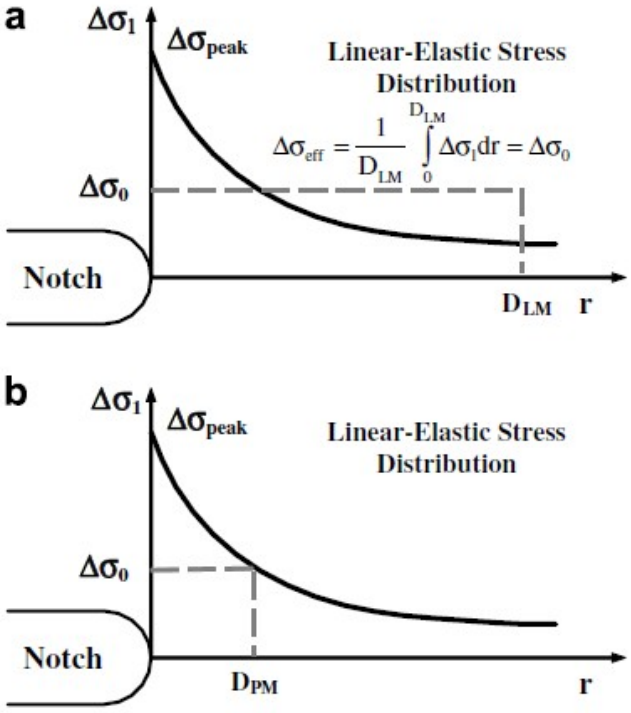

FIGURE 1.25 – (a) Méthode de la ligne de Neuber et (b) méthode du point de Peterson (b), Susmel [2008]

La TCD suppose que la structure entaillée est en condition de limite d'endurance si la contrainte effective $\Delta\sigma_{eff}$ (la contrainte effective est une contrainte équivalente qui dépend de la distribution des contraintes principales dans le voisinage du point chaud) est égale à la limite d'endurance $\Delta\sigma_0$:

$$\Delta\sigma_{eff} = \Delta\sigma_0. \tag{1.37}$$

En notant $\Delta\sigma_1$ la plus grande contrainte principale avec les notations décrites figure 1.26, il vient les différentes formulations de la TCD. La méthode de la ligne (LM) s'écrit :

$$\Delta\sigma_{eff} = \frac{1}{2L}\int_0^{2L} \Delta\sigma_1(\theta = 0, r)dr = \Delta\sigma_0. \tag{1.38}$$

où $2L = D_{LM}$ dans le formalisme décrit figure 1.25.

Dans Tanaka [1983] et dans Taylor [1999], la méthode du point PM se traduit par :

$$\Delta\sigma_{eff} = \Delta\sigma_1(\theta = 0, r = \frac{L}{2}) = \Delta\sigma_0. \tag{1.39}$$

avec ici $L/2 = D_{PM}$.

À l'inverse, Lazzarin et al. [1997] utilise $L = D_{PM}$ ainsi qu'une fonction correctrice adimensionnelle :

$$\Delta\sigma_{eff} = \Delta\sigma_1(\theta = 0, r = L)\frac{1 + \sqrt{2}\frac{L}{r_n}}{1 + \frac{L}{r_n}} = \Delta\sigma_0. \tag{1.40}$$

faisant ainsi dépendre la contrainte effective du rayon d'entaille r_n.

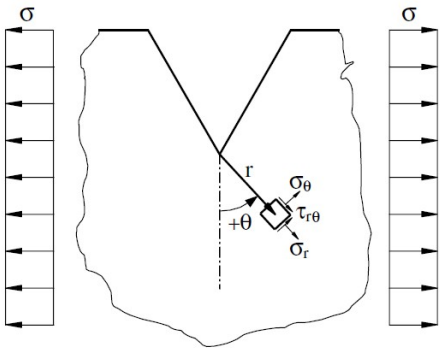

FIGURE 1.26 – Éprouvette entaillée soumise à un chargement de fatigue uniaxial : notations

Les méthodes PM et LM ont été comparées dans Susmel and Taylor [2003]. Les résultats obtenus pour des matériaux très variés démontrent une bonne corrélation avec l'expérience dans le régime mégacyclique (c.f. figure 1.27)

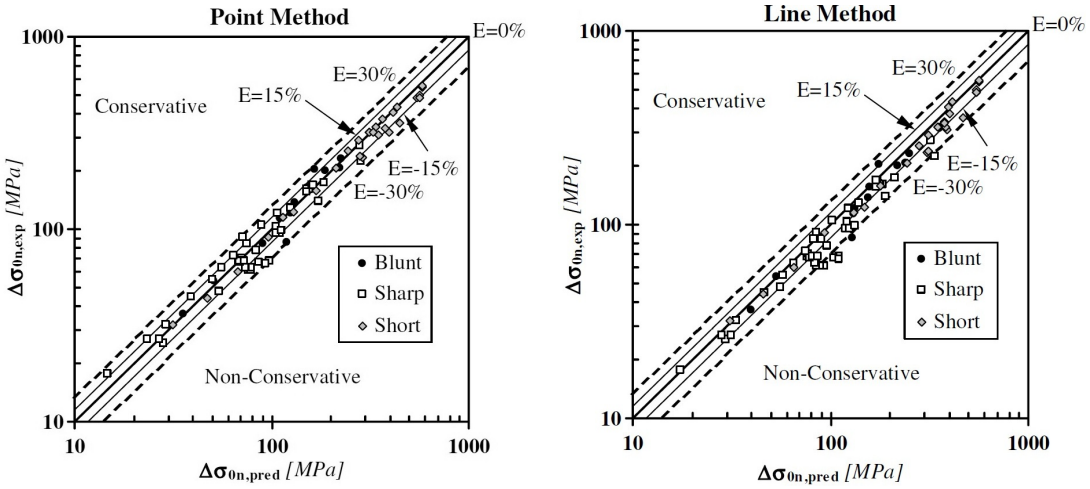

(a) Méthode du point (PM) selon l'équation 1.39

(b) Méthode de la ligne (LM) selon l'équation 1.38

FIGURE 1.27 – Théorie de la distance critique : limite d'endurance expérimentale en fonction de la limite calculée, Susmel and Taylor [2003]

Par extension, dans Taylor [1999], les auteurs moyennent la contrainte dans une aire semi-circulaire (AM :*Area Method*) :

$$\Delta\sigma_{eff} = \frac{4}{\pi L} = \int_{-\frac{\pi}{2}}^{\frac{\pi}{2}} \int_0^L \Delta\sigma_1(\theta, r) dr d\theta = \Delta\sigma_0 \tag{1.41}$$

Cette méthode montre des résultats comparables aux deux précédentes, mais nécessite une analyse plus complexe du champ de contraintes.

Il est également possible de pondérer la contrainte. Weixing [1993] a ainsi développé une approche basée sur le calcul d'une contrainte σ_{FI}. Celle-ci est définie par :

$$\sigma_{FI} = \frac{1}{V} \int_\Omega f(\underline{\underline{\sigma}}) \varphi(\vec{r}) dv \tag{1.42}$$

Ω étant la zone de rupture par fatigue et $\vec{r}$ le vecteur position (avec les notation de la figure 1.26). **Cette région n'a pu être corrélée systématiquement à une taille**

physique de mécanisme d'endommagement et sert de variable d'ajustement expérimentale.

La fonction f fournit une quantité scalaire à partir du tenseur des contraintes $\underline{\underline{\sigma}}$. La première contrainte principale est un exemple d'une telle fonction.

La fonction de pondération φ détermine le poids de la contrainte au point $P(\vec{r})$ rapporté $O(\vec{r}=0)$. Généralement, cette fonction est une fonction décroissante de $|\vec{r}|$ et dépend uniquement du chargement et de la géométrie d'entaille. En prenant pour fonction de pondération la fonction identité ($\varphi(\vec{r}) = 1, \forall \vec{r}$), cette méthode revient à moyenner la contrainte dans un volume (VM : *Volume method*).

1.4.3 Effet d'entaille en élasto-plasticité

Comme vu dans la partie 1.4.2, le coefficient théorique de concentration de contraintes permet de décrire les phénomènes observés en élasticité linéaire. Néanmoins, en présence d'entaille, la contrainte maximale peut rapidement atteindre et dépasser la limite d'élasticité linéaire et plastifier le matériau.

Gradient de contrainte d'une distribution élasto-plastique

En plus des grandeurs habituelles, Brand and Sutterlin [1980] ont introduit le gradient de contrainte χ :

$$\chi(x) = \frac{1}{\sigma(x)} \frac{d\sigma(x)}{dx} \tag{1.43}$$

x étant la profondeur et $\sigma(x)$ la contrainte en ce point. Lorsque x n'est pas précisé, χ représente le gradient de contrainte en fond de fissure, il sera noté ici χ^0 pour plus de clarté :

$$\chi^0 = \lim_{x \to 0} \frac{1}{\sigma(x)} \frac{d\sigma(x)}{dx} \tag{1.44}$$

Dans le cas d'une zone élasto-plastique en fond d'entaille, et considérant qu'il y'a relaxation des contrainte dans cette zone, la distribution de contrainte et du gradient des contraintes peut se décomposer en 3 parties (voir figure 1.28) :

— *La zone I* inclut le point X_m de contrainte maximale σ_m. Dans le cadre de l'élasto plasticité, et avec relaxation des contraintes, la contrainte maximale diffère de celle en fond d'entaille : $X_{max} \neq 0$.

— *La zone II* délimité par le point X_{max} et la distance effective X_{eff}. Cette dernière est définie comme le premier minimum local de la fonction χ et considérée comme la limite spatiale du processus physique de fatigue. En rapport avec le TCD (voir 1.4.2), X_{eff} peut-être vue comme la distance critique.

— *La zone III* peut être modélisée par une loi puissance :

$$\sigma_{yy} = \frac{C}{x^{\alpha}} \tag{1.45}$$

C et α dépendant du matériau et de la géométrie. Les contraintes dans cette zone sont comparativement faibles et impactent peu l'endommagement en fatigue.

Ainsi, dans Qylafku [1999], les auteurs utilisent le gradient de contrainte conjointement à la formulation de l'équation 1.42 :

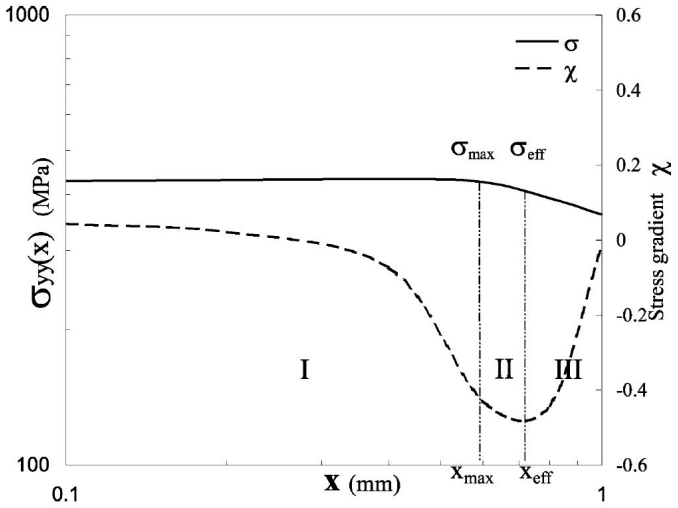

FIGURE 1.28 – Exemple d'évolution de la contrainte d'ouverture et du gradient relatif en fonction de la distance dans le cas d'une barre avec congé de rayon $\rho = 3.18\,\text{mm}$ (calcul éléments finis), Adib and Pluvinage [2003]

$$K_f = \frac{1}{S_N X_{ef}} \int_0^{X_{ef}} \sigma_{yy}[1 - x.\chi(x)]dx \tag{1.46}$$

σ_{yy} étant la contrainte normale au plan de chargement et S_N la contrainte nominale loin de l'entaille. La limite d'endurance d'une éprouvette entaillée sera alors :

$$\sigma_{FI} = K_f S_N = \sigma_s \tag{1.47}$$

σ_s étant la limite d'endurance d'une éprouvette lisse (*smooth specimen*).

Expérimentalement, dans Qylafku [1999], des éprouvettes en acier doux sont soumises à des essais de fatigue par flexion rotative. Les caractéristiques mécaniques du matériau sont : résistance à la traction R_m=500 MPa, limite élastique R_e=312 MPa et module de Young E=186000 MPa. Plusieurs critères sont appliqués à des éprouvettes entaillées avec deux rayons d'entaille ρ=0.2 et ρ=0.4 mm. Les résultats sont présentés dans le tableau 1.4 où K_t a été déterminé par un calcul aux éléments finis.

Les résultats se montrent trop conservatifs pour l'ensemble des critères excepté celui de l'auteur Qylafku [1999]. Il faut cependant nuancer ce résultat en notant que les critères de type "point chaud" ne sont pas adaptés aux entailles de faibles rayons (Heywood [1952]; Peterson [1959]). Le critère de Brand (Brand and Sutterlin [1980]) étant lui calculé ici pour des courbes $S - N$ à 90%, et non 50% de probabilité de rupture comme les autres, il n'est pas directement comparable. De plus, sous chargement uniaxial, le critère de Qylafku [1999] n'est pas restreint aux éprouvettes présentant une entaille semi-circulaire et peut s'appliquer à une géométrie quelconque d'entaille.

Effet d'entaille en fatigue oligocyclique

Une première approche, basée sur la TCD, consiste à introduire une zone volumique de processus de fatigue. Ainsi, dans Bentachfine [1999], les auteurs étudient l'acier 35NCD16, sur éprouvettes cylindriques lisses et entaillées (de rayon d'entaille $\rho = 0.4$ et 1.2 mm) et ce en déformation contrôlée. L'amplitude de contrainte cyclique $\Delta\sigma$ est supposée suivre la loi de Ludwick :

Table 1.4 – Limite d'endurance d'éprouvettes entaillées pour plusieurs critères, extrait de Qylafku [1999]. Les écarts en pourcentages ont pour référence la limite d'endurance obtenue en essai.

Rayon d'entaille (mm)		$\rho = 0.2$	$\rho = 0.4$
K_t		$2,995$	$2,5$
Auteur, [Ref]	K_f	limite d'endurance σ_0 (MPa)	
Essai		89.6	107.3
Peterson [1959]	$1+\frac{K_t-1}{1+\left(\frac{a'}{r_n}\right)}$	130.6 (46%)	122.3 (14%)
Neuber [1958]	$1+\frac{K_t-1}{1+\sqrt{\frac{a^*}{r_n}}}$	125.25 (40%)	127.34 (18.7%)
Kuhn and Hardraht [1952]	$1+\frac{K_t-1}{1+\frac{\pi}{\pi-\omega}\sqrt{\frac{f(R_m)}{r_n}}}$	132.48 (48%)	133.6 (24.5%)
Brand and Sutterlin [1980]	$\frac{K_t}{A\log(\chi^0)+B}$	249	196
Qylafku [1999]	$\frac{1}{X_{ef}S_n}\int_0^{X_{ef}}\sigma_{yy}[1-x\chi(x)]dx$	87.09 (-2.8%)	106.34 (-0.9%)

$$\Delta\sigma = K'.(\Delta\varepsilon_p)^{n'} \tag{1.48}$$

où $\Delta\varepsilon_p$ est l'amplitude de déformation plastique et (K',n') les paramètres de la loi de Ludwick.

L'énergie de déformation plastique ΔW_p^* est alors calculée à partir de la relation de Halford, Halford [1966] :

$$\Delta W_p^* = \left(\frac{1-n'}{1+n'}\right)\Delta\sigma\Delta\varepsilon_p \tag{1.49}$$

qui avec l'équation 1.48 donne :

$$\Delta W_p^* = \left(\frac{1-n'}{1+n'}\right)(K')^{(-1/n')}(\Delta\sigma)^{(1+n'/n)} \tag{1.50}$$

L'énergie totale de déformation s'écrit alors :

$$\Delta W^* = \Delta W_p^* + \Delta W_e^* \tag{1.51}$$

l'énergie élastique ΔW_e^* étant calculée à partir de la limite d'élasticité monotone σ_y et du module de Young E :

$$\Delta W_e^* = \frac{\sigma_y^2}{E} \tag{1.52}$$

De manière analogue à la méthode du gradient de contrainte (cf. figure 1.28), l'énergie totale de déformation ΔW^* est calculée dans la profondeur par la méthode des

éléments finis (cf. figure 1.29). Les 3 zones décrites sont identiques à celles présentées en 1.4.3. En utilisant la théorie de la distance critique sur un volume, il est alors possible de calculer l'énergie de déformation effective ΔW^*_{ef} :

$$\Delta W^*_{ef} = \frac{1}{V_{ef}} \int_{V_{ef}} \Delta W^*(\vec{r}) dV \tag{1.53}$$

V_{ef} étant le volume effectif. Il est ici définit comme un cylindre de diamètre X_{ef} et de même épaisseur que la structure, la 3e dimension n'étant pas précisée.

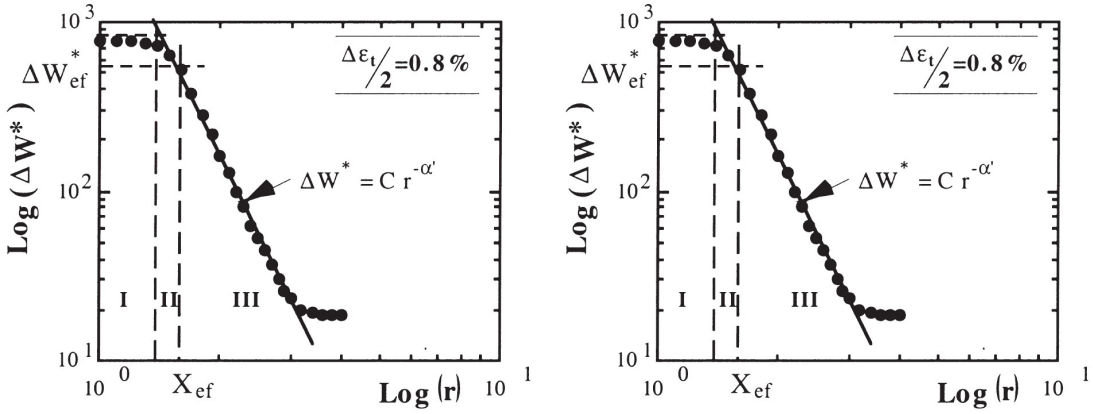

FIGURE 1.29 – Calcul par éléments finis de l'énergie de déformation en fond d'entaille pour un rayon d'entaille (a) : $\rho = 0,4$ mm et (b) : $\rho = 1,2$ mm. Avec ΔW^* en MJ/m^3 et r en mm, Bentachfine [1999]

L'énergie de déformation en fonction du nombre de cycles à rupture suit alors une loi puissance :

$$\Delta W^* = A.N_R^a \tag{1.54}$$

N_R étant le nombre de cycles à rupture, A et a deux constantes dépendantes du matériau et de la géométrie d'entaille. Pour les essais avec entailles, ΔW^* est remplacée par ΔW^*_{ef}. Le calcul permet alors la prévision de durée de vie des éprouvettes entaillées avec une bonne précision (cf. figure 1.30), en notant que la courbe en trait plein correspond à la régression sur les seuls essais sur éprouvettes lisses.

L'étude d'éprouvettes entaillées a été développée afin de prendre en compte les accidents géométriques : usinés dans le cas de structures avec par exemple un rayon de raccordement, ou liés au procédé lorsque des défauts apparaissent pendant le procédé de fabrication. Il est a noté que les rayons de courbures sont bien plus faibles dans le cas de défauts (de l'ordre du micromètre).

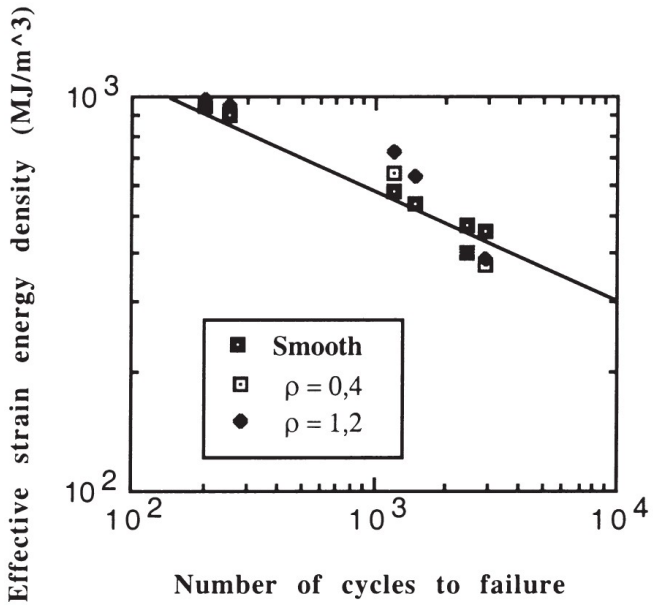

FIGURE 1.30 – Nombre de cycles à rupture en fonction de l'énergie de déformation plastique calculée (énergie effective dans les cas d'éprouvettes entaillées). Le trait plein correspond à la régression sur les essais sur éprouvettes lisses, Bentachfine [1999]

1.5 Conclusions (French and English)

Français Dans un premier temps, l'étude bibliographique a fait une brève synthèse de la métallurgie des alliages d'aluminium, de la composition chimique au procédés d'élaboration. De nombreux éléments d'alliages peuvent être ajoutés pour réaliser des alliages sur-mesure, alors que d'autres, comme le fer, sont considérés comme des impuretés et leurs présences doivent être minimisées.

Par la suite, la fatigue des alliages d'aluminium a été présentée et illustrée au travers d'exemples. Plus particulièrement, plusieurs études concernant l'influence de la porosité ont été présentées et démontrent la criticité de celles-ci pour la prévision de la durée de vie en fatigue oligocyclique. La littérature scientifique propose de nombreux critères pour prendre en compte les défauts dans le domaine de la fatigue à moyenne et grande durée de vie, mais moins d'études sont disponibles quant à l'effet de défauts en fatigue oligocyclique. Quelques critères énergétiques sont enfin présentés et montrent de bons résultats sur des nuances similaires à celle de cette étude.

Enfin, les essais sur géométries entaillées sont présentés. En comparaison des éprouvettes lisses, l'hétérogénéité des contraintes rend l'étude des éprouvettes entaillées plus complexe.

English Fist off, the literature survey gives an overview of aluminium alloys (from chemical composition to material process). Several alloy elements can be added to provide specific material properties, whereas other elements, such as Iron, are harmful and must be minimized.

Then, fatigue of aluminium alloys is detailed and examples shown. More precisely, studies on low cycle fatigue demonstrate void defects are critical features for the fatigue life. While several fatigue criteria can take defects into account for medium and high cycle fatigue, fewer studies are available on low cycle fatigue. Finally, a few energy criteria are presented and they show promising results on aluminium alloys similar to

the one studied.

In the last section, notch geometries are studied. Compared with smooth specimen, the heterogeneous stress field makes the study of notch specimens more complex.

Chapitre 2

Material study

This chapter focuses on the microstructure of the considered alloy. The classical features are first presented (chemical composition, material phases). The literature survey has shown that void defects are the main fatigue initiation causes (this will be discussed in chapter 4). In order to better understand these mechanisms, the first step is characterizing the population of defects. Therefore, the distribution of defect size is established and the robustness of the parameter inference evaluated. Then, using specific tools, the spatial distribution of these defects is also simulated using totally random point processes (Poisson) and clustered point processes (Thomas and Matérn processes). These simulation models will allow the generation of virtual synthetic simplified microstructures, which will later be confronted to the critical configuration observed on fatigue tests, thus helping better understand the critical features of defects.

2.1 Material microstructure

2.1.1 Material elaboration

The material used in this study is a Alumnium-Silicon-Copper based cast aluminium. For confidentiality reasons, the nominal composition is not presented and only the measured one is (see table 2.1). The specimens were cast in 2 cm diameter and 20 cm long round bars. These bars then underwent a thermal treatment : after casting, the specimens were cooled by forced air current, and then artificially aged for approximately 5 hours at 230 °C.

Table 2.1 – Measured aluminium alloy composition.

	Si	Cu	Mg	Ti	Fe	Mn	Zn	Ni	Al
Measured(%)	7.86	3.18	0.33	0.14	0.34	0.23	0.35	0.04	balance

2.1.2 Dendritic and eutectic phase

The microstructure exhibits dentritic solidification shown in Figure 2.1. The secondary dendritic arm spacing (SDAS) was measured over 1 mm^2 in the center of the round bar, corresponding to the fatigue tested zone. Table 2.2 shows the observed mean

SDAS value of 24 µm, which is among the smallest values observed in the literature for similar casting process (Shabestari and Moemeni [2004]).

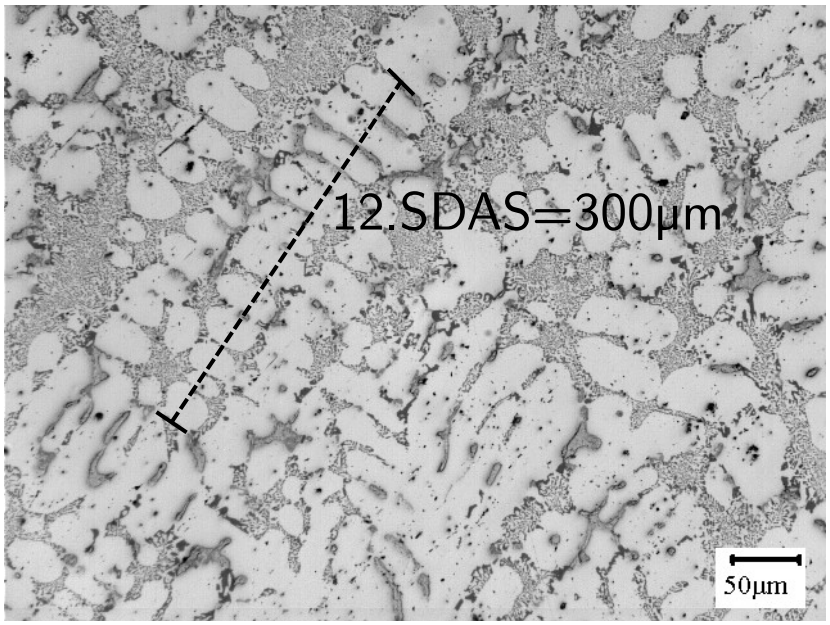

FIGURE 2.1 – Optical microstructure of specimen and SDAS measurement.

Table 2.2 – Secondary Dendritic Arm Spacing measurements

Quantity	Value (µm)
Mean	24
Max	38
Min	16
Standard deviation	5

The dendritic structure was further investigated using Energy-dispersive X-ray spectroscopy (EDS) shown in Figure 2.2, displaying how the silicon is rejected at the dendrite surface during the casting process (Nafisi et al. [2008]). The addition of strontium modifies the eutectic silicon phase from coarse plate-like to fine fibrous network (a discussion on this growth mechanisms can be found in [Timpel et al., 2012]).

Figure 2.3 displays the main smaller microscopic features. Image analysis of this Figure shows the eutectic Si particles (label (1), Figure 2.3) have an average size of 2.5 µm. Fe-rich intermetallics appear as an intermediate grey tone (label (2) Figure 2.3). Due to the specimen preparation (mirror finish polishing), the hardening brittle precipitates Al_2Cu appear as small black dots amidst the soft aluminium dendrites on the micrography, despite their small size (around 100 nm, see Section 3.2.2).

2.1.3 Intermetallics

Fe-rich content intermetallics were identified using EDS (Figure 2.4). They are located between dendrites and are of the same order of magnitude as the dendrite arm spacing (although some appear fractured and therefore smaller in size). During the cooling process, the α-Al dendritic network forms around 610 °C, while pre-eutectic intermetallics start precipitating only below 600 °C. Most of the dendrites being already

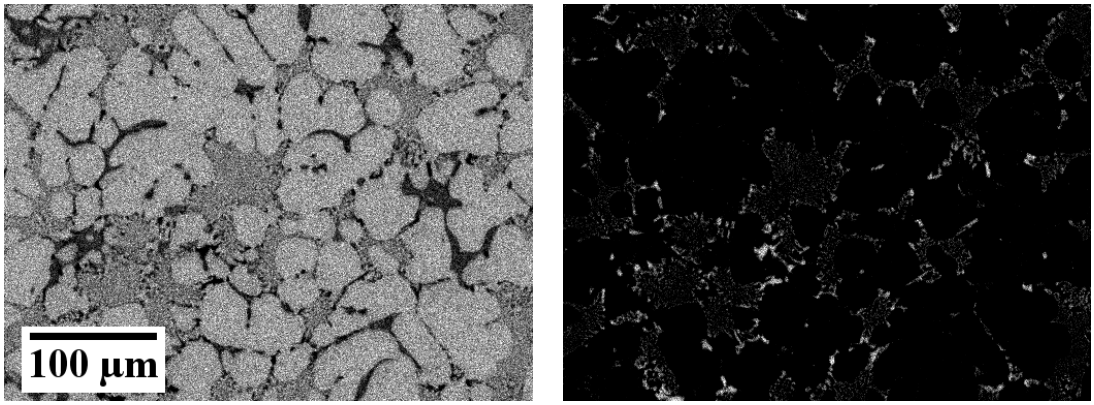

(a) Aluminium cartography (b) Silicon cartography

FIGURE 2.2 – EDS cartography

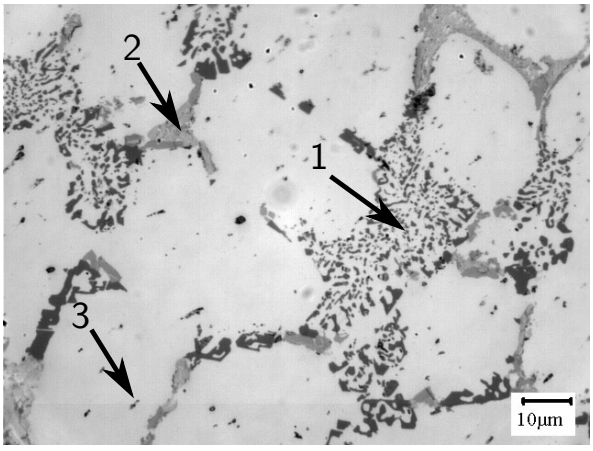

FIGURE 2.3 – Optical microscopy of the material microstructure: (1) small eutectic Si particle, (2) Fe rich intermetallics, (3) Strengthening precipitates trace caused by mirror finish polishing.

formed, the intermetallics precipitate in between the network, giving them a tentacular aspect.

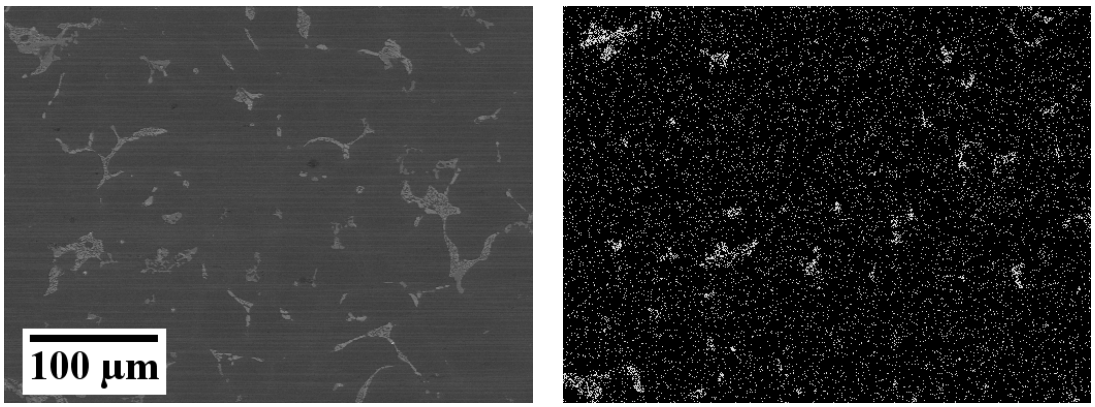

(a) SEM mode (b) Iron cartography

FIGURE 2.4 – EDS cartography of iron content

Quantifying the shape aspect was done by image analysis of a backscattered secondary electron (BSE) image (Figure 2.6a). While it represents a small area (0.74 mm, numerous visual observation did not reveal different intermetallic morphologies, and this image is considered representative. Due to the high content of iron, intermetallics appear as white particle analysed by image thresholding. Circularity (or isoperimetric quotient) C_p of a particle is defined as :

$$C_p = \frac{4\pi A}{P^2} \tag{2.1}$$

where A is the particle area and P the perimeter. These features are automatically calculated using MATLAB™ image analysis. The isoparametric inequality gives $C_p \leq 1$, with equality only in the case of the circle.

For each intermetallic, the Feret diameter is also measured. This measurand is defined as the largest [1] distance between two parallels tangent on opposite sides (Merkus [2009], Figure 2.5). The Feret diameters are calculated using MATLAB™ and the *imFeretDiameter* package (available from the Matlab filexchange platform, fileID: #30402). Figure 2.6b shows the largest intermetallics are the less circular ones.

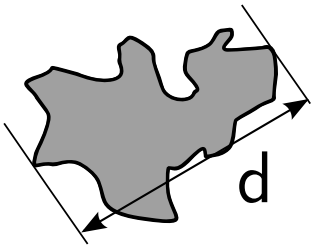

FIGURE 2.5 – Diagram of Feret diameter (d) measurement.

1. Rigorously, the Feret diameter d_θ is defined for a particular direction θ, but it commonly refers to d, the maximum in all directions : $d = \max_{\theta=[0,180]} d_\theta$

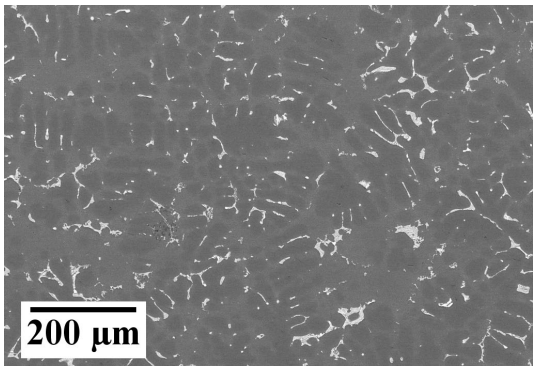

(a) BSE microscopy, intermetallics appear in white.

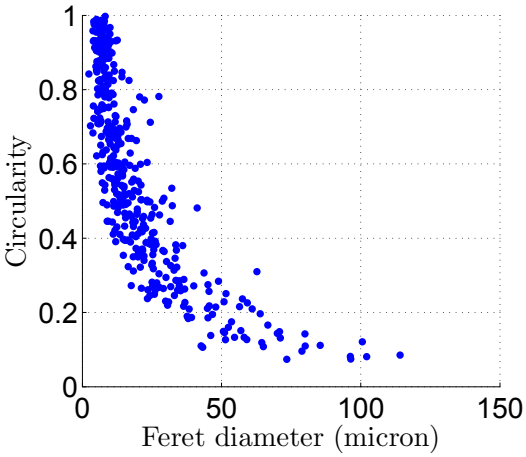

(b) Intermetallic circularity as a function of Feret diameter

FIGURE 2.6 – Intermetallic shape analysis

2.2 X-ray micro-tomography and porosity observation

2.2.1 X-ray microtomography

In order to observe the microstructure of a material, X-ray micro-tomography has been growingly used in material observation (see Salvo et al. [2003] for a review of microtomography possibilities in material science).

First, X-ray radiographies (Figure 2.7a) of a specimen are taken for a large number of sample orientation (Figure 2.7b). Radiography intensity is linked to the integral along the photon path of the absorption coefficient of the material, which can be variable along the path.

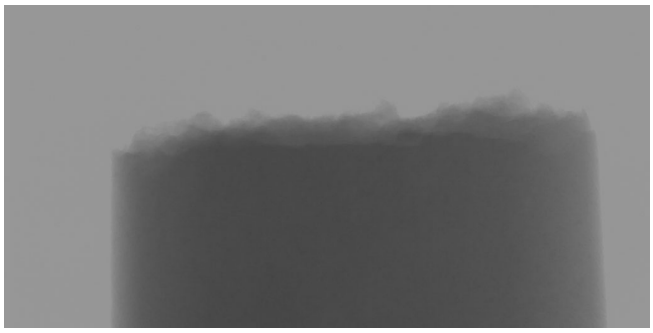

(a) X-ray radiography of broken sample taken by the CCD camera.

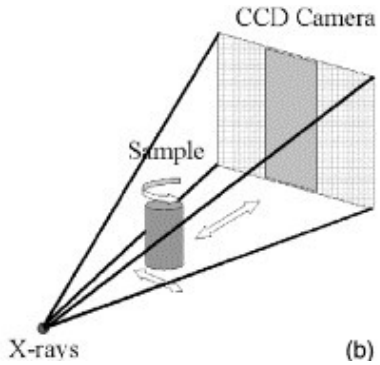

(b) X-ray microtomography (Salvo et al. [2003])

FIGURE 2.7 – X-ray microtomography

A filtered back projection can then be used: the goal is to find the 3D structure "compatible" with all the 2d projections. For high-resolutions ($< 10\,\mu m$), the sample must be placed very near the X-ray source causing artefacts. Indeed, most algorithms presuppose a parallel beam source, whereas laboratory X-ray microtomography is based on a conical source. This leads to highly heterogeneous beam hardening artefacts:

extreme areas at the top and bottom of the sample are darker and cannot be analysed. For example, specimen 125T5 (Figure 2.8) was originally 1000 voxels high, but only 800 could be used.

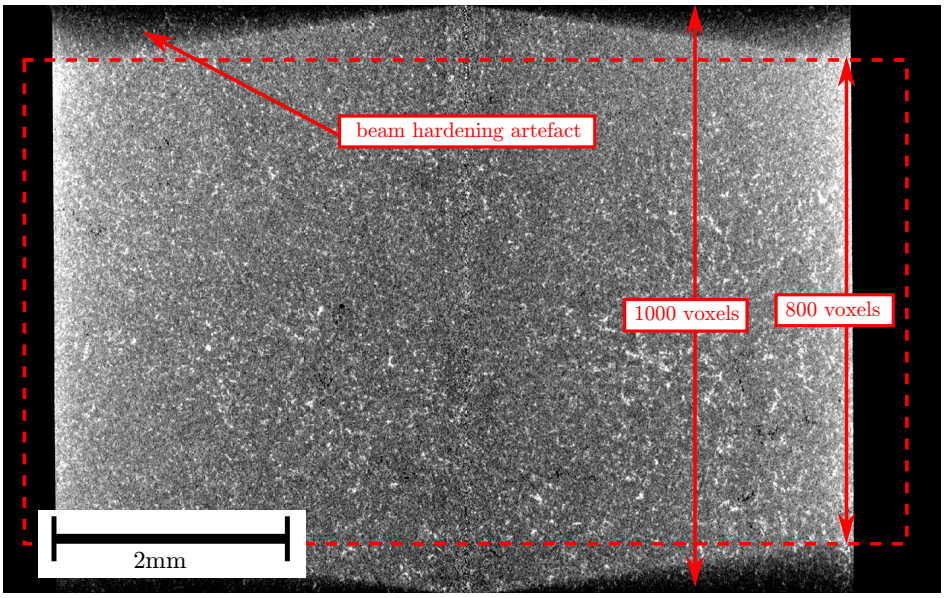

FIGURE 2.8 – Beam hardening effect: reduction of analysed volume.

2.2.2 Image correction

X-ray micro-tomography also causes radial beam hardening artefacts. While some samples are initially corrected (samples analysed on a different experimental setup), others present artefacts causing thresholding difficulties. A post-processing treatment similar to the rolling ball algorithm (Sternberg [1983]) has therefore been created and implemented in 3D.

Figure 2.9a shows the initial tomography section of a broken sample before the post-processing treatment : in particular, the edges of the sample are overly bright. This can be seen by observing the normalized pixel profile along the line L (shown in Figure 2.9e) from the original tomography. The material having only small heterogeneities, the local average intensity value across the material should be constant. A 3D Gaussian smoothing kernel filter [2] with standard deviation of 40 pixels (equivalent to 112 µm) was applied (Figure 2.9c). This smoothed image was then combined with a mask (Figure 2.9b) to avoid edge effects. The average normalized intensity ranges between 0.46 and 0.7.

The resulting treated image 2.9d is the difference between the smoothed data and the original tomography. The resulting line profile "d: treated" on graph 2.9e has much lesser average intensity variations and can be used for thresholding. A detailed image (Figure 2.10) also shows the post processing does not appear to cause a loss of information and the micro-structural features are not modified.

2. For each voxel, the Gaussian filter produces a weighted average of the voxel and the voxel neighbours using the Gaussian distribution.

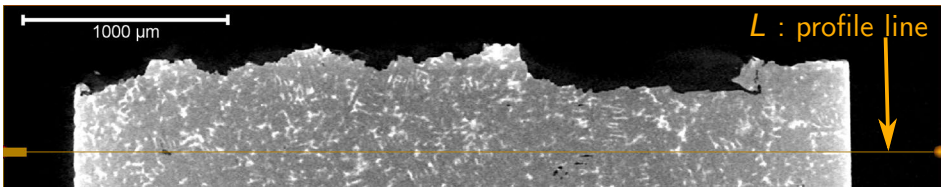

(a) Original tomography

(b) Mask

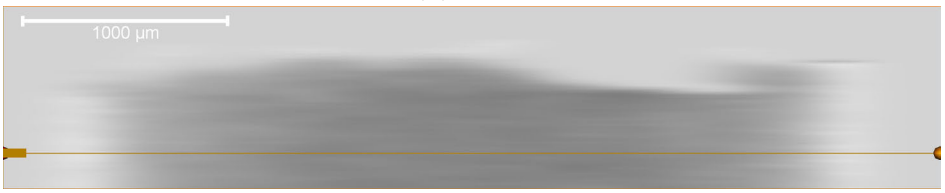

(c) Smoothed tomography

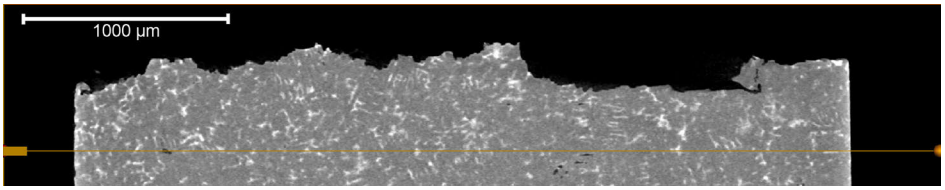

(d) Treated tomography

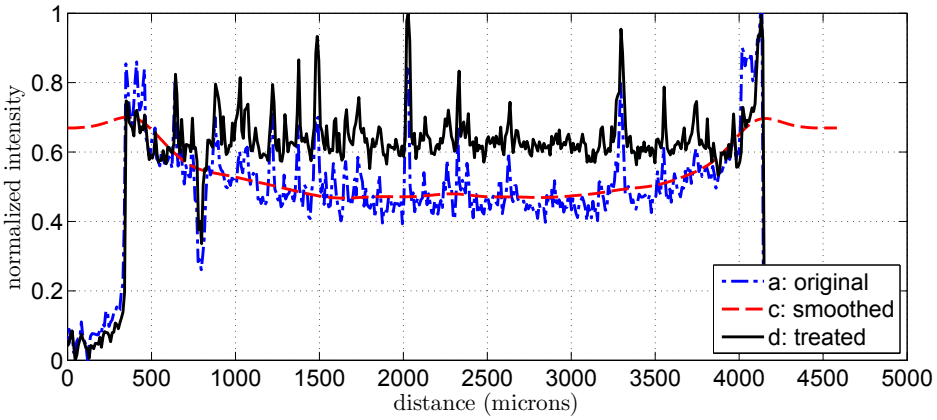

(e) Line profile intensity measurement

FIGURE 2.9 – Tomography post processing removing beam hardening artefacts.

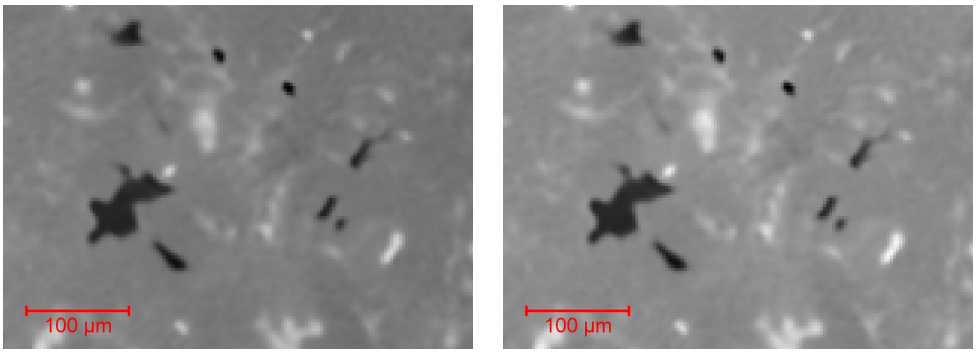

(a) Original tomography (b) Treated tomography

FIGURE 2.10 – Tomography post processing removing beam hardening artefacts: zoom.

2.2.3 Image thresholding

The main purpose of the tomographies used in this study is porosity detection. Given the important noise in the image, a 3D Gaussian filter of 1 pixel (commonly used value) standard deviation is firstly applied (Figure 2.12). Then a threshold is applied to differentiate the void from the material. However, the highly non-linear aspect of the measuring and reconstruction method makes thresholding highly dependent on the data itself. Only data measured consecutively on the same machine and the same operator can be directly compared. Even in this case, great care must be taken to avoid deviation caused by hidden automatic parameters (for example automatic image range scaling).

In order to compare specimens from different set of measurements, two sample are compared (specimens 12T5 and 125T5, see further details in section 2.3.1). These two samples are made of the same material and the same batch, but were analysed on different tomography systems, hence the slightly different aspect of the distributions, noticeably for the distribution tails. In order to compare these two samples, a correction is manually applied: a linear correction of the data is made (Figure 2.11) to match grey histograms. The linear scaling is done to match the two main peaks:

— the first peak around 12 000 corresponds to the void value: after reconstruction, the void intensity value is not strictly zero;

— the second peak is the mean material intensity;

Applying this method requires the two tomographic analysis are similar, i.e. they must contain the same proportion of material and void, otherwise the peaks can be artificially shifted. This artificial shift is mainly vertical: for example, the first peak of a sample with more exterior void would increase. However, given the noise and dispersion of the data, this could also cause a horizontal shift.

After these image corrections, phase separation can be made by data thresholding. Figure 2.13, 2.15 and 2.14, show the effect of different thresholding levels of (15000, 20000 and 22000). Following the histogram, three different values of thresholding could be used:

— the mean void intensity value (x-value labelled (1) in Figure 2.11, around 12 000): this value appears clearly as the maximum of the first peak. However, visual comparison shows this value underestimates the porosity value. Even for a higher thresholding of 15 000 (see Figure 2.13), visual identification of voids does not match the binary thresholding.

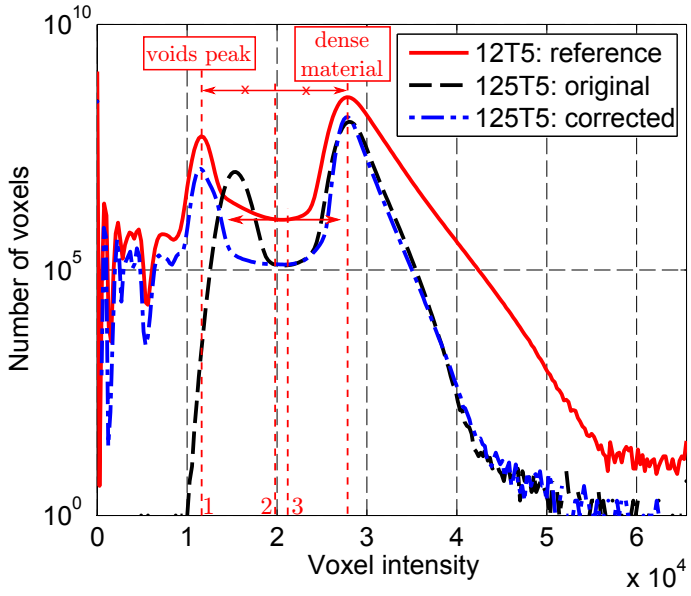

FIGURE 2.11 – Histogram equalisation: specimen 125T5 is from a different source than specimen 12T5, the intensity is manually corrected (linear correction) for the two local maximums to fit.

— the local minima between the two peaks (x-value labelled (3) in Figure 2.11, around 22 000): given the minimum curvature, this value is highly imprecise and cannot be used as a robust indicator. The visual comparison (see Figure 2.14) shows voids might be slightly overestimated, and noise voxels wrongly identified as voids.

— the middle distance between the two peaks (x-value labelled (2) in Figure 2.11, here 20 000), can be used to provide a robust thresholding value. Figure 2.15 shows that large porosities edges are correctly detected, while smaller voids (of only a few voxels) might go undetected. This value is set as the reference value for further analyses.

In the end, the threshold value of 20 000 is chosen as the reference by visual comparison. The threshold problematic arises not only to detect the edges (an error of measurement of 1 or 2 voxels on total defect size has little impact), but first and foremost for void separation: because of the highly tortuous shape of shrinkage defects, numerical thresholding can separate or coalesce two or more close voids. The visual comparison of void identification shows a thresholding value of 22 000 could also have been chosen. Following Section 2.3 shows that these two values (20 000 and 22 000) have little impact on size distribution fitting, while the underestimated value (15 000) distribution size distribution is slightly different.

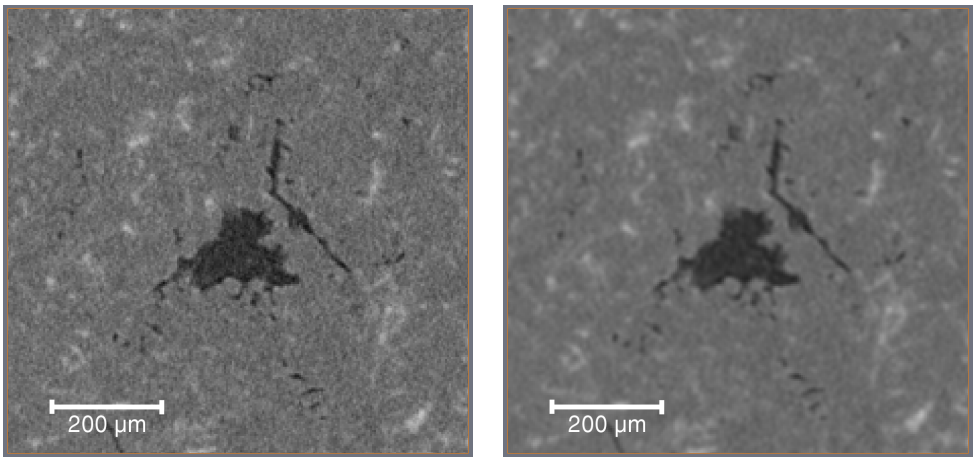

(a) Original tomography (b) Filtered tomography

FIGURE 2.12 – Tomography slice of large porosity. Image is displayed at full range.

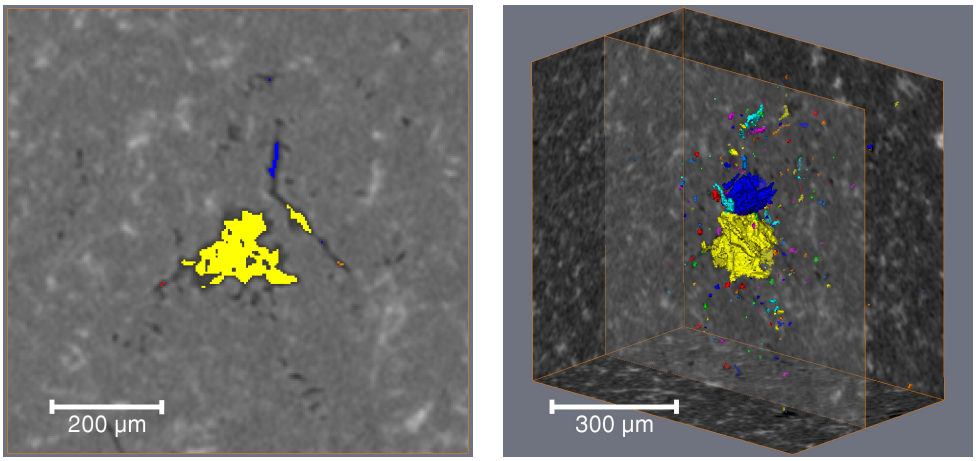

(a) 2D slice of middle section (b) 3d view of identified porosity

FIGURE 2.13 – Phase identification by thresholding (threshold=15000): underestimated threshold.

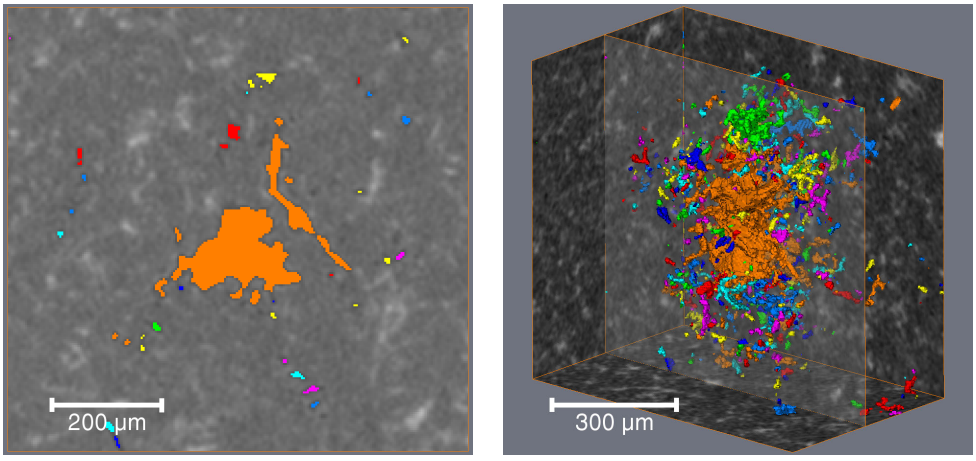

(a) 2D slice of middle section (b) 3d view of identified porosity

FIGURE 2.14 – Phase identification by thresholding (threshold=22000): overestimated threshold.

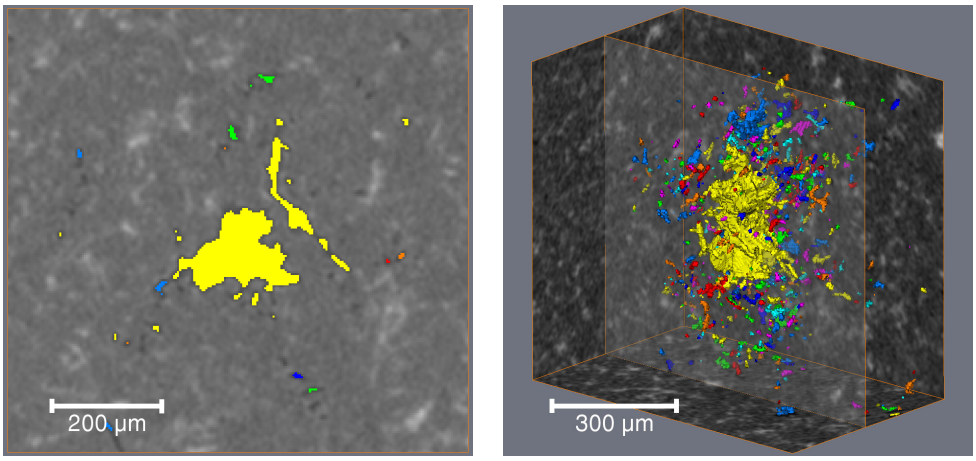

(a) 2D slice of middle section (b) 3d view of identified porosity

FIGURE 2.15 – Phase identification by thresholding (threshold=20000): correct threshold value.

2.3 Statistical treatment of porosity size

This Section presents the method developed in collaboration with Prof. Sudret (see Sudret [2014]). As will be later discussed in the chapter on fatigue mechanisms (chapter 4), material porosity plays a key role in fatigue crack initiation. It is therefore crucial to characterize these defects (gas porosities and shrinkage defects) in terms of size. X-ray tomography allows for such a study. Using particle size analysis, the defects are considered as particles and can be measured and morphologically characterized. However, the high number (thousands) of data requires appropriate statistical treatments. Bias caused by measurement methods, focus on critical data (large defects) are some of the problems that will be addressed in the following Section. The question is: can a statistical distribution be inferred and used to represent the population of defects in a given specimen?

In this Section, defects are considered as bi-variate samples: Feret diameter (the 2D definition in Section 2.1.3 is easily extended to 3D) and sphericity (later defined in Section 2.3.4). The main focus being on their Feret diameter which has the advantage of being easily measured on fracture surfaces and by tomography. The defect population spatial distribution (i.e. location in the specimen) is discussed in the next Section 2.4.

2.3.1 Data input

In order to establish statistical data, three different specimens are analysed (see Table 2.3). The first two, specimens 12T5 and 202F, were analysed at PLACAMAT (UMR, CNRS, Bordeaux, France) on a Versa 500 Zeiss®. The specimen 125T5 is analysed at Renault SAS (Guyancourt, France) on an General Electrics® phoenix X-Ray nanotom®. The two first specimens were reconstructed by two consecutive tomographies providing 3.7x3.7x3.7µm voxel, while the last sample was scanned at once with a slightly larger 4.8x4.8x4.8µm voxel.

The 202F specimen is an as-cast specimen. However, the applied heat-treatment (T5) is considered to have no effect on the porosity distribution and the observed data are considered comparable to the other specimens.

The section of the fatigue specimen scanned is presented in Figure 2.16a with an

Table 2.3 – Specimens analysed by tomography

specimen	volume	size	resolution
12T5	7x7x6.5mm	1920x1920x1750 pixels	3.7 µm
202F	7x7x6.5mm	1920x1920x1750 pixels	3.7 µm
125T5	7x7x4mm	1450x1450x800 pixels	4.8 µm

example of an extracted slice in Figure 2.16b. The reconstructed volume represents a cylinder of 7 mm in diameter and a 4 or 7 mm length depending on the tomograph used.

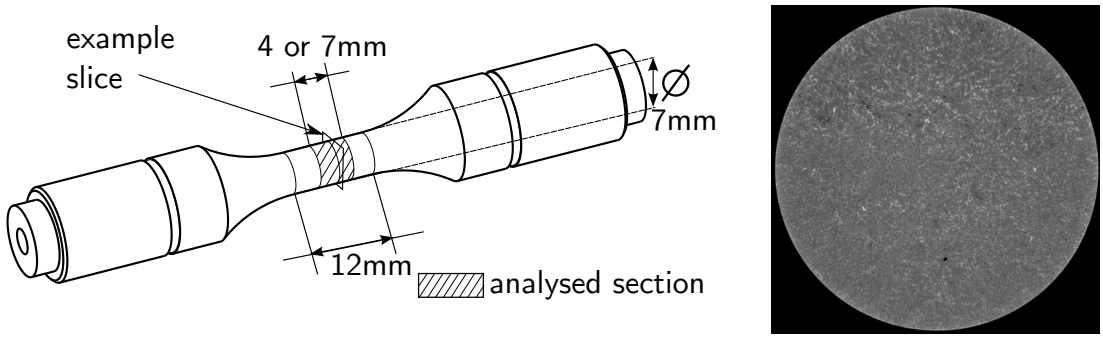

(a) Section of fatigue specimen analysed. The 12 mm zone is the fatigue tested zone.

(b) Example of slice

FIGURE 2.16 – Analysed section of fatigue specimen

The data are then thresholded using the method described in part 2.2.3 and the different porosities are labelled. In order to study the sensitivity to grey level thresholding, the first specimen 12T5 was studied with 3 different grey thresholds (15000, 20000 and 22000), while the two other specimens 202F and 125T5 were only studied for one level of grey thresholding (20000). Different statistical quantities of the Feret diameter are presented in Table 2.4 and in Figure 2.17, where the names are "sample name - thresholding value".

Table 2.4 – Feret diameter: statistical quantities (µm), std dev being the standard deviation and "# data" the number of data points identified per sample.

	12T5-15000	12T5-20000	12T5-22000	202F-20000	125T5-20000
# data	1974	20169	39400	8147	8801
Min	4.36	4.36	4.36	4.36	6.08
Max	390.9	497.6	523.2	240.9	473
Mean	17.9	19.8	23.1	20.2	19.2
std dev	20.9	16.6	19.4	15.9	16.6

2.3.2 Statistical tools

Kernel density estimate A probability density function can be visualized using kernel density estimate (KDE). For an observed univariate sample $\mathbf{X_n} = \{x_1, ..., x_n\}$ of size n, whose underlying distribution function is f_X, an estimate $\hat{f}_X$ of f_X is given by:

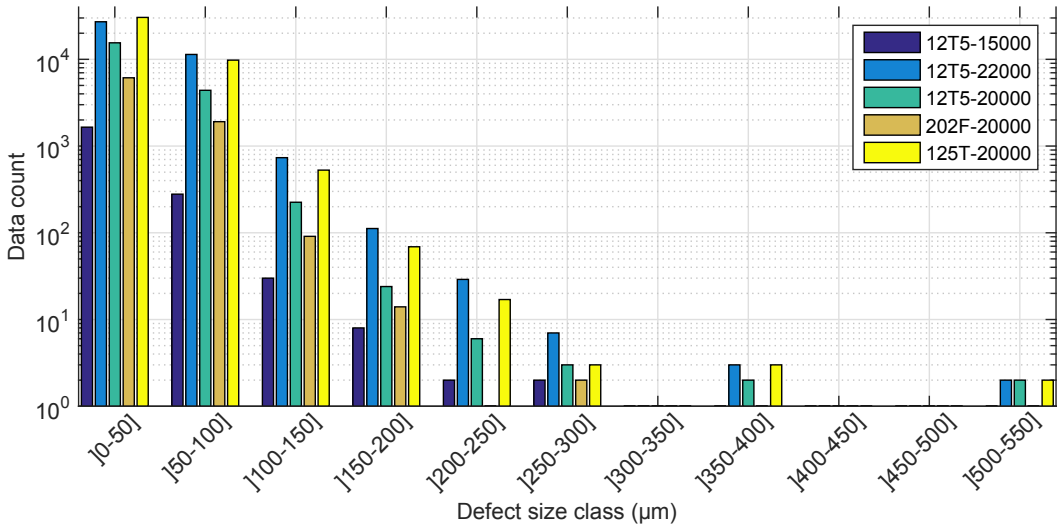

FIGURE 2.17 – Feret diameter: histogram for the different specimens.

$$\hat{f}_X(x) = \frac{1}{n}\sum_{i=1}^{n} K_k\left(\frac{x - x_i}{h}\right) \tag{2.2}$$

$K_k(.)$ being the kernel function and h_{opt} the bandwidth of the estimator. Both were chosen as default value: h_{opt} is the optimal bandwidth for normal densities (unless otherwise specified) and K_k is chosen as the PDF of a standard normal distribution:

$$K_k(x) = \varphi(x) = \frac{1}{\sqrt{2\pi}} \exp\left[-x^2/2\right] \tag{2.3}$$

More details on kernel density estimation can be found in Silverman [1986] and Wand and Jones [1995].

Maximum likelihood For a univariate observed sample $\mathbf{X_n} = \{x_1, ..., x_n\}$, and a probability density $f(x; \boldsymbol{\theta})$, the likelihood function $L_{lh}(.)$ is defined by:

$$L_{lh}(\boldsymbol{\theta}) = \prod_{i=1}^{n} f(x_i; \boldsymbol{\theta}) \tag{2.4}$$

$\boldsymbol{\theta}$ being a vector parameter to optimize. For numerical derivations, it is more practical to use the log-likelihood l_{lh} defined by:

$$l_{lh}(\boldsymbol{\theta}) = \ln L_{lh}(\boldsymbol{\theta}) = \sum_{i=1}^{n} \ln f(x_i; \boldsymbol{\theta}) \tag{2.5}$$

Given a true parameter $\boldsymbol{\theta}_0$ of the unknown distribution that generated the sample, the maximum likelihood estimator $\hat{\boldsymbol{\theta}}$ of $\boldsymbol{\theta}_0$ is obtained by maximizing the likelihood (or likewise the log-likelihood):

$$\hat{\boldsymbol{\theta}} = \arg\max_{\boldsymbol{\theta}} l_{lh}(\boldsymbol{\theta}) \tag{2.6}$$

2.3.3 Inference statistics of Feret diameter

Grey thresholding sensitivity Figure 2.18a shows the kernel density estimate of specimen 12T5 for 3 different thresholding values T_g. The densities have the same

overall shape, but the increase in thresholding values shift the density distribution to the right (i.e. the detected porosities are larger).

Regardless of the thresholding value, the densities appear bimodal. However, the first mode at 4.6 µm is solely the result of porosities of 1 voxel, which can be considered as noise (see Figure 2.18b).

For large porosities (≥50 µm), using the threshold T_g=15000 the tail of the distribution (see Figure 2.18c) appears highly irregular: only a few data points are identified.

For T_g=20000 and T_g=22000, the density estimates are very similar. For further data, a threshold T_g=20000 is chosen: it allows sufficient data points to be robust and appears visually as the actual threshold (see 2.2.3).

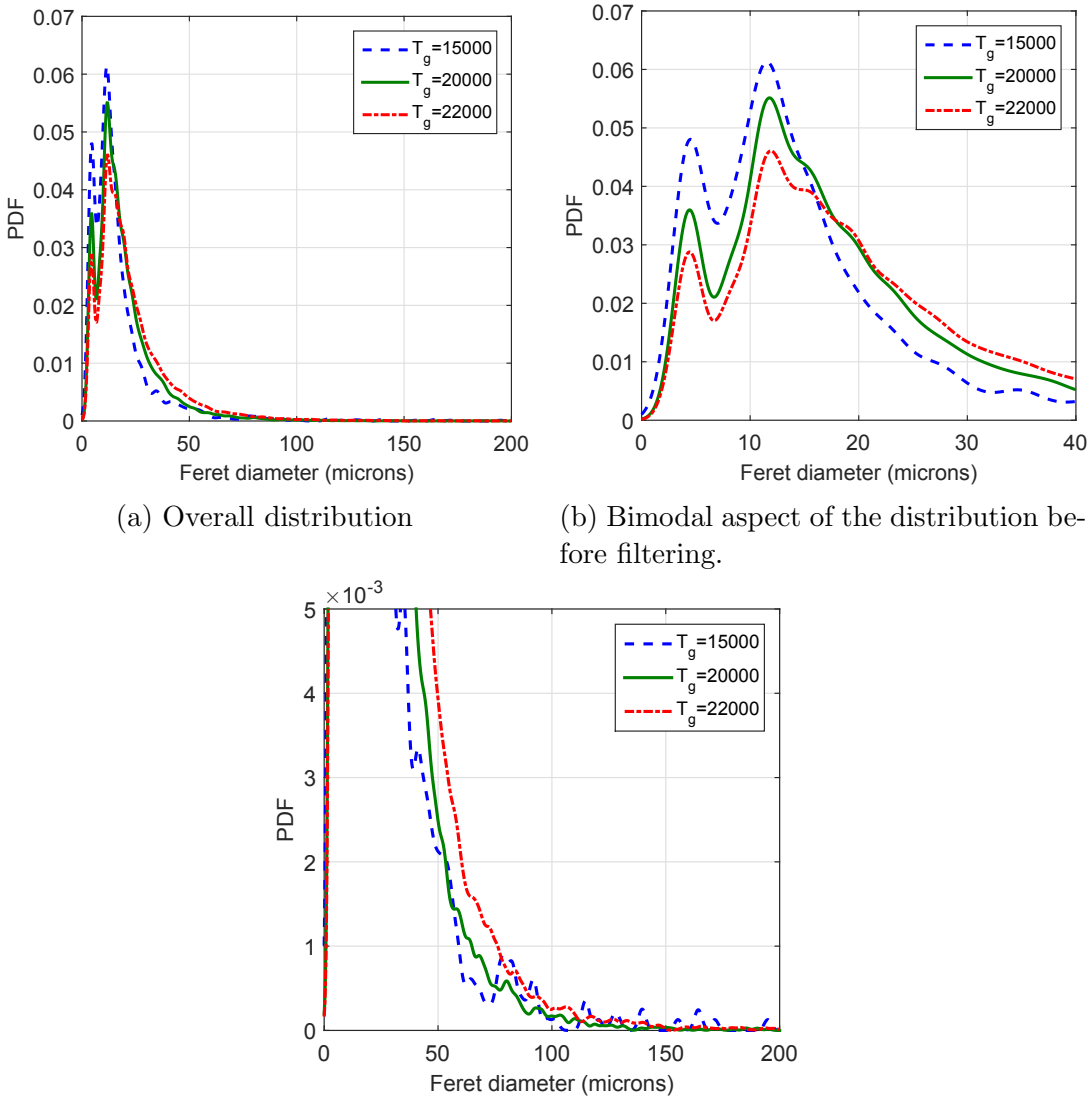

(a) Overall distribution

(b) Bimodal aspect of the distribution before filtering.

(c) Tail of distribution

FIGURE 2.18 – Kernel density estimate of sample 12T5 for different thresholding T_g values.

Distribution fitting and data filtering Initially, the data appears bimodal. In order to confirm the first mode is solely caused by unique voxel defects (which are likely to be caused by image noise), Figure 2.19 shows the effect of removing defects smaller than 5 µm. The global distribution then appears unimodal. This confirms the underlying distribution is indeed unimodal, and the first 5 µm mode is caused by unique

voxel defects. Therefore, standard unimodal distributions can be used to identify the defect population.

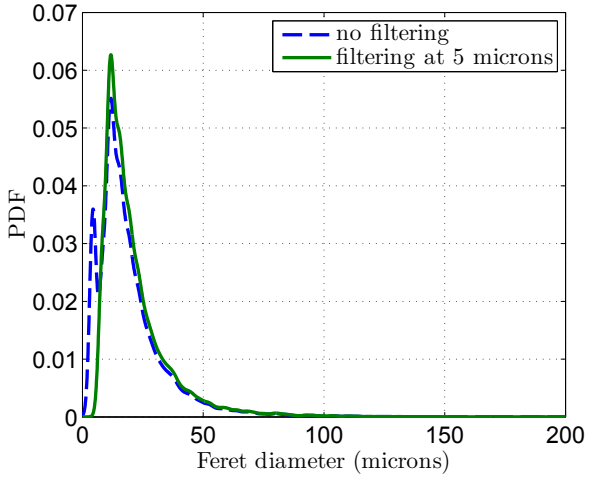

FIGURE 2.19 – Small unique voxel defects removal.

Of interest to analyse is only the larger porosities (over 100 µm). Size-thresholding is therefore extended to larger filtering values (0-60 µm), and focus is set on these larger defects.

Many distributions were tested (exponential, extreme value, gamma distribution, Rayleigh, Weibull) but only the three best fits are presented: the log-normal distribution (Logn), the generalized extreme value distribution (GEV) and the generalized Pareto distribution (GPD).

The probability density function (PDF) of the Logn distribution f_{logn} is:

$$f_{logn}(x) = \frac{1}{\sigma_{logn}\sqrt{2\pi}} \exp\left[-\frac{(\ln x - \mu_{logn})^2}{2\sigma_{logn}^2}\right], x > 0 \tag{2.7}$$

where μ_{logn} is the location parameter and σ_{logn} the scale parameter. The Logn distribution is defined only for positive values.

The GEV distribution PDF f_{gev} is given by:

$$f_{gev}(x) = \frac{1}{\sigma_{gev}}\left[1 + \xi_{gev}\left(\frac{x-\mu_{gev}}{\sigma_{gev}}\right)\right]^{(-1/\xi_{gev})-1} \exp\{-\left[1 + \xi_{gev}\left(\frac{x-\mu_{gev}}{\sigma_{gev}}\right)\right]^{-1/\xi_{gev}}\} \tag{2.8}$$

where μ_{gev} is the location parameter, $\sigma_{gev} > 0$ the scale parameter and ξ_{gev} the shape parameter. For the data sample analysed, ξ_{gev} is always positive, meaning the PDF is defined for $x_{gev} > \mu_{gev} - \sigma_{gev}/\xi_{gev}$.

Finally, the GPD probability density function f_{gpd} is defined by:

$$f_{gpd}(x) = \frac{1}{\sigma_{gpd}}\left(1 + \frac{\xi_{gpd}(x-\mu_{gpd})}{\sigma_{gpd}}\right)^{-\frac{1}{\xi_{gpd}}-1} \tag{2.9}$$

where ξ_{gpd} is the shape parameter, μ_{gpd} the location parameter and σ_{gpd} the scale parameter. The GPD was introduced by Pickands [1975] to approximate conditional excess distributions. Given a random variable X of cumulative distribution function F_X, the conditional excess distribution F_{μ_e} for a threshold μ_e is defined by:

$$F_{\mu_e}(y) = P(x - \mu_e \leq y | X > \mu_e) \tag{2.10}$$

and $y = x - \mu_e$ are the excesses. For numerous underlying cumulative distributions F_X, and for large threshold μ_e, the GPD approximates well F_{μ_e}.

In order to study the effect of size thresholding on distribution fitting, different levels of filtering x_f are applied. For each level, the maximum likelihood is used to fit the different distributions (Logn, GEV and GPD) and the log-likelihood calculated. Table 2.5 shows for each value:

— the filtering level x_f;

— the sample size: after thresholding, the smaller values are deleted and the sample size decreases as the level x_f increases;

— the three log-likelihood values l_{logn}, l_{gev} and l_{gpd} for the different distribution fitting, respectively the lognormal distribution, the generalized extreme value and the generalized Pareto distribution.

Table 2.5

filter level x_f (µm)	sample size	l_{logn}	l_{gev}	l_{gpd}
0	20169	-76522	-76638	-80296
5	17742	-66059	-65173	-67875
10	16236	-60459	-58617	-57798
20	6915	-27207	-25818	-25494
40	1617	-6939	-6480	-6400
60	524	-2397	-2214	-2192

To visualize this data, for each level x_f, the log-likelihood is compared to that of the GPD taken as reference. If the ratio is below 1, then the other distribution better fits the data, else, the GPD is the best choice. Figure 2.20 shows the different ratios obtained. If the smaller porosities are of interest ($\leq 10\,\mu m$), the lognormal distribution and the generalized extreme values are the best choices. On the other hand, if larger porosities are of interest, the generalized Pareto distribution becomes the best choice.

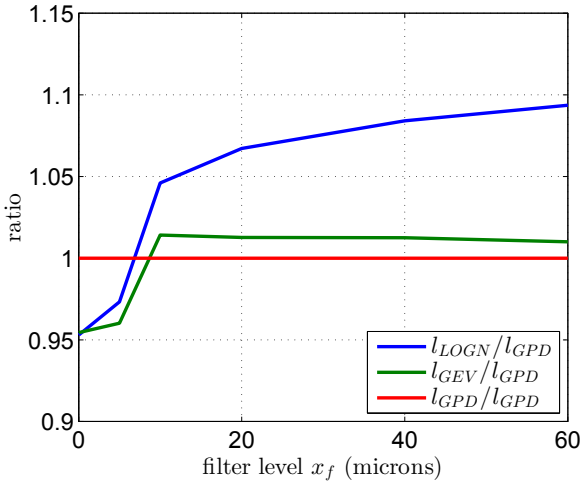

FIGURE 2.20 – Effect of data thresholding by size on distribution fitting.

Finally, a filtering level x_f of 40 µm is chosen and the GPD fitted (see Table 2.6). The level allows for sufficient data points (1617) to ensure a robust fit (see Figure 2.22a)

and correctly infer the tail of the experimental density estimate (see Figure 2.22b). For comparison purposes, the same fits are shown for a size thresholding of 5 µm (see Figure 2.21). No distribution correctly represents the data, especially for larger porosities. Notice difference in the y-scale: with the data filtering set at 40 µm (see Figure 2.22b), the proportion of larger defects (≥ 100 µm) in the sample is higher than for the 5 µm filtering (see Figure 2.21b). this higher proportion also causes the Kernel estimates of the distribution tails to appear smoother (the optimal bandwidth h_{opt} being also modified). Naturally, for the maximum likelihood method, the associated weight for these larger defects data points will therefore be larger and better represented.

Table 2.6 – Parameters for the fitted generalized Pareto distribution filtered at 40 µm, the thresholding parameter μ_{gpd} is imposed while σ_{gpd} and ξ_{gpd} are optimized by maximum likelihood estimation.

parameter	value
σ_{gpd}	15.51
ξ_{gpd}	0.2159
μ_{gpd}	40

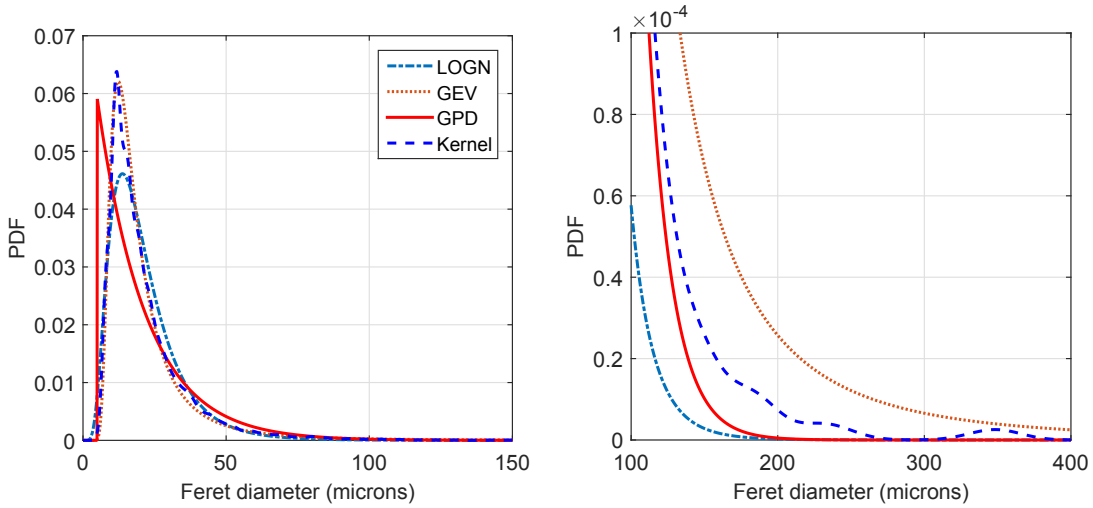

(a) Overall distribution (b) Tail of distribution

FIGURE 2.21 – Kernel density estimate of sample 12T5 and distribution fitting: size thresholding of 5 µm

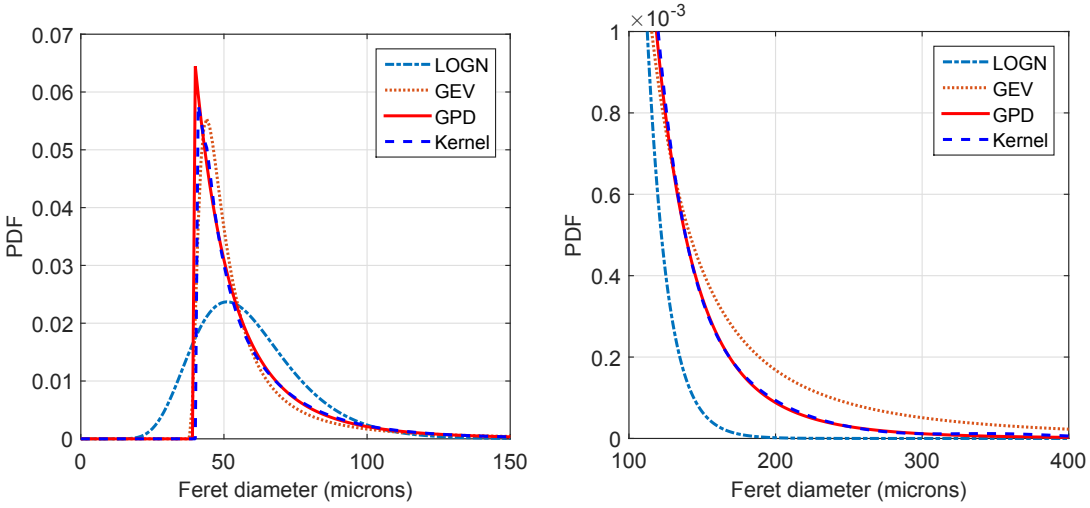

(a) Overall distribution (b) Tail of distribution

FIGURE 2.22 – Kernel density estimate of sample 12T5 and distribution fitting: final size thresholding value of 40 µm

2.3.4 Sphericity inference

The second studied parameter is the sphericity S:

$$S = \frac{\pi^{1/3}(6V)^{2/3}}{A} \tag{2.11}$$

where A is the particle area and V the particle volume. This parameter compares the shape of a particle to a sphere: only a perfect sphere will have a sphericity of 1(see Figure 2.23).

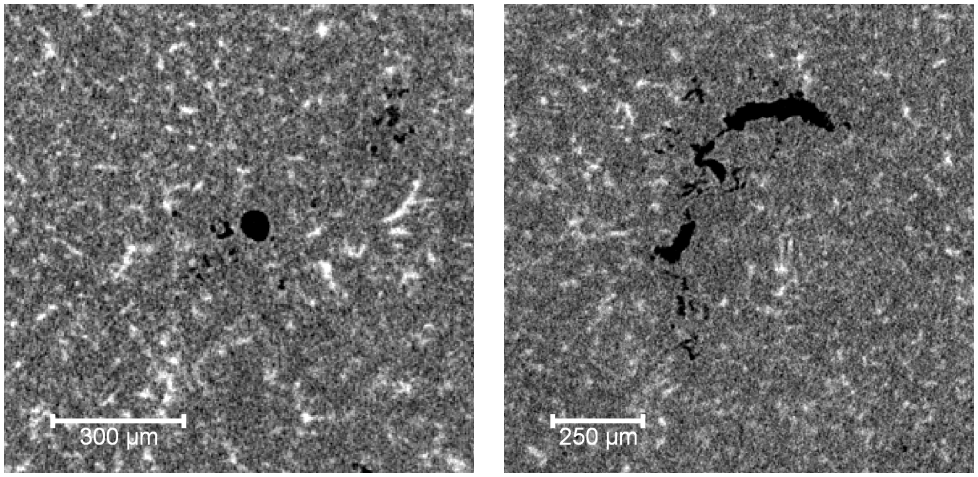

(a) Spherical gas type porosity: S=0.8 (b) Large shrinkage defect: S =0.27

FIGURE 2.23 – Types of defect type found and corresponding porosity

The same data as the previous Section 2.3.3 is used: all the particles with a Feret diameter smaller than 40 µm are not considered. Given the data sample is bounded by 0 and 1, the choice of a suitable distribution for fitting is restricted, only the three best are shown in Figure 2.24 as well as the log-likelihood obtained after the maximum likelihood estimate in Table 2.7.

The logit-normal distribution PDF is:

$$f_{logit}(x) = \frac{1}{\sigma_{logit}\sqrt{2\pi}} \frac{1}{x(1-x)} \exp\left[-\frac{(\text{logit}(x) - \mu_{logit})^2}{2\sigma_{logit}^2}\right], x \in [0;1] \tag{2.12}$$

where μ_{logit} is the mean and σ_{logit} the standard deviation. The definition of the logit function being the inverse of the sigmoidal logistic function:

$$\text{logit}(p) = \ln\left(\frac{p}{1-p}\right) \tag{2.13}$$

The beta distribution PDF f_{beta} is:

$$f_{beta}(x) = \frac{x^{\alpha_{beta}-1}(1-x)^{\beta_{beta}-1}}{\int_0^1 u^{\alpha_{beta}-1}(1-u)^{\beta_{beta}-1}du}, x \in [0;1] \tag{2.14}$$

where α_{beta} and β_{beta} are two shape parameters.

Finally, the Kumaraswamy (Kumaraswamy [1980]) distribution is similar to the beta distribution, but has a closed form PDF f_{Kuma}:

$$f_{Kuma}(x) = a_{Kuma} b_{Kuma} x^{a_{Kuma}-1}(1 - x^{a_{Kuma}})^{b_{Kuma}-1}, x \in [0; 1] \tag{2.15}$$

where a_{Kuma} and b_{Kuma} are two shape parameters.

As is shown visually in Figure 2.24, and confirmed by the log-likelihood values presented in Table 2.7, the three distribution give a similar fit. The log-likelihood of the beta distribution fit is slightly better and is chosen for the following analysis with parameters in Table 2.8.

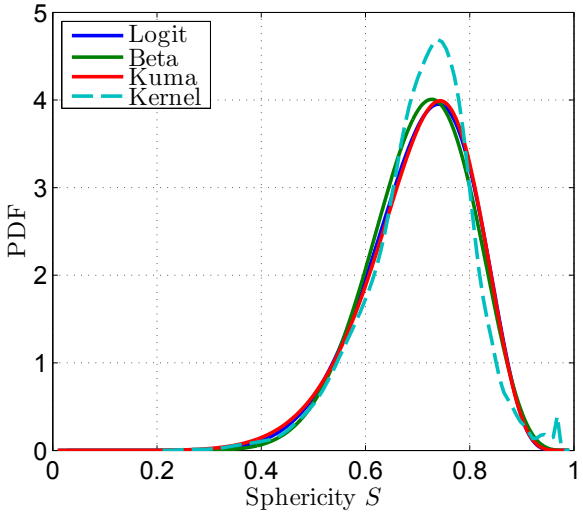

FIGURE 2.24 – Sphericity distribution fitting.

Table 2.7

distribution	log-likelihood
logit-normal	1450
Kumaraswamy	1465
Beta	1489

Table 2.8 – Parameters for the fitted beta distribution.

parameter	value
α_{beta}	14.59
β_{beta}	6.10

2.3.5 Copula of joint law (d,S)

In order to better characterize the link between size and shape, statistical tools can be used to simulate this link. These tools can then be used to compare different specimens and draw conclusion on representativeness: is there a link between size and shape and if so, is this link identical for different specimens (see following Section 2.3.6)?

Correlation coefficient

The Feret diameter d and the sphericity S are *a priori* uncorrelated. However, Buffière et al. [2002] have shown that for large porosities, which mostly correspond to shrinkage cavities, the sphericity decreases as the size increases (*i.e.* large porosities are highly tortuous). This can be seen in Figure 2.25.

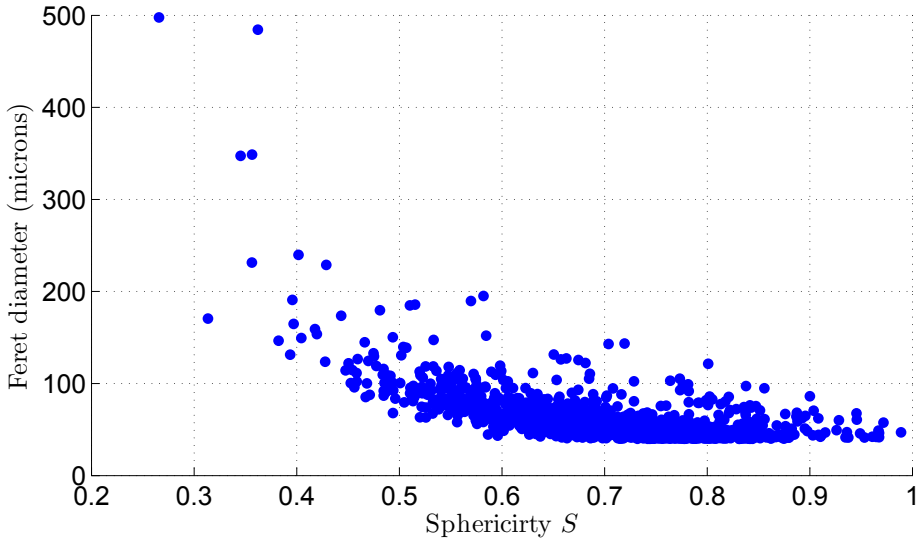

FIGURE 2.25 – Feret diameter d as a function of sphericity S, specimen 12T5.

To study the correlation between the sample $\mathbf{d} = \{d_i, i = 1, ..., n\}$ of Feret diameter and the sample $\mathbf{S} = \{s_i, i = 1, ..., n\}$ of sphericity, n being the total number of data points, three different correlation coefficients can be used:

— the linear coefficient of Bravais-Pearson ρ_P (also commonly referred to as coefficient R):

$$\rho_P = \frac{\sum_{i=1}^{n}(d_i - \bar{d})(s_i - \bar{s})}{\sqrt{\sum_{i=1}^{n}(d_i - \bar{d})^2}\sqrt{\sum_{i=1}^{n}(s_i - \bar{s})^2}} \tag{2.16}$$

with $\bar{d}$ and $\bar{s}$ the sample mean values of the Feret diameter and sphericity, respectively:

$$\bar{d} = \frac{1}{n}\sum_{i=1}^{n} d_i, \qquad \bar{s} = \frac{1}{n}\sum_{i=1}^{n} s_i \tag{2.17}$$

— The Spearman rank coefficient is based on the rank of each data point in the sample. For the sample $\mathbf{d}$ and $\mathbf{S}$, r_d and r_s are the ranks of each point in the Feret diameter and sphericity sample, respectively. The coefficient ρ_{sp} is defined by:

$$\rho_{sp} = \rho_P(r_d, r_s) \tag{2.18}$$

or similarly can be calculated by:

$$\rho_{sp} = 1 - \frac{6}{n}\frac{\sum_{i=1}^{n}(r_{d,i} - r_{s,i})^2}{n^2 - 1} \tag{2.19}$$

— The Kendall rank correlation coefficient (or Kendall's tau coefficient) τ is derived based on the number of *concordant* observations N_c and *discordant* observations N_d. For a set of observations $\{\{(d_i, s_i), (d_j, s_j)\}, 1 \leq i < j \leq n\}$, an observation is said to be *concordant* if $d_i < d_j$ and $s_i < s_j$, or if $d_i > d_j$ and $s_i > s_j$. Conversely, an observation is *discordant* if $d_i < d_j$ and $s_i > s_j$, or if $d_i > d_j$ and $s_i < s_j$. The coefficient is defined as:

$$\tau = \frac{N_c - N_d}{n(n-1)/2} \tag{2.20}$$

While the linear coefficient of Bravais-Pearson is a measure of linear dependence, both the Spearman rank coefficient and the Kendall's tau are measures of association. These measures of association do not assume a linear dependency, but only describe the degree of monotonicity.

The different values of the coefficients are displayed in Table 2.9. As for the linear coefficient, all coefficient vary in the [-1,1] range, where an absolute value of 1 means the two variables have a perfectly monotonic relationship (and not necessarily linear), and 0 if there is no relationship.

Table 2.9 – Correlation coefficients comparison of specimen 12T5

	Pearson ρ_P	Spearman ρ_{sp}	Kendall τ
Value	-0.633	-0.685	-0.516

All the different correlation coefficients show a relationship between size and shape of defects: the larger the defect, the more tortuous it is, whatever the measure of association chosen. Care must however be taken: the sphericity measure is greatly affected by the measurement resolution. The use of data filtering over 40 µm allows alleviating part of this bias. Indeed, a 40 µm defect is approximately 10 times larger than the unit voxel, and sphericity measuring more significant.

Copula definition

The marginal distributions f_D and f_S of the Feret diameter and the sphericity have been identified in Sections 2.3.3 and 2.3.4, respectively. However, considering the Feret diameter and sphericity as random variables D and S, this inference is insufficient to fully characterize the joint distribution of (D, S).

The joint distribution can be defined by the joint cumulative distribution function F_{DS}:

$$F_{DS}(d, s) = \mathbb{P}(D < d, S < s) \tag{2.21}$$

or by the joint probability density function f_{DS}:

$$f_{DS}(d, s) = \frac{\partial F_{DS}(d, s)}{\partial d \partial s} \tag{2.22}$$

The marginal distributions can be derived from the joint distribution:

$$f_D(d) = \int_{\mathcal{D}_S} f_{DS}(d, y)dy = \frac{\partial F_{DS}(d, \sup \mathcal{D}_S)}{\partial d} \tag{2.23}$$

$$f_S(s) = \int_{\mathcal{D}_D} f_{DS}(y, s)dy = \frac{\partial F_{DS}(\sup \mathcal{D}_D, s)}{\partial s} \tag{2.24}$$

where $\sup \mathcal{D}_D$ and $\sup \mathcal{D}_S$ are the upper bounds (eventually $+\infty$) of the distribution support of the Feret diameter and the sphericity, respectively. In this case, the bounds are: $\sup \mathcal{D}_D = +\infty$ and $\sup \mathcal{D}_S = 1$. The opposite is not true: knowing the marginal distributions f_D and f_S, there is an infinity of joint distributions compatible with these marginal distributions.

The copula theory (an introduction to copula theory can be found in Nelsen [2006]) can be used to represent the joint distribution by using the marginal distributions f_D and f_S, as well as a dependency function: the *copula* C. For the joint distribution f_{DS}, Sklar's theorem can associate the corresponding copula:

$$F_{DS}(d, s) = C(F_D(d), F_S(s)) \tag{2.25}$$

Therefore, for a given joint distribution with continuous marginals, the corresponding unique copula C is defined by:

$$C(u, v) \overset{\text{def}}{=} F_{DS}(F_D^{-1}(u), F_S^{-1}(v)) \tag{2.26}$$

Copula inference

Four different copulas are used to identify the joint distribution of the Feret diameter D and the sphericity S:

— The Gaussian copula $C^{\mathcal{N}}$ is defined for a correlation coefficient θ_{corr} by:

$$C^{\mathcal{N}}(u, v; \theta_{corr}) = \Phi_2[\Phi^{-1}(u), \Phi^{-1}(v); \theta_{corr}] \tag{2.27}$$

where Φ^{-1} is the inverse cumulative distribution function of the normal distribution and Φ_2 is the bivariate normal distribution:

$$\Phi_2(x, y; \theta_{corr}) = \int_{-\infty}^{x} \int_{-\infty}^{y} \frac{1}{2\pi\sqrt{1 - \theta_{corr}^2}} \exp\left[-\frac{1}{2}\frac{u^2 - 2\theta_{corr}uv + v^2}{1 - \theta_{corr}^2}\right] dudv \tag{2.28}$$

— The Clayton copula is an Archimedean copula. The general form for an Archimedean copula $C^{\mathcal{A}}$ is:

$$C^{\mathcal{A}}(u, v) = \varphi_g^{-1}[\varphi_g(u) + \varphi_g(v)] \tag{2.29}$$

where φ_g is a monotonically decreasing convex function on $[0, 1[$ called the generator function. The Clayton generator φ_C function is:

$$\varphi_C(t) = \frac{1}{\theta_{corr}}(t^{-\theta_{corr}} - 1) \tag{2.30}$$

— The Frank copula is also an Archimedean copula of generator function φ_F:

$$\varphi_F(t) = -\ln \frac{e^{-\theta_{corr} t} - 1}{e^{-\theta_{corr}} - 1} \tag{2.31}$$

— The Gumbel copula is also an Archimedean copula. Its generator function φ_G reads:

$$\varphi_G(t) = -\ln t^{\theta_{corr}} \tag{2.32}$$

For each copula, a 1000 data point sample is generated and is shown in Figure 2.26, that illustrates the (u, v) dependency. Correlation coefficients are purposely chosen higher than studied samples to illustrate this dependency. Each copula has a particular tail distribution dependency: Clayton copula has a particular asymmetric behaviour; Gumbel and Gaussian have similar behaviours; Frank copula has a low tail dependency strength.

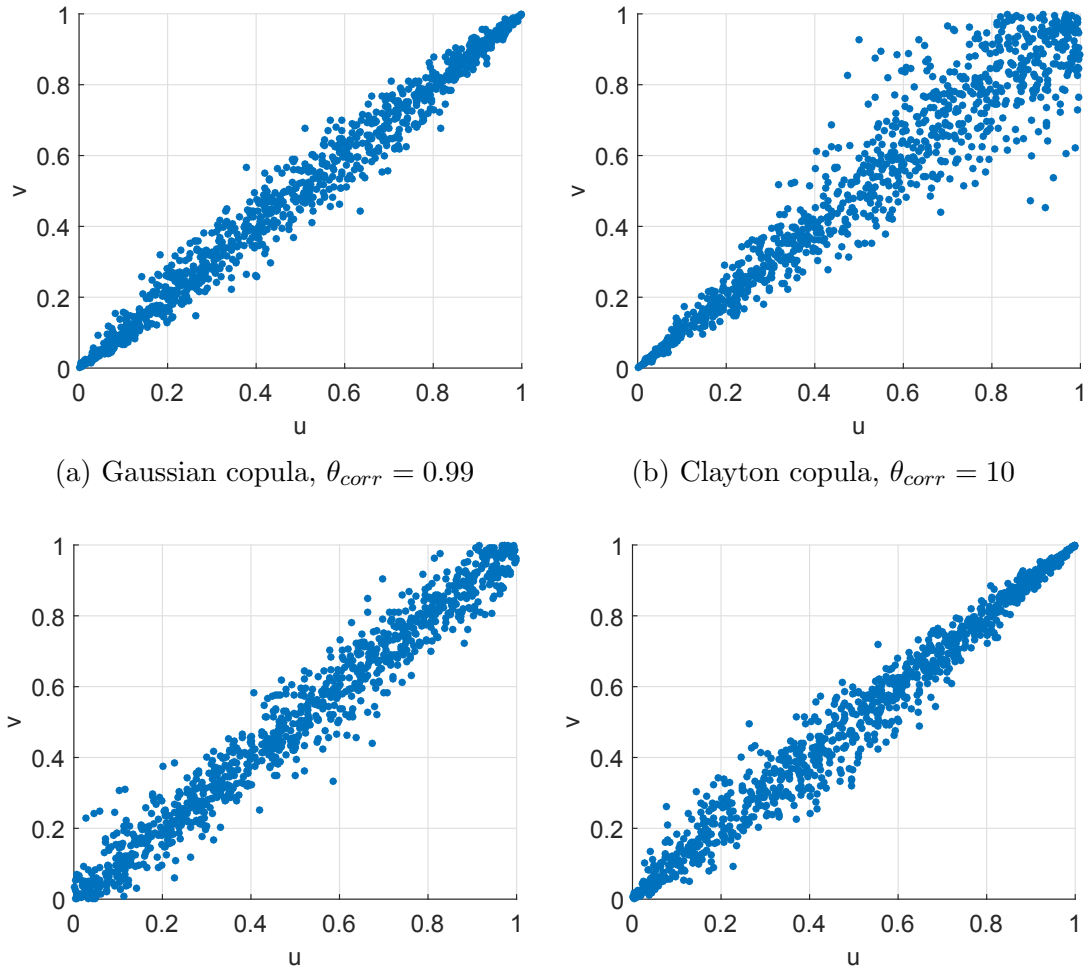

(a) Gaussian copula, $\theta_{corr} = 0.99$

(b) Clayton copula, $\theta_{corr} = 10$

(c) Frank copula, $\theta_{corr} = 30$

(d) Gumbel copula, $\theta_{corr} = 10$

FIGURE 2.26 – Example of copulas

For the described copulas, formulas can be used to derive the θ_{corr} parameter based on the Kendall τ:

— for the Gaussian copula, the θ_N can be derived by (a demonstration can be found in Fang et al. [2002]) :

$$\theta_N = \sin\left(\frac{\pi}{2}\tau\right) \tag{2.33}$$

— for an Archimedean copula, the relationship between the Kendall τ and the generator φ_g is (Genest and MacKay [1986]):

$$\tau = 1 + 4 \int_0^1 \frac{\varphi_g(t)}{\varphi_g'(t)} dt \tag{2.34}$$

While the Frank copula parameter requires a computational evaluation of the integral, the Clayton copula parameter is simply:

$$\theta_C = \frac{2\tau}{1-\tau} \tag{2.35}$$

and for the Gumbel copula:

$$\theta_G = \frac{1}{1-\tau} \tag{2.36}$$

The values are reported in Table 2.10, the complementary of the sphericity $(1 - S)$ is taken as to have a positive correlation, necessary for copula inference.

Table 2.10 – θ_{corr} parameter inference for different copulas

	Kendall's τ	θ_N (Gaussian)	θ_C (Clayton)	θ_F (Frank)	θ_G Gumbel
Value	0.516	0.724	2.130	6.030	2.065

The simulated samples can then be used to choose the best fit. Some statistical means are also available, but in this case, the main goal is to robustly simulate the large porosities and visual verification is considered sufficient. The 4 different copulas used are shown in Figure 2.27. All the copulas except the Gumbel copula overestimate the sphericity of the larger porosities (>200 µm).

The simulated samples are chosen to illustrate the different discrepancies with the experimental data and several simulations were observed. The good agreement of the Gumbel copula can be verified by the trend that appears when simulating several samples (50). Figure 2.28 illustrates this and shows the Gumbel copula model used is capable of correctly simulating all the data points, and especially the larger porosities.

2.3.6 Statistical representativeness

The sample named "12T5" (see Table 2.3) is used to infer the statistical parameters of the Feret diameter distribution as well as the sphericity distribution. Two other samples, namely "202F" and "125T5", are used to compare the statistical properties and confirm (or infirm) the robustness of the model inferred.

Table 2.11 shows the different parameter estimates for the different samples. The Feret diameter distribution parameters are, for both samples 202F and 125T5, close to the ones identified on sample 12T5. Graphically, Figure 2.29 shows good agreement for both samples 12T5 and 202F, the 125T5 sample shows slight differences, especially on the tail of the distribution. Three main causes are likely to explain this difference:

— the 12T5 sample used for the parameters identification may not be representative.

— the difference in tomography resolution: the 125T5 sample was done with a lower resolution (5.16 µm versus 3.7 µm)

— the tomography instrument setting: the data is corrected in order to provide homogeneity across all the samples. However, the two first sample 12T5 and 202F were analysed consecutively using the same settings, while the third 125T5 was done on a different machine.

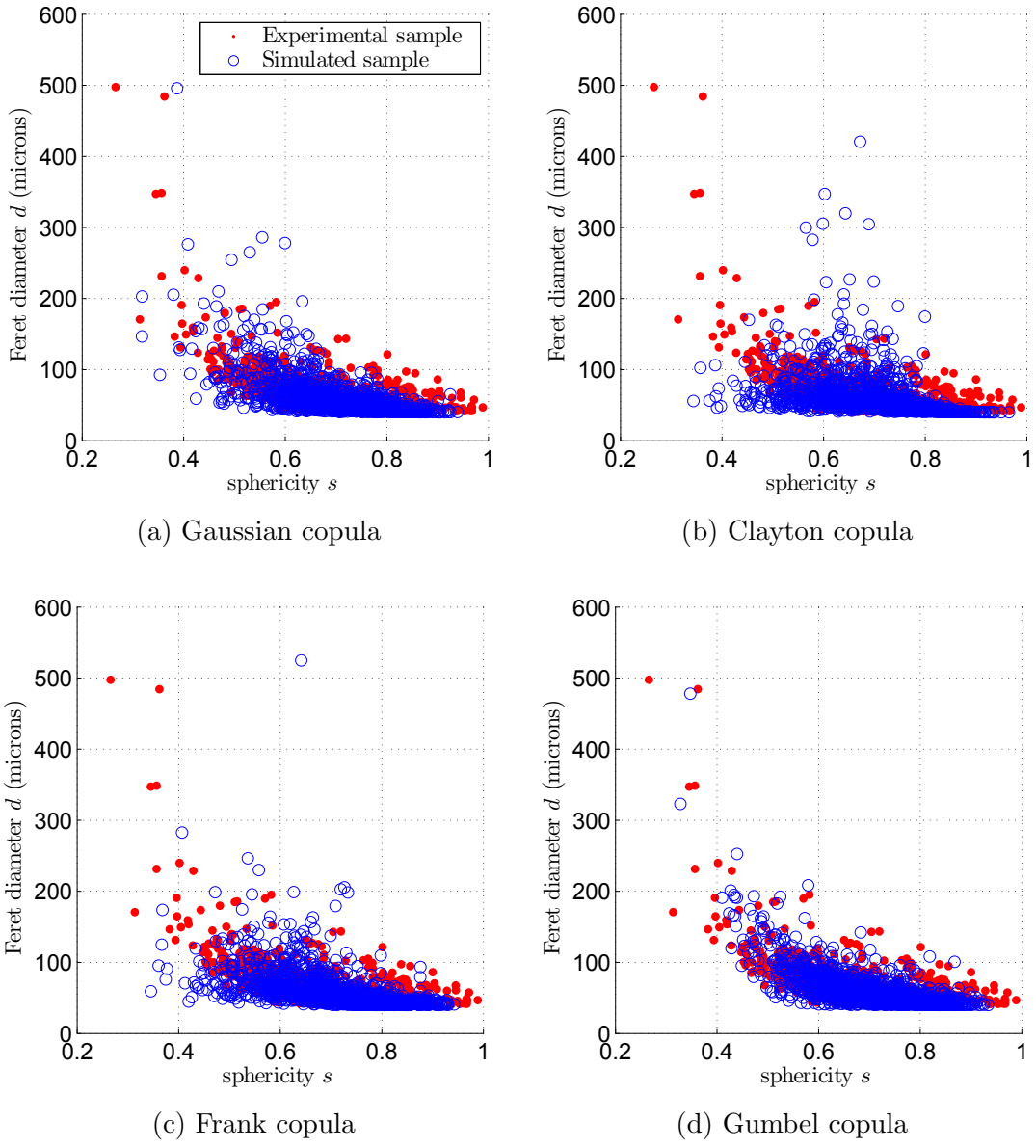

(a) Gaussian copula

(b) Clayton copula

(c) Frank copula

(d) Gumbel copula

FIGURE 2.27 – Comparison of copula-simulated samples with the observed sample.

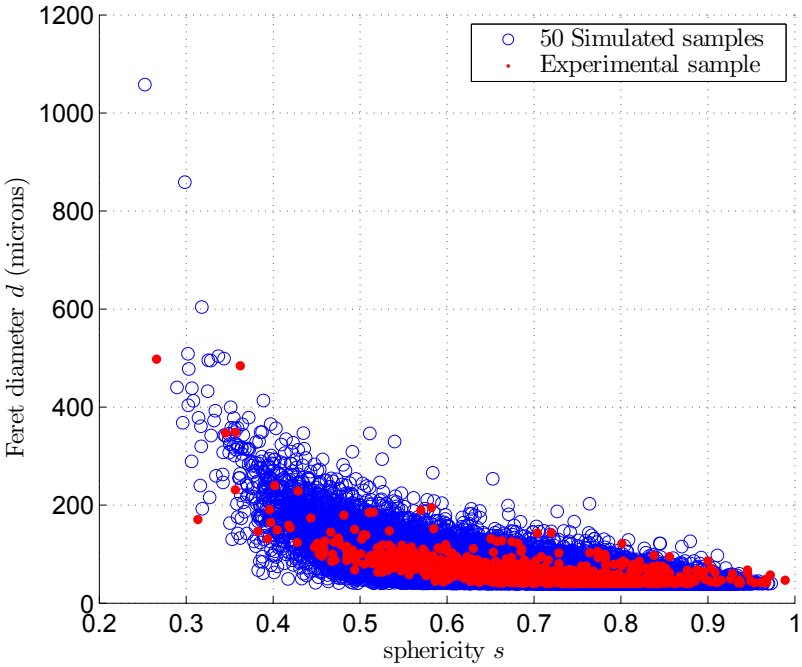

FIGURE 2.28 – Simulation of 50 samples using the Gumbel copula.

The same conclusions apply to the sphericity parameters estimate: the first two samples are similar while the third (125T5) appear slightly different. In this case, the lower resolution appears to cause an overestimate of the particle sphericity, but the correlation coefficients remains similar to the two other samples. While difficult to interpret, the similarity of the copula parameters also indicate that for each sample, the correlation of size with sphericity is similar, and all samples have similar defect populations.

Table 2.11 – Parameter inference of the different specimens.

		Feret diameter			Sphericity		Copula	
Specimen	resolution (µm)	σ_{gpd}	ξ_{gpd}	μ_{gpd}	α_{beta}	β_{beta}	τ	θ_G
12T5	3.7	15.5	0.216	40.0	14.6	6.10	0.516	2.07
202F	3.7	15.7	0.168	40.0	14.8	5.22	0.544	2.19
125T5	5.6	16.3	0.243	40.0	12.8	3.84	0.537	2.16

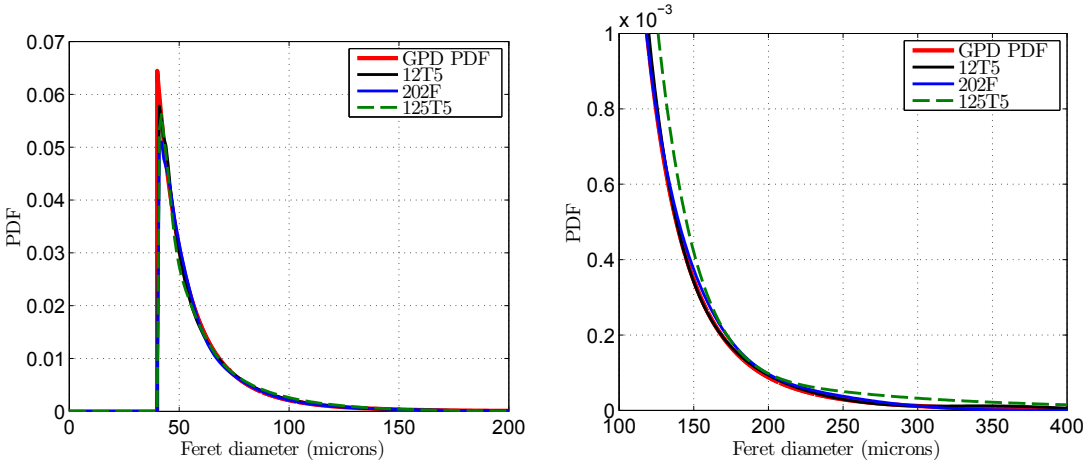

(a) Overall distribution (b) Tail of distribution

FIGURE 2.29 – Kernel density estimate of three experimental samples and Generalized Pareto Distribution (GPD) PDF identified on specimen 12T5 in Section 2.3.3

2.4 Spatial distribution of defects

This Section presents the method developed in collaboration with Prof. Sudret (see Sudret [2015a]) to study the spatial distribution of defects. Given the high number of data points in each sample, visual identification is insufficient and statistical tool of points processes have to be used. The theory is first presented, noticeably with the metrics used, and then applied to a real data set obtained by tomography.

2.4.1 Theory of point processes

Introduction and definitions

Given a set of n points $\mathbb{X} = \{\boldsymbol{x}_i \in W \subset \mathbb{R}^{d_R}, i = 1, ..., n\}$, point process theory is used to characterize the spatial distribution of the points (usually $d_R = 2, 3$). In many cases, the process occurs in a large subset $S_{sub} \subset \mathbb{R}^{d_R}$, but can only be observed in a smaller window $W \subset S_{sub}$. Specific tools were developed to infer properties of the underlying process given a limited observation window W.

A point process $\mathbb{X}$ is a given set of $n_{\mathbb{X}}$ points, $n_{\mathbb{X}}$ also being a random variable, defined on a subset $S_{sub} \subset \mathbb{R}^{d_R}$:

$$\mathbb{X} = \{\boldsymbol{X}_i, i = 1, ..., n_{\mathbb{X}}\} \tag{2.37}$$

where the $\boldsymbol{X}_i$ are also random vectors. For ease of calculations, the considered observation windows are all rectangles (2D) or rectangular cuboids (3D):

$$W = [x_{min}, x_{max}] \times [y_{min}, y_{max}] \qquad \text{(for 2D case)} \tag{2.38}$$

$$W = [x_{min}, x_{max}] \times [y_{min}, y_{max}] \times [z_{min}, z_{max}] \qquad \text{(for 3D case)} \tag{2.39}$$

Hypotheses are made concerning the studied point processes:

— Simple point process: there are not repeated points, i.e. $\boldsymbol{X}_i \neq \boldsymbol{X}_j$ if $i \neq j$;

— Homogeneous (stationary) point process: all properties of the point process are not modified by a translation.

The Poisson point process

A stationary point process is a Poisson point process if:

— the number of points in a subset $B_{sub} \subset W$ follows a Poisson distribution of parameter $\lambda|B|$, $|B|$ being the volume of B_{sub}:

$$\mathbb{P}(N(B_{sub}) = k) = \frac{[\lambda|B_{sub}|]^k}{k!} e^{-\lambda|B|} \tag{2.40}$$

— λ is the point process intensity, which corresponds to the average number of points per volume unit ($\mathbb{E}$ being the statistical expected value):

$$\lambda = \frac{\mathbb{E}[\mathbb{N}(\mathbb{B}_{\sim\approx}]}{|B_{sub}|} \tag{2.41}$$

— For m disjoints sets $B_1, ..., B_m$, the random variables $N(B)_1, ..., N(B)_m$ are independent.

The Poisson point process is used to represent Complete Spatial Randomness (CSR): each point is stochastically independent, and there is absolutely no interaction between them (see Figure 2.30a). Therefore, the Poisson point process serves as reference to evaluate if a point process is clustered (the points are attracted to each other, see Figure 2.30b) or regular (the points repulse each other, see Figure 2.30c).

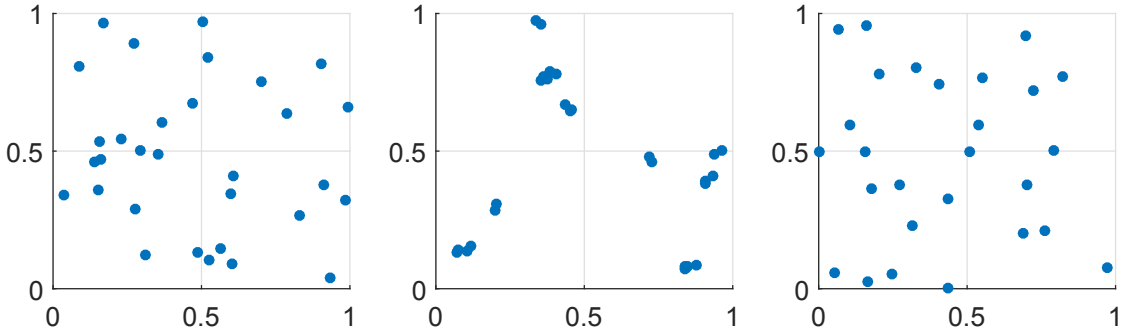

(a) Poisson: the points are randomly distributed.

(b) Cluster (Matern cluster process): points are attracted and appear in small groups called clusters.

(c) Regular (Matern 1 process): interactions repulses points, no two points are very close to each other

FIGURE 2.30 – Different examples of point processes

Cluster process

Cluster point processes occur when groups of points, or clusters, form: in each cluster, the distance between points is smaller than the overall average smallest distance between points. In nature, these appear when parents (for example a tree), produces children (for example seeds), that stay in close proximity of their parent.

3D reconstruction of tomographic data visually shows such clusters of porosities (see Figure 2.31), and the clustered point process chosen to model their spatial distribution.

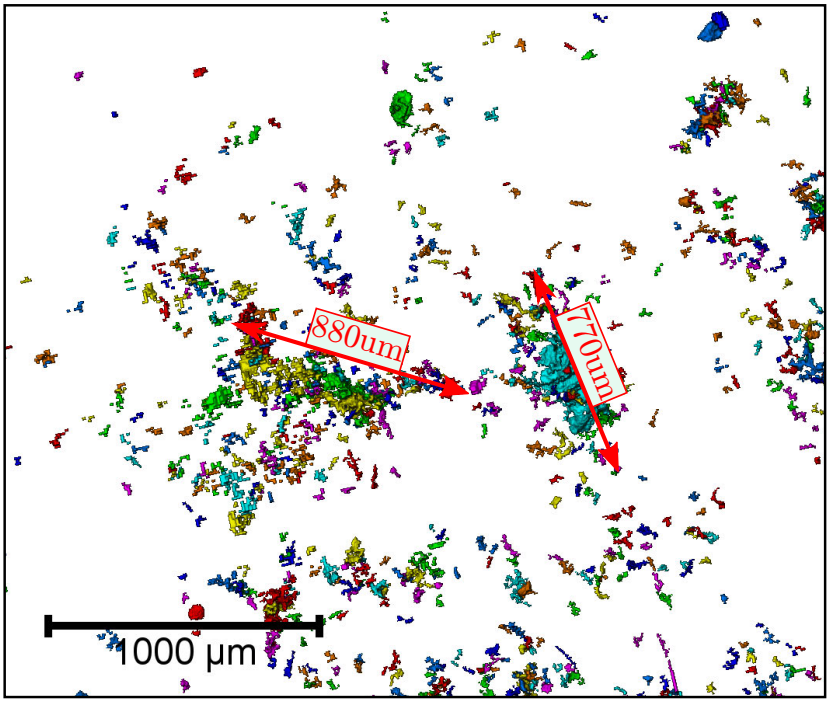

FIGURE 2.31 – Porosity reconstruction by tomography: cluster of porosities. The 2D representation gives the impression the clusters are closer than they really are.

Mathematically, a cluster point process is defined by:

— A parent point process $\mathbb{X}_p$;

— For each parent $c \in \mathbb{X}_p$, a child point process $\mathbb{Z}_c$.

The cluster point process $\mathbb{X}$ is therefore:

$$\mathbb{X} = \bigcup_{c \in \mathbb{X}_p} \mathbb{Z}_c \tag{2.42}$$

The parent process $\mathbb{X}_p$ is used solely in the construction process and is not included in the final process, and parent points are not considered in the final sample.

Neyman-Scott processes: Matérn-cluster and modified Thomas processes

A Neyman-Scott process (Neyman and Scott [1952]) is defined by 3 steps (see Illian et al. [2007], p. 384):

1. The parent process $\mathbb{X}_p$ is a homogeneous Poisson point process of intensity λ_p;
2. Each parent $c \in \mathbb{X}_p$, produces N_{ch} children points given by a discrete probability distribution. For the considered cases, the distribution is a Poisson distribution with parameter $\bar{c}$:
$$\mathbb{P}(N_{ch} = k) = e^{-\bar{c}} \frac{\bar{c}^k}{k!} \tag{2.43}$$
3. The N_{ch} children are independently drawn around the cluster centre c (rigorously, the children probability distribution is defined conditionally by the cluster centre).

Matérn cluster For this particular Neyman-Scott process, the children are randomly distributed in a R_0 radius ball centred on the parent point c:

$$z \in \mathbb{Z}_c \sim \mathcal{U}(b(c, R_0)) \tag{2.44}$$

where $\mathcal{U}$ is the uniform distribution, and $b(c, R_0)$ the ball of radius R_0 centred on c. Figure 2.32 illustrates such a point process.

Modified Thomas For this other Neyman-Scott process, the children are distributed around the parent point with a multivariate ($d_R = 2, 3$) Gaussian distribution centred on the parent point c, and of covariant matrix $\sigma_T^2 \mathbf{I}_{d_R}$ (the d_R-dimension identity matrix $\mathbf{I}_{d_R}$ implies there is no correlation between the different dimensions):

$$z \in \mathbb{Z}_c \sim \mathcal{N}(c, \sigma_T^2 \mathbf{I}_{d_R}) \tag{2.45}$$

where $\mathcal{N}$ is the multivariate Gaussian distribution. An example of such a point process is given in Figure 2.33.

2.4.2 Process metrics and the Ripley's K function

Definitions

Several metrics can be used to study the spatial distribution of points:

— The spherical contact distribution function F_{scd} is the probability function of the radius of a sphere when it encompasses the first neighbouring point, the centre of the sphere being any location in space besides the actual process points.

— The nearest neighbour distribution G is the same as the function F_{scd}, except the center of the sphere is a point of the process.

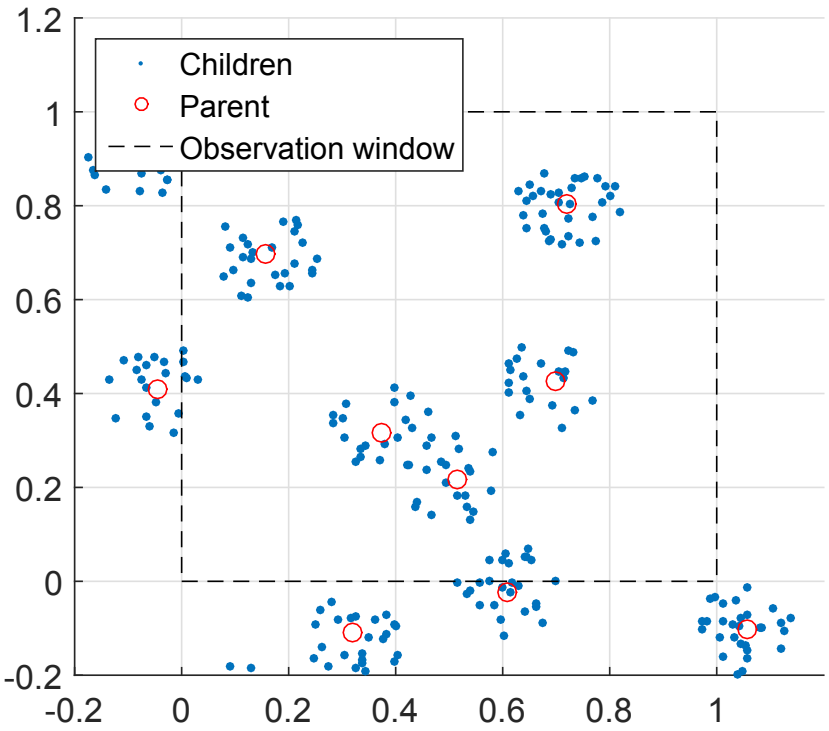

FIGURE 2.32 – Example of Matérn cluster point process: $\lambda_p = 35, \hat{c} = 25, R_0 = 0.1$. The unity observation window shows children points can be observed, despite the parent point being outside the window.

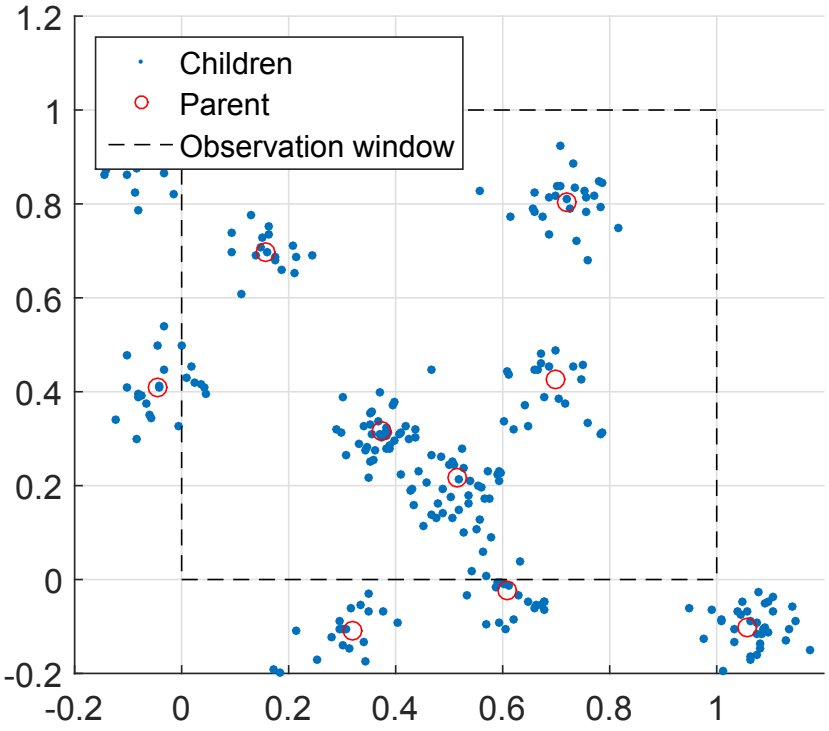

FIGURE 2.33 – Example of modified Thomas cluster point process: $\lambda_p = 35, \hat{c} = 25, \sigma_T = 0.05$. the infinite support of the Gaussian distribution can create children who appear isolated.

— The J-function (Lieshout and Baddeley [1996]) is defined by:

$$J(r) = \frac{1 - G(r)}{1 - F_{scd}(r)} \tag{2.46}$$

This function is used to compare a given distribution to a Poisson process. If $J(r) = 1$, then the process is a Poisson point process, if $J(r) > 1$ (i.e. $G(r) < F_{scd}(r)$) then the point process is regular, and if $J(r) < 1$ (i.e. $G(r) > F_{scd}(r)$) then the point process is clustered.

While these three functions provide qualitative informations about the spatial distribution, the K Ripley function is often chosen to infer statistical properties.

The Ripley's K function is defined for a point process $\mathbb{X}$ by:

$$K(r) = \frac{1}{\lambda}\mathbb{E}_{\boldsymbol{x}}\left[N\Big(b(\boldsymbol{x}, r)\backslash\{\boldsymbol{x}\}\Big)\right], \quad r > 0 \tag{2.47}$$

where λ is the intensity of the point process. The function is the average number of points in a r-radius sphere, where each sphere center is a point of the process itself but is not counted.

For a stationary Poisson point process (PPP) in a d_R dimension, the Ripley's K function is exactly the volume of the sphere $V_{d_R}(r)$ (since the K function is normalized by $1/\lambda$):

$$K^{PPP}(r) = \pi r^2 \qquad \text{(for 2D case)} \tag{2.48}$$

$$K^{PPP}(r) = \frac{4}{3}\pi r^3 \qquad \text{(for 3D case)} \tag{2.49}$$

For a clustered process, and a small radius r_1, there is a locally higher number of points (given the center of the counting sphere is also part of the daughter point process), than for a Poisson point process which represents Complete Spatial Randomness. Therefore, locally, the clustered $K^{cluster}$ Ripley function follows:

$$K^{cluster}(r_1) > K^{PPP}(r) = V_{d_R}(r) \tag{2.50}$$

Conversely, for a regular point process, the $K^{regular}$ Ripley function follows:

$$K^{regular}(r) < K^{PPP}(r) = V_{d_R}(r) \tag{2.51}$$

For example, a Cartesian regular unit grid (i.e. a data point is located at each intersection of the grid) is an extreme case of a regular point process realisation. In this case, the K^{grid} function is minimal:

$$K^{grid}(r) = 0 \qquad \text{for } r < 1 \tag{2.52}$$

As for the F, G and J_{scd} functions, the Ripley's K function can be used to evaluate if a point process is close to a Poisson distribution, clustered, or regular, by comparing it to the volume of the sphere V_{d_R}. This is done by the Besag L_B function (Besag [1977]):

$$L_B(r) = \left(\frac{K(r)}{V_{d_R}(1)}\right)^{1/d_R} \tag{2.53}$$

which translates for specific dimensional cases:

$$L_B(r) = \sqrt{\frac{K(r)}{\pi}} \qquad \text{(for 2D case)} \tag{2.54}$$

$$L_B(r) = \sqrt[3]{\frac{3K(r)}{4\pi}} \qquad \text{(for 3D case)} \tag{2.55}$$

Similarly, of interest is the comparison to the Poisson point process, whose Besag function L_B^{PPP} is:

$$L_B^{PPP}(r) = r \tag{2.56}$$

which can then be used to defined the L^* (or H) function:

$$L_B^*(r) \stackrel{\text{def}}{=} L(r) - r \tag{2.57}$$

For small radii, the L_B^* function positiveness (resp. negativeness) implies a clustered point process (resp. regular point process). Compared with the Ripley function, the L-Besag function stabilizes variance (Penttinen and Stoyan [2000]) and the L_B^* function can be used to identify the clusters radii (by using the L_B^* function maximum, although this is true mostly for idealized conditions, Kiskowski et al. [2009]).

Analytical expressions

In order to provide robust parameter inference, analytical formulas of the different Ripley K functions are preferred. Of concern here are the Matérn and modified Thomas (see Illian et al. [2007], p.376-377). The modified Thomas point process could not be found in 3 dimensions in the scientific literature and had to be derive.

For the Neymann-Scott process, the K^{NS} Ripley function can be written as:

$$K^{NS}(r) = K^{PPP}(r) + \frac{\mathbb{E}[N(N-1)]}{\lambda_p \bar{c}^2} F_d(r) \tag{2.58}$$

where λ_p and $\bar{c}$ are the parent point process intensity and the average number of children, respectively. F_d is the cumulative distribution function of the distance between two children points of a same cluster.

For Matérn and modified Thomas point process, the expected value $\mathbb{E}[N(N-1)]$ can be simplified: both processes parent points generate N children following a Poisson of expected value $\bar{c}$ (which is also equal to the variance). Therefore, $\mathbb{E}[N(N-1)] = \bar{c}^2$ and specifically for Matérn and modified Thomas point processes:

$$K^{NS}(r) = K^{PPP}(r) + \frac{1}{\lambda_p} F_d^{NS}(r) \tag{2.59}$$

while some cumulative distribution functions can be found in Illian et al. [2007], others had to be derived for some cases. The results can be found in Table 2.12.

2.4.3 Estimates

Intensity estimate

The first and most important parameter to estimate, is the process intensity λ. For an observation window W, the average number of points in this window is:

$$\mathbb{E}[N(W)] = \lambda |W| \tag{2.60}$$

where $|W|$ is the window volume (or surface in the 2D case). For a particular process realisation of n points, an unbiased intensity estimate $\hat{\lambda}$ is:

$$\hat{\lambda} = \frac{n}{|W|} \tag{2.61}$$

Table 2.12 – Analytical probability density function (PDF) and cumulative distribution function (CDF) of the distance between two children points of a same cluster (see Illian et al. [2007])

Matérn 3D	PDF	$f_d(r) = \frac{3r^2}{2R_0^6}\left(R_0 - \frac{r}{2}\right)^2\left(2R_0 + \frac{r}{2}\right)$
	CDF	$F_d(r) = \frac{3}{16R_0^6}\left(\frac{r^6}{6} - 3R_0^2 r^4 + \frac{16}{3}R_0^3 r^3\right)$
Modified Thomas 3D	PDF	$f_d(r) = \frac{r^2}{\sqrt{4\pi}\sigma_T^3}\exp\left(-\frac{r^2}{4\sigma_T^2}\right)$
	CDF	$F_d(r) = 2\Phi\left(\frac{r}{\sqrt{2}\sigma_T}\right) - \frac{\sqrt{2}r}{\sigma_T}\varphi\left(\frac{r}{\sqrt{2}\sigma_T}\right) - 1$

With $\varphi(x) = 1/\sqrt{2\pi}\exp(-x^2/2)$ and $\Phi(x) = \int_{-\infty}^{x}\varphi(t)dt$

Whereas for usual statistical inference, an observation is a specific realisation and cannot provide statistical quantities, a point process realisation on an observation window provides many informations on the underlying process. The variance for a Poisson point process is exactly:

$$\mathrm{Var}[\hat{\lambda}] = \frac{\lambda}{|W|} \tag{2.62}$$

which is also a good approximation for a non-Poisson process (see Illian et al. [2007], p.190).

Ripley's K function estimation and edge correction

First, the symmetric distance matrix (d_{ij}) is calculated. For n observed points $(\boldsymbol{x}_i)_{\{i=1\ldots n\}}$, the $n \times n$ distance matrix is:

$$d_{ij} = ||\boldsymbol{x}_i - \boldsymbol{x}_j|| \tag{2.63}$$

where $||\bullet||$ is the usual Euclidian distance. For a finite observation window W, a biased estimate of λK is:

$$\lambda\hat{K}_{bias}(r) = \frac{1}{n}\sum_{i=1}^{n}\sum_{i\neq j}\#\{d_{ij} \leq r\} \tag{2.64}$$

where $\#(\bullet)$ counts the number of data that verifies the condition. This estimate places n radius balls centred on all the $\boldsymbol{x}_i$ (which belong to the point process), and counts the average number or points in the balls. In Figure 2.34, the counting centred on $\boldsymbol{x}_1$ provides an accurate estimate of the local intensity. For the ball centred on $\boldsymbol{x}_2$, the number of process points is artificially lower due to the unobserved points outside the W window, even if $r_1 = r_2$, thus causing a strong bias in the estimator.

Different methods can be used to avoid this strong edge effect and provide an unbiased estimate (see Illian et al. [2007], chapter 4):

— Reduced observation window $W_{\ominus r}$ (see Figure 2.35a) for a radius r, only the points inside the reduced window $W_{\ominus r}$ are considered for the estimation (the

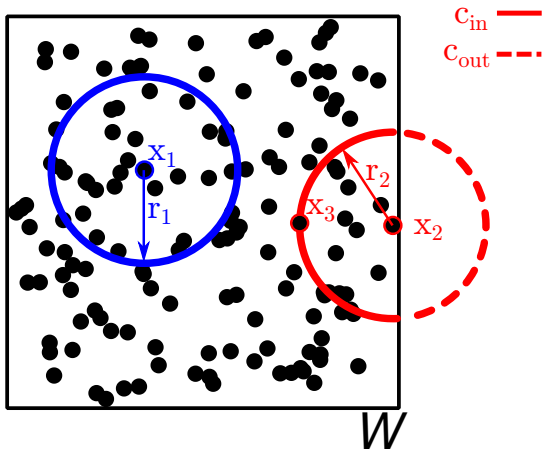

FIGURE 2.34 – Ripley's K function estimate: the ball centred on $\boldsymbol{x}_1$ correctly estimate the local intensity (number of points divided by circumference), whereas it is clearly underestimated by the ball centred on $\boldsymbol{x}_2$.

points in the outside strip are used for the counting, but balls centred on these outside points are not used):

$$\lambda \hat{K}_{edge}(r) = \frac{1}{n'} \sum_{i=1}^{n} \sum_{i \neq j} \#\{(\boldsymbol{x}_i, \boldsymbol{x}_j) \in W_{\ominus r} \times W : \ d_{ij} \leq r\}, \quad n' = N(W_{\ominus r}) \tag{2.65}$$

While easy to compute, this method looses a lot of data and increases the variance of the estimate. Furthermore, it is approximately unbiased only for large datasets and under reasonable assumptions (Baddeley et al. [2015]).

— Isotropic correction (see 2.35b): each counting is weighed by a factor:

$$\lambda \hat{K}_{iso}(r) = \frac{1}{n} \sum_{i=1}^{n} \sum_{i \neq j} \frac{1}{w^{iso}(\boldsymbol{x}_i, \boldsymbol{x}_j)} \#\{d_{ij} \leq r\} \tag{2.66}$$

this factor accounts for the circumference (or surface for the 3D case) reduction of the ball, if not entirely in the observation window. For example in 2D, Figure 2.34, the correction factor for $(\boldsymbol{x}_2, \boldsymbol{x}_3)$ is the proportion of the disc circumference inside the observation window:

$$w_{iso}(\boldsymbol{x}_2, \boldsymbol{x}_3) = \frac{c_{in}}{c_{in} + c_{out}} \tag{2.67}$$

While easy to implement in 2D, the 3D correction factor requires deriving the surface of the sphere inside the rectangular cuboid. These were expressed in Baddeley et al. [1993], but are extremely complex.

— Translation correction: for a homogeneous point process, the edge effect can be corrected by using a translated window $W_{\boldsymbol{x}^*}$:

$$W_{\boldsymbol{x}^*} = \{\boldsymbol{u} + \boldsymbol{x}^*, \boldsymbol{u} \in W\} \tag{2.68}$$

which is used to calculate the correction factor w^{trans}:

$$w^{trans}(\boldsymbol{x}_i, \boldsymbol{x}_j) = \frac{|W \cap W_{\boldsymbol{x}_j - \boldsymbol{x}_i}|}{|W|} \tag{2.69}$$

An example is shown in Figure 2.35c. The area for two points $\boldsymbol{x}_1$ and $\boldsymbol{x}_2$, $|W \cap W_{\boldsymbol{x}_2-\boldsymbol{x}_1}|$, corresponds to the shaded area. The K function estimate is then:

$$\lambda \hat{K}_{trans}(r) = \frac{1}{n}\sum_{i=1}^{n}\sum_{i\neq j}\frac{1}{w^{trans}(\boldsymbol{x}_i,\boldsymbol{x}_j)}\#\{d_{ij}\leq r\} \tag{2.70}$$

Underlying this correction is the probability of observing two points far from each other. For very close points, the window bias is rather small and only a small number of pair of points are unobserved. The further apart the points are (i.e. for large r), the larger number of pair of points are not counted.

In the context of this work, the translation correction is finally chosen to study the data. It provides an accurate unbiased estimate with relative ease of calculation compared to other methods.

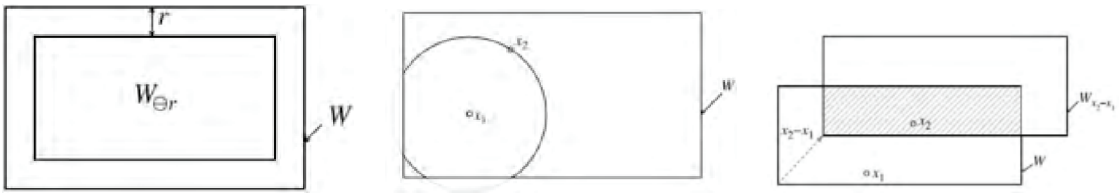

(a) Reduced observation window correction (b) Isotropic correction (c) Translation correction

FIGURE 2.35 – Different methods of correction to estimate the Ripley's K function, Illian et al. [2007] chapter 4.

Parameter optimisation: method of minimum contrast

After a model is chosen to fit experimental data, the parameters must be inferred. First, for an experimental set of points $\mathbb{X} = \{\boldsymbol{x}_i, i = 1, ..., n_{\mathbb{X}}\}$, the experimental estimate $\hat{K}_{exp}(r)$ function is calculated. For a set of parameters $\boldsymbol{\theta}$, the experimental function is compared with the analytical Ripley function $K_{\boldsymbol{\theta}}(r)$ (derived in the previous Section 2.4.2) by using the contrast function $D(\boldsymbol{\theta})$:

$$D(\boldsymbol{\theta}) = \int_{r_{min}}^{r_{max}} \left[\hat{K}_{exp}(r)^{q_1} - K_{\boldsymbol{\theta}}(r)^{q_1}\right]^{q_2} dr, \tag{2.71}$$

where $(q_1, q_2) \in \mathbb{R}^2$. This method consist in minimizing a certain q_1-norm of the Ripley functions (to the power of q_2) between two radii r_{min} and r_{max}.

For a clustered process, the different values suggested in Waagepetersen [2006] are used:

— $r_{min} = 0$ and r_{max} is half the minimum observation window size;

— $q_2 = 2$ as in the least square method;

— $q_1 = \frac{1}{4}$

The method is then used to find the best parameters $\boldsymbol{\theta}^*$ in the admissible space $\mathcal{D}_{\boldsymbol{\theta}}$:

$$\boldsymbol{\theta}^* = \underset{\boldsymbol{\theta}\in\mathcal{D}_{\boldsymbol{\theta}}}{\arg\min}\, D(\boldsymbol{\theta}) \tag{2.72}$$

This optimal parameter set is achieved by minimizing the $D(\boldsymbol{\theta})$ function. Three different optimization methods were used:

— a grid search method: a discrete grid of the components of the parameters is built, and the contrast function is calculated for each points. For example, the modified Thomas process requires optimizing λ_p and σ_T. This is done by computing the contrast function on the discrete grid $[\lambda_p^{(i)}, \sigma^{(j)}]_{\{i,j\}=\{1,..,n\times 1,...,m\}}$, therefore requiring $n \times m$ calculations. This method is highly unoptimized but provides an exhaustive method to find possible global minimums.

— A simple gradient-based search.

— A hybrid genetic algorithm (described in Section 3.2.3) combining a genetic algorithm followed by a subsequent local search;

A test case is used to validate the optimizing process: a modified Thomas point process is simulated on a unit window (see Figure 2.37a), and the original parameters are inferred based on this unique observation. The number of children $\bar{c} = 50$ is not directly part of the optimisation process. Indeed the estimated intensity $\hat{\lambda}$ and the number of parents λ_p provide the number of children:

$$\bar{c} = \frac{\hat{\lambda}}{\lambda_p} \tag{2.73}$$

The results are presented in Table 2.13. The different optimisation methods provide similar results, and are not longer further differentiated (although the gradient and hybrid method were systematically used to assert the results). The cluster "size" σ is well identified by the optimisation process, but the parent intensity process is overestimated. This bias could be caused by:

— The edge effect: although the Ripley's K function uses an edge correction, the relative small sample size could still cause some bias.

— The simulation uniqueness: a point process is a random process and one simulation (i.e. observation) cannot capture all the statistical quantities.

— Parameter uniqueness: Figure 2.36 shows the grid search results for different parent process intensity λ_p. While the correct value ($\lambda_p = 15$) is clearly not the global minimum, values between $\lambda_p = 20$ and $\lambda_p = 25$ can all provide similar minimum contrast values for corresponding σ_T close to 0.04.

The optimized parameters are different from the original ones, but the adjusted Ripley's K function closely fits the empirical observed one (see Figure 2.37b). The optimisation process does not provide a stable result: different parameters give similar Ripley's K functions and must be used with care. An identical procedure is done using a Matérn point process ($\lambda_p = 10$, $\bar{c} = 100$, $R_0 = 0.25$ on a $[0, 2]^3$ observation window), and leads to the same conclusions (see Table 2.14).

Table 2.13 – Parameter inference of a modified Thomas point process. The significant Figures are provided to show the different methods do not provide the exact same optimisation.

Parameter	Original	Grid Search	Gradient	Hybrid genetic
λ_p	15	23.650	23.634	23.633
σ_T	0.04	0.038	0.038	0.038

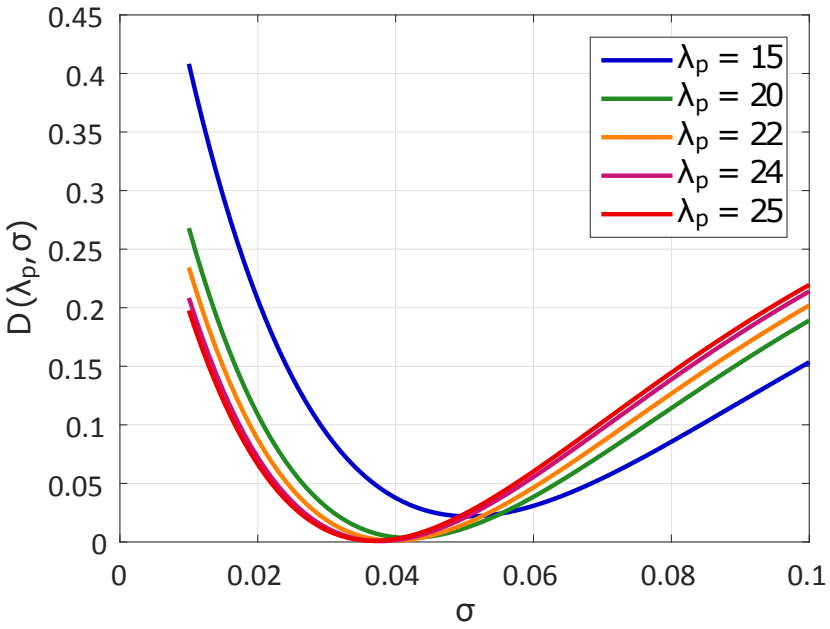

FIGURE 2.36 – Parameter optimisation search: several parameters points provide similar contrast minimum.

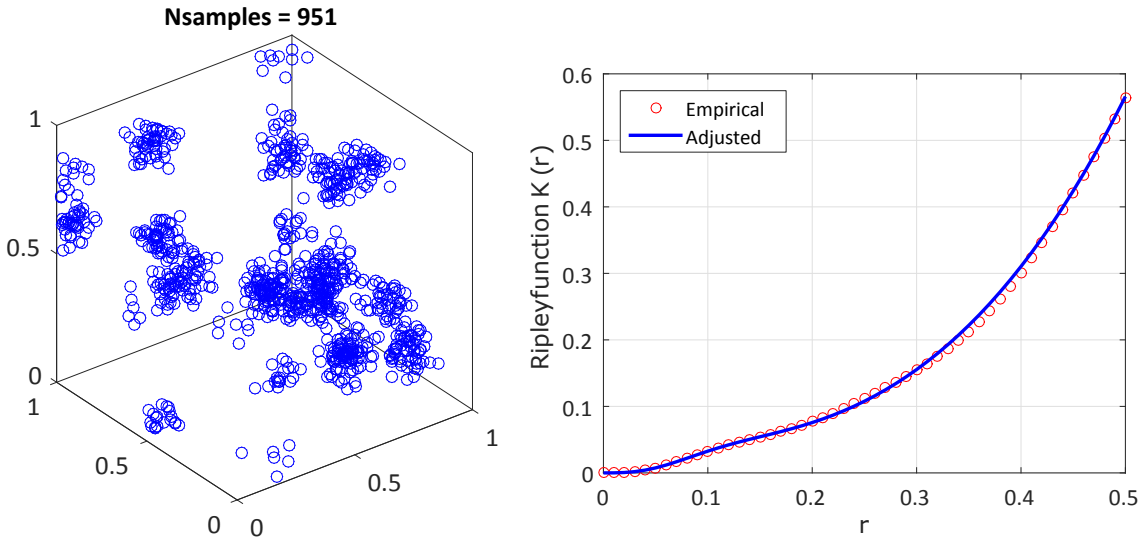

(a) Simulation of a modified Thomas point process

(b) Empirical and adjusted (by hybrid genetic algorithm) K-Ripley function.

FIGURE 2.37 – Modified Thomas point process ($\lambda_p = 15$, $\bar{c} = 50$, $\sigma_T = 0.04$): comparison between empirical and adjusted K-Ripley function.

Table 2.14 – Parameter inference of a Matérn point process ($\lambda_p = 10$, $\bar{c} = 100$,$R_0 = 0.25$)

Parameter	Original	Grid Search	Gradient	Hybrid genetic
λ_p	10	18.250	17.809	17.797
R_0	0.25	0.200	0.203	0.203

2.4.4 Application to tomographic data

Model fit

The parameter inference is carried out on the thresholded and filtered data of specimen 12T5 (gray level thresholding of 20000 and 3d Feret filtering: L3D>40 µm, see Section 2.3.3 for further details). Each porosity is represented by its barycentre, which is considered as a point. However, given the developed edge correction methods, the observation window must be a rectangular cuboid. Therefore, the largest possible cuboid is extracted from the initial cylindrical data (see Figure 2.38), and only the data points therein are considered. The total volume of the cuboid is 159.25 mm^3 and 1 323 points remain after filtering. The estimated intensity in the cube is:

$$\hat{\lambda} = \frac{1323}{159.29} = 8.31 \text{points/mm}^3 \tag{2.74}$$

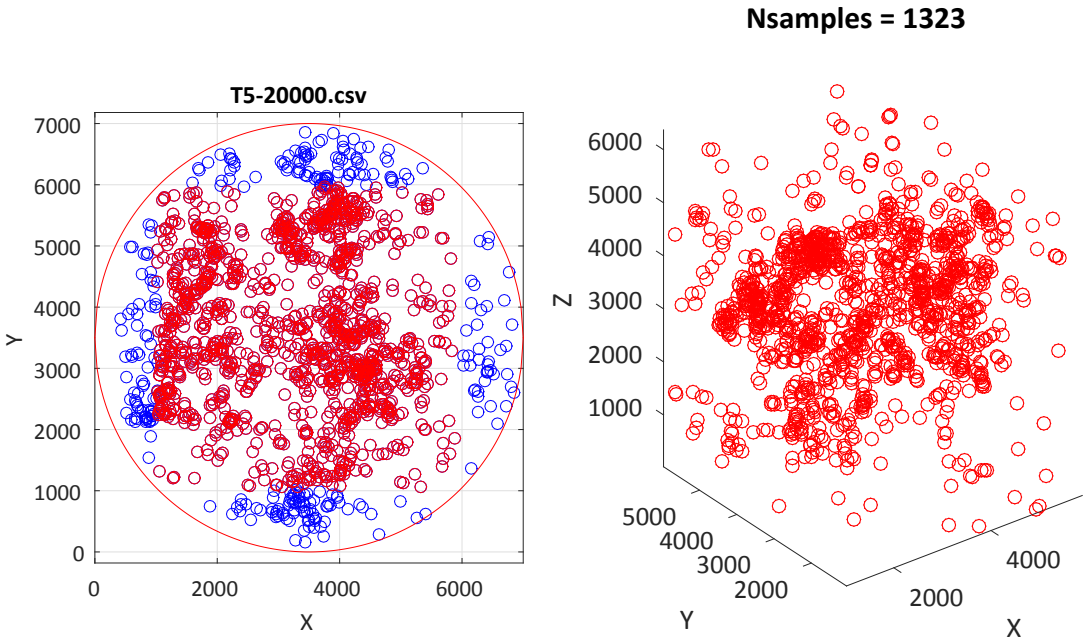

(a) Only the points in the central square are used for statistical inference.

(b) 3d representation of the data points used.

FIGURE 2.38 – Visualisation of the data selection of the T5 specimen (gray level thresholding of 20000 and 3d Feret filtering: x_f>40 µm)

Using the minimum contrast with $p = 2$ and $q = 1/4$, the optimisation method is applied to the experimental data for both Thomas modified and Matérn point process. The results are reported in Table 2.15, and the Ripley K functions are compared in Figure 2.39.

The Poisson point process is clearly unable to represent the observed data, whereas both the modified Thomas and the Matérn point process give a better and similar fit.

However, the clustered simulated processes slightly overestimates the Ripley's K function for radii r between 1 and 2 mm, and underestimate for $r > 2$ mm. As seen in Figure 2.40, the clustered process is unable to capture the seemingly isolated data points outside the clusters shown on real data (see Figure 2.38b). To maintain the global intensity of the process, the number of children $\bar{c}$ has to be higher to compensate, thereby increasing Ripley's K function for short distances ($r < 2$ mm). For the longer

ranges ($r > 2\,\text{mm}$), there are no isolated data points and the simulated Ripley's K function is lower than observed. The isolated points could be linked to isolated gas porosities, and an added Poisson point process could be superposed in order to simulate these isolated data points. However, the parameter inference robustness would suffer from the added complexity.

Table 2.15 – Infered parameters for the T5 specimen with the data thresholded at 20 000, and the length filtered x_f>40 µm.

	λ_p	σ_T (mm)	R_0 (mm)	$\bar{c} = \hat{\lambda}/\lambda_p$
Thomas	0.0305	0.5973	-	272.8
Matérn	0.0312	-	1.2534	266.6

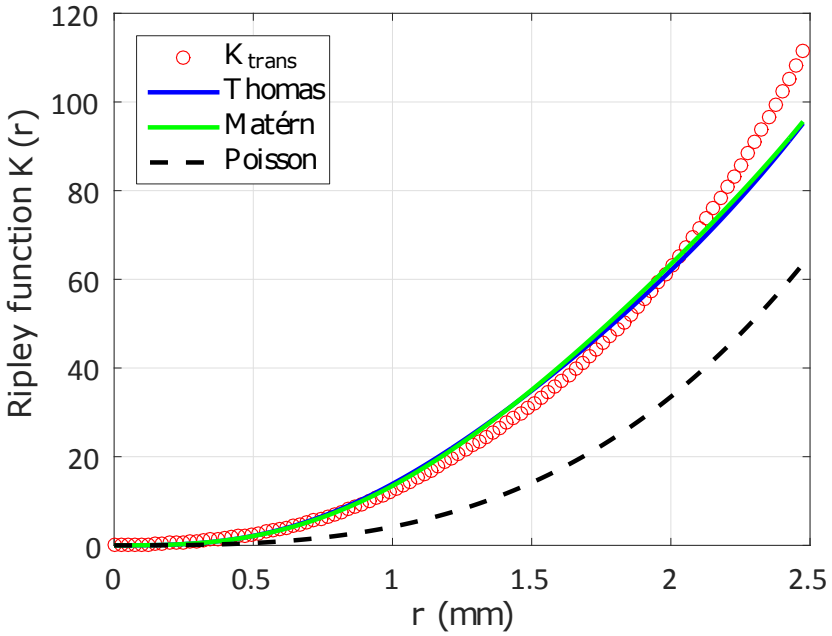

FIGURE 2.39 – Spatial statistics inference: the experimental Ripley's function K_{trans} is close to the optimized Matérn and Thomas point process ones. The Poisson point process distribution is unable to capture the spatial data.

To validate and ascertain the robustness of the model, simulation envelops are drawn: N_{repl} simulated samples are drawn and their empirical K function calculated. These envelops are compared to the observed function K_{trans}, based on the real experimental data. Results shown in Figure 2.41 confirm Poisson process cannot be used to simulate the observed spatial point processes. For the clustered points process (modified Thomas and Matérn), the observed Ripley function K_{trans} is well inside the envelopes, confirming the model robustness.

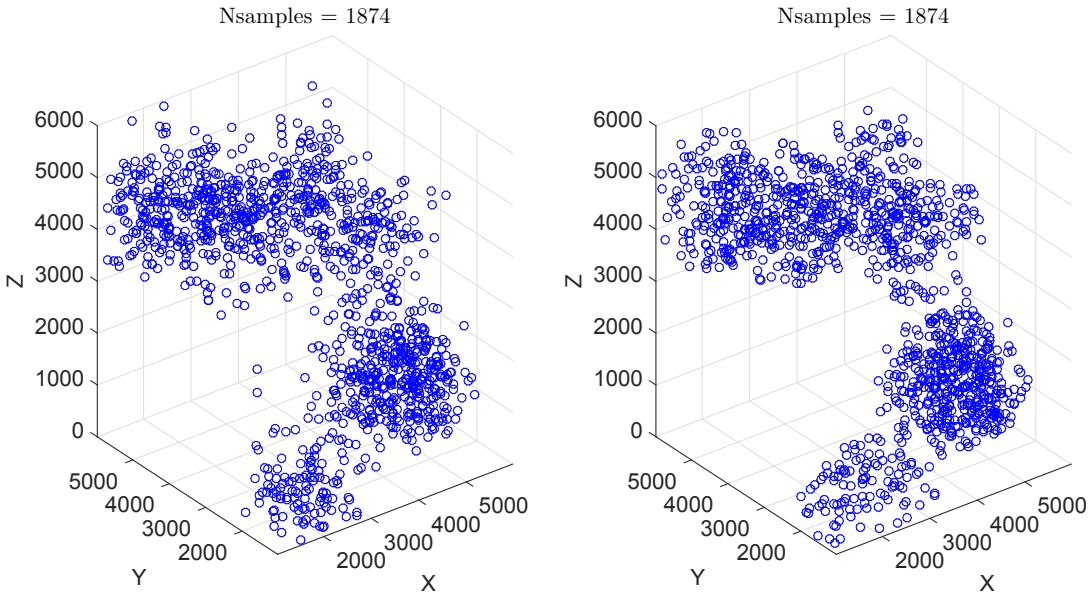

(a) Modified Thomas point process. (b) Matérn point process

FIGURE 2.40 – Simulated porosity of specimens. The parent process is unchanged for both specimens by fixing the random seed for comparison purposes.

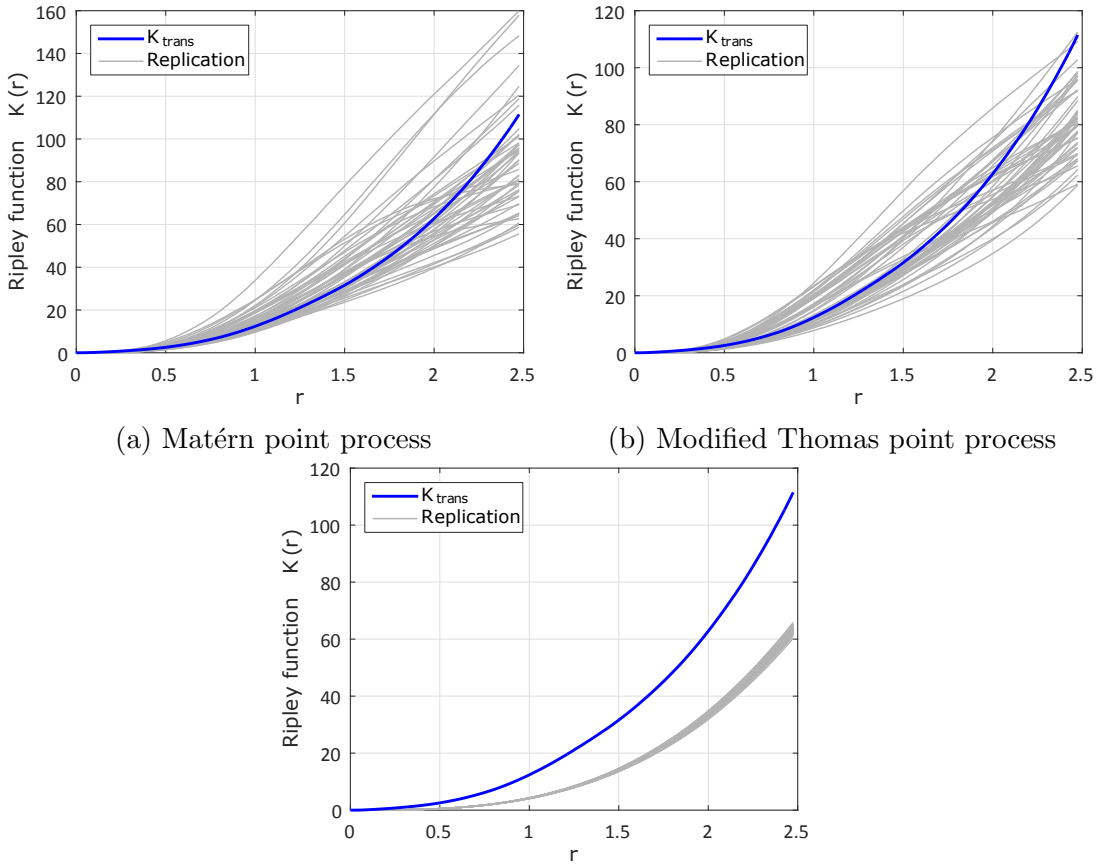

(a) Matérn point process (b) Modified Thomas point process

(c) Poisson point process

FIGURE 2.41 – Simulations envelopes for different points processes for T5 specimen, N_{repl}=50

2.4.5 Marked Point Process

In order to **study the correlation between the defects position and size** (hereafter considered as points), marked point processes can be used. For a point, the mark can be a qualitative or a quantitative one, and represents a characteristic. For the scope of this study, **the mark of interest is therefore the defect size**. This study was done in collaboration with Prof. Sudret, and the results are fully reported in Sudret [2015b].

Several theoretical models can be applied to study marked point processes:

— *Random marks*: for this case, spatial and mark distribution are considered independent. The spatial distribution is characterized and for each point, the mark is considered as independent of its position (and consequently, independent of its neighbours marks).

— *Random superposition*: for quantitative marks m defined in $\{m_1, ..., m_Q\}$ with $Q \in \mathbb{N}$, Q sub process are defined for each mark class. The final process is defined by superposition of the Q sub processes $\{\mathbb{X}_i, i = 1, ..., Q\}$:

$$\mathbb{X}_i = \{\boldsymbol{x}_j^{(i)}, j = 1, ..., n_i\}, i = 1, ..., Q \tag{2.75}$$

$$\mathbb{X} = \bigcup_{i=1}^{Q} (\mathbb{X}_i \times \{m_i\}) = \left\{(\boldsymbol{x}_j^{(i)}, m_i), j = 1, ..., n_i; i = 1, ...Q\right\} \tag{2.76}$$

— *Geostatic marks*: here, the marks are defined based on a random continuous field $Z(\boldsymbol{x}, \omega)$. Once the point position $\boldsymbol{x}_j$ is known, the corresponding mark is $Z(\boldsymbol{x}_j)$. Hence the process $\mathbb{W}$:

$$\mathbb{X} = \{(\boldsymbol{x}_j, Z(\boldsymbol{x}_j)), j = 1, ..., n\} \tag{2.77}$$

For this study, sample "12T5-20 000" is used (i.e. sample 12T5 with a 20000 gray threshold, see Section 2.3.1 for more details). Here, the largest defects are no longer the main concern, and therefore, only defects smaller than 10 µm are excluded (rather than 40 µm). The defect size remains the 3D Feret diameter which is considered as the point mark.

First order characteristics

For qualitative marks $m_1, ..., m_Q$, the probability distribution is defined by:

$$p_i = \mathbb{P}(M = m_i) \tag{2.78}$$

The probability p_i is easily obtained with the sub process intensity λ_i containing solely the marks m_i:

$$p_i = \frac{\lambda_i}{\lambda} \tag{2.79}$$

where λ is the intensity of the spatial point process as defined in Section 2.4.1 (i.e. all point considered, with no mark differentiation).

For quantitative marks $M \in \mathcal{D}_M$, let us consider a subspace $B_{sub} \in W$ and a subset $]-\infty, m_0]$. For a given m_0, a sub process can be defined by considering all marks such as $m \leq m_0$. The number of points in this subspace is therefore:

$$\mathbb{E}[N(B_{sub}; m(\boldsymbol{x}) \leq m_0)] \stackrel{\text{def}}{=} \lambda(m_0)|B| \tag{2.80}$$

where $|B_{sub}|$ is the volume of B_{sub} (in 3 dimensions). When m_0 approaches infinity, all the marks are considered, and therefore:

$$\lim_{m_0 \to \infty} \lambda(m_0) = \lambda \tag{2.81}$$

Consequently, the cumulative distribution of marks F_M is defined by:

$$F_M(m) = \frac{\lambda(m)}{\lambda} \tag{2.82}$$

from which the probability density function (pdf) can be obtained $f_M(m) = F'_M(m)$. The mean and variance are defined by:

$$\mu_m = \int_{\mathcal{D}_M} m f_M(m) dm \tag{2.83}$$

$$\sigma_m^2 = \int_{\mathcal{D}_M} (m - \mu_m)^2 m f_M(m) dm \tag{2.84}$$

These different quantities can be easily estimated. For an observed volume W, the mark mean estimate is:

$$\hat{\mu_m} = \frac{1}{n} \sum_{\boldsymbol{x} \in W} m(\boldsymbol{x}) \tag{2.85}$$

and the mark variance:

$$\hat{\sigma_m}^2 = \frac{1}{n} \sum_{\boldsymbol{x} \in W} (m(\boldsymbol{x}) - \hat{\mu_m})^2 \tag{2.86}$$

Nearest neighbour correlation index

The nearest neighbour correlation index aims at pointing out if there is a correlation between the mark of a point, and the mark of the nearest point. For $\boldsymbol{x} \in \mathbb{X}$, the nearest neighbour is referred to as nei($\boldsymbol{x}$):

$$\text{nei}(\boldsymbol{x}) = \underset{\boldsymbol{y} \in \mathbb{X} \setminus \{x\}}{\arg\min} ||\boldsymbol{y} - \boldsymbol{x}|| \tag{2.87}$$

Using the nearest neighbour, three indexes can be defined (Illian et al. [2007]):

— The nearest neighbour mean:

$$\boldsymbol{n}_1 = \mathbb{E}_{\boldsymbol{x}}[m(\text{nei}(\boldsymbol{x}))]/\mu_m \tag{2.88}$$

— The mean mark product:

$$\boldsymbol{n}_{mm} = \mathbb{E}_{\boldsymbol{x}}[m(\boldsymbol{x}) m(\text{nei}(\boldsymbol{x}))]/\mu_m^2 \tag{2.89}$$

— The variographic mark index:

$$\boldsymbol{n}_\gamma = \mathbb{E}_{\boldsymbol{x}} \left[(m(\boldsymbol{x}) - m(\text{nei}(\boldsymbol{x})))^2 \right] / \sigma_m^2 \tag{2.90}$$

These indexes are to be distinguished from correlation indexes, for they can be greater than 1. Due to the normalisations, they are to be compared to one: a value close to one indicating a lack of correlation. These index estimates are readily obtained, for edge effect introduces only a small bias and no edge correction method are necessary (Pommerening and Stoyan [2006]).

These indexes are calculated for the tomographic observed data and shown in Table 2.16. All the values are all close to one, which is a first step indicating the lack of correlation between defect size and position.

Table 2.16 – Nearest neighbour correlation index for specimen 12T5

index	$\boldsymbol{n}_1$	$\boldsymbol{n}_{mm}$	$\boldsymbol{n}_\gamma$
value	0.9985	1.0001	0.9509

Weighted K-Ripley and L-Besag functions

Detailed study of marked point process can be achieved by using the weighted Ripley K function. For an unmarked point process, the Ripley K function (in Equation 2.47) can be rewritten:

$$K(r) = \frac{1}{\lambda}\mathbb{E}_{\boldsymbol{x}}\left[\sum_{\boldsymbol{y}\in\mathbb{X}\setminus\boldsymbol{x}} \mathbf{1}_{b(\boldsymbol{x},r)}(\boldsymbol{y})\right] \tag{2.91}$$

where $\mathbf{1}_{b(\boldsymbol{x},r)}$ is the indicator function centred on $\boldsymbol{x}$ of radius r. The weighted Ripley K-function K_{mm} is:

$$K_{mm}(r) = \frac{1}{\lambda\mu_m^2}\mathbb{E}_{\boldsymbol{x}}\left[\sum_{\boldsymbol{y}\in\mathbb{X}\setminus\boldsymbol{x}} m(\boldsymbol{x})m(\boldsymbol{y})\mathbf{1}_{b(\boldsymbol{x},r)}(\boldsymbol{y})\right]. \tag{2.92}$$

As for unmarked point process (see Section 2.4.2), an L Besag function can be defined using the unit volume sphere in d dimension V_{d_R}:

$$L_{mm}(r) = \left(\frac{K_{mm}(r)}{V_{d_R}(1)}\right)^{1/d}, \tag{2.93}$$

which translates in 3 dimensions to:

$$L_{mm}(r) = \left(\frac{3K_{mm}(r)}{4\pi}\right)^{1/3}. \tag{2.94}$$

As for unmarked point process, the K_{mm} Ripley weighted function estimation requires an edge correction method. The same method of translation correction is applied (see Equation 2.70 in Section 2.4.3):

$$\lambda\mu_m^2\hat{K}_{mm,trans}(r) = \frac{1}{n}\sum_{i=1}^{n}\sum_{i\neq j}\frac{m(\boldsymbol{x}_i)m(\boldsymbol{x}_j)}{w^{trans}(\boldsymbol{x}_i,\boldsymbol{x}_j)}\#\{(\boldsymbol{x}_i,\boldsymbol{x}_j)\in W : d_{ij}\leq r\} \tag{2.95}$$

The weighted K_{mm} Ripley function is compared to the K Ripley function, which is calculated without the marks. If spatial and mark distribution are uncorrelated, these two functions are equal.

The L Besag function can also be estimated by:

$$\hat{L}_{mm,trans}(r) = \left(\frac{3}{4\pi\hat{\lambda}\hat{\mu_m}^2}\frac{1}{n}\sum_{i=1}^{n}\sum_{i\neq j}\frac{m(\boldsymbol{x}_i)m(\boldsymbol{x}_j)}{w^{trans}(\boldsymbol{x}_i,\boldsymbol{x}_j)}\#\{(\boldsymbol{x}_i,\boldsymbol{x}_j)\in W : d_{ij}\leq r\}\right)^{1/3} \tag{2.96}$$

For reading easiness, the estimate functions using translation correction are hereafter simply referred to as $\hat{K}_{mm}$ and $\hat{L}_{mm}$.

Lastly, a mark independence test can be used to test spatial and mark distributions independence. Given a sample, marks of this sample are randomly permuted creating B_{sub} artificial samples. For each artificially generated sample k, the L Besag function

$\hat{L}_{mm}^{(k)}$ is calculated creating a sheaf of curves. The extreme curves are then defined for each abscissa r by:

$$L_{mm,min}(r) = \min_{k=1,\dots,B} \hat{L}_{mm}^{(k)}(r) \tag{2.97}$$

$$L_{mm,max}(r) = \max_{k=1,\dots,B} \hat{L}_{mm}^{(k)}(r) \tag{2.98}$$

Independence between spatial and mark distribution is then checked by plotting $L_{mm,min} - \hat{L}_{mm}$ and $L_{mm,max} - \hat{L}_{mm}$ and comparing with the null hypothesis, represented by the abscissa axis.

The K_{mm} weighted Ripley function is shown in Figure 2.42a. Both the weighted and the standard Ripley function appear perfectly equal, confirming the independence of point mark and position indicated by the different indexes (see Table 2.16). However, the mark independence test shown in Figure 2.42b shows there is in fact a small interaction of marks for shorter distances.

As first order approximation, and for the rest of the study, point mark and position (i.e. defect size and position), will be considered independent. Further work could be done to investigate more precisely the relationship between size and position, but no clear correlation is unveiled through the study of marked point process, and the independence hypothesis appears reasonable.

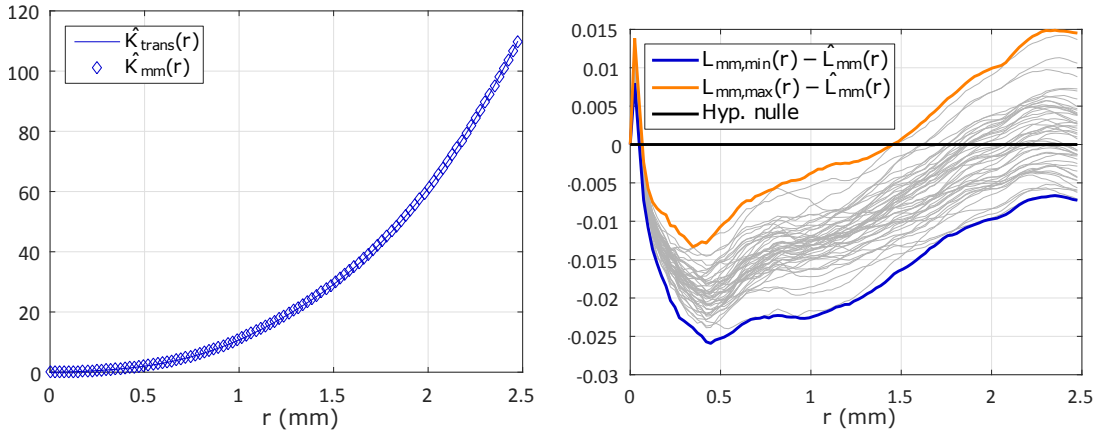

(a) K Ripley function and weighted K_{mm} Ripley function

(b) Mark independence test.

FIGURE 2.42 – Study of spatial and mark distributions correlation by marked point processes.

2.5 Conclusions

Classical 2D methods are first used to study the considered aluminium alloy microstructure. Dendrites, eutectic zone, and intermetalics are studied and the different material scales shown. Laboratory X-Ray tomography is then used to investigate in details the 3D nature of porosities. Indeed, as will be shown in the following chapters, porosities play a key role in the low-cycle fatigue of aluminium, and statistical features need to be thoroughly investigated.

After presenting the issues of image data treatment in the complex case of tomography, the porosity defects are characterized by their 3D Feret diameter. The generalized Pareto distribution provides a convenient fit: since tomography has difficulties for the smaller elements, a minimal size threshold overcomes the problem, and the parameter estimation focuses on the larger defects (which are the most critical for fatigue,

see Murakami [1993]). Sphericity is also characterized, and the correlation with size established. Three different statistical samples from three different specimens are analysed using this method. They all provide similar inferred distributions, thus showing that a single sample contains a large enough number of defects to be statistically representative.

Then, point process statistics is used to understand and model the nature of spatial distribution of defects. The developed tools are applicable to 3D populations, and can capture statistical distances between points accurately (using the K-Ripley function). It is clearly shown that the Poisson point process cannot simulate the defect spatial distribution (i.e. defects are not distributed completely randomly). Use of clustered point processes such as Thomas or Matérn, allows for a better simulation. However, the high number of parameters does not provide robust fits (several set of parameters give similar identification results, yet describe different spatial distribution).

Visual comparisons are difficult given the 3D nature of the data. For example, comparing real 3D data in Figure 2.38 with simulated data in Figure 2.40a does not seem to provide correct simulations. However, using 2D representation of a 2 mm high of 3.5 mm radius (corresponding to the real sample radius), with identical representation features shows similar features (see Figure 2.43). As discussed in Section 2.4.4, the simulated processes overestimate the cluster nature of the point processes. Despite the differences, visual comparison shows similar features, and distances between defects and global behaviour of the point process seem to be respected.

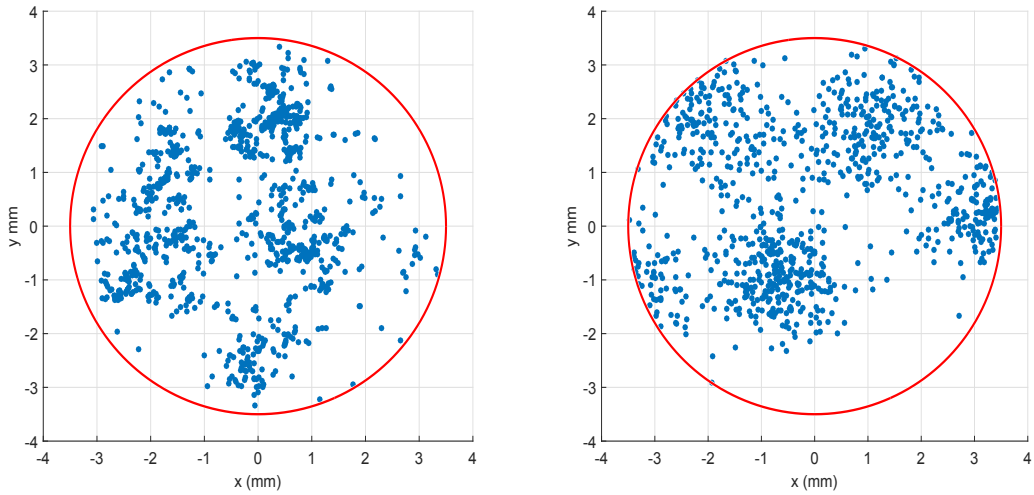

(a) Real cylinder section of 12T5 sample

(b) Simulated cylinder section of sample (Thomas point process)

FIGURE 2.43 – Simulation of spatial point process: experimental and simulated point process.

Finally, marked point processes are used: the theory enables to determine the correlation between spatial and size distribution of defects. It is shown that while such a correlation might exist, it is not a strong one.

Chapitre 3

Fatigue tests

A fatigue tests campaign is conducted under various strain and temperature loadings. The results are first presented and commented, and especially, evolution of the different quantities with time. The fatigue test results are interpreted with the classical Coffin-Manson criterion, but several issues are underlined. An equivalent energy is then introduced. Combined with a classical power-law, this shows good results for all the studied temperatures, and provides unified parameters. Then, the observed scatter is modeled by using non constant standard deviation, which captures more accurately the observed results. Finally, in the conclusion, the results of the implementation on an industrial component are presented.

3.1 Test setup

3.1.1 Experimental setup

Fatigue tests are performed on Renault standard cylindrical low-cycle fatigue specimens (shown in Figure 3.1a). The specimens are machined from round bars specially cast for this study. The tested zone is a 7 mm diameter cylinder and 14 mm high. A 12 mm gauge class 0.5 extensometer is used to perform strain controlled tests. The loading is applied by an Instron 8500 servo-hydraulic machine equipped with a furnace (see Figure 3.1b). The strain imposed signal waveform is triangular as to maintain a constant strain-rate ($\dot{\varepsilon}$) of 1.10^{-3}s^{-1}, and of varying amplitudes ($\Delta\varepsilon/2$) between $\pm 0.2\%$ and 0.4% and a strain ratio $R_\varepsilon = \varepsilon_{min}/\varepsilon_{max} = -1$. Tests are conducted in air under 4 different constant and controlled temperatures: 20 (ambient), 150, 200 and 250 °C. While some figures show evolution of stress amplitude after onset of crack initiation for illustration purposes, the number of cycles to failure is always defined by a 10% stress drop from the trend line.

3.1.2 Uncertainty evaluation

The uncertainty in low-cycle fatigue testing are done accordingly to the procedure described in Kandil [2000].

Specimen cross-section The machined specimen diameters are measured on all the specimens before testing, all the measures lie between 6.99 and 7.01 mm for a nominal diameter d =7 mm. The uncertainty in the diameter u_d is therefore:

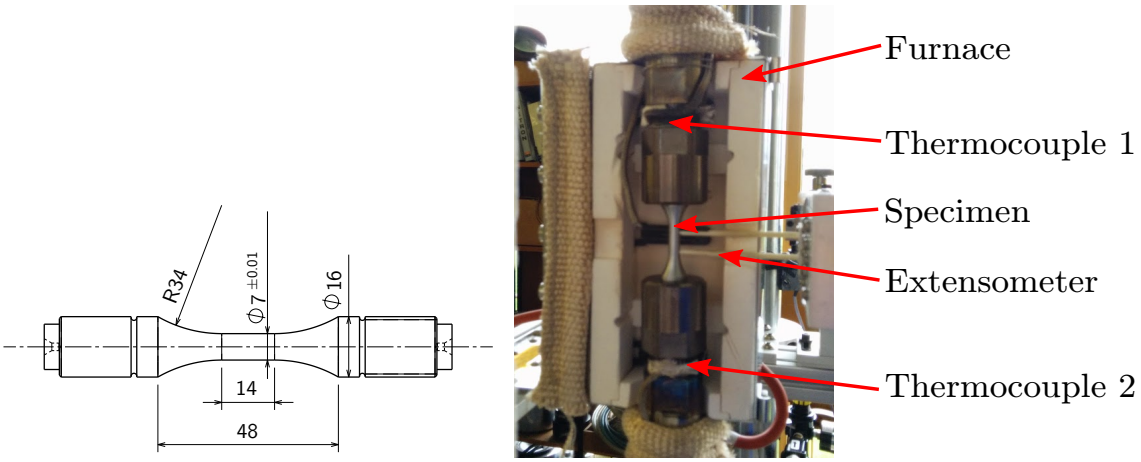

(a) Specimen geometry for low-cycle fatigue test.

(b) Experimental setup of furnace.

FIGURE 3.1 – Experimental setup

$$u_d = \pm 0.01\,\text{mm} \quad (d = 7\,\text{mm}) \tag{3.1}$$

The uncertainty u_{A0} in the cross section $A0$ is given by:

$$u_{A0} = \sqrt{\frac{\pi^2 d^2 u_d^2}{4}} \tag{3.2}$$

which numerically is:

$$u_{A0} = 0.11\,\text{mm}^2 \quad (A0 = 38.48\,\text{mm}^2) \tag{3.3}$$

Strain measurement The $L_0 = 12\,\text{mm}$ gauge extensometer meets or is better than class 0.5, the uncertainty u_e associated with the displacement e is:

$$u_e = \pm 0.5\,\mu\text{m}, \text{ or } \frac{u_e}{e} = \pm 0.5\% \text{ whichever is the greatest} \tag{3.4}$$

For each test, the extensometer is reset before the test, care was taken as to maintain the initial displacement below $50\,\mu\text{m}$. For most of the tests, the initial length was corrected for the strain calculation, so the uncertainty u_{L_0} represents the upper range:

$$u_{L_0} = \pm 50\,\mu\text{m} \tag{3.5}$$

The relative uncertainty u_ε on the strain ε is expressed by:

$$\frac{u_\varepsilon}{\varepsilon} = \sqrt{\left(\frac{u_e}{L_0}\right)^2 + \left(\frac{u_{L_0}}{L_0}\right)^2} \tag{3.6}$$

For example, the uncertainty for a fully reverse test where $\Delta\varepsilon/2 = 0.003$, then $u_{\Delta\varepsilon} = 0.00006$.

Stress measurement The uncertainty of the force measurement u_F is given by the calibration of the force sensor. It is taken as the highest relative uncertainty u_F/F (F being the force) measured in the used range ($\pm 10\,\text{kN}$):

$$\frac{u_F}{F} = 0.26\% \tag{3.7}$$

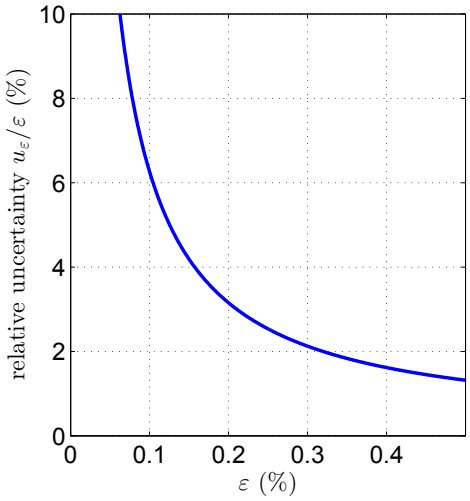

FIGURE 3.2 – Relative strain uncertainty as a function of strain

The total stress relative uncertainty u_σ can then be expressed by :

$$\frac{u_\sigma}{\sigma} = \sqrt{\left(\frac{u_F}{F}\right)^2 + \left(\frac{u_{A0}}{A_0}\right)^2} = 0.38\% \tag{3.8}$$

For example: $F = 5.000\,\text{kN}$ ($\sigma = 129.9\,\text{MPa}$) implies an uncertainty $u_\sigma = 0.50\,\text{MPa}$.

The measurement uncertainties (strain and stress) are very small and controlled for the tests, and are not considered in the rest of the study. Rigorously, misalignment should also be considered as a measurement uncertainty, but most of the tests being in generalized plasticity, it cannot be directly evaluated. The alignment procedure is done accordingly to standard (ASTM [2004]) .

3.1.3 Temperature control

Tests were conducted in laboratory air under constant temperature according to ASTM standard (ASTM [2004]). For a set point temperature T_{sp}, the measured temperatures T_i in the gauge length ($L_0 = 12\,\text{mm}$) must be included in the interval:

$$T_i \in [T_{sp} \pm \Delta T] \tag{3.9}$$

where ΔT is the tolerated variation:

$$\Delta T = \max(2\,^\circ\text{C}, 1\%.T_{sp}) \tag{3.10}$$

In order to achieve this accuracy, the furnace temperature is regulated by means of 2 thermocouples (1 and 2 in Figure 3.1b) which set points are configured to obtain the desired set point in the specimen. After calibration with an instrumented specimen equipped with thermocouples on its gauge length, this setup allows for good accuracy and stability (see for example in Figure 3.3b) after a 30 minutes preheating. It also alleviates the need to instrument each specimen by adding thermocouples which can act as stress concentrators. The results for the different temperatures are shown in Table 3.1, the interval for the measured temperature T_m being the union of 3 repeated tests for each temperature. For ambient temperature, the grips watercooling remains active to ensure a stable temperature (around 22 °C). For easiness of presentation, these tests are referred to as 20 °C.

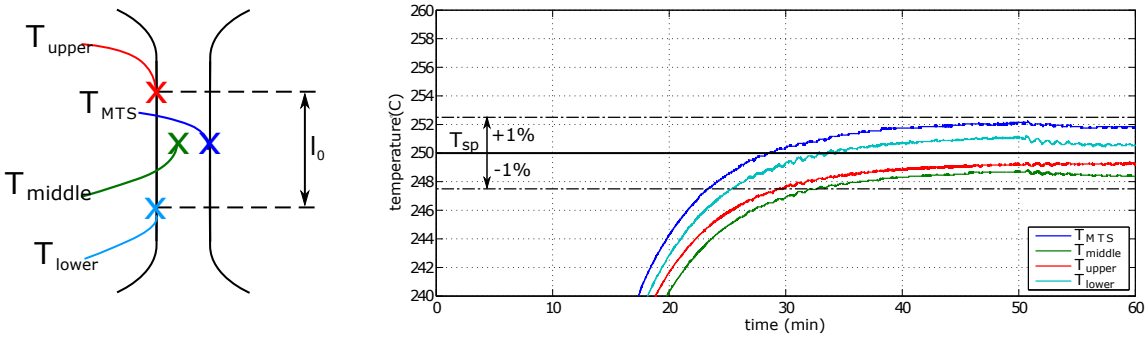

(a) Calibration instrumented specimen with thermocouple location.

(b) Temperature versus time plot for different thermocouples of instrumented specimen for a set point temperature of $T_{sp} = 250\,°C$

FIGURE 3.3 – Temperature calibration for $T_{sp} = 250\,°C$

Table 3.1 – Set point temperature T_{sp} and measured temperature in useful section T_m

T_{sp} (°C)	22	150	200	250
T_m (°C)	[22.1;22.7]	[148.4;150.9]	[199.4;200.4]	[248.7;250.7]

3.2 Material behaviour

3.2.1 Cyclic behaviour

The cyclic response of first and mid-cycle [1] are presented in Figures 3.5 through 3.8. For each test, the first cycle is used to measure the Young modulus. Figure 3.4 and Table 3.2 display a significant decrease of the Young modulus and yield strength with temperature. In order to take all the tests into account, the Yield Strength is taken for a 0.02% plastic strain. For temperatures of 20 to 150 °C, the cyclic behaviour is stable, as confirmed from the evolution of the stress amplitude in Figures 3.9 and 3.10. For $T = 200\,°C$ and 250 °C, cycle softening due to ageing occurs (see Figures 3.11 and 3.12, see also part 3.2.2). For all tests, the mean stress remains close to zero. This can be seen in Figure 3.13: stress variation (cyclic mean stress divided by cyclic stress amplitude) remains below 5%.

Table 3.2 – Evolution of both the Young modulus and the Yield stress ($\varepsilon_p = 0.02\%$) with test temperature.

T (°C)	20	150	200	250
number of tests	7	11	6	11
E (GPa)	77.4 ± 1.1	73.0 ± 1.0	70.9 ± 0.9	67.6 ± 1.1
Ys (MPa)	149.4 ± 4.4	148.1 ± 3.5	137.1 ± 5.1	114.2 ± 3.3

1. The number of cycles to failure, N_f, is taken as a 10% load drop. The mid-cycle is the cycle taken at $N_f/2$.

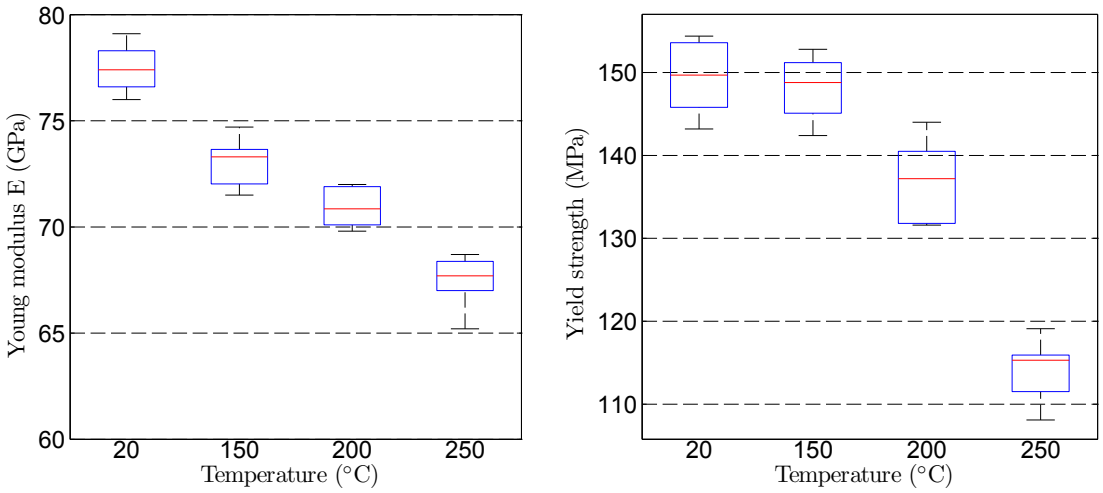

(a) Evolution of Young modulus with test temperature.

(b) Evolution of 0.02% Yield strength with test temperature.

FIGURE 3.4 – Evolution of mechanical quantities with temperature.

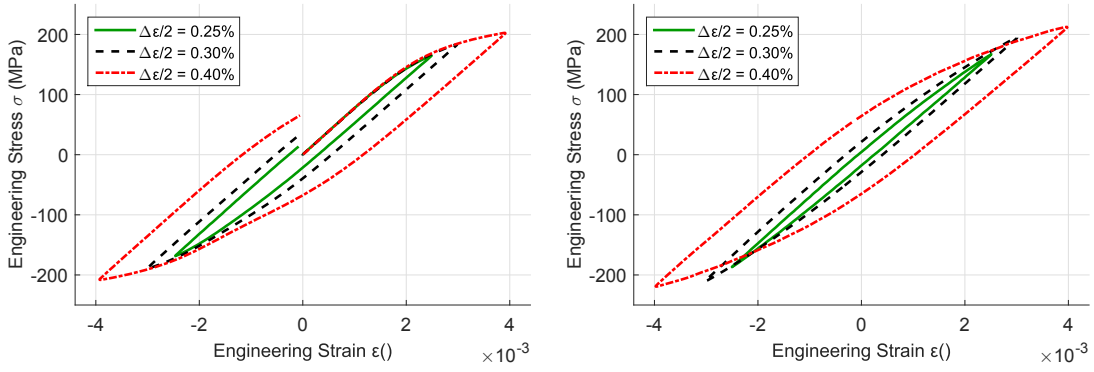

(a) First cycle

(b) Mid-cycle

FIGURE 3.5 – Stress-strain curve for $T = 20\,°C$

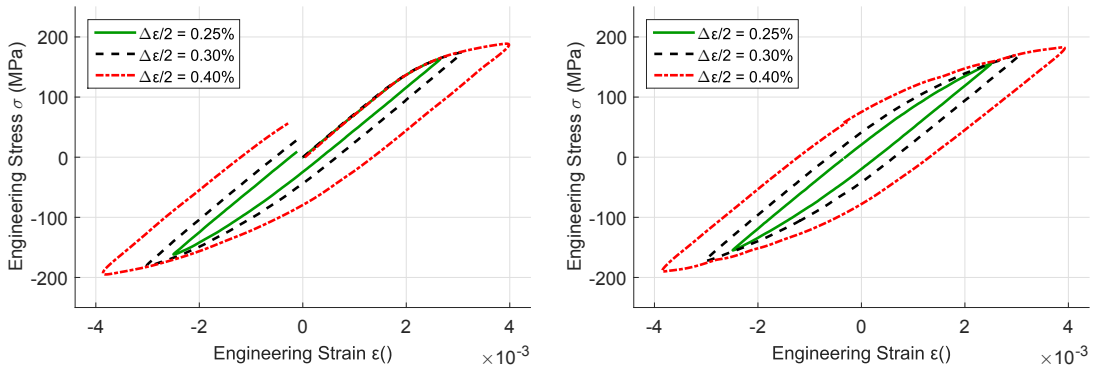

(a) First cycle

(b) Mid-cycle

FIGURE 3.6 – Stress-strain curve for $T = 150\,°C$

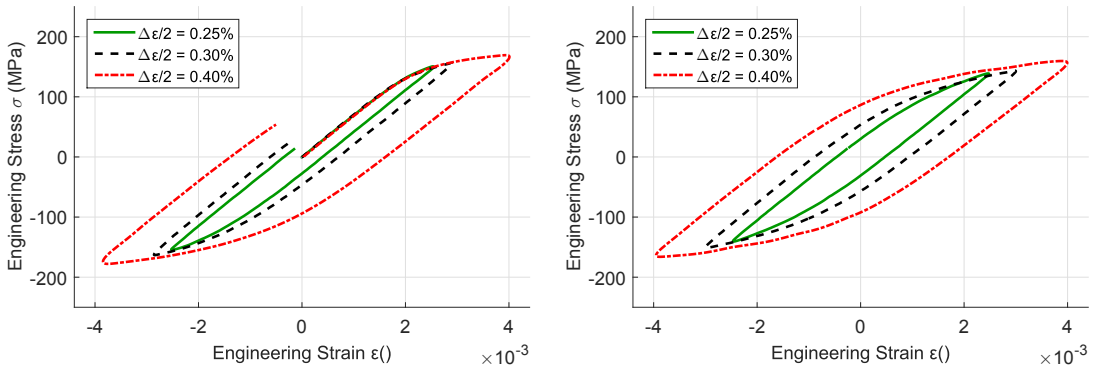

(a) First cycle (b) Mid-cycle

FIGURE 3.7 – Stress-strain curve for $T = 200\,°C$

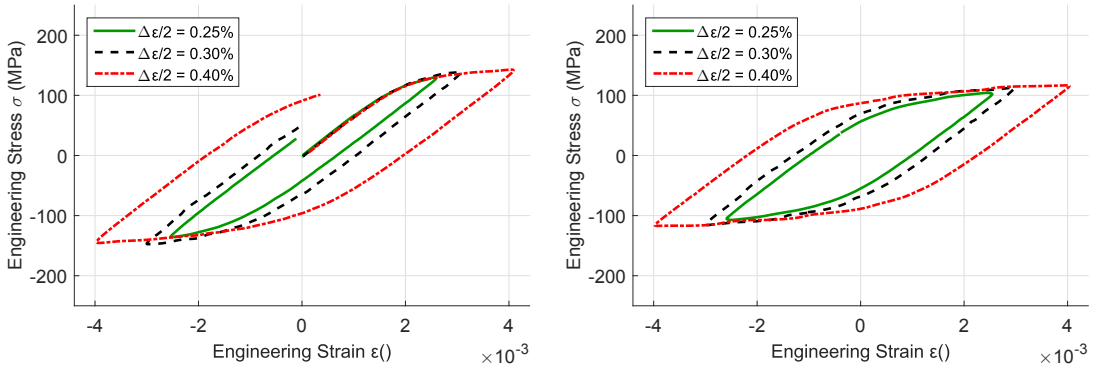

(a) First cycle (b) Mid-cycle

FIGURE 3.8 – Stress-strain curve for $T = 250\,°C$

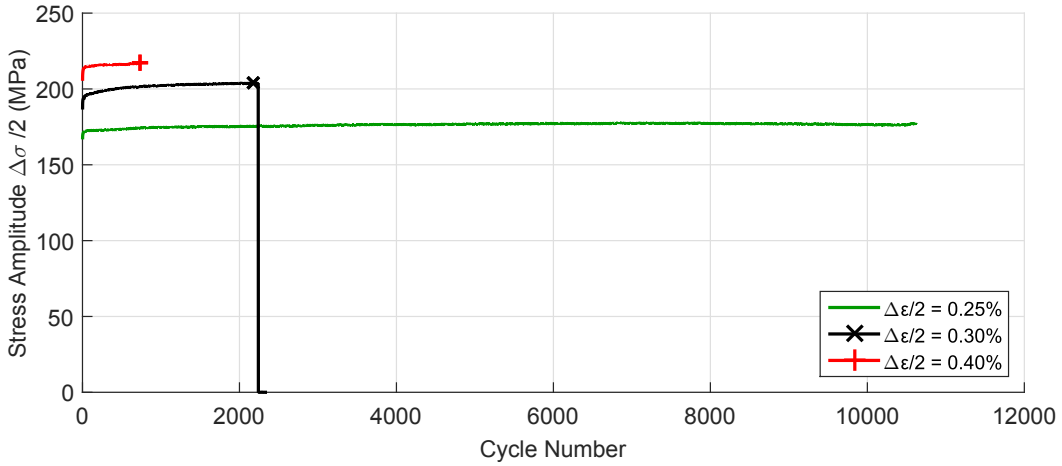

FIGURE 3.9 – Evolution of stress amplitude for $T = 20\,°C$, $R_\varepsilon = -1$

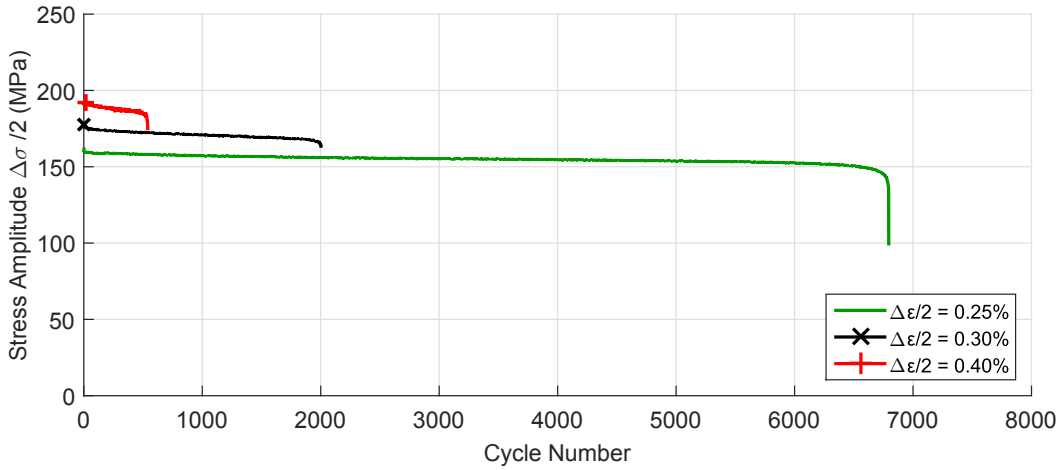

FIGURE 3.10 – Evolution of stress amplitude for $T = 150\,°\mathrm{C}$, $R_\varepsilon = -1$

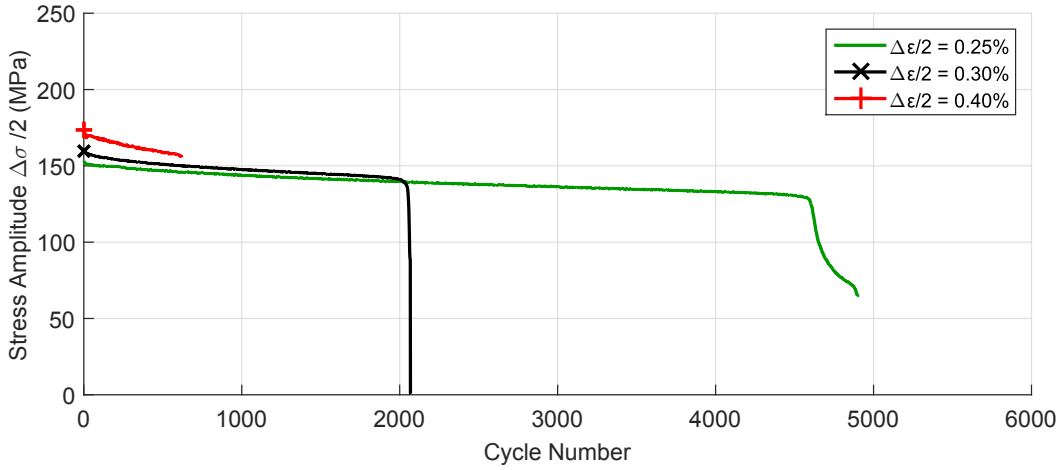

FIGURE 3.11 – Evolution of stress amplitude for $T = 200\,°\mathrm{C}$, $R_\varepsilon = -1$

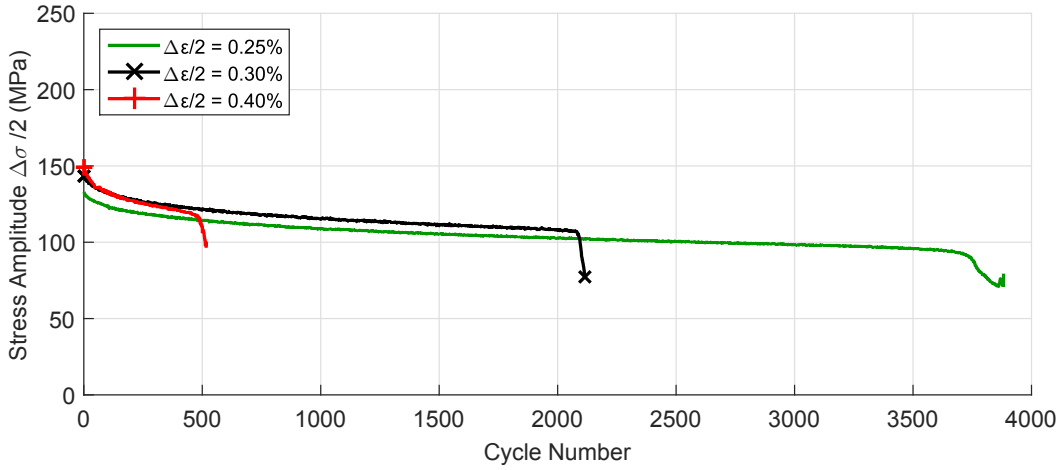

FIGURE 3.12 – Evolution of stress amplitude for $T = 250\,°\mathrm{C}$, $R_\varepsilon = -1$

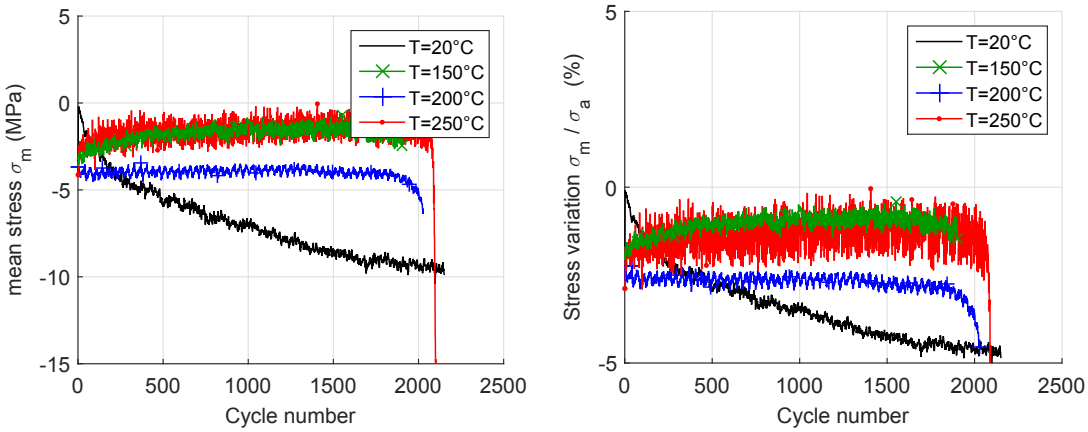

(a) Mean stress σ_m (b) Mean stress variation σ_m/σ_a

FIGURE 3.13 – Evolution of mean stress for different temperatures ($\Delta\varepsilon/2 = \pm 0.3\%$, $R_\varepsilon = -1$)

3.2.2 Ageing

For elevated temperatures (150 °C and higher), the material exhibits softening: the constant imposed strain amplitude leads to a decreasing stress amplitude as seen in Figure 3.14. To differentiate cyclic strain-softening from ageing softening, two specimens undergo the same thermal loading, and a different mechanical loading. Table 3.3 gives the different thermal and mechanical histories for the two specimens: specimen 61 is mechanically loaded after 270 min of ageing at $T = 250\,°C$, while specimen 62 is mechanically loaded right after temperature stabilization. Despite their different mechanical loading history, both cyclic behaviours are identical with respect to ageing time. This proves the mechanical behaviour can be uniquely described by the thermal history the specimen underwent. The mechanical history does not substantially modify the cyclic behaviour, thus eliminating the hypothesis of a mechanical isotropic softening caused by the cumulative plastic strain.

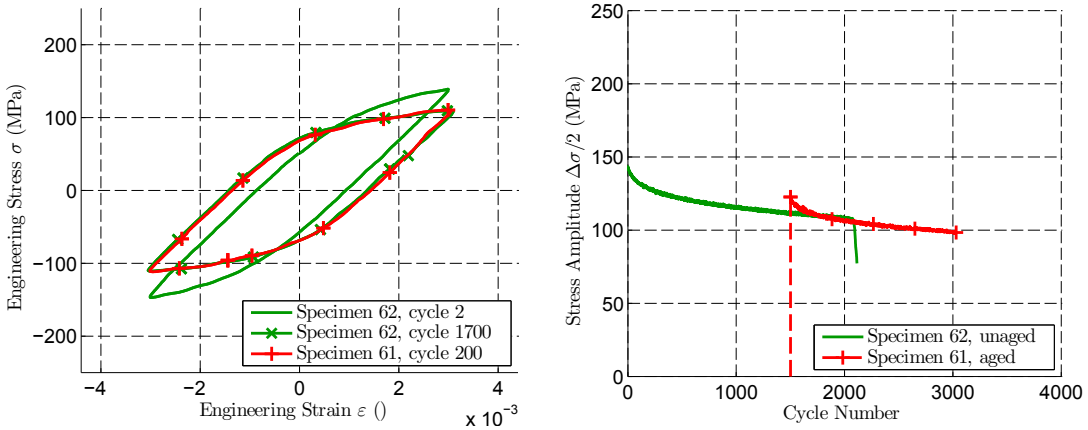

(a) Cyclic behaviour comparison

(b) Evolution of stress amplitude for $T = 250\,°C$ with and without pre-ageing. A thousand cycles is equivalent to 3.3 hours

FIGURE 3.14 – Ageing mechanism identification.

Table 3.3 – Ageing behaviour testing

	Specimen 62 load	Specimen 61 load
t=-30 min	stabilisation heating	stabilisation heating
t=0 min	mechanical and thermal	thermal
t=270 min (≡ 1500 cycles)	mechanical and thermal	mechanical and thermal

In order to confirm the microstructural origin of the thermal ageing, Transmission Electron Microscopy is used on two material samples:

— Initial condition: the sample underwent a T5 thermal treatment.

— Aged condition: a sample in initial condition is thermally aged at 250 °C for 72 hours.

The TEM observations are displayed in Figure 3.15. The diffraction pattern could not be obtained, but the morphological observations of the precipitates confirms they are Al_2Cu precipitates (see Martinez et al. [2013]). The precipitate diameter size is measured by manual image analysis. Indeed, the plate-like precipitates as seen on the different figures correspond to a 2D projection, and the diameter can be inferred (see

Figure 3.15b). After ageing, the precipitate diameter strongly increases. The main diameter grows from 74 to 249 nm (see Figure 3.16). The results are similar to those observed in Barlas [2003] for a similar material (AS7U3G T5), even though the precipitates appear larger in our study. This bias could be the result of the modifications in the heat treatment or in the material composition, or the influence of the long natural ageing in our study (2 years). The results observed in Martinez et al. [2013] and the repeatability of fatigue tests performed at the beginning and the end of this study (tests conducted at the beginning of the study and after 2 years of natural ageing displayed identical cyclic behaviour), tend to prove that natural ageing has little influence on the precipitate size evolution.

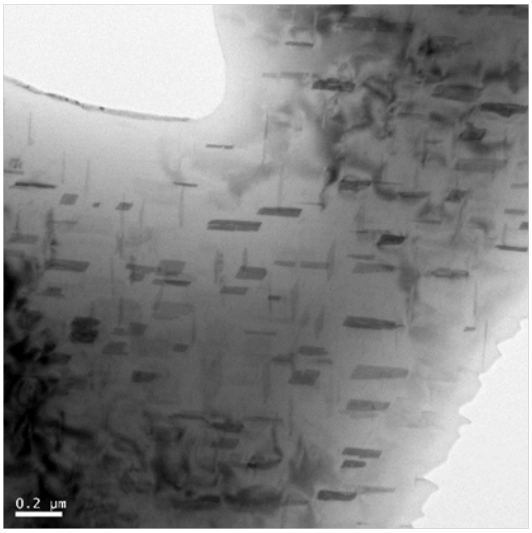

(a) Light field TEM: initial condition

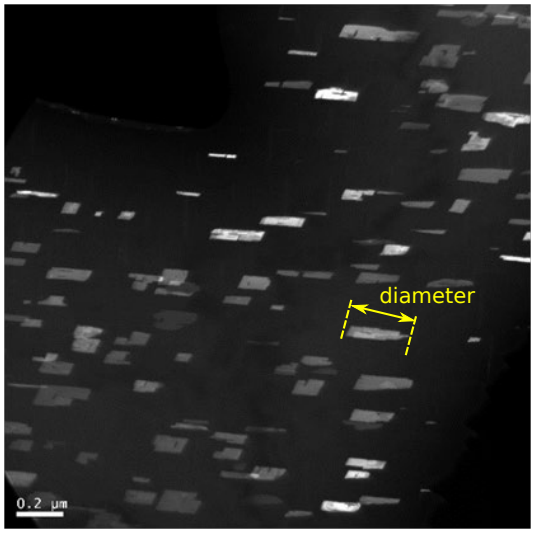

(b) Dark field TEM: initial condition

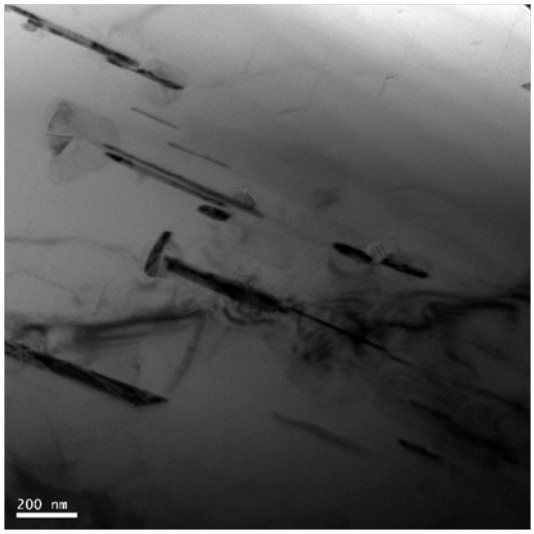

(c) Light field TEM: aged condition (72h)

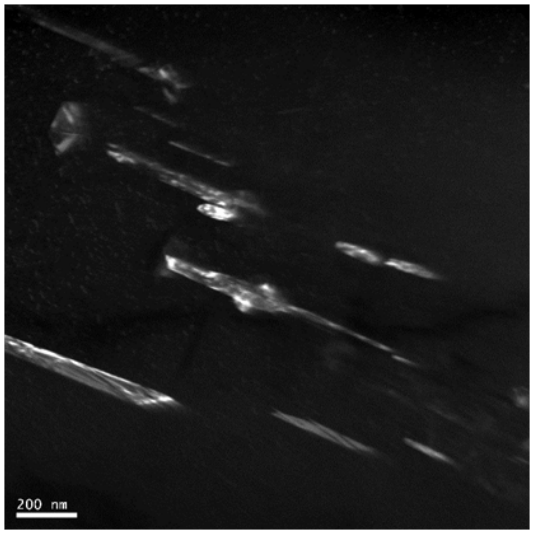

(d) Dark field TEM: aged condition (72h)

FIGURE 3.15 – Al_2Cu precipitates evolution with thermal ageing by TEM microscopy.

3.2.3 Simulation of the cyclic behaviour of the material

Simulation model

Cyclic behaviour is simulated using the Armstrong-Fredericks non-linear kinematic hardening model Armstrong and Fredericks [1966] with no isotropic hardening. The

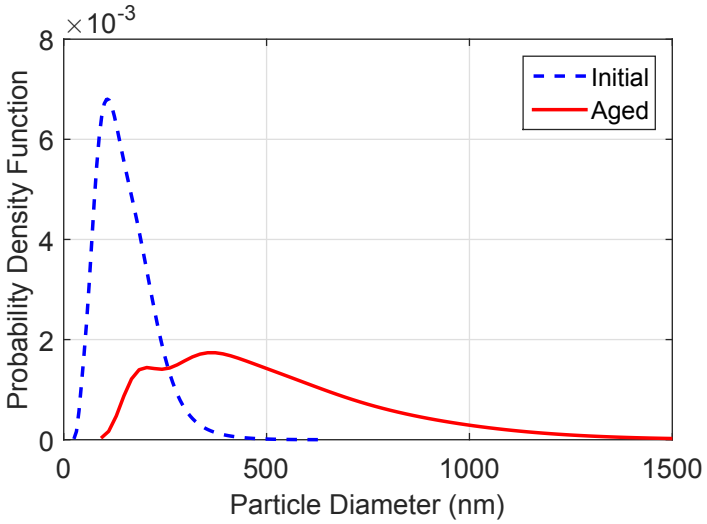

FIGURE 3.16 – TEM particle Analysis: evolution of Al_2Cu precipitates.

kinematic hardening rule is:

$$d\underline{\underline{X}} = C_k \mathrm{d}\underline{\underline{\varepsilon}}_p - \gamma_k \underline{\underline{X}} \mathrm{d}p \tag{3.11}$$

where C_k and γ_k are two material parameters, and dp the derivative of the cumulative plastic strain p:

$$p = \int_0^t \sqrt{\frac{2}{3}\dot{\underline{\underline{\varepsilon}}}_p(\tau) : \dot{\underline{\underline{\varepsilon}}}_p(\tau)} \mathrm{d}\tau \tag{3.12}$$

In order to simulate the cyclic behaviour, the identification of 4 parameters is necessary:

— Young modulus E: although the Young modulus can be identified on monotonic curve (or during the first cycle), it is here considered as an adjustable parameter. This method allows for a better fit, given the slight asymmetry of the cyclic curve between loading and unloading.

— Elastic limit σ_y: once again, this parameter can be defined and evaluated on monotonic curve (for example the 0.2% or the 0.02% yield strength). However, the actual numerical value of σ_y is difficult to define and measure (the choice of a specific yield strength being rather arbitrary), therefore, the elastic limit is considered as an optimisation parameter.

— The kinematic parameters C_k and γ_k

Optimisation process

Given a set of parameters $\boldsymbol{\theta} = (E, \sigma_y, C_k, \gamma_k)$, the error e_k between experimental and simulation results for a test k is defined as:

$$e_k(\boldsymbol{\theta}) = \sqrt{\frac{1}{N_{pts}} \sum_{i=1}^{N_{pts}} (\sigma_{sim}^{(i)}(\boldsymbol{\theta}) - \sigma_{exp}^{(i)})^2} \tag{3.13}$$

where N_{pts} is the number of data points used to compare experimental and simulated results, σ_{exp} the experimental stress data points, and σ_{sim} the simulated data points. The simulated data points were obtained as follows:

— the measured strain is used as simulation input

— the first 15 cycles are simulated

— the error is calculated between the 10th and the 15th cycle

For a given set of n tests (here all the tests for a given temperature), the global error e_n is defined as:

$$e_n(\boldsymbol{\theta}) = \sum_{k=1}^{n} w_k e_k(\boldsymbol{\theta}), \quad \sum_{k=1}^{n} w_k = 1 \tag{3.14}$$

The optimisation process aims at finding the optimal parameter $\boldsymbol{\theta}_{opt}$ which minimizes the global error:

$$\boldsymbol{\theta}_{opt} = \arg\min_{\boldsymbol{\theta}} e_n(\boldsymbol{\theta}) \tag{3.15}$$

This is achieved by using two different algorithms (referred to as hybrid genetic algorithm):

1. Genetic algorithm (example in Figure 3.17a): this global algorithm is very efficient at finding global minimums, but very demanding in computing resource. It is used to find a point in the basin of attraction containing the global minimum.
2. Simplex search method (Nelder and Mead [1965], example in Figure 3.17b): the final value of the genetic algorithm is used as a starting point for this derivative free method, which can handle discontinuities.

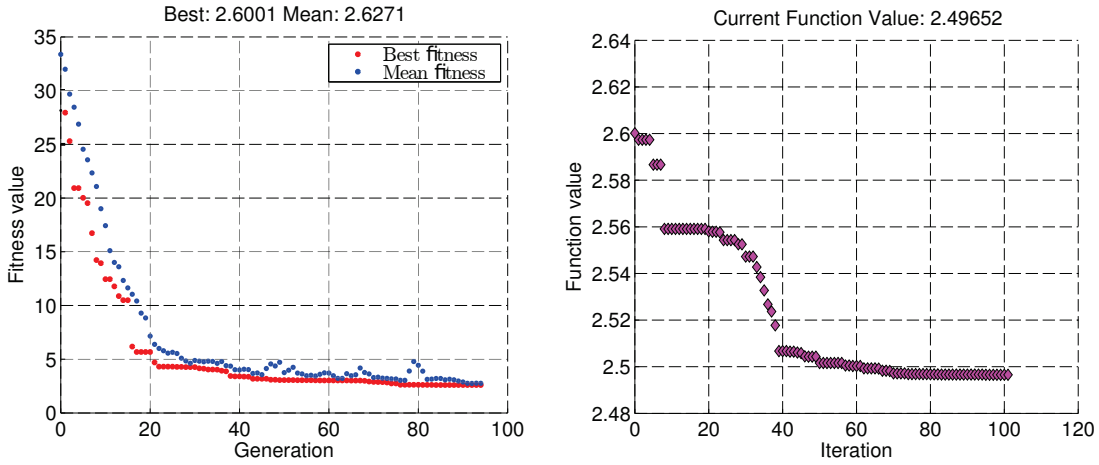

(a) Evolution of the best and mean fitness value (here chosen as the global error e_n) for 20 individuals generations.

(b) Simplex search method: the final parameter of the genetic algorithm is used as a starting point for this method.

FIGURE 3.17 – Parameter optimisation of $\boldsymbol{\theta}$ for three test conditions at 150 °C ($\Delta\varepsilon/2 = \pm$ 0.25; 0.3; 0.4%, $R_\varepsilon = -1$)

Simulation results

Results are shown in Figures 3.18, 3.19, 3.20 and 3.21. For each temperature, 3 different imposed strains are shown ($\Delta\varepsilon/2 = \pm$ 0.25; 0.3; 0.4%). The optimal value of the Young modulus used for simulation is higher than the experimental measured value (see Figure 3.4), but shows the similar trend and decreases monotonously with

temperature. The same decreasing trend is found for the elastic limit. The complete results (all the parameters) the optimization procedure and the numerical parameters are not disclosed for confidentiality reasons.

The ageing phenomenon was not simulated. Previous work (such as Barlas [2003] and Martinez et al. [2013]) have successfully implemented ageing simulation where the elastic limit depends on thermal history. However, for industrial purposes, these models are too cumbersome for a systematic use. **Therefore, the simulations presented here focus on the virgin material (after 10 cycles) and the influence of ageing on the fatigue criterion will be later discussed (see Section 3.3.2)**. These restrictions allow for the simple kinematic hardening to provide accurate simulation results of the first cycles.

Table 3.4 – Simulation (E_{sim}) and experimental (E_{exp}) value of Young modulus

temperature (°C)	E_{sim}	E_{exp}
20	72.2	77.4
150	69.4	73.0
200	68.2	70.9
250	65.7	67.6

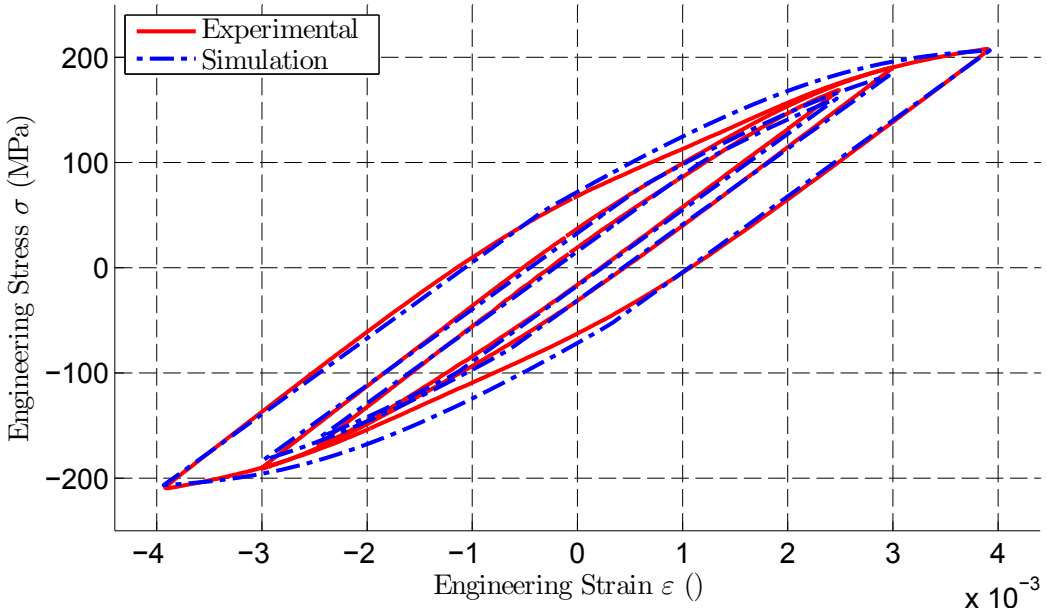

FIGURE 3.18 – Numerical simulation of 3 strain controlled tests ($\Delta\varepsilon/2 = \pm$ 0.25; 0.3; 0.4%) at 20 °C, 10th cycle

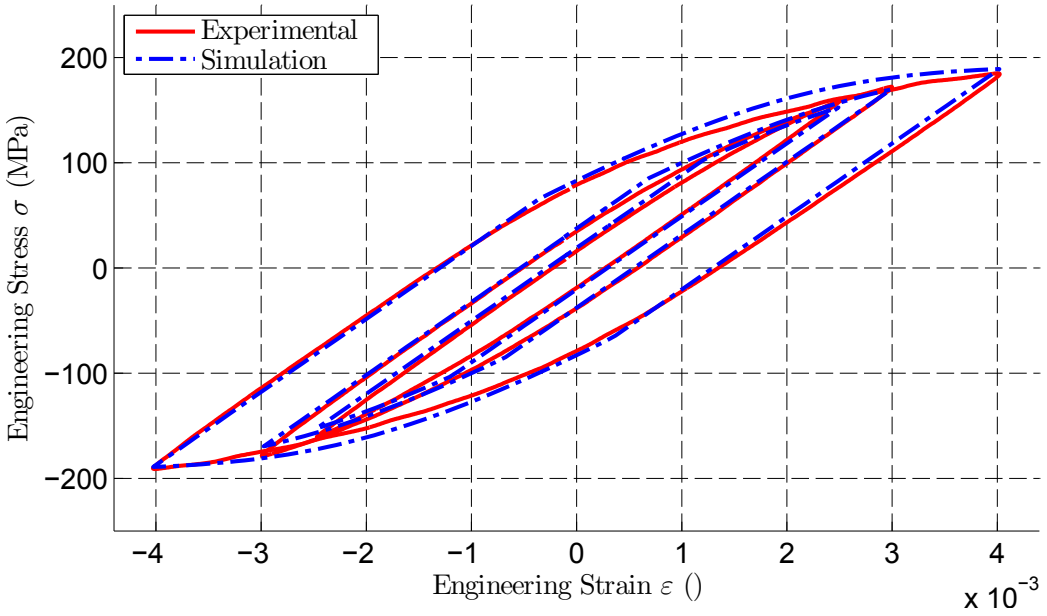

FIGURE 3.19 – Numerical simulation of 3 strain controlled tests ($\Delta\varepsilon/2 = \pm$ 0.25; 0.3; 0.4%) at 150 °C, 10th cycle

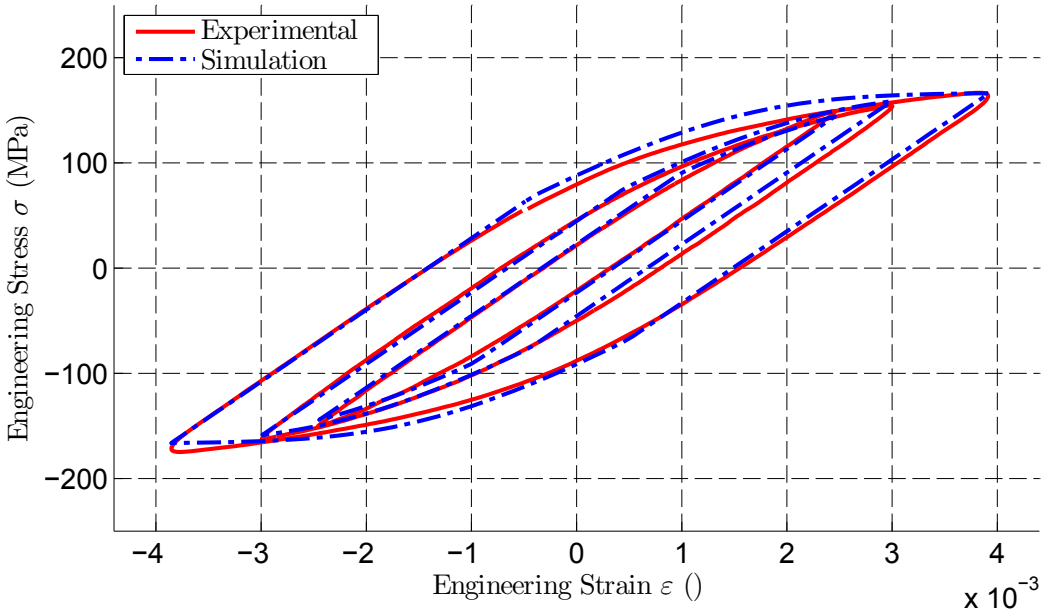

FIGURE 3.20 – Numerical simulation of 3 strain controlled tests ($\Delta\varepsilon/2 = \pm$ 0.25; 0.3; 0.4%) at 200 °C, 10th cycle

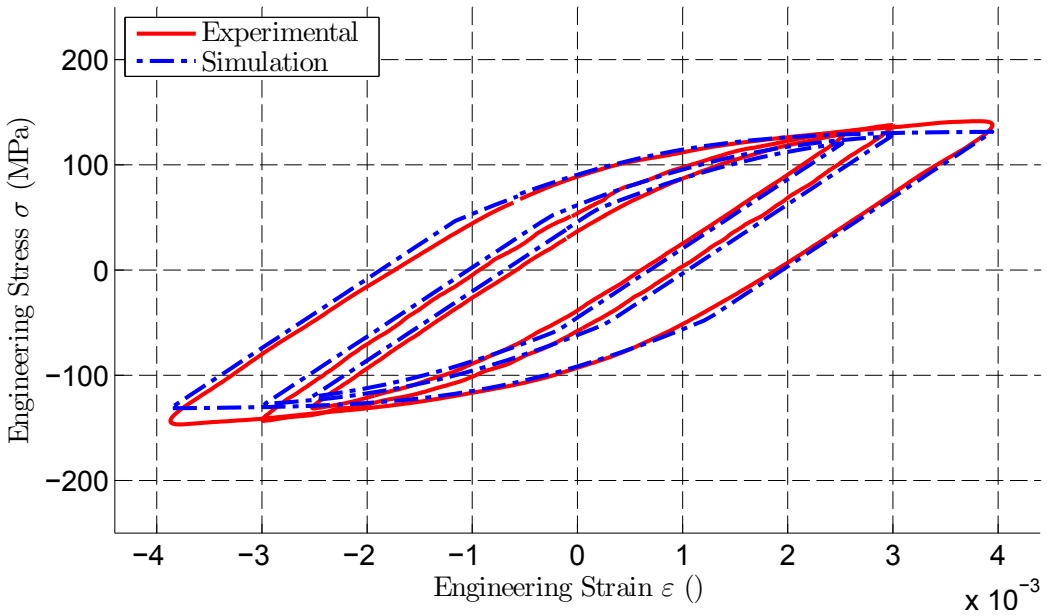

FIGURE 3.21 – Numerical simulation of 3 strain controlled tests ($\Delta\varepsilon/2 = \pm$ 0.25; 0.3; 0.4%) at 250 °C, 10th cycle

3.3 Fatigue tests results

3.3.1 Coffin Manson

Firstly, fatigue tests results are analysed using Coffin-Manson law where:

$$\frac{\Delta\varepsilon_p}{2} = \varepsilon'(2N_f)^c \tag{3.16}$$

— N_f: number of cycles to failure, defined as a 10% stress drop from the trend line.
— $\Delta\varepsilon_p/2$: plastic strain amplitude. It is taken at a fraction of the specimen lifetime (for example 0.5 is equivalent to the midlife cycle), and averaged over 10 cycles.

Only the plastic strain is considered for the Coffin-Manson law. Given the high levels of plasticity, the elastic part is neglected to simplify the analysis when studying the impact of ageing. In order to identify the parameters, a linear regression is used. The plastic strain amplitude $\Delta\varepsilon_p/2$ is considered as the explanatory variable, and the number of cycles to failure N_f the dependant variable. This assumption is important, as we consider the plastic amplitude strain $\Delta\varepsilon_p/2$ to be known, and the number of cycles to failure N_f to be the result of this loading, and not the other way around. Equation 3.16 is therefore rewritten:

$$2N_f = \left(\frac{2\Delta\varepsilon_p}{\varepsilon'}\right)^{1/c} \tag{3.17}$$

Which can be transformed using the natural logarithm:

$$\ln(2N_f) = \frac{1}{c}\ln(\Delta\varepsilon_p) - \frac{1}{c}\ln(2\varepsilon') \tag{3.18}$$

This matches the linear regression form:

$$Y = aX + b \tag{3.19}$$

where:
— $X = \ln(\Delta\varepsilon_p)$
— $Y = 2N_f$
— $a = \frac{1}{c}$
— $b = -\frac{1}{c}\ln(2\varepsilon')$

Using the least-square regression method implies the dependant variable Y has a normal distribution, hence the number of cycles to failure N_f has a lognormal distribution for a given plastic strain amplitude.

Table 3.5 and Figure 3.22 display the results of this method. From 20 to 200 °C, the fatigue ductility exponent c is close to the universal slope of -0.6 (see Manson [1965]). For a test temperature of 250 °C, the slope is much lower ($c = -0.40$).

Table 3.5 – Coffin Manson law parameters for different temperatures.

T (°C)	25	150	200	250
ε'	0.096	0.069	0.118	0.019
c	-0.70	-0.64	-0.67	-0.40

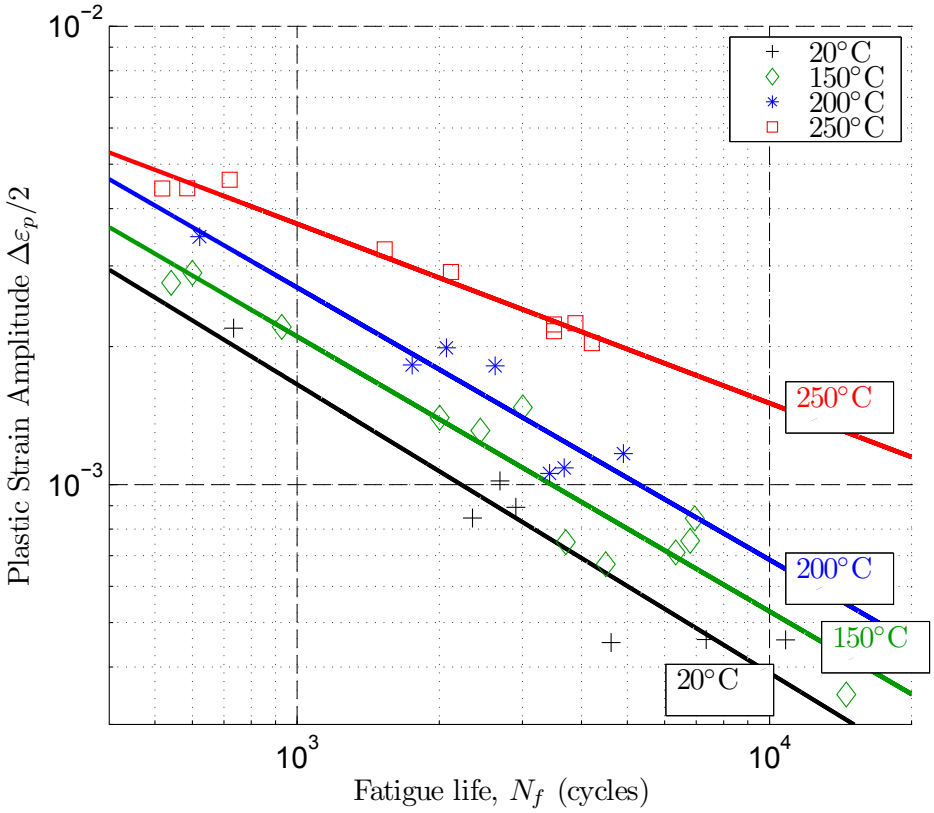

FIGURE 3.22 – Stress amplitude per cycle as a function of cycle number

This phenomenon is due to the material ageing which leads, given the test conditions, to a continuous evolution of cyclic behaviour. Figure 3.23a shows the importance of cycle choice to estimate the fatigue ductility exponent c, which increases at high temperatures, and decreases at ambient temperature. As the exponent c and the coefficient ε' are highly correlated, Figure 3.23b illustrates the opposite trend for the fatigue ductility coefficient.

In conclusion, no choice of cycle to evaluate the plastic amplitude strain $\Delta\varepsilon_p$ provides a robust estimation of the Coffin Manson parameters. Indeed, these parameters appear highly variable with test temperature. This aspect is particularly relevant for the shorter fatigue life. While the cyclic behaviour stabilizes after a few hours (see Section 3.2.2), the shorter tests only last a few hours, meaning there is no stabilization of the plastic strain amplitude, and no unique Coffin Manson parameters.

3.3.2 Plastic and total dissipated energy

The use of plastic strain amplitude being problematic to establish a fatigue criterion, different energetic quantities are studied. First, their evolution with respect to time is studied in order to determine a stable equivalent energetic quantity. Indeed, a fatigue criterion is only defined for a stable mechanical state. For the higher temperatures, such a state is never reached during the tests. An equivalent energy allows defining a stable quantity which can be used with a fatigue criterion (even though the mechanical state is not rigorously stabilized).

The plastic energy dissipated ΔW_p during a cycle is defined by:

$$\Delta W_p = \int_{cycle} \underline{\underline{\sigma}} : \dot{\underline{\underline{\varepsilon}}}_p dt \tag{3.20}$$

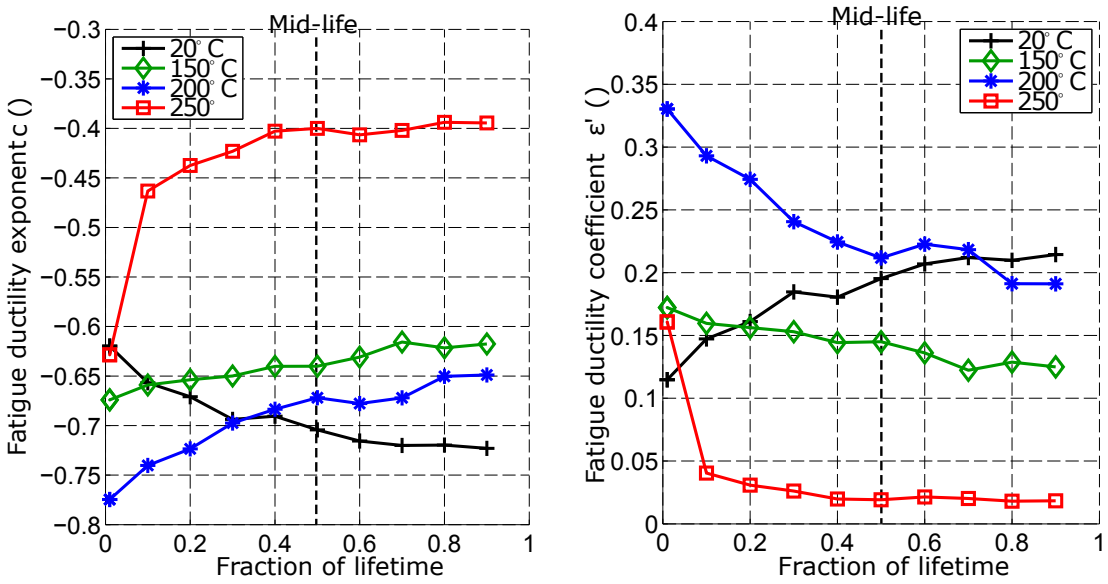

(a) Evolution of fatigue ductility exponent c

(b) Evolution of fatigue ductility coefficient ε'

FIGURE 3.23 – Evolution of Coffin Manson parameters as a function of the cycles used to calculate plastic amplitude strain.

While the elastic energy ΔW_e is defined as:

$$\Delta W_e = \frac{1}{E}(\max_{cycle}(\text{tr}\ \underline{\underline{\sigma}}))^2 \tag{3.21}$$

Due to ageing phenomenon, these quantities evolve during the fatigue test (see Figure 3.24b). To capture this variation, a total equivalent energy W_T, similar to that of Koh (Koh [2002]), is introduced:

$$\Delta W_T = (1-\alpha)\Delta W_p + \alpha \Delta W_e \tag{3.22}$$

where α is a material parameter. This parameter is often used as fatigue material parameter to optimize a fatigue life criterion (see for example Tabibian et al. [2012]). Here, it is considered to minimize the variation of the total equivalent energy during the tests. For each test k, a deviation factor [2] is $\tilde{\sigma}_k$ can be defined by:

$$\tilde{\sigma}_k(\alpha) = \left(\frac{\Delta W_T^{90\%}(\alpha) - \Delta W_T^{5\%}(\alpha)}{\Delta W_T^{90\%}(\alpha)} \right)^2 \tag{3.23}$$

where:

— $\Delta W_T^{5\%}$: total equivalent energy of cycle at 5% of specimen lifetime (strictly the average energy from 5% to 10%)

— $\Delta W_T^{90\%}$: total equivalent energy of cycle at 90% of specimen lifetime (strictly the average energy from 85% to 90%)

It must be noted this deviation factor formula can only be applied to monotonous variation of quantities (which is here the case). A deviation factor for each temperature can then be created, where each test condition (strain amplitude and temperature), the

2. While noted by a standard deviation symbol, it must be noted the deviation factor is not caused by scattering.

same weight is given and their sum normalized. This takes into account the different number of tests for each specific condition. For example, at 150 °C, there are 5 tests for $\Delta\varepsilon/2 = \pm 0.25\%$ and only one for $\Delta\varepsilon/2 = \pm 0.4\%$.

Results are shown in Figure 3.24a. For elevated temperature tests, a minimum close to 0.5 is found, whereas room temperature tests show no optimal parameter. The global deviation factor, $\tilde{\sigma}_{all}$ shows a minimum for $\alpha_{opt} = 0.45$. An example of total equivalent energy using this optimal parameter is shown for a 250 °C test in Figure 3.24b.

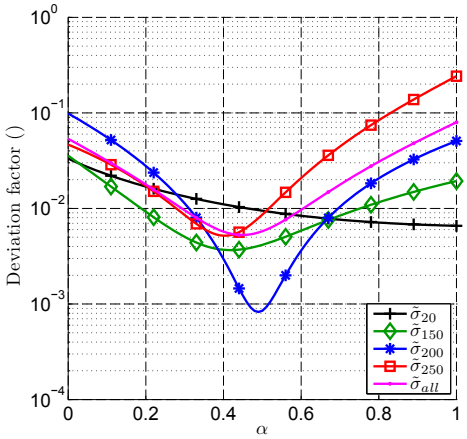

(a) Global minimization of deviation factor $\tilde{\sigma}_{all}$ using α parameter, the global minimum is $\tilde{\sigma}_{all} = 0.005$ when $\alpha_{opt} = 0.45$.

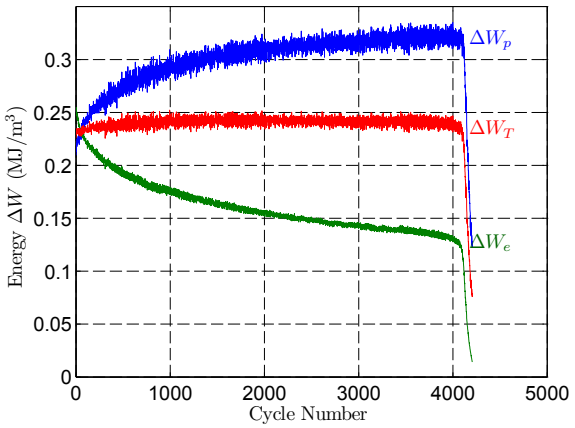

(b) Energy variation for fatigue test 29: $\Delta\varepsilon/2 = \pm 0.25\%$ and $T = 250$ °C. Plastic dissipated energy ΔW_p, elastic energy ΔW_e and total energy ΔW_T, $\alpha = \alpha_{opt} = 0.45$

FIGURE 3.24 – Study of energy variation during fatigue test.

3.3.3 Results of energy criterions

A power-law criterion is used to derive the fatigue lifetime:

$$N_f = B(\Delta W)^a \tag{3.24}$$

where B and a are 2 material parameters. Results using plastic energy ΔW_p are shown in Figure 3.26a, and total equivalent energy ΔW_T in Figure 3.26b.

For both cases, parameters B and a are evaluated using a linear regression (statistical regression methods are further investigated in Section 3.4). For each test i, the mid-life hysteresis loop [3] is used to evaluate the cyclic energy ΔW^i (plastic or elastic), and the power-law is used to compare to the corresponding number of cycles to failure N_f^i. The optimal parameters B_{opt} and a_{opt} are then evaluated using the N valid tests (37):

$$(B_{opt}, a_{opt}) = \underset{(B,a)}{\arg\min} \left(\sum_{i=1}^{N} \left(\log(B(\Delta W^i)^a) - \log N_f^i \right)^2 \right) \tag{3.25}$$

To ascertain the robustness of the criterion and the choice of the mid-life cycle, energy variation is also shown in Figures 3.26a and 3.26b. While the mid-life cycle is used to evaluate parameters B and a, energy value at 5% ($\Delta W^{5\%}$) and 90% ($\Delta W^{90\%}$)

3. Whenever a quantity is evaluated on a j^{th} cycle, the value is averaged over the cycles $[j-5; j+5]$

are displayed (see Figure 3.25). If plastic energy is used solely, corresponding to $\alpha = 1$, the deviation factor $\tilde{\sigma}_{all} = 0.9$ is high and the power-law criterion is highly dependent on the cycle chosen to evaluate the plastic energy. For the total equivalent energy, α is also used to optimise the fatigue criterion. The optimal value $\alpha = 0.375$ is close to the optimal value for minimal deviation factor $\alpha = 0.45$, and the corresponding deviation factor remains low ($\tilde{\sigma}_{all} = 0.006$).

Results using the total equivalent energy are well in the classical $[\times 2, /2]$ band. For all the temperatures and imposed strains, the test results are centred on the regression line.

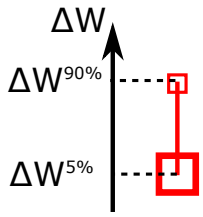

FIGURE 3.25 – Graphical illustration of energy evolution.

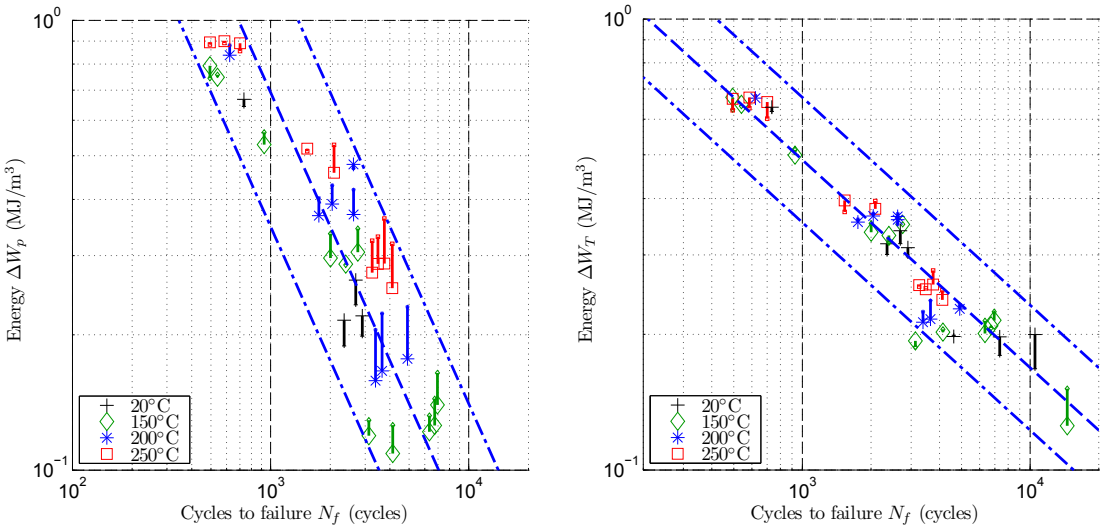

(a) Power-law criterion using plastic energy evaluated at mid-life.

(b) Power-law criterion using total energy evaluated at mid-life.

FIGURE 3.26 – Energy versus number of cycles to failure. The dispersion lines use factors $\times 2$ and $\times 0.5$

Using material simulation described in Section 3.2.3, the stress strain cycle is simulated at the 10^{th} cycle. As for the experimental results, the simulated elastic and plastic dissipated energies can then be derived. For all the tests, simulated and experimental total equivalent energy values are within 10% (see Figure 3.27a). The power law fatigue criterion can then be used using the simulated values of total equivalent energy (see Figure 3.27b) showing good agreement between the estimated and the observed fatigue life. The higher scattering observed for the longer fatigue tests will be analysed in the next section (section 3.4).

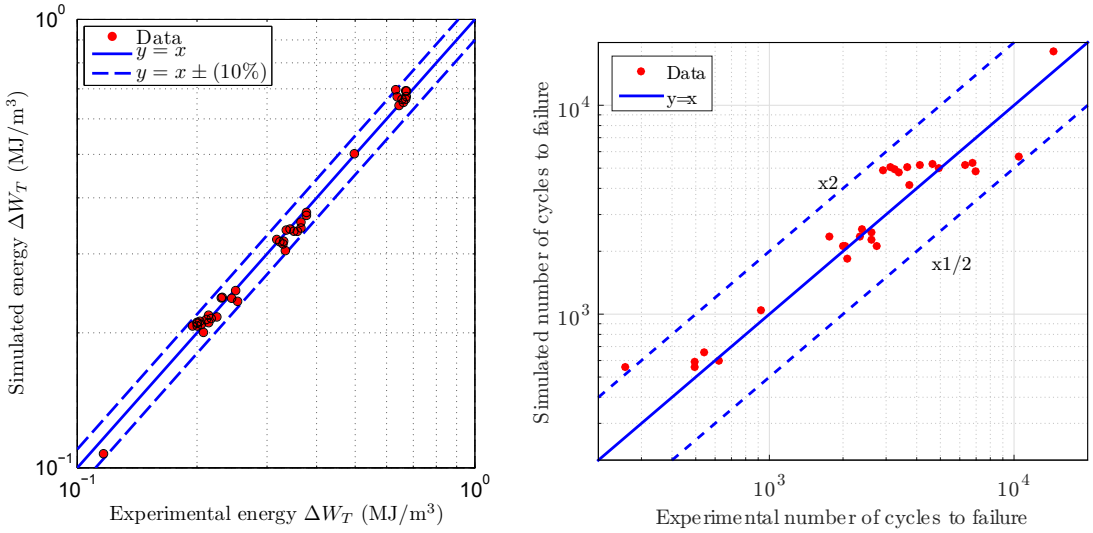

(a) Numerical simulation of total equivalent energy at the 10^{th} cycle

(b) Experimental vs simulated number of cycles to failure.

FIGURE 3.27 – Numerical simulation of the fatigue tests.

3.4 Statistical regression

As a first approach to study dispersion, an empirical model is fitted. The different sources of scatter are introduced, and the experimental data show the constant deviation factor model (which is the same as a standard linear regression) is not the best suited. Indeed, using heteroscedastic [4] model, the model provides a better fit and reduces the model uncertainties for the lower fatigue lives.

3.4.1 Statistical model description

For each test i, the quantities x_i and y_i are defined from the total equivalent energy ΔW_T^i (derived at mid lifetime) and the number of cycles to failure N_f^i:

$$x_i = \log \Delta W_T^i \tag{3.26}$$

$$y_i = \log N_f^i \tag{3.27}$$

The parameter α used to calculate the total energy was fixed: $\alpha = 0.375$, corresponding to the optimal value for linear regression. This enables comparison of the different statistical models, x_i and y_i being fixed.

The power-law criterion:

$$N_f = B(\Delta W)^a \tag{3.28}$$

can be rewritten:

$$y_i = b + ax_i, \quad b = \log(B) \tag{3.29}$$

We now consider the log-fatigue life to be a random variable Y depending on the log of the total equivalent energy x:

$$Y = b + ax + \varepsilon \tag{3.30}$$

4. As opposed to a homoscedastic model, a collection of heteroscedasctic random variables can have different variabilities (such as quantified by the variance).

ε being the error. This error is caused by multiple factors:

— *model error*: the model is based on several hypotheses. Therefore, it can only partially transcribe the physical reality of the implied phenomenons.

— *measurement errors*: these errors were described in Section 3.1.2 and remain low. Therefore, they are not further taken into account.

— *the intrinsic probabilistic nature of fatigue*: given two identical specimens tested in fatigue with identical conditions, their number of cycles to failure will seldom be rigorously identical. This intrinsic nature can arguably be attributed to the length scale used to identify two identical specimens: there is always a microstructural scale where these two specimens will be different.

Variability in the power law criterion is introduced by the random nature of the fatigue life Y. The model considers for each level of energy ΔW_T (equivalently $x = \log(\Delta W_T)$) the fatigue life follows a log-normal distribution (i.e. the log-variable $y = \log(N_f)$ follows a normal distribution).

The model can then be written:

$$Y(x) = \lambda_{N_f}(x) + \sigma_{zero}(x) \tag{3.31}$$

where $\lambda_{N_f}(x)$ is the expected fatigue life value for a given x, and $\sigma_{zero}(x)$ is a zero-mean random normal variable. The collection of random variables $Y(x)$ are homoscedastic (resp. heteroscedastic) if all random variables have the same finite variance (resp. there exist at least two sub-populations with different variances).

The model also considers the random variables $Y(x)$ to be perfectly correlated, i.e. a specimen can be "good" or "bad" with respect to the fatigue life, but this feature does not depend on the test condition. Therefore Equation 3.31 can be rewritten:

$$Y(x) = \lambda_{N_f}(x) + \sigma_f(x)U \tag{3.32}$$

where $\sigma_f(x)$ is now a deterministic function of x and U a standard normal random variable of probability density function φ:

$$\varphi(x) = \frac{1}{\sqrt{2\pi}} e^{-x^2/2} \tag{3.33}$$

The use of a random normal variable for the log-fatigue life is equivalent to choosing a log-normal distribution for the actual fatigue-life. The expected life value is then taken as a linear function (2 variables a_{N_f} and b_{N_f}):

$$\lambda_{N_f}(x|a_{N_f}, b_{N_f}) = b_{N_f} + a_{N_f} x \tag{3.34}$$

The function associated with the standard deviation σ_f is defined by 2 variables γ_{N_f} and δ_{N_f}:

$$\sigma_f(x|\gamma_{N_f}, \delta_{N_f}, a_{N_f}, b_{N_f}) = \gamma_{N_f} + \delta_{N_f} \lambda_{N_f}(x|a, b) \tag{3.35}$$

The probability density function of Y is therefore:

$$f_Y(y, x|a_{N_f}, b_{N_f}, \gamma_{N_f}, \delta_{N_f}) = \frac{1}{\sigma_f(x|\gamma_{N_f}, \delta_{N_f})} \varphi\left(\frac{y - \lambda_{N_f}(x|a_{N_f}, b_{N_f})}{\sigma_f(x|\gamma_{N_f}, \delta_{N_f})}\right) \tag{3.36}$$

3.4.2 Standard deviation model *ct*

Constant function Firstly, the standard deviation is considered constant (i.e. $\delta_{N_f} = 0$). The corresponding function is:

$$\sigma_{ct}(x) = \gamma_{N_f} \tag{3.37}$$

The numerical results are given in Table 3.6 and graphically represented in Figure 3.28. The 5 and 95% confidence intervals lie close to the usual multiplicative curves (x2 and /2).

The results are identical to that of a linear regression (in a least squares sense). Indeed, if the errors ε are considered to be normally distributed in Equation 3.30, of uniform variance (homoscedascity) and uncorrelated, both results are equivalent. The use of the maximum likelihood estimator (MLE) provides the information criteria (in our case AIC and BIC Tables) which can be compared to other statistical models.

Single variable linear function (model *lin*1) As in Pascual and Meeker [1997], the standard deviation is chosen directly proportional to the expected fatigue life:

$$\sigma_{lin1}(x|\gamma_{N_f}, a_{N_f}, b_{N_f}) = \delta_{N_f}\lambda_{N_f}(x|a_{N_f}, b_{N_f}) \tag{3.38}$$

with δ_{N_f} a strictly positive parameter, hence:

$$\lambda_{N_f} > 0 \implies \sigma_{lin1} > 0 \tag{3.39}$$

The standard deviation function is chosen proportional to the expected fatigue life value, to ensure

$$\lambda_{N_f} \to 1 \implies \sigma_{lin1} \to 0 \tag{3.40}$$

this implies, for a thought experiment, a severe enough loading will break the specimen deterministically at the first cycle.

The information criterion AIC and BIC (in Table 3.7) show the model is a better fit than the constant standard deviation one, though this is only implies a slight difference of the confidence intervals for high energy tests (see Figure 3.28, and for two particular conditions see Figure 3.29).

Two variable linear function (model *lin*2) The chosen standard deviation function is:

$$\sigma_{lin2}(x|\gamma_{N_f}, \delta_{N_f}, a_{N_f}, b_{N_f}) = \gamma_{N_f} + \delta_{N_f}\lambda_{N_f}(x|a_{N_f}, b_{N_f}) \tag{3.41}$$

This model gives the best agreement with the data (shown in Figure 3.28 and information criterions in Table 3.7). However, it cannot be extended under a certain expected fatigue life value λ for which the standard deviation becomes negative, and the positive condition translates to:

$$\sigma_{lin2} > 0 \implies \lambda_{N_f} > -\frac{\gamma_{N_f}}{\delta_{N_f}} \tag{3.42}$$

which numerically is:

$$\lambda_{N_f} > 1.231 \implies N_f = \exp(\lambda_{N_f}) > 124\text{cycles} \tag{3.43}$$

In conclusion, the standard linear regression provides a efficient way of finding the parameters of the expected fatigue life λ. However, to model the observed scatter, use

Table 3.6 – Parameters (standard deviation) of the different statistical models used.

model	b_{N_f}	a_{N_f}	δ_{N_f}	γ_{N_f}
σ_{ct}	5.66 (0.21)	-1.86 (0.17)	-	0.240 (0.055)
σ_{lin1}	5.63 (0.18)	-1.90 (0.16)	0.0293 (0.0068)	-
σ_{lin2}	5.59 (0.13)	-1.94 (0.14)	0.0762 (0.0473)	-0.367 (0.33)

Table 3.7 – Information criterions of the different models used (lower is better)

model	AIC	BIC
σ_{ct}	5.38	12.57
σ_{lin1}	1.48	8.66
σ_{lin2}	0.055	4.53

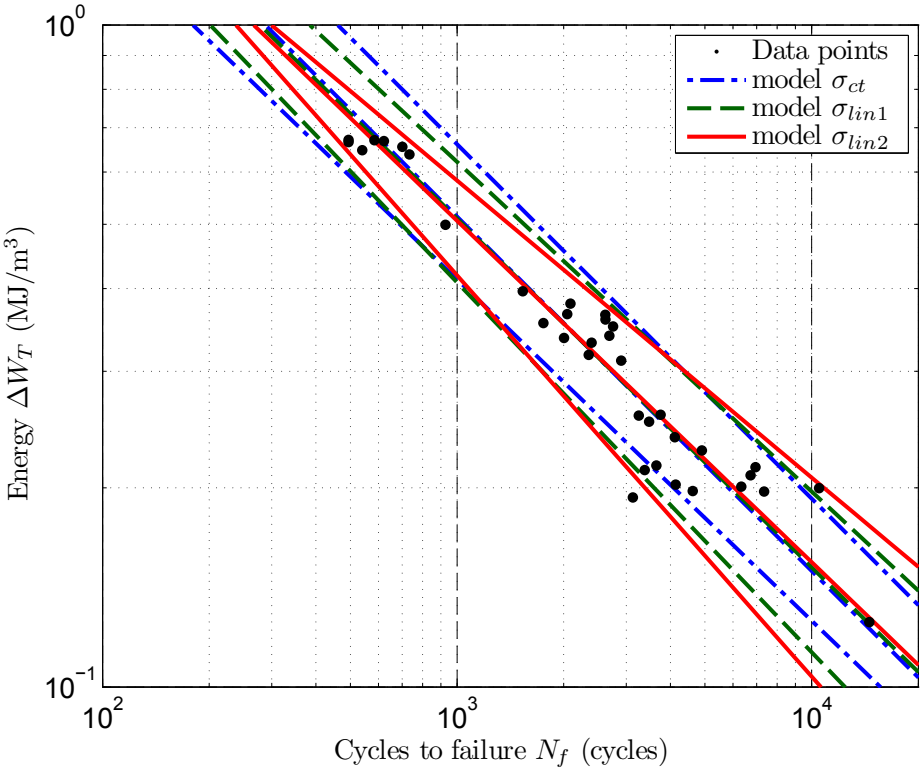

FIGURE 3.28 – Cycles to failure as a function of the total strain energy density per cycle. For each model, 5, 50 and 95% confidence interval.

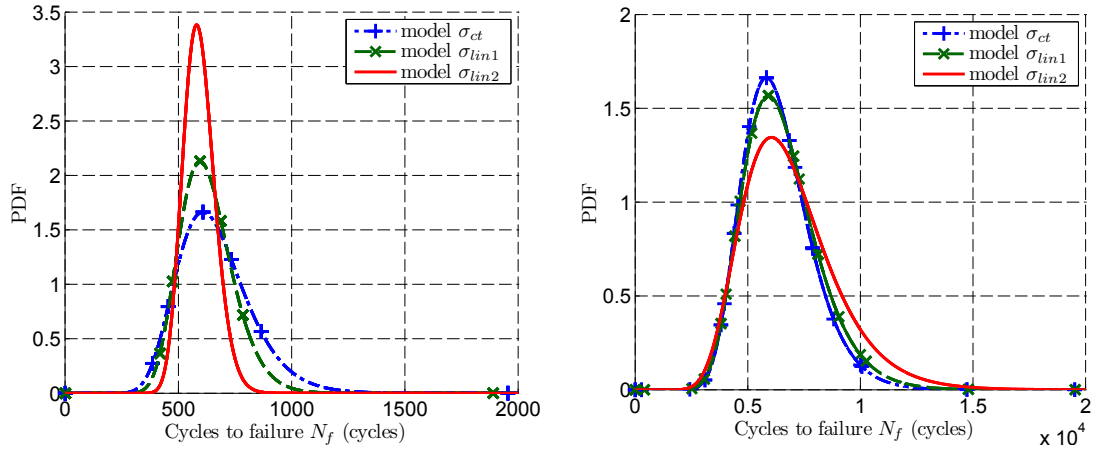

(a) High total energy $\Delta W_T = 0.67$ (b) Low total energy $\Delta W_T = 0.2$

FIGURE 3.29 – Cycles to failure PDF for the different standard deviation models and for a given total energy.

of variable variance allows for a better fit, thereby confirming the dispersion decreases for the lower fatigue lives (as has been observed in literature, see A. Karolcsuk [2013]). However, more series with exact same test conditions are needed to clearly differentiate the effect of fatigue scatter from the scatter caused by the model approximations, noticeably for the longer fatigue lives.

3.5 Conclusion and component application

In this chapter, the fatigue tests results were analysed together with the material cyclic behaviour. For the higher temperatures, the material ageing causes the material to change during the test, and no stabilization occurs. The material ageing, as opposed to cyclic softening caused by mechanical isotropic softening, is analysed by mechanical tests and by TEM observations which reveal the Al_2Cu precipitate growth.

The fatigue tests results are then analysed using the Coffin-Manson law. While adapted for unique temperatures, and stable cyclic behaviour, it is here not fitted to this aluminium alloy. Contrarily, using an equivalent strain energy density provides a unified criterion, much better suited to the LCF tests. Using only 3 parameters, this criterion captures the different fatigue behaviours (temperature and ageing), and provides a robust fatigue life estimation.

The fatigue test series provides a reliable database for the study of an applicable fatigue criterion. Despite the ageing phenomenon for the higher temperatures, causing a continuous drop of the yield strength throughout the test, the equivalent strain energy criterion provides a good predictive value of the fatigue life. Moreover, the parameters are independent of the test temperature, suggesting a possible application for thermo-mechanical fatigue.

The fatigue criterion was implemented in Abaqus © post-processing software and tested on a sub-model of a cylinder head. Even though the fatigue criterion is fitted on low-cycle isothermal fatigue tests (LCF), it is used on a thermomechanical fatigue (TMF) model. Several studies have used similar energy based criterion (see Charkaluk et al. [2002], Tabibian et al. [2012]) which provide good results for similar aluminium alloys. The equivalent energy criterion identified in the previous Section using parameters temperature independent, it can be applied to TMF simulations as a first approach.

While plastic dissipated energy per cycle ΔW_p requires no particular precaution, the elastic energy ΔW_e has to be adapted. For a cycle of length t_0, we consider time $t \in [0, t_0]$; a temperature field $T(t, \boldsymbol{x})$, where $\boldsymbol{x}$ is a point in the structure; and $E(T)$ the Young modulus depending on the temperature. For each point in the structure, the elastic energy $\Delta W_e(\boldsymbol{x})$ is defined as:

$$\Delta W_e(\boldsymbol{x}) = \max_{t \in [0,t_0]} \left(\frac{(\operatorname{tr} \underline{\underline{\sigma}}(\boldsymbol{x}))^2}{E(T(t, \boldsymbol{x}))} \right) \tag{3.44}$$

The different quantities are interpolated at nodes, in order to have access to the nodal temperatures.

A cylinder block and cylinder head global model of a diesel engine is simulated, from which a unique cylinder sub-model is then simulated. The material coefficients identified in 3.2.3 are used to simulate a thermal cycle between ambient temperature and high temperature (approximately 250 °C [5]). The maximum thermal values field can be seen in Figure 3.30. This temperature field is calculated based on the cylinder explosion, causing the higher temperatures on the cylinder head center.

The different energies (ΔW_e and ΔW_p) are then calculated (see Figure 3.31). Plastic dissipated energy is highly localized in the critical intervalve regions of the intervalve bridge and the injection port (respectively label (a) and (b) in Figure 3.31b), while elastic energy is more diffuse (see Figure 3.31a).

Total equivalent energy (see Figure 3.32a) and number of cycles to failure (see Figure 3.32b) can then be simulated. The critical regions such as the intervalve bridge are well identified, but closer investigation of correlation of the number of cycles to failure has yet to be done.

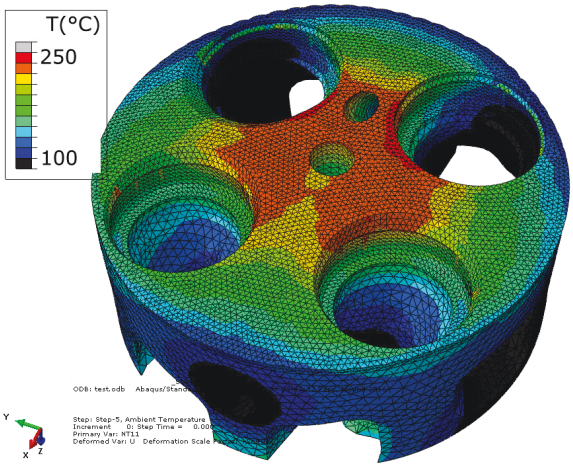

FIGURE 3.30 – Temperature field (modified values for confidentiality)

5. For confidentiality reasons, actual values have been slightly modified in text and graphics.

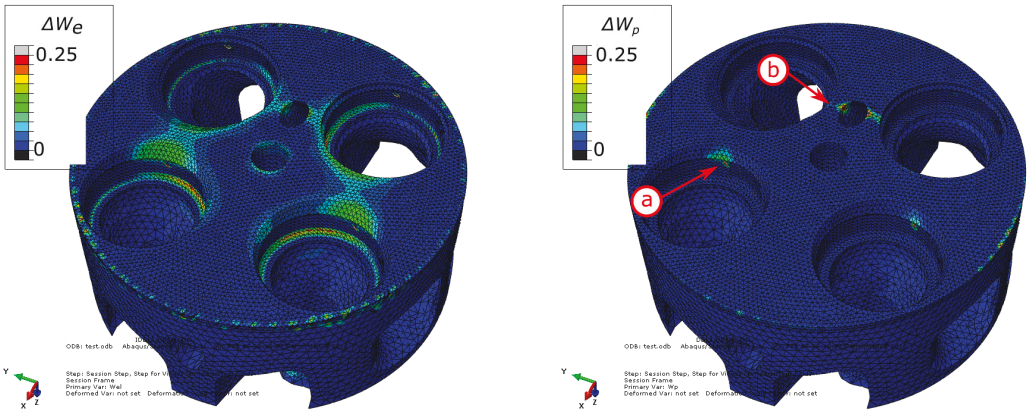

(a) Elastic energy (b) Plastic dissipated energy

FIGURE 3.31 – Simulated energy quantities (modified values for confidentiality reasons)

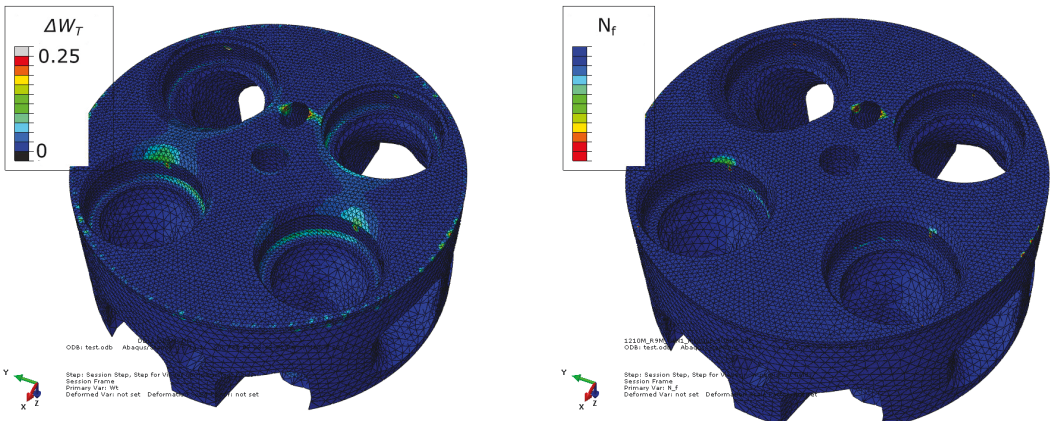

(a) Total equivalent energy (b) Simulated number of cycles to failure

FIGURE 3.32 – Simulated number of cycles to failure. The lowest values are in the low cycle fatigue regime, but are not shown for confidentiality reasons.

Chapitre 4

Fatigue damage mechanisms

Like for most of the metallic alloys, the low cycle fatigue life of cast aluminium can be divided into three parts. These are illustrated on specimen 88T5 ($\Delta\varepsilon/2 = \pm 0.25\%$, $R_\varepsilon = -1$, 20 °C, $N_f = 10823$ cycles) shown in Figure 4.1:

— crack initiation: for low-cycle fatigue, initiation occurs early (see Section 4.3.2) in the fatigue lifetime and the number of cycles to failure is mainly governed by crack propagation (Wang et al. [2001a]). As shown in Figure 4.1b, crack initiates on a shrinkage defect very close to the specimen surface. For example, in this specimen, there is a strong interaction between defects, and the initiation zone occurs in the 0-500 µm range below the specimen surface (see Figure 4.1c). In this case, for the first stages of transition from initiation to propagation, the crack appears to propagate mainly in mode II. The defect properties (size, type and position) are further discussed in Section 4.2.

— steady-crack propagation, bounded by the crack frontier in Figure 4.1a: most of the fatigue life is spent in steady-crack propagation. SEM observations reveal a rather flat and horizontal surface corresponding to a mode I crack propagation, which can also be seen in Figure 4.1c in the range 500-1250 µm. As opposed to the fast fracture stage, the steady-crack propagation shown in Figure 4.1a displays fewer intermetallics (white particles) on the fracture surface. The initiation and the steady crack propagation mechanisms and kinetics are detailed in Section 4.3.

— fast fracture propagation (> 1250 µm in Figure 4.1c), on the other side of the crack frontier: at or very close to the end, final fracture occurs rapidly and a high surface fraction is composed by intermetallics. The surface remains perpendicular to the loading direction (mode I crack), but the surface roughness increases compared to steady crack propagation. Details on the fast-fracture properties, and noticeably temperature effect, are discussed in Section 4.3.5.

To study the mechanisms of crack initiation and propagation, several observation have been used:

— SEM microscopy in BSE mode and EDS analysis;

— X-ray laboratory tomography;

— Digital camera for crack propagation monitoring.

These techniques are presented in the following Section 4.1.

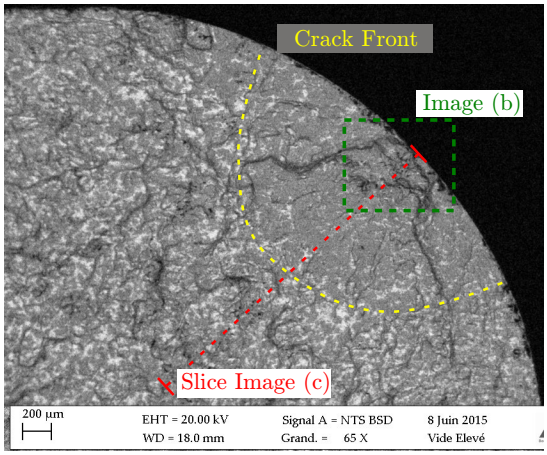

(a) SEM-BSE image of general crack observation.

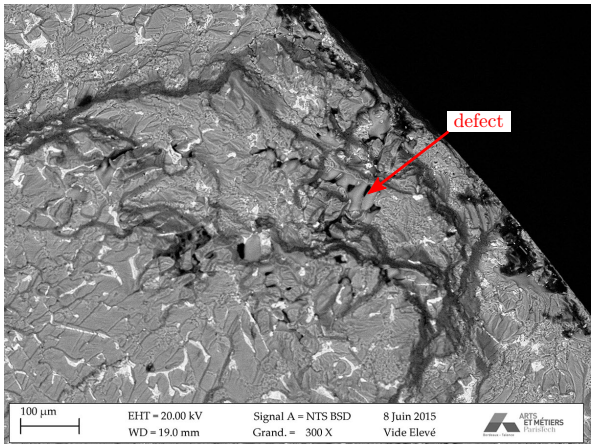

(b) Zoom: crack initiation on shrinkage defect close to specimen edge.

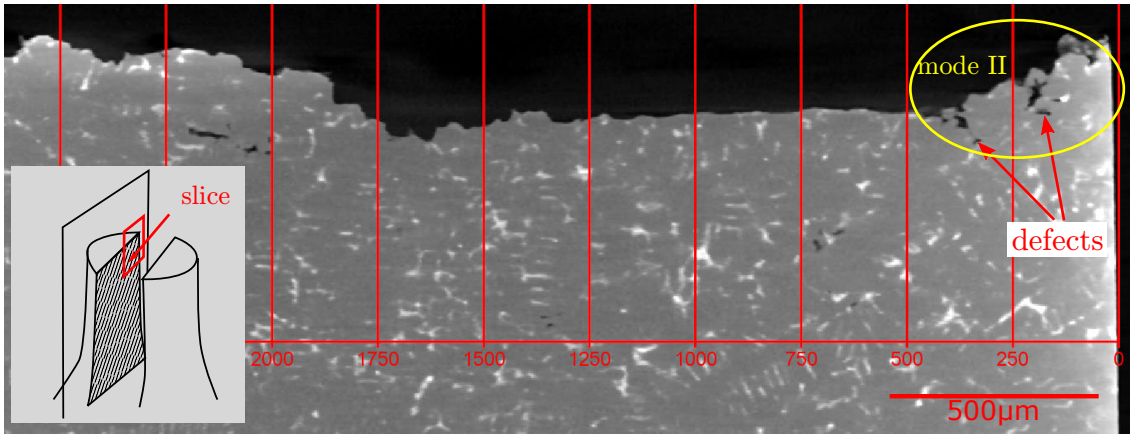

(c) Tomography: vertical slice of crack propagation (scale in (µm))

FIGURE 4.1 – SEM-BSE image of fractured surface showing the different crack regions (specimen 88T5, $\Delta\varepsilon/2 = \pm 0.25\%$, $R_\varepsilon = -1$, 20 °C, $N_f = 10823$ cycles)

4.1 Observation techniques

4.1.1 Microscopy

After fatigue testing, fractured specimens are systematically analysed using optical microscopy and scanning electron microscopy (SEM). Given the crack propagation mechanisms and the material microstructure, back-scattered secondary electron mode (BSD) reveals more discerning details than type I secondary electron mode (SE1), as shown in Figure 4.2.

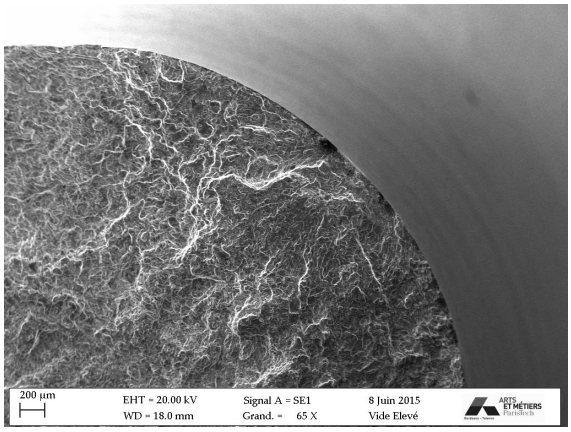

(a) SEM SE1: this mode reveals features of the fracture surface topography

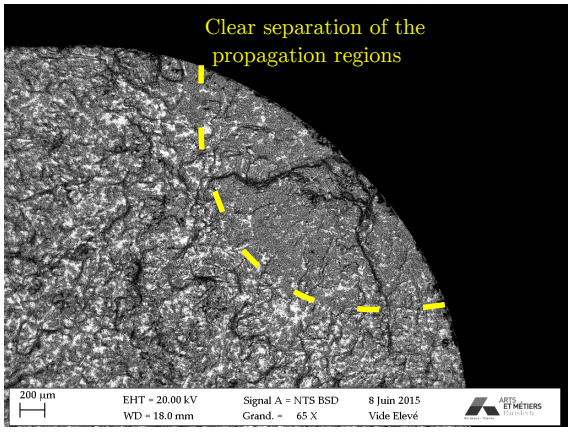

(b) SEM BSD: this mode reveals information on the fractured surface composition which, given the crack propagation mechanisms, allows for a clear identification of the different regions.

FIGURE 4.2 – Differences in scanning electron microscopy (SEM) modes a fractured surface (specimen 88T5, $\Delta\varepsilon/2 = \pm 0.25\%$, $R_\varepsilon = -1$, 20 °C, $N_f = 10823$ cycles)

Microstructure chemical composition is identified and analysed by Energy-dispersive X-ray spectroscopy (EDS) on specimen 68T5 ($\Delta\varepsilon/2 = \pm 0.3\%$, $R_\varepsilon = -1$, 20 °C, $N_f = 2552$ cycles). This method allows identifying the characteristic features appearing on the fracture surface. For example, Figure 4.3 shows the differentiation between an Al-Cu particle and a Fe-rich intermetallic.

4.1.2 Tomography

Laboratory X-ray microtomography is used to study interrupted tests and fractured specimens. Given the number of tests to analyse, fast scanning was done by limiting the exposition time to achieve under 2 hours scanning. Post-processing using Avizo© using non-local means filtering (Buades et al. [2005]) allowed to reduce noise to signal ratio and provide robust thresholding. Figure 4.4 shows an example on a 210x210 voxel slice. The microstructure boundaries details as well as the crack surface are preserved, and the noise is significantly reduced. The following parameters are used for filtering (the numerical values are presented in Table 4.1):

— Search Window: diameter in voxel of the search area. It has to be large enough to contain similar features as the base point.

— Local neighbourhood: size of the windows centred on each voxel of the search window. The weight of each voxel in the search window on the base point is

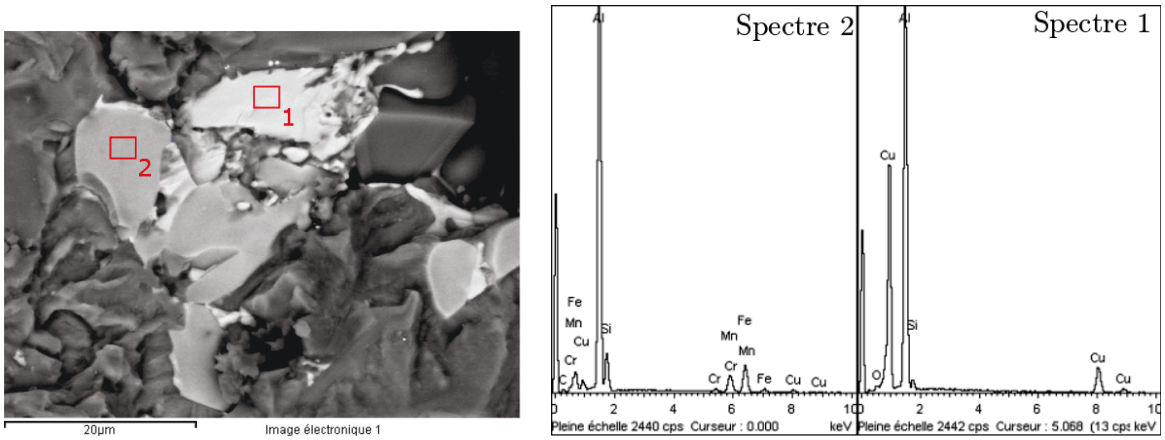

(a) SEM-BSE image (b) Corresponding EDS spectrum

FIGURE 4.3 – Energy dispersive X-ray (EDS) analysis of Al-Cu (Spectrum 2) and intermetallics (Spectrum 1) particles (specimen 68T5, $\Delta\varepsilon/2 = \pm 0.3\%$, $R_\varepsilon = -1$, 20 °C, $N_f = 2552$ cycles)

determined by comparing the local neighbourhood of the searched voxel to the local neighbourhood of the base point. This value highly affects the run-time, and the chosen value represents a compromise.

— Similarity value: this value determines the similarity value assigned to each voxel. To summarize, the higher the value, the smoother the output image will be.

These values were optimized visually to reveal the microscopic features. Since no quantitative analyses were done on these specimens, these value did not require further study (such as a sensitivity study).

Table 4.1 – 2D non local means filtering parameters

Parameter	Value
Search window	21
Local neighbourhood	5
Similarity value	0.8

All tomography illustrations are coloured using surface normals directions. Isosurface are calculated and local unit normals $\vec{n}$ are projected on the normal direction $\vec{z}$ (corresponding to the loading axe) as shown in Figure 4.5.

This method provides 2 interests:

— 2D rendering: 3d surface can give much qualitative information, but these can be difficult to convey through 2d representations.

— surface information: surface can be very rough, and height colouring (where the surface colour is a function of height) masks this information

Figure 4.6 shows an example of surface rendering using the colourization process. While not done in this study, the surface reconstruction could also have been processed using surface roughness measurement.

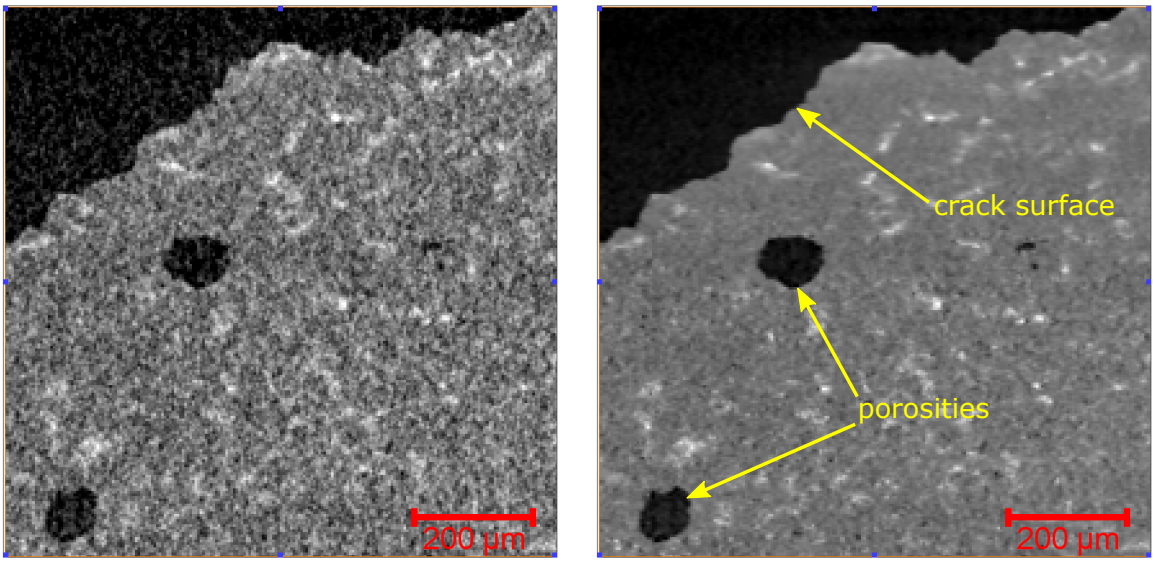

(a) Raw data. (b) 2D Non local means filtering

FIGURE 4.4 – Application of non local means filtering to tomographic data: slice example.

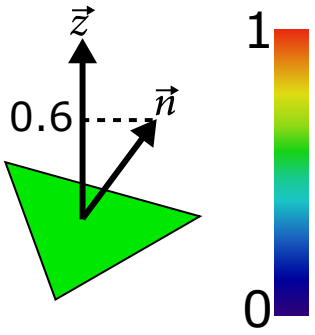

FIGURE 4.5 – Legend scale for isosurface rendering

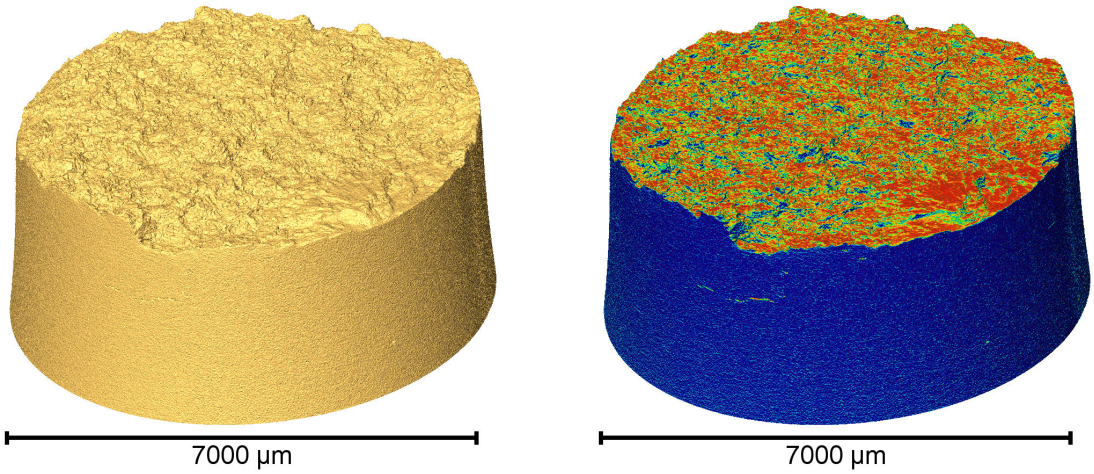

(a) Isosurface rendering (b) Isosurface with scale coloring.

FIGURE 4.6 – Cracked specimen surface rendering (specimen 88T5, $\Delta\varepsilon/2 = \pm 0.25\%$, $R_\varepsilon = -1$, 20 °C, $N_f = 10823$ cycles)

4.1.3 Crack propagation monitoring

Specimens with artificial micro defects were machined to follow crack propagation. A hemisphere of 400 µm was machined by electro discharge. Figure 4.7a shows micro defect in the middle part of a test specimen, while Figure 4.7b shows SEM image used to measure the micro defect diameter before fatigue testing. All diameters are in the interval [389 - 401 µm], corresponding to a ±3% range. Only specimen 29T5 which was used to configure the electro discharge machining machine is well below the nominal value (359 µm, i.e. -10%). For later crack propagation calculations, the measured value is used avoiding part of the bias caused by this smaller defect.

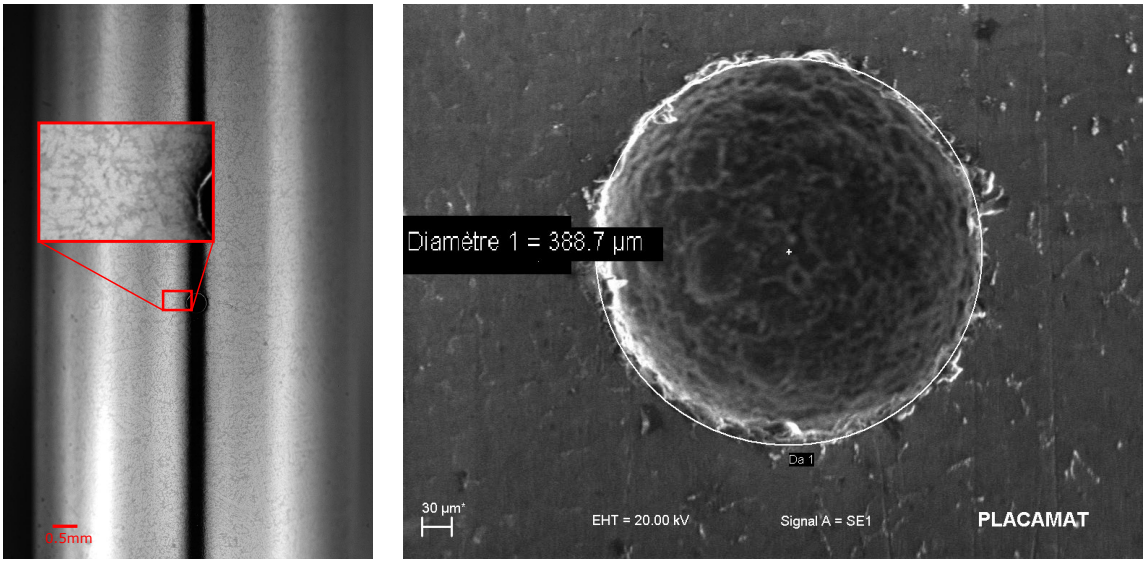

(a) Digital picture of specimen with microdefect.

(b) SEM image prior to testing measuring micro defect diameter: 389 µm

FIGURE 4.7 – Test setup of crack monitoring specimens.

Table 4.2 – Micro defect diameter measurements.

Specimen	Diameter (µm)
20T5	389
29T5	359
76T5	401
89T5	393

The evolution of crack propagation is monitored using a digital camera with macro lens and extension tubes (see 4.8):

— Digital Camera: a Canon EOS 40D with a 10.1 megapixels sensor is used. It has a 3888×2592 CMOS sensor of 22.2 mm×14.8 mm.

— Macro Lens: a Canon EF 180mm f/3.5L Macro USM is used. It has a maximum 1× magnification (i.e. the photographed object is the same size on the sensor).

— Extension tubes: 5 extension tubes are used to increase focal length ($12 + 20 \times 2 + 36 \times 2 = 124$ mm) resulting in a 1.8× magnification.

— A micrometric table: the apparatus is fixed on a micrometric table allowing to precisely aim the test specimen artificial defect, and rigid enough to avoid camera

shaking (this shaking is also minimized by using mirror lock-up: the mirror is locked in high position prior to taking the picture).

— Fiber optic lighting: specimen illumination is crucial for correct image result. This is achieved by indirect illumination: the fibre optic light actually illuminates the white furnace walls, which are reflected by the specimen surface providing uniform illumination (as opposed to direct illumination of the specimen that causes local shining on cylindrical surfaces). However, the small hole (which is meant to let the extensometer through) used by the camera to take the picture is not lit, causing the vertical black strip seen in Figure 4.7a.

— Camera tuning: After several tests, with the given lighting setup, the pictures are taken at $f/8$, 1/13s, iso 1000. This is a trade-off of four main factors: the light available, the depth-of-field, the specimen displacement and the signal to noise ratio.

— Camera trigger: The camera is event triggered by the extensometer. For a given strain amplitude, the extensomter range is set to $\pm 10\,\mathrm{V}$, and a trigger event is set up on $+9\,\mathrm{V}$. The picture is therefore taken each time the specimen is under tension, and for the maximum crack opening.

— Image treatment: given the high iso setting of the camera (iso 1000), the noise to signal ratio is high. In order to take advantage of the numerous images taken, a Gaussian Filter is applied after registering the images (to correct the slight translations that appear between pictures). The image I_k of the k^{th} cycle is the Gaussian average of the $k \pm 5$ images. Results are shown in Figure 4.9: the image treatment allows to clearly distinguish the crack tip as well as the material microstructure.

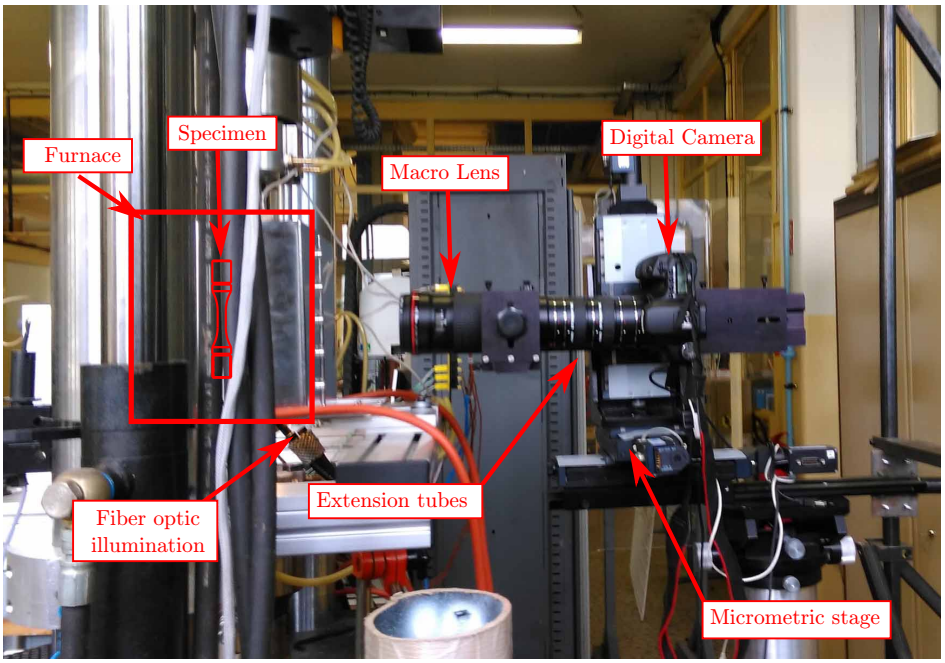

FIGURE 4.8 – Crack propagation monitoring setup.

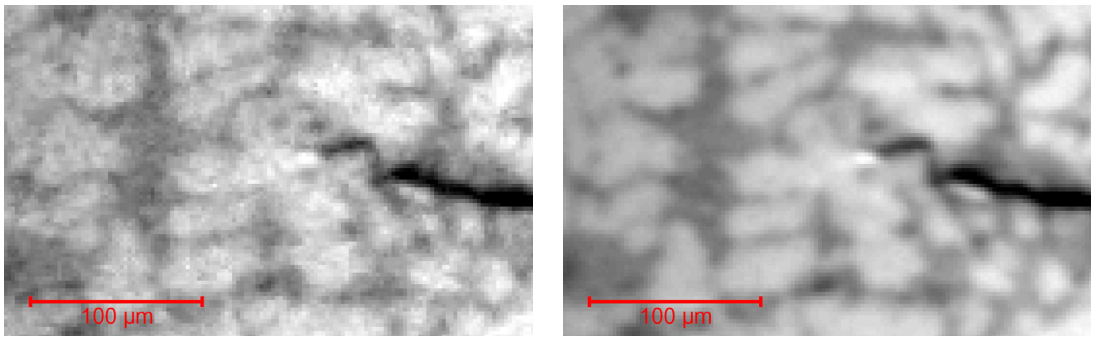

(a) Raw image without treatment. (b) Image after Gaussian filtering.

FIGURE 4.9 – Image treatment of crack propagation monitoring.

4.2 Origins of crack initiation

4.2.1 Initiation on defects

For all the observed test conditions (27), crack initiation always appears on defects. Four types of defects are identified (see 4.3 for number of concerned test):

- Gas porosity: large gas porosities (>100 µm) are found on the specimen edge. They appear as high sphericity defects on the fractured surface.
- Casting shrinkage: large shrinkages (>100 µm) are also found on specimen edges. They are characterized by lower sphericity, and boundaries harder to clearly identify.
- Defect cluster: also located on the edge of specimens, they appear larger than isolated defects (>500 µm).
- Large oxides: in three cases, large oxides are identified by optical microscopy (see Figure 4.10). No special test condition (imposed strain or temperature) reveals this type of initiation. These oxides are a consequence of the casting process: no oxide filter is used before casting, whereas these filters are present for real component casting. Therefore, they are not considered in the rest of the document and are neglected.

Table 4.3 – Main crack initiation defect (temperatures indicates for which test conditions the initiating defects were found)

Defect type	number of test	test temperatures
oxide	3	20 °C
gas porosity	3	150 °C, 200 °C
shrinkage	16	20 °C, 150 °C, 200 °C, 250 °C
cluster	3	20 °C, 150 °C
unknown	2	250 °C
total	27	

Gas porosities

Gas presence (noticeably hydrogen) during casting process causes gas porosities, which is the main crack initiation defect in 4 cases. Figure 4.11 shows such a porosity

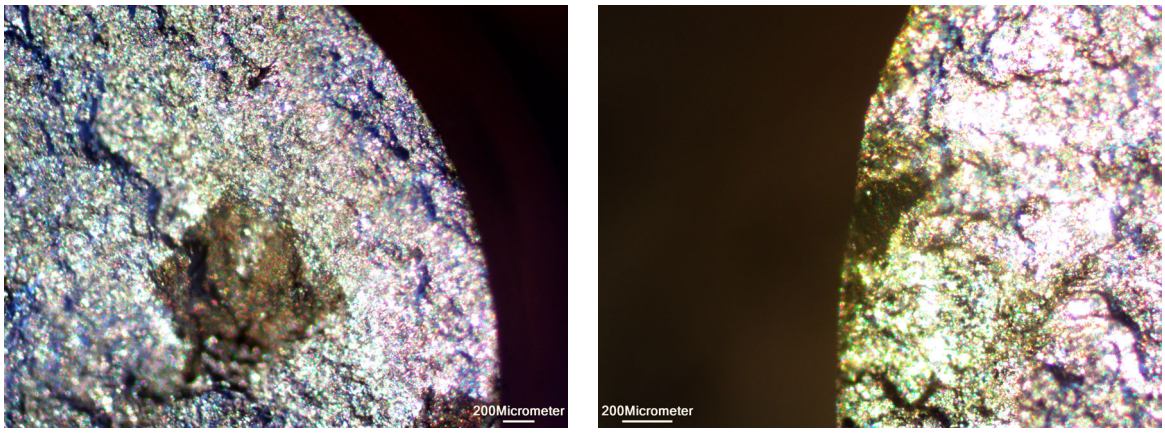

(a) Large oxide (specimen 4T5, $\Delta\varepsilon/2 = \pm 0.4\%$, $R_\varepsilon = -1$, 20 °C,$N_f = 257$ cycles)

(b) Small oxide close to specimen edge (specimen 15T5, $\Delta\varepsilon/2 = \pm 0.25\%$, $R_\varepsilon = -1$, 20 °C,$N_f = 4625$ cycles)

FIGURE 4.10 – Crack initiation: oxides

identified by micro-tomography. It is located only 180 µm from the surface, and the crack logically appears at the equator (with respect to the loading direction), where the stress concentration factor is the highest.

Figure 4.12 shows a gas porosity almost intersecting the specimen surface. A few dendrite extremities appear inside the gas porosity, cutting a smooth surface, which looks like an eutectic zone. Small shrinkage is also present close to the gas porosity, but it is unclear if they are randomly located, or linked to the gas presence.

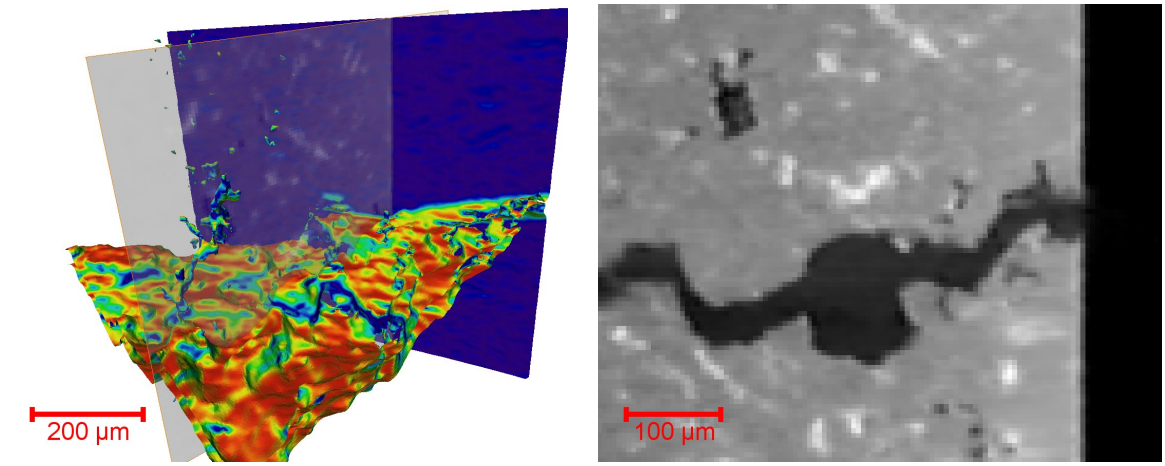

(a) 3D isosurface rendering of crack initiation

(b) Corresponding 2D slice.

FIGURE 4.11 – Gaz spherical porosity identified by micro-tomography (specimen 62T5, $\Delta\varepsilon/2 = \pm 0.3\%$, $R_\varepsilon = -1$, 250 °C)

Shrinkage defect

Shrinkage defects are detected in almost half the tests (13/27). Figure 4.13 shows such a case, for an interrupted test. The defect has a low sphericity and high acuteness, and is close to the specimen surface (120 µm). A large gas porosity is also present close to the main crack. No crack initiation is detected on the gas porosity, due to the lower acuteness and higher distance to surface (350 µm).

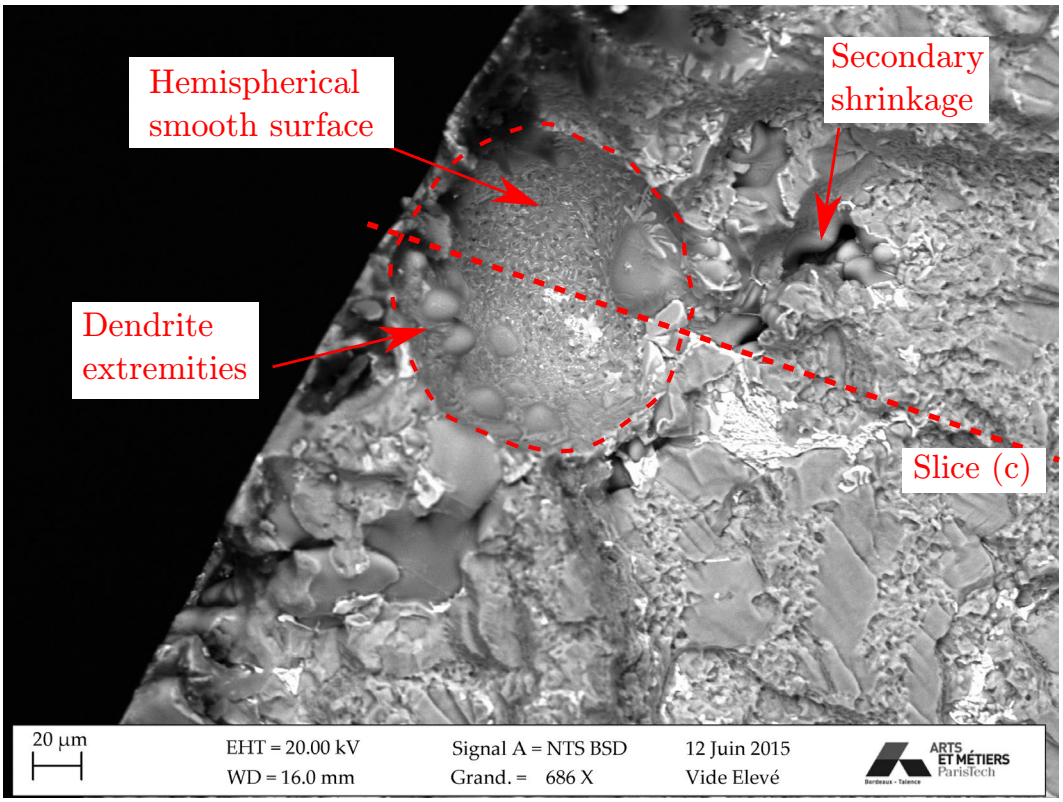

(a) SEM top view

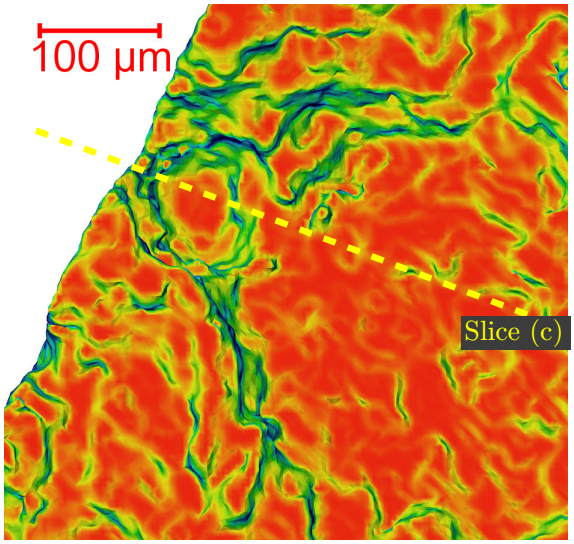

(b) Tomography 3D reconstruction: Top view

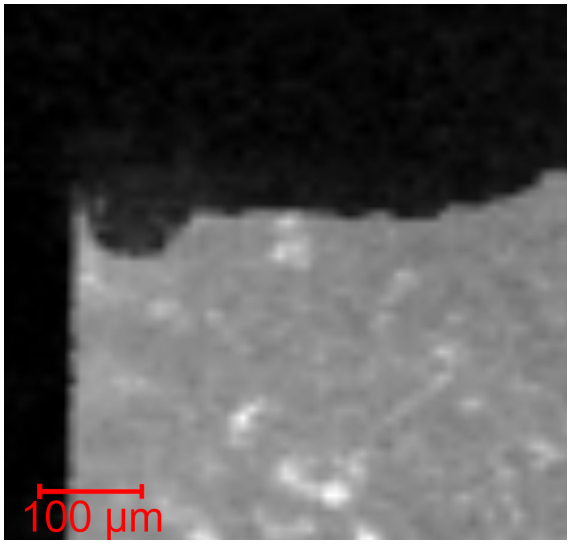

(c) Corresponding 2D slice.

FIGURE 4.12 – SEM-BSE image and tomographic analysis of gas porosity at specimen edge, (specimen 67T5, $\Delta\varepsilon/2 = \pm 0.3\%$, $R_\varepsilon = -1$, 200 °C)

Figure 4.14 shows a fractured specimen for which the main crack initiated on a shrinkage defect. The propagation scenario allows to differentiate the main defect from the secondary ones (further described in Section 4.3): the main defect (a) is surrounded by a flat surface corresponding to the first stage of the propagation, whereas (b) is located on a slant fracture surface.

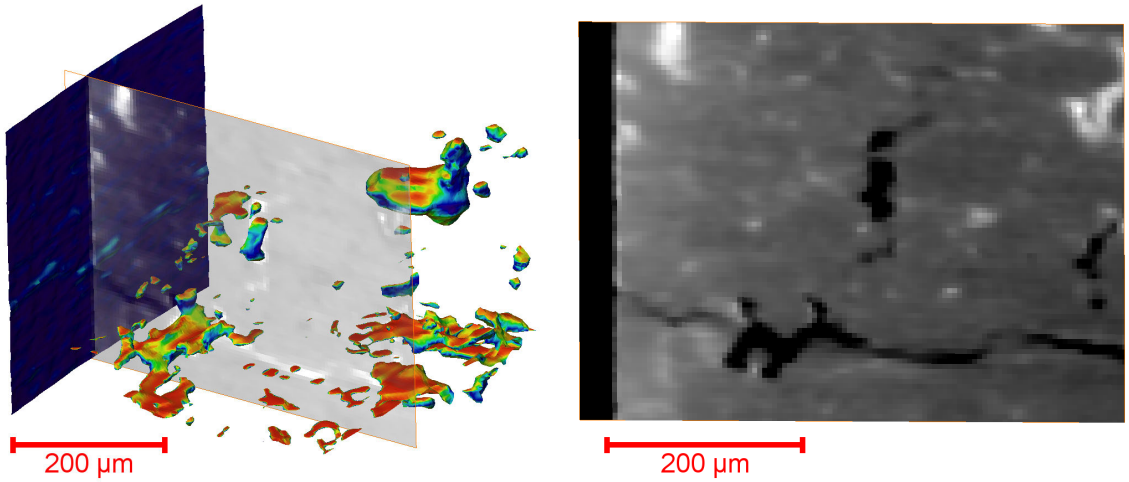

(a) 3D isosurface rendering of crack initiation. The Feret diameter of the initiating shrinkage is 120 µm, and the Feret diameter of the gas porosity is 169 µm

(b) Corresponding 2D slice.

FIGURE 4.13 – Shrinkage defect identified by micro-tomography (specimen 130T5, $\Delta\varepsilon/2 = \pm 0.3\%$, $R_\varepsilon = -1$, 150 °C)

Cluster of defects

For three tests (see table 4.6), crack initiation appears on large cluster defects (around 500 µm). Figure 4.15 shows multiple shrinkage defects from which the main crack initiated. Each defect cannot be clearly identified, but the clustering of defects is obvious.

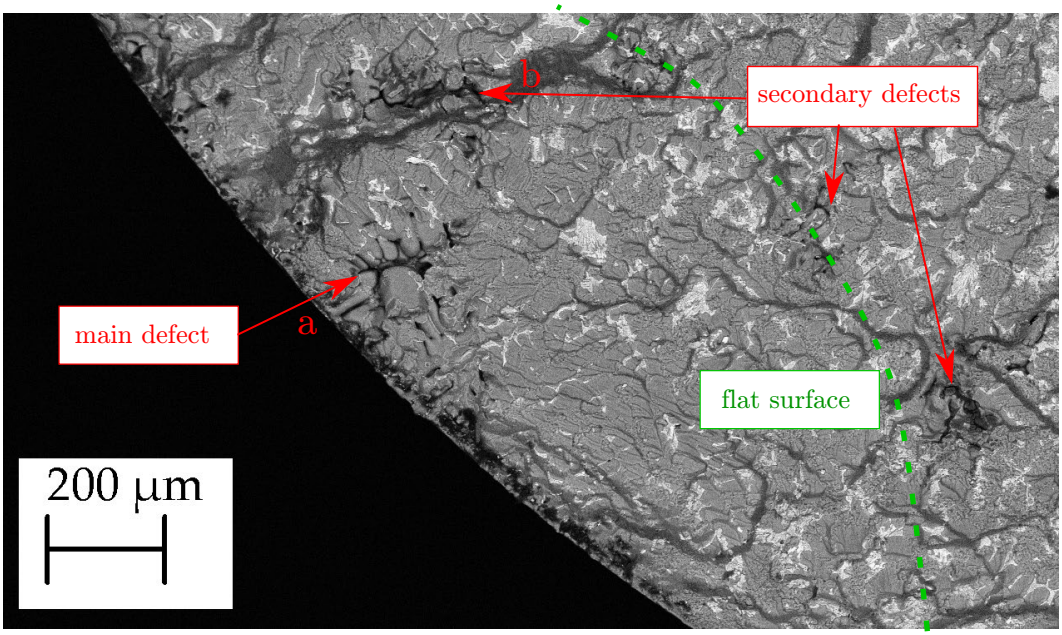

FIGURE 4.14 – SEM-BSE image of shrinkage at specimen edge, (specimen 56T5, $\Delta\varepsilon/2 = \pm 0.25\%$, $R_\varepsilon = -1$, 150 °C, $N_f = 4137$ cycles).

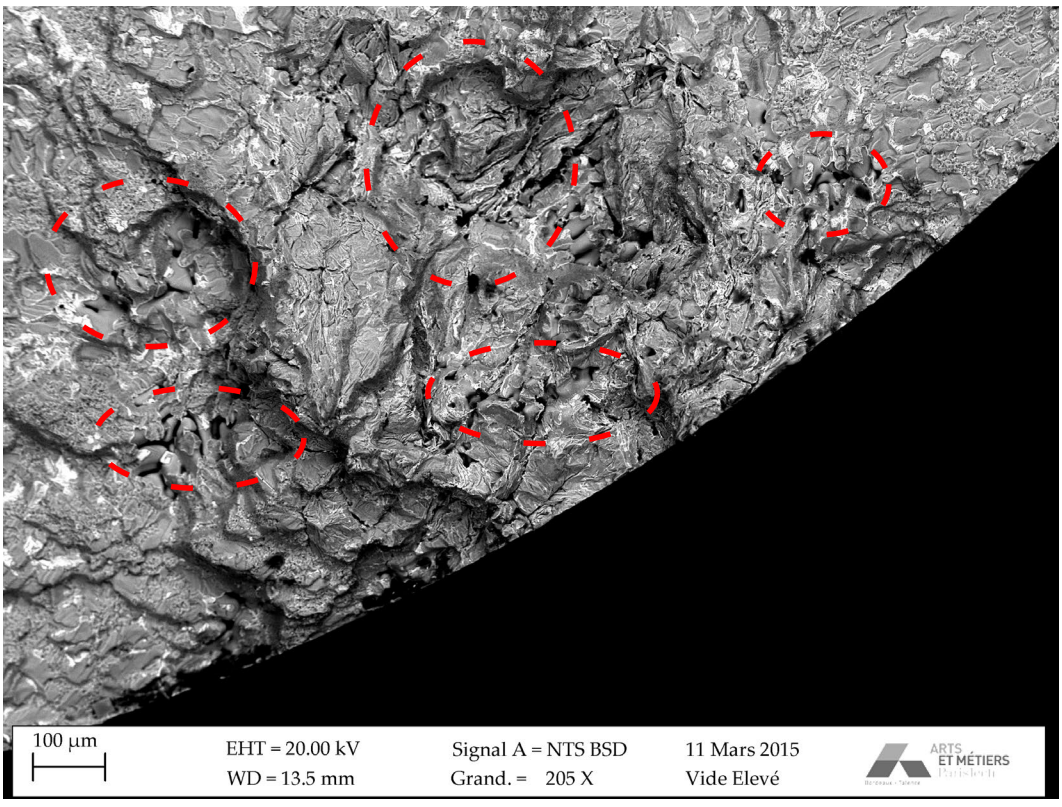

FIGURE 4.15 – SEM-BSE image of defect cluster (specimen 22T5, $\Delta\varepsilon/2 = \pm 0.3\%$, $R_\varepsilon = -1$, 20 °C, $N_f = 2689$ cycles)

4.2.2 Defects size

Gas porosities and shrinkage defects

In order to systematically measure defects size, SEM images are manually binarized. Figure 4.16 shows such an example of image processing. Given the image features, no automatic treatment of defect identification could be done.

After binarization, the resulting images are treated using particle analysis to measure the Feret diameter (as defined in Section 2.1.3). Assumptions or limitations are made concerning this measurand (depicted in Figure 4.16a):

— defect type: no distinction is made between gas porosities and shrinkage defects. While this information is available for defects observed on fractured surface (the characteristics are clearly identifiable), tomography results do not allow such a clear distinction. Therefore, for the latter comparison of database results (defects of fractography surfaces and tomography identified defect populations), defect size is not segmented by defect nature.

— 2D aspect: surface topography is not strictly horizontal and perpendicular to the loading direction. The uneven rough patches (see "a" in Figure 4.16a) confirms the 3D nature of the surface. Therefore, the different quantities are measured on the 2D projection of the surface. However, the height differences appear limited and the effect of projection negligible.

— surface intersection: the original microstructural defect can appear to be sliced by the specimen initial machining (see "b" in Figure 4.16a). The measurand can therefore be smaller than the as-cast defect.

— defect coalescence: some boundaries are unclear, and possible defect clustering can make identification complicated (see "c" in Figure 4.16a, which could be considered as the boundary between 2 defects).

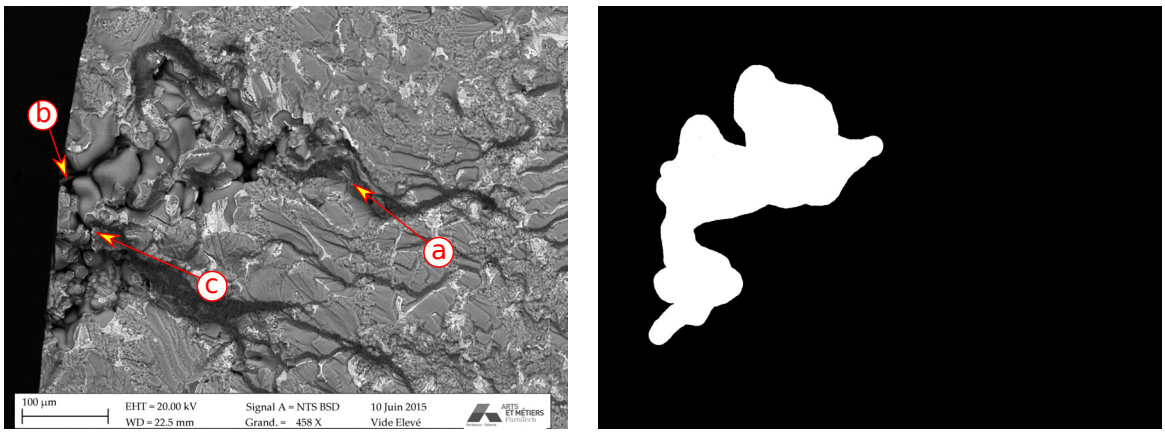

(a) Raw SEM image of initiating defect.

(b) Manually binarized defect identification (2D Feret diameter: 356 µm)

FIGURE 4.16 – Manual identification of defects. (specimen 87T5, $\Delta\varepsilon/2 = \pm 0.30\%$, $R_\varepsilon = -1$, 20 °C)

The measured defect Feret diameters are between 127 and 415 µm. The empirical cumulative distribution is presented in Figure 4.17 together with the 2 best distribution fitting (see Table 4.4). The number of data points is insufficient to establish which distribution is a better fit. Nevertheless, the two distributions provide an acceptable fit.

Table 4.4 – Defect distribution fitting, see Section 2.3.3 for distribution and parameter definitions

distribution	parameters	log-likelihood
GEV: generalized extreme value	$\xi_{gev} = -0.0937$; $\mu_{gev} = 209$; $\sigma_{gev} = 74.5$	-111.12
LOGN: log-normal distribution	$\mu_{ln} = 5.44$; $\sigma_{ln} = 0.371$	-111.03

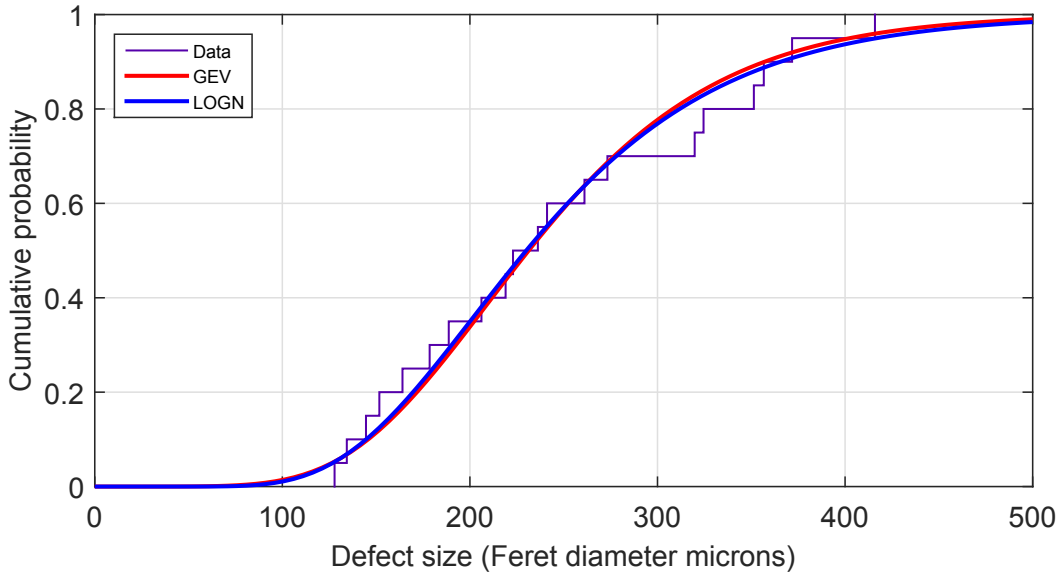

FIGURE 4.17 – Empirical cumulative distribution and distribution fit of defect size (GEV: generalized extreme value distribution, LOGN: log-normal distribution)

Clustering defects

For three tests (see table 4.6), no main defect can be clearly identified, but only a defect cluster. Figure 4.18a shows such a defect, as well as its measured diameter. This diameter has the same order of magnitude as the standard deviation identified by the spatial distribution ($\sigma = 567\,\mu m$, see Section 2.4). Table 4.5 presents the size of the measured clusters, which have the same order of magnitude. However, their dimensions are greatly affected by measuring uncertainty.

Clusters are differentiated from the shrinkage defects (considered as isolated), but some cases could be classified in both categories. For example, Figure 4.18b shows a large main defect, and close secondary defects. This case is categorized in the shrinkage defects (as opposed to the cluster defects).

Table 4.5 – Defect cluster size

Specimen	cluster diameter (µm)
22T5	1100
35T5	1050
36T5	1900

4.2.3 Distance to the surface

Distance to the surface is measured from the closest edge of the defect to the specimen surface (see Figure 4.19a). Using this method, the distance to the surface of

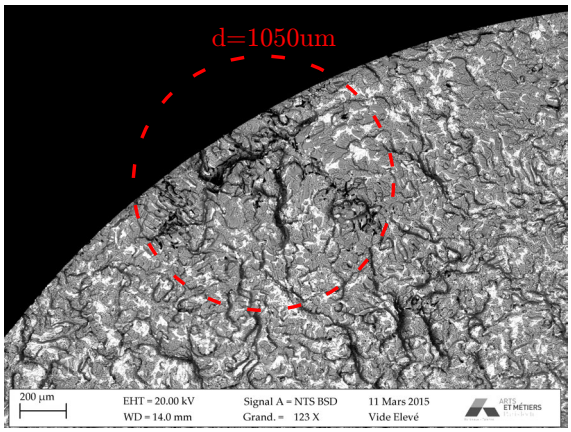

(a) SEM-BSE image of defect cluster: diameter measurement (specimen 35T5, $\Delta\varepsilon/2 = \pm 0.25\%$, $R_\varepsilon = -1$, 150 °C, $N_f = 3134$ cycles)

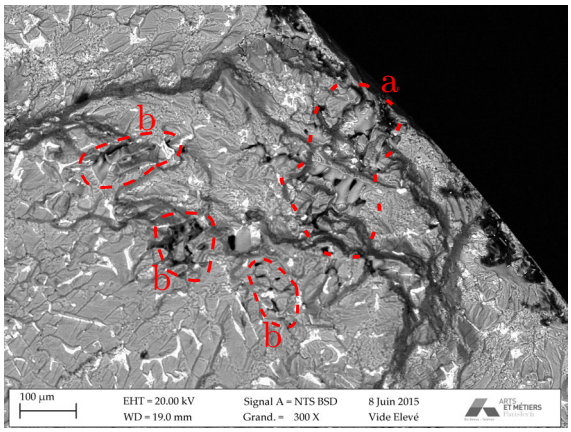

(b) SEM-BSE image of defect cluster: (a) main defect; (b) secondary defects (specimen 88T5, $\Delta\varepsilon/2 = \pm 0.25\%$, $R_\varepsilon = -1$, 20 °C, $N_f = 10500$ cycles)

FIGURE 4.18 – Identification of defect clusters.

a defect intersecting the specimen surface is equal to 0. As specified in Section 4.2.2, smaller defects (< 100 µm) can appear close to the main defect, but are neglected. Indeed, these smaller defects appear on the fracture surface as a consequence of the main crack interacting with these smaller defects, but would have not initiated a main crack had they been isolated.

Histogram 4.19b shows distance to edge for identified defects (oxides are still not considered). 13 of the 20 initiation defects occurred at or very close to specimen edge, and all were less than 260 µm from the specimen edge.

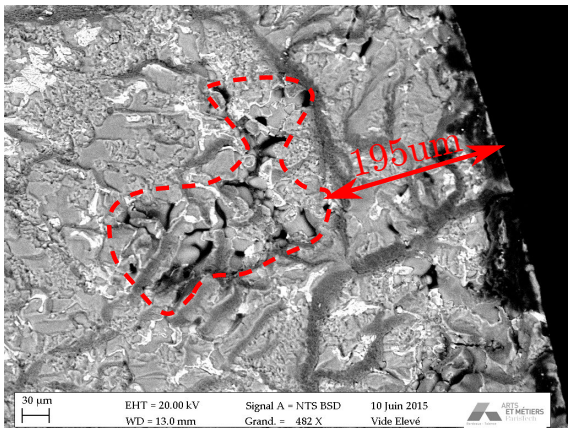

(a) Distance to surface measuring (specimen 71T5 $\Delta\varepsilon/2 = \pm 0.3\%$, $R_\varepsilon = -1$, 200 °C, $N_f = 2622$ cycles)

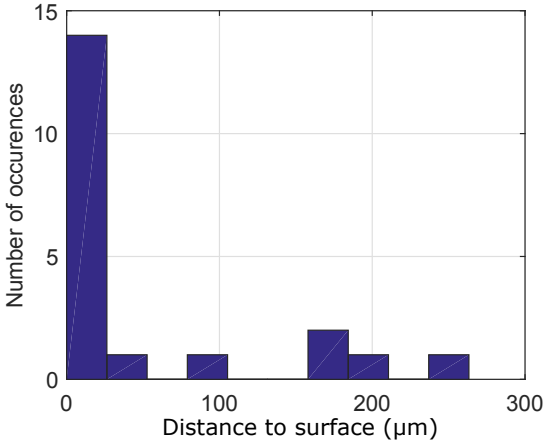

(b) Histogram of critical defect distance to specimen surface: all defects are located very close to the surface, the center of the specimen is at 3500 µm.

FIGURE 4.19 – Distance of critical defects to the surface.

No direct link was established between defect size and distance to surface given the sparse data (see Figure 4.20). However, there seem to be a minimal critical defect size (all the critical defects measured are larger than $d_{min} \approx 100$ µm), and a trend (illustrated by line y in the same Figure 4.20): for a defect to be critical, the furthest

it is from the surface, the larger it has to be. This is further discussed in the following Section 4.2.4.

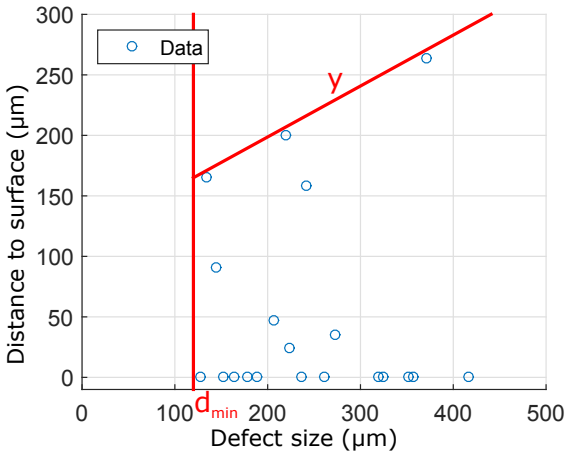

(a) Distance to the surface as a function of critical defect size.

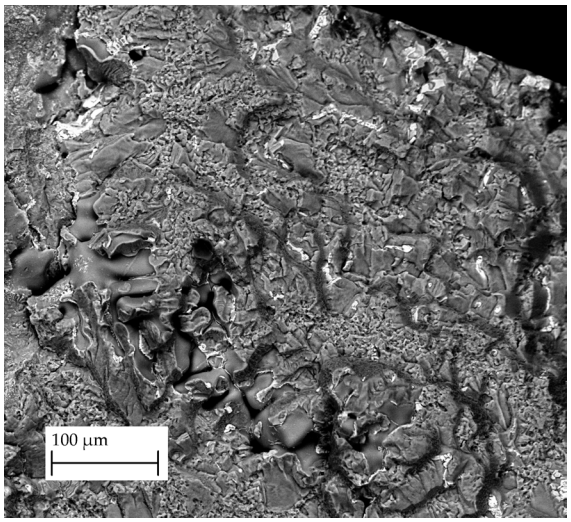

(b) Furthest defect from specimen surface (specimen 59T5, $\Delta\varepsilon/2 = \pm 0.25\%$, $R_\varepsilon = -1$, 200 °C, $N_f = 3650$ cycles)

FIGURE 4.20 – Distance to edge of critical defects.

4.2.4 Defect harmfulness

To further investigate defect harmfulness, Table 4.6 resumes defect type, size and distance to edge. In high-cycle fatigue regime, crack initiation accounts for a major part of fatigue lifetime. Therefore, while defect area is the first criteria, defect shape and acuity are also of paramount importance (Murakami [1993]). In contrast, in low-cycle fatigue regime, crack initiation occurs rapidly and most of the fatigue life is spent in crack propagation (this is further investigated in Section 4.3). Consequently, it is considered that the defect shape is of lesser importance than defect size: the initiating defect rapidly initiates a crack independently of its shape.

However, as stated in Section 4.2.3, most of initiating defects are very close to specimen surface and all are less than 260 µm from the surface, similarly to the findings of De-Feng et al. [2010]. To confirm this, two specimens were analysed by tomography before complete rupture:

— specimen 130T5 ($\Delta\varepsilon/2 = \pm 0.3\%$, $R_\varepsilon = -1$, 150 °C, $N_f = 2396$ cycles). The initiating defect is a shrinkage porosity shown in Section 4.2.1, in Figure 4.13.

— specimen 62T5 ($\Delta\varepsilon/2 = \pm 0.3\%$, $R_\varepsilon = -1$, 250 °C, $N_f = 2089$ cycles). The initiating defect is a gas porosity shown in Section 4.2.1, in Figure 4.11.

Firstly, defect distribution is compared with the identified General Pareto distribution identified in Section 2.3.3. All defects located outside the crack region are used to estimate the kernel density of defect size. Comparison is shown in Figure 4.21a. While specimen 130T5 has a very similar distribution to that of virgin specimen, distribution of specimen 62T5 appears to have shifted to the right, i.e. the defects are larger. This size increase could be caused by:

— specimen representativeness: the considered specimen has a different defect population

Table 4.6 – Defect harmfulness

T°C	$\Delta\varepsilon/2$	N_f (cycles)	type	distance to edge	Feret	specimen
20	0.25	7349	artificial	0	400	32T5
		10823	shrinkage	0	236	88T5
	0.30	2352	shrinkage	0	351	68T5
		2689	cluster	0	1178	22T5
		2904	shrinkage	0	356	87T5
150	0.25	3704	cluster	0	968	35T5
		4503	shrinkage	0	178	56T5
		4570	artificial	0	400	20T5
		6950	gas	159	241	14T5
	0.30	2004	shrinkage	0	320	72T5
		2443	shrinkage	90	144	130T5
		3004	shrinkage	30	223	28T5
	0.35	928	shrinkage	0	189	70T5
	0.40	622	shrinkage	0	325	170T5
	0.40	494	cluster	0	1900	36T5
200	0.25	3423	shrinkage	0	152	49T5
		3675	shrinkage	263	371	59T5
	0.30	1567	gas	0	128	67T5
		2070	shrinkage	35	273	25T5
		2625	shrinkage	195	219	71T5
250	0.30	2089	gaz	180	130	62T5
	0.40	494	shrinkage	0	164	105T5

— damage: for the higher temperatures (here 250 °C), damage is less localized and is detectable with the given resolution. Small clusters of defects coalesce and larger defects are detected (see figure 4.21b and following Section 4.3.2).

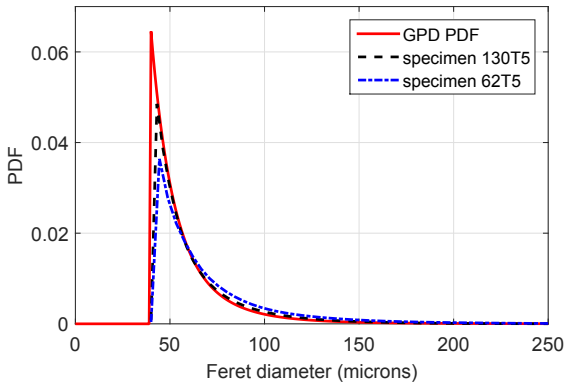

(a) Comparison of General Pareto distribution PDF (GPD PDF, identified on virgin specimen), and kernel density of cycled specimen 130T5 and 62T5 (all the data is truncated for defects smaller than 40 µm)

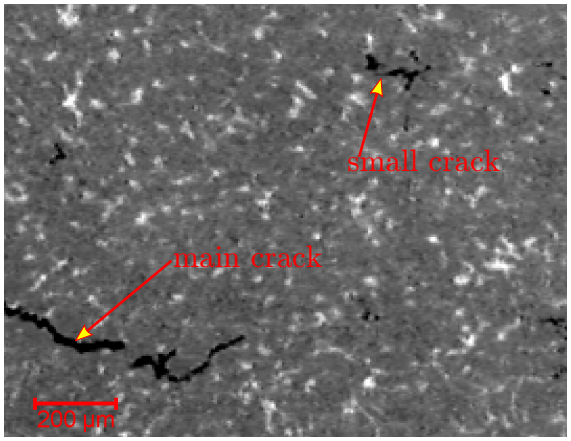

(b) Specimen 62T5: small cracks increase measured defect size. The tomography does not allow to clearly differentiate initial void from damage void.

FIGURE 4.21 – Defect population of cycled specimens.

Figure 4.22 shows all defects measured as well as the identified crack initiation one. Specimen 130T5 analysis (see Figure 4.22b) confirms the harmfulness of edge effect: the critical defect is the largest one close to the surface (160 µm), but not the overall largest one (280 µm). For the high-temperature test (specimen 62T5, see Figure 4.22a), the critical defect (130 µm) is much smaller than the largest one (463 µm), and also very near the specimen edge (200 µm). However, due to the higher temperature, more cracks are detectable (as will be discussed in Section 4.3.2, the small crack final length is larger for the higher temperatures). This is especially true at specimen edge, where crack initiation is facilitated. Figure 4.23 shows such a defect/crack. Due to the small crack, the Feret diameter is overestimated by a factor $\times 2$

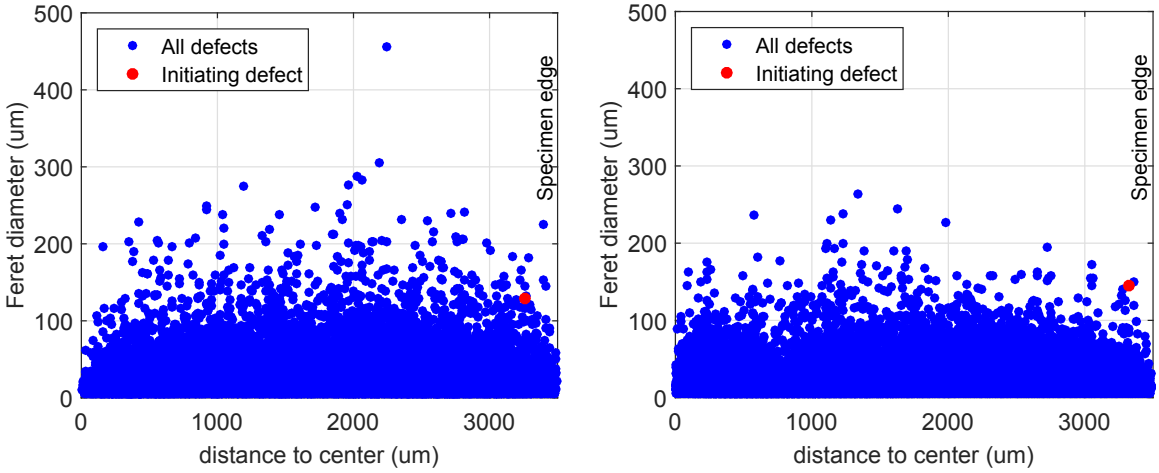

(a) Specimen 62T5: $\Delta\varepsilon/2 = \pm 0.3\%$, $R_\varepsilon = -1$, 250 °C, $N_f = 2089$ cycles

(b) Specimen 130T5: $\Delta\varepsilon/2 = \pm 0.3\%$, $R_\varepsilon = -1$, 150 °C, $N_f = 2396$ cycles

FIGURE 4.22 – Defect population of cycled specimens: the crack-initating defect is not the largest in the whole volume.

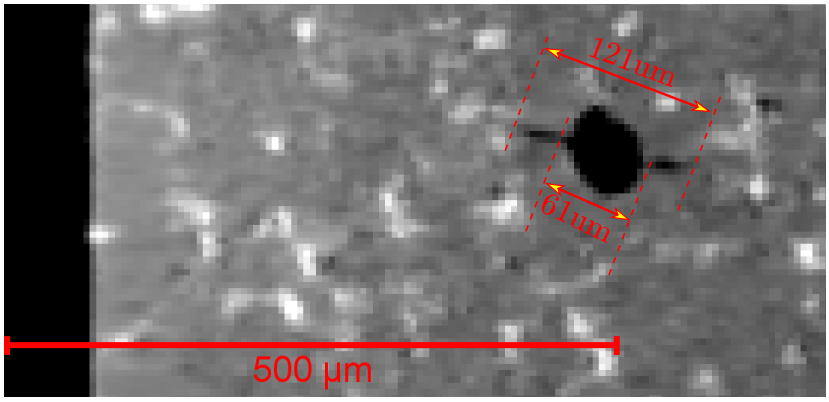

FIGURE 4.23 – Tomogaphy analysis reveals secondary cracks that increase the defect measurement size (Specimen 62T5: $\Delta\varepsilon/2 = \pm 0.3\%$, $R_\varepsilon = -1$, 250 °C, $N_f = 2089$ cycles)

4.3 Propagation mechanisms and kinetic

In order to study the crack initiation and propagation mechanisms, the fatigue fracture surfaces are studied and crack propagation was monitored on 4 specimens.

Firstly, crack monitoring experiments results are resumed in Section 4.3.1. The results of the crack propagation monitoring are briefly introduced to give an overview.

Secondly, the results of monitoring combined with the observations on classical smooth specimens are then used to study the kinetics and mechanisms of crack initiation in Section 4.3.2.

Thirdly, always using the combination of monitored cracks and post mortem observation, steady-crack propagation is studied in Section 4.3.3. A particular emphasis is put on crack interactions with other cracks and with neighbouring defects. The influence of temperature is also of concern.

4.3.1 Crack growth monitoring

Using the test set-up described in Section 4.1.3, crack length is monitored for 4 specimens. The main details can be found in Table 4.7. The micro defects (the 400 µm hemisphere) all initiate a crack, but for $T = 250\,°C$, the crack initiated by this artificial is not the crack that lead to final failure, or "main crack".

N_{init} specifies the number of cycles to initiation for the left and right edge of the artificial defect, while N_f is the number of cycles to failure (failure being a 10% load-drop from the trend line). The value a_0 is the initial crack size, considered equal to the artificial defect diameter. This strong hypothesis considers the defect to act as a crack at the test start. The measure a_f is the final crack size (i.e. the size of the crack at cycle N_f).

Table 4.7 – Crack monitoring experiments: summary. The values of cycles to initiation N_{init} are identified on the left and the right edge of the defect (left;right). The value "main" indicates if the crack leading to failure started on the artificial defect.

Test	$\Delta\varepsilon/2$	T (°C)	N_{init}	$N_{init}/N_f(\%)$	N_f	a_0 (µm)	a_f (µm)	main
20 T5	0.25	150	1440;1000	31;21	4574	389	3260	yes
76 T5	0.4	20	316;186	43;25	731	401	2150	yes
29 T5	0.25	250	1060;1450	25;34	4100	359	1100	no
89 T5	0.4	250	83;226	11;31	719	393	1450	no

Figure 4.24 shows the first and last cycle of a crack monitoring experiment. The large field of view (10×4 mm is in focus) also allows to detect numerous crack initiation on the rest of the surface.

The monitoring of crack length is shown in Figure 4.25, and will be further discussed in Section 5.2.

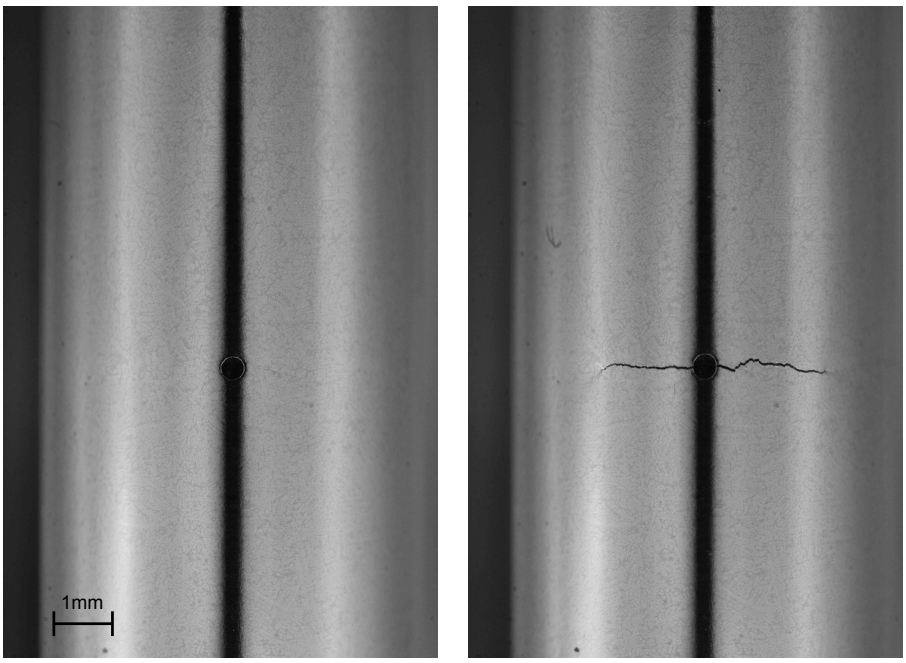

(a) Cycle 1

(b) Cycle 4574 (cycle before final failure)

FIGURE 4.24 – Crack propagation monitoring (Specimen 20T5: $\Delta\varepsilon/2 = \pm 0.25\%$, $R_\varepsilon = -1$, 150 °C, $N_f = 4574$ cycles)

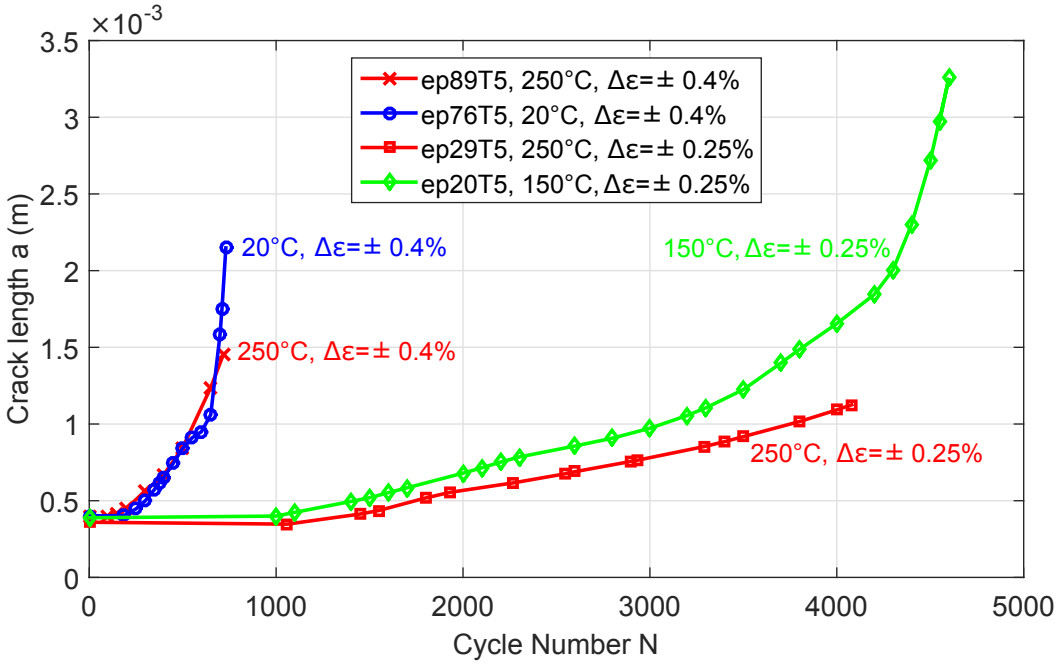

FIGURE 4.25 – Crack propagation curves of artificial defect generated cracks.

4.3.2 Crack initiation and small cracks

As shown in the summary Table 4.7, for cracks started on artificial defects, the number of cycles to crack initiation N_{init} is non-negligible and ranges from 11% to 43% (no clear effect of temperature or applied strain range can be made given the small number of tests). Figure 4.26 shows the monitoring of crack initiation. While this detection is hard to convey through still images, the use of video allows for a relatively robust visual detection.

This high proportion of initiation to propagation contradicts with the fact that low cycle fatigue life is governed by crack propagation (Wang et al. [2001a]). However, the effect of defect machining process, as well as the low acuteness of the artificial defect compared to real defects cannot be neglected.

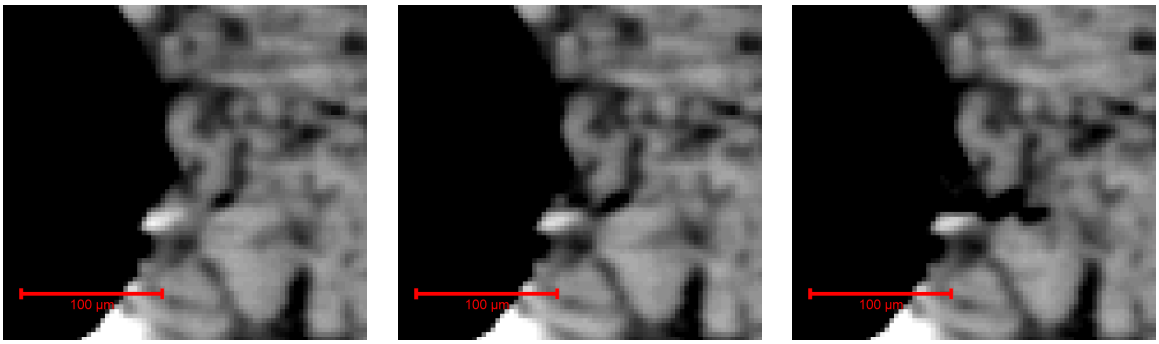

(a) Cycle 1 (b) Cycle 200 (c) Cycle 300

FIGURE 4.26 – Crack initiation on artificial defect. The contrast is purposely set too high revealing crack initiation, which is detected at 186 cycles (Specimen 76T5: $\Delta\varepsilon/2 = \pm 0.4\%$, $R_\varepsilon = -1$, 20 °C, $N_f = 731$ cycles)

To overcome the bias caused by the artificial defect, small cracks naturally initiated are investigated. Figure 4.27 shows such a crack. The crack initiation occurs rapidly ($N_{init}/N_f = 220/4100 = 5\%$) and propagates to a 325 µm crack. The cycle 3400 is displayed in Figure 4.27d, since latter cycles are impacted by the main crack propagating, causing smaller secondary crack opening. Post-mortem analysis is done by SEM (see Figure 4.27e) to compare the crack measurement: the real crack length is actually 10% (360 µm) longer than measured by digital crack monitoring. However, the digital crack monitoring final length is considered as reference, since all the crack measurements are not systematically replicated by SEM.

For most of the cracks, the initiating cause is not identified. For one case, the initial defect intersects the surface and can be seen from the start of the fatigue test (see figure 4.28a). The crack is too small to clearly identify the crack initiation cycle, but Figure 4.28b reveals the crack starts in the eutectic zone on the edge porosity (see Figure 4.28b).

The effect of the eutectic zone can also be seen in Figure 4.29. While the origin of the crack cannot be identified (it could be a subsurface defect), the growth of the small crack occurs only in the eutectic zone.

To confirm the effect of the eutectic zone on crack initiation, EDS analysis is used on a crack seen on a fractured surface. Figure 4.30 shows an energy dispersive X-ray analysis (EDS) of crack initiation on a defect porosity edge. Even though this method is semi-quantitative, it allows for comparative studies when significant differences appear. Spectrum 1 refers to the α-aluminium matrix, corresponding to a dendrite. Spectrum 2 is a silicon-rich area, corresponding to the aluminium eutectic phase. Due to the high

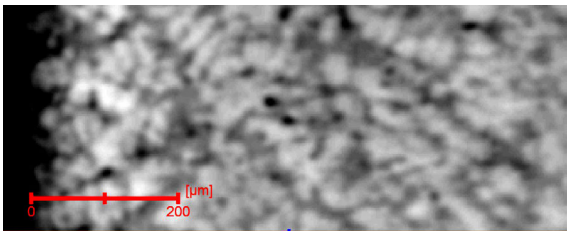

(a) Cycle 1

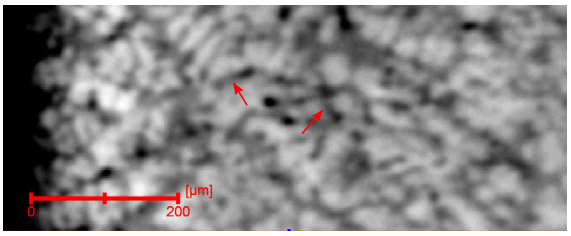

(b) Cycle 220

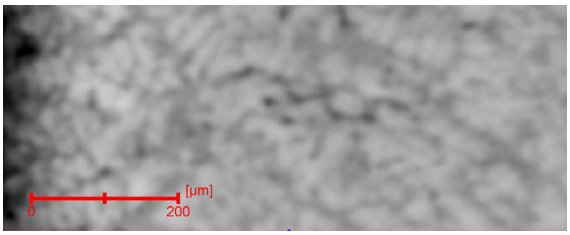

(c) Cycle 1400

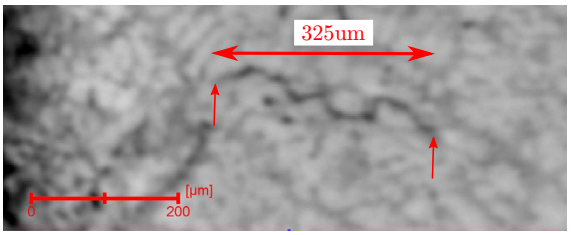

(d) Cycle 3400

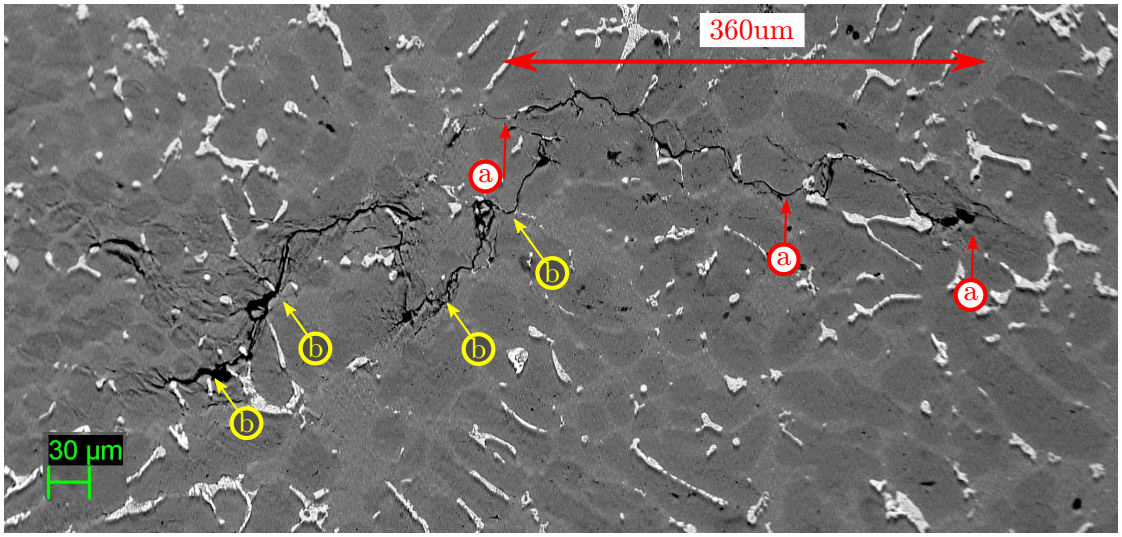

(e) Post-mortem SEM Analysis.

FIGURE 4.27 – Natural crack initiation. Crack (a) and (b) are considered different cracks, for their coalescence is only detected by SEM post-mortem analysis.(Specimen 29T5: $\Delta\varepsilon/2 = \pm 0.25\%$, $R_\varepsilon = -1$, 250 °C, $N_f = 4100$)

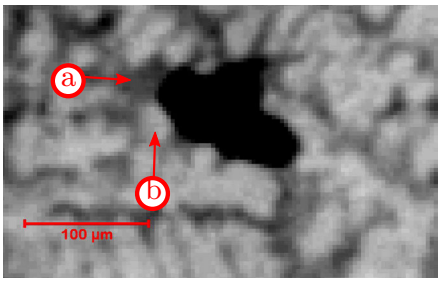

(a) Cycle 1

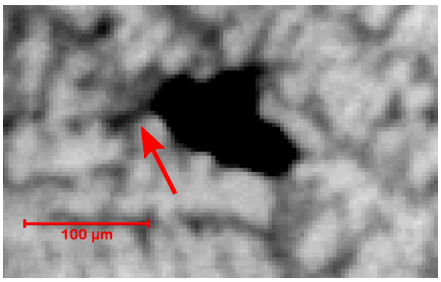

(b) Cycle 731

FIGURE 4.28 – Crack initiation on natural shrinkage defect. Gray area (a) is the eutectic zone and the more white (b) an aluminium dendrite (Specimen 76T5: $\Delta\varepsilon/2 = \pm 0.4\%$, $R_\varepsilon = -1$, 20 °C, $N_f = 731$ cycles)

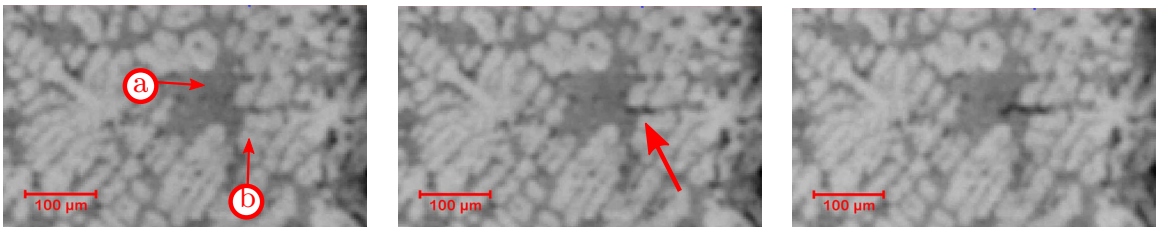

(a) Cycle 1 (b) Cycle 336 (c) Cycle 731

FIGURE 4.29 – Crack initiation of small crack. Gray area (a) is the eutectic zone and the more white (b) an aluminium dendrite (Specimen 76T5: $\Delta\varepsilon/2 = \pm 0.4\%$, $R_\varepsilon = -1$, 20 °C, $N_f = 731$ cycles)

Young modulus of silicon particles (at room temperature, 130GPa versus 70GPa for the alumnium matrix, Yi et al. [2004]), combined to the stress concentration created by the shrinkage defect, crack initiates on the defect boundary at the junction with eutectic zone. The other brittle particles (label (II) Fe-rich intermetallics and label (III) Al-Cu particles in Figure 4.30b) are also present on initiating defect edges.

An arrested crack was also detect on a smooth specimen analysed by tomography. Figure 4.31 shows the 3D reconstruction. This analysis clearly shows the elliptic shape of small cracks.

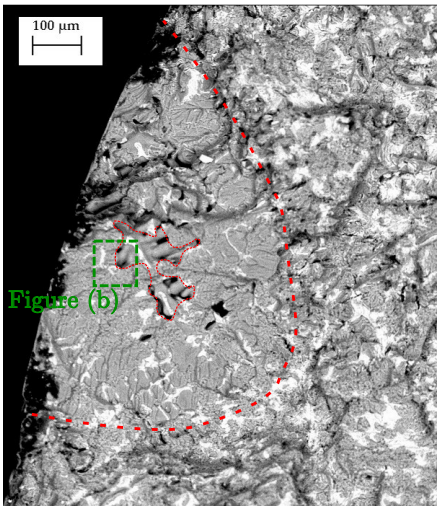

(a) General view of crack and shrinkage defect.

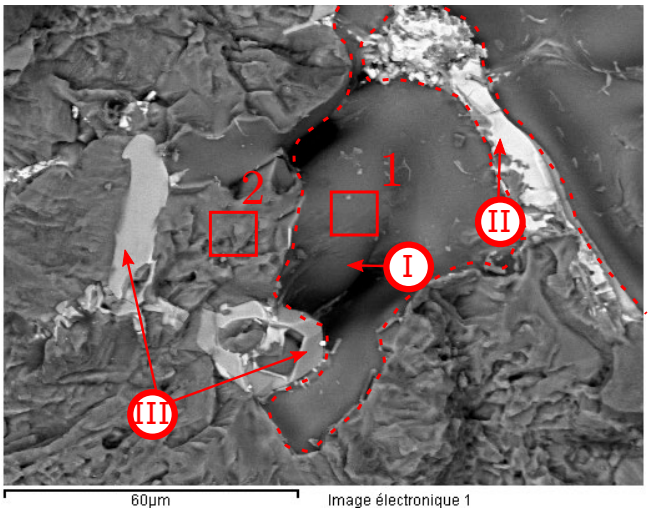

(b) SEM-BSE image of crack initiation

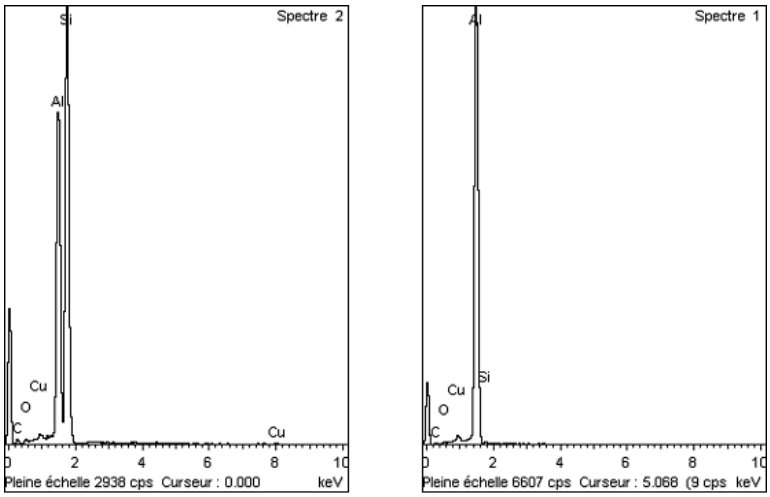

(c) Corresponding EDS spectrum

FIGURE 4.30 – Energy dispersive X-ray (EDS) analysis of crack initation. (I) is the shrinkage defect, (II) an intermetallic and (III) an Al-Cu particle. (specimen 68T5, $\Delta\varepsilon/2 = \pm 0.3\%$, $R_\varepsilon = -1$, 20 °C, $N_f = 2552$ cycles)

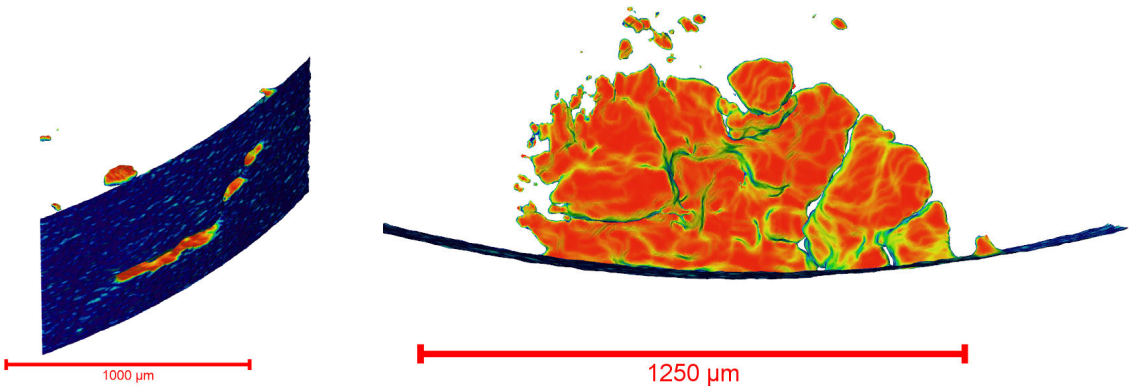

(a) 3d view

(b) Top view

FIGURE 4.31 – Crack initiation of small crack (Specimen 14T5: $\Delta\varepsilon/2 = \pm 0.25\%$, $R_\varepsilon = -1$, 150 °C, $N_f = 6950$ cycles).

For all the specimens where cracks were monitored, the observable surface was investigated and the small cracks detected (with the limitation of the observation method). The number of cycles to crack initiation N_i is measured as well as the final crack length a_f. The summary values are shown in Table 4.8 and graphical results presented in Figure 4.32. The artificial defect generated crack is not taken into account, nor are the cracks that interact with it. The total number of cracks observed on each specimen (#cracks in Table 4.8) is slightly higher than presented on the graphical representation (in Figure 4.32). Indeed, some cracks were detected but the number of cycles to crack initiation could not be detected.

For all specimens, some natural cracks initiate rapidly (less than 10% of the total fatigue life). The number of specimens (4) is too low to distinguish the influence of temperature and the influence of plastic strain amplitude on the number of cracks detected. However, specimen 20T5 ($\Delta\varepsilon/2 = \pm 0.25\%$, $R_\varepsilon = -1$, 150 °C, $N_f = 4574$) indicates low temperature and low plastic strain amplitude combined initiate very few cracks (2 on the observed surface). For the higher temperatures, it is also observed that small cracks propagate more than for the lower temperatures.

Most of the crack initiation detections are well below 20% of the fatigue lifetime. Given the relatively low resolution, this observation method tends to overestimate this number, thus proving crack initiation accounts only for a small part of the low cycle fatigue life. The relatively high fractions N_i/N_f observed for artificial defects can be attributed to several factors:

— the defect generation process modifies the defect surface;

— the artificial defects have low acuteness;

— compared to natural defects, the artificial ones are, *a priori*, not located in cluster of defects.

Table 4.8 – Crack initiation of small surface cracks on crack monitored specimens. (#cracks) being the total number of cracks observed on the specimen surface.

Test	$\Delta\varepsilon/2$	T (°C)	N_f	$\Delta\varepsilon_p(10^{-3})$	#cracks	min (N_i/N_f) (%)	$\overline{N_i/N_f}$ (%)
20 T5	0.25	150	4574	0.25	2	8.3	12.35
76 T5	0.4	20	731	1	15	2.3	17.1
29 T5	0.25	250	4100	0.5	12	1.5	16.6
89 T5	0.4	250	719	2	17	1.5	9.2
all					11.5	3.4	13.8

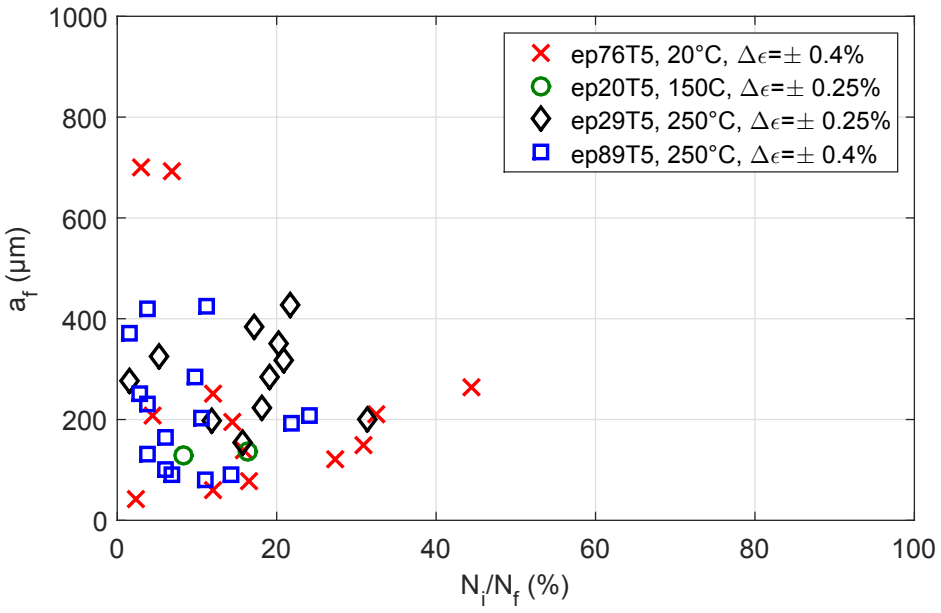

FIGURE 4.32 – Final crack lengths vs fraction of number of cycles to initiation to number of cycles to failure. Each marker represents a unique small crack.

4.3.3 Crack propagation

General mechanisms

In order to present the general mechanisms, specimen 88T5 ($\Delta\varepsilon/2 = \pm 0.25\%$, $R_\varepsilon = -1$, 20 °C, $N_f = 10823$) is studied by high resolution tomography (voxel=$2.96 \times 2.96 \times 2.96\,\mu m^3$) and shown in Figure 4.33. Label (a) identifies the main initiating defect, while label (b) shows the steady crack propagation. The analysed sample had to be machined to reduce its size and allow for the higher resolution (laboratory X-Ray tomography requires the sample to be very close to the X-Ray source for the higher resolutions), hence the particular shape of the analysed sample in Figure 4.33a. The SEM Figure 4.33b of the defect is rotated to match the other Figures.

The final crack width, and transition to fast-fracture propagation, is around 3.1 mm. While the kinetics of this test are not measured, the specimen 20T5 ($\Delta\varepsilon/2 = \pm 0.25\%$, $R_\varepsilon = -1$, 150 °C, $N_f = 4574$ cycles) has similar test conditions and propagation monitoring exhibits a final crack length $a_f = 3.3$ mm before final failure. These facts demonstrate the frontier between the smooth surface and the rougher one are indeed the separation from the fatigue steady-crack to final tension failure. Furthermore, the crack propagation monitoring experiments (see 4.3.1) show the crack growth follows an exponential trend. Therefore, the last stages of the crack growth occur in a few cycles, and a robust characterization of the transition to fast-fracture does not appear necessary.

Steady-crack and final tension fracture comparison

Detailed mechanisms are shown on specimen 87T5 ($\Delta\varepsilon/2 = \pm 0.3\%$, $R_\varepsilon = -1$, 20 °C, $N_f = 2904$ cycles). Firstly, Figure 4.34 gives an overview of the fracture surface by SEM and tomography surface reconstruction. The difference between final tension fracture and steady-crack propagation crack morphology is shown in the two zoomed Figures (a similar study can be found in Gall et al. [2000] for a cast A356-T5 Al alloy):

— Steady-crack propagation (see Figure 4.35): the initiating porosity defect appears on the left side, and after rough areas surrounding the defect, corresponding to the crack initiation stage, large flat areas perpendicular to the loading direction appear, corresponding to mode I crack propagation. These can better be seen in Figure 4.36a where 3 morphological features appear: label (a) is the flat perpendicular to loading regions, corresponding to crack propagation in the aluminium dendrites; label (b) shows the eutectic region, connecting the different flat surfaces; label (c) shows a sliced intermetallic. The propagation mechanisms in the aluminium dendrites is shown in Figure 4.36b: fine fatigue striations marks, similar to the ones found in Song et al. [2011]. An approximate size measurement gives an inter-striation distance of 1.5 µm/cycle (it is supposed that each cycle causes one striation), compatible with the order of magnitude found in Section 5.2.

— Fast fracture surface (see Figure 4.37): in comparison, the final fast fracture area exhibits much higher roughness. There are no flat surfaces, corresponding to dendrite fracture, and a higher number of sliced intermetallics. The difference between flat and rough surface and their correspondence with dendrite and eutectic structure is analysed using EDS on a small crack on specimen 68T5 ($\Delta\varepsilon/2 = \pm 0.3\%$, $R_\varepsilon = -1$, 20 °C, $N_f = 2552$ cycles) in Figure 4.38. Spectrum (1) serves as reference: inside the shrinkage defect, the surface morphology is clearly identified as a aluminium dendrite. Spectrum (2) has identical features, showing the flat

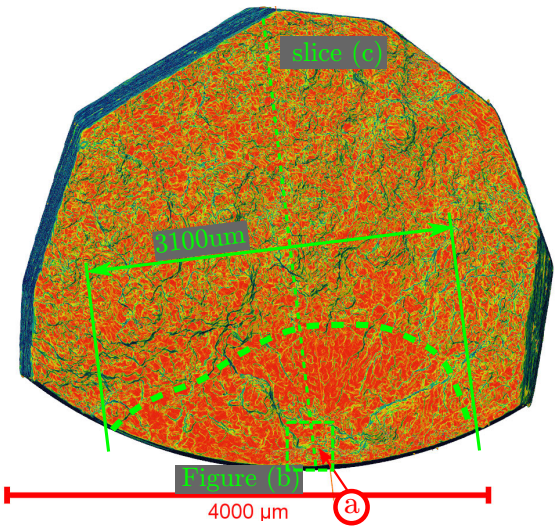

(a) Tomography surface reconstruction: top view

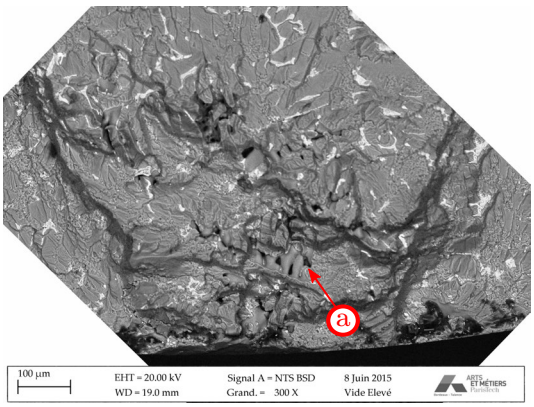

(b) SEM close-up of initiating defect

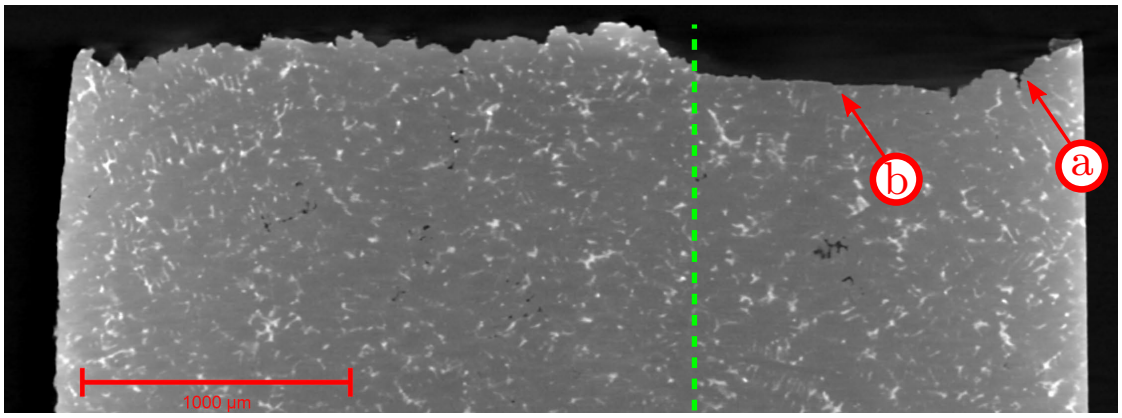

(c) Tomography slice

FIGURE 4.33 – Steady-crack propagation (Specimen 88T5: $\Delta\varepsilon/2 = \pm 0.25\%$, $R_\varepsilon = -1$, 20 °C, $N_f = 10823$ cycles)

surfaces are indeed sliced aluminium dendrites. Finally, spectrum (3) illustrates the eutectic nature of rough surfaces. The number of intermetallics is investigated by image analysis. The intermetallic analysis area shown in Figure 4.34 is reproduced in Figure 4.39a. It is then binarized (see Figure 4.39b), and the density of intermetallic is calculated for each vertical line, displayed in Figure 4.39c. The raw linear density is smoothed to display the underlying trend, and compared with the mean value, which is calculated using the exact same procedure on a control virgin sliced specimen, providing the intermetallic mean surface density (which equals the density found for and arbitrary straight cut surface of an untested sample). This analysis shows the surface density of intermetallics rises progressively, rather than abruptly, and is always superior to the mean surface density.

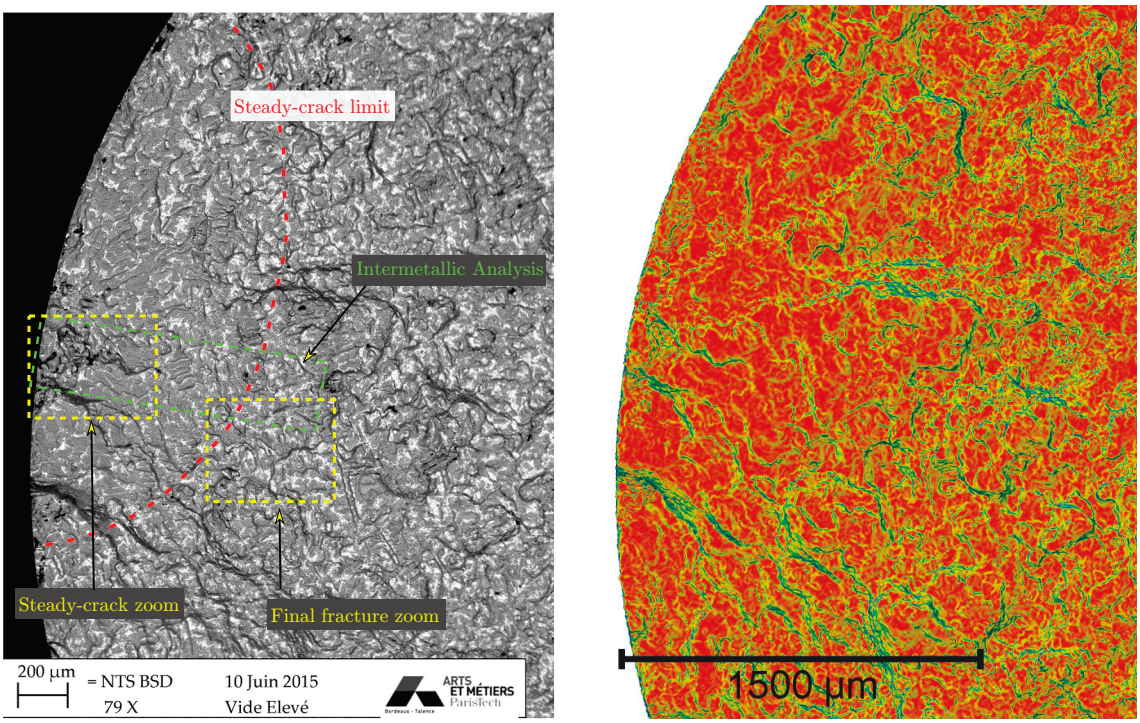

(a) SEM-BSE of fracture surface

(b) Tomography surface reconstruction: top view

FIGURE 4.34 – Steady-crack propagation (Specimen 87T5: $\Delta\varepsilon/2 = \pm 0.3\%$, $R_\varepsilon = -1$, 20 °C, $N_f = 2904$ cycles).

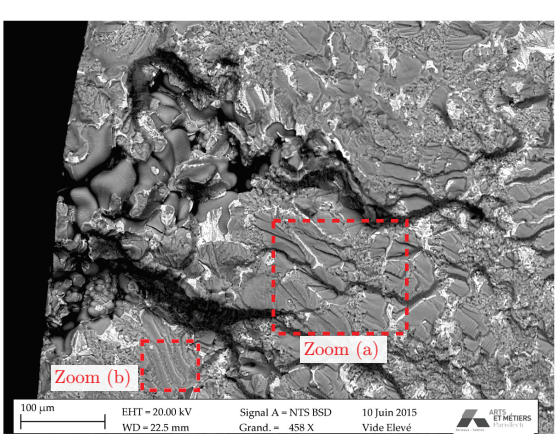

(a) SEM-BSE of fracture surface, zooms are presented in Figure 4.36

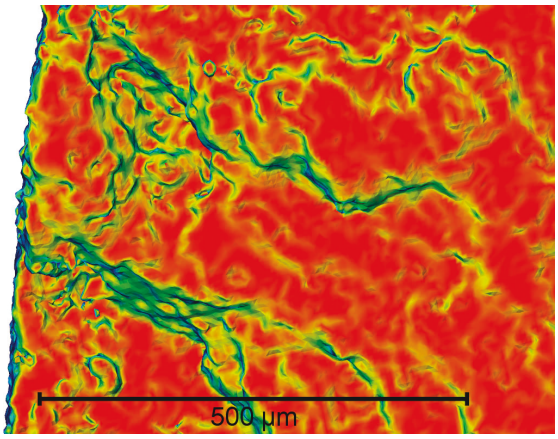

(b) SEM-BSE of fracture surface

FIGURE 4.35 – Steady-crack propagation (Specimen 87T5: $\Delta\varepsilon/2 = \pm 0.3\%$, $R_\varepsilon = -1$, 20 °C, $N_f = 2904$ cycles).

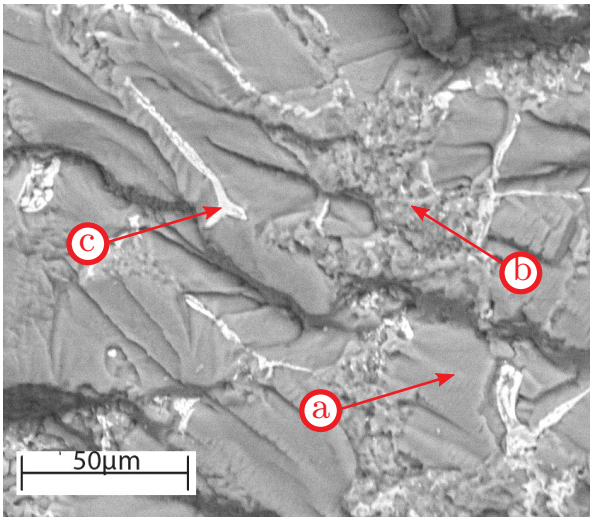

(a) SEM-BSE detailed of steady crack

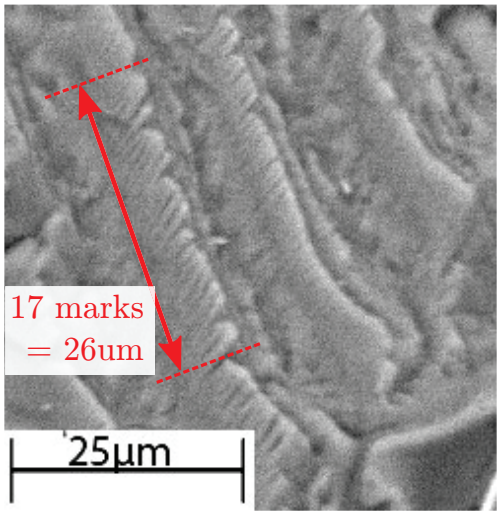

(b) Fatigue striations (tire tracks)

FIGURE 4.36 – Steady-crack propagation (Specimen 87T5: $\Delta\varepsilon/2 = \pm 0.3\%$, $R_\varepsilon = -1$, 20 °C, $N_f = 2904$ cycles).

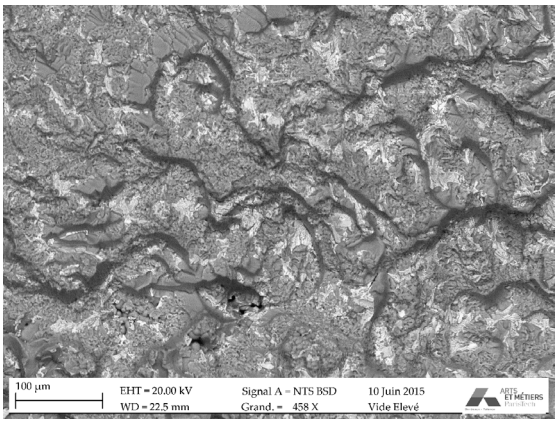

(a) SEM-BSE of fracture surface

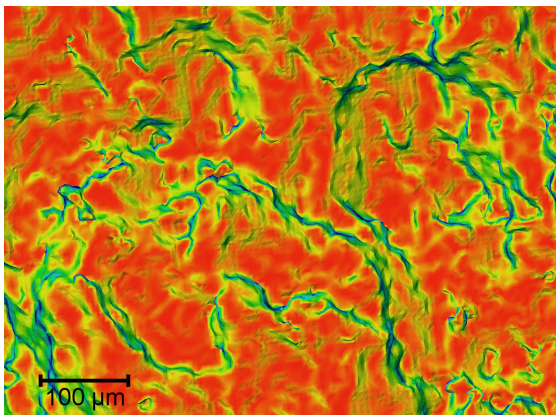

(b) Tomography surface reconstruction: top view

FIGURE 4.37 – Final tension fracture surface (Specimen 87T5: $\Delta\varepsilon/2 = \pm 0.3\%$, $R_\varepsilon = -1$, 20 °C, $N_f = 2904$ cycles).

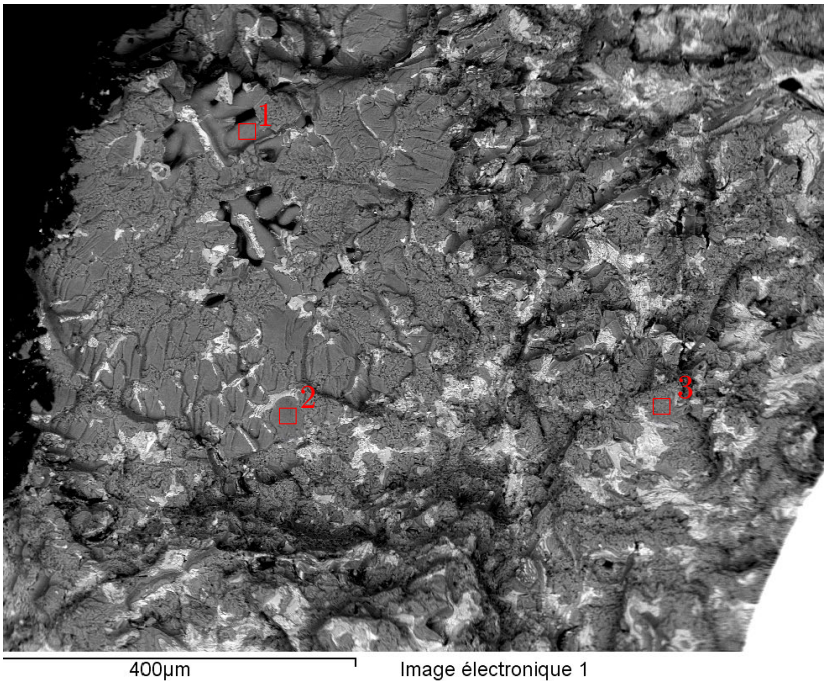

(a) SEM-BSE image of EDS analysed surface

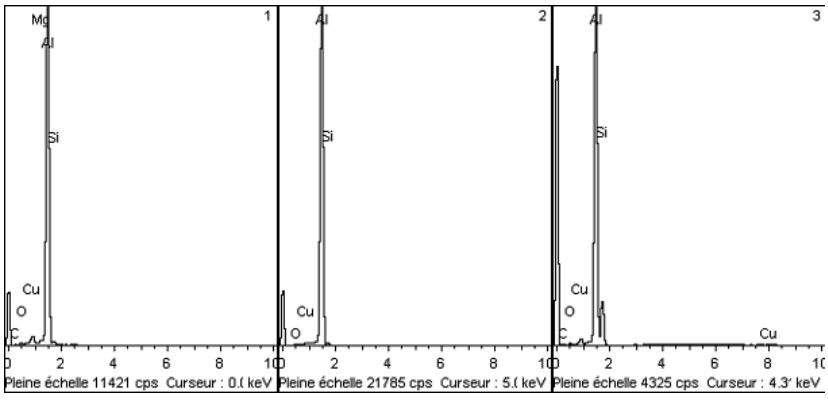

(b) Corresponding EDS spectrum

FIGURE 4.38 – EDS analysis of different stages of crack propagation (specimen 68T5, $\Delta\varepsilon/2 = \pm 0.3\%$, $R_\varepsilon = -1$, 20 °C, $N_f = 2552$ cycles).

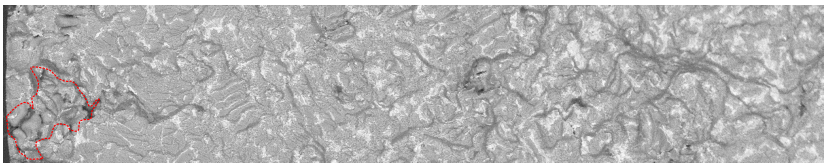

(a) SEM-BSE of analysed area

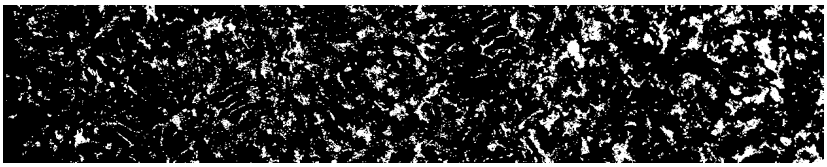

(b) SEM-BSE of analysed area

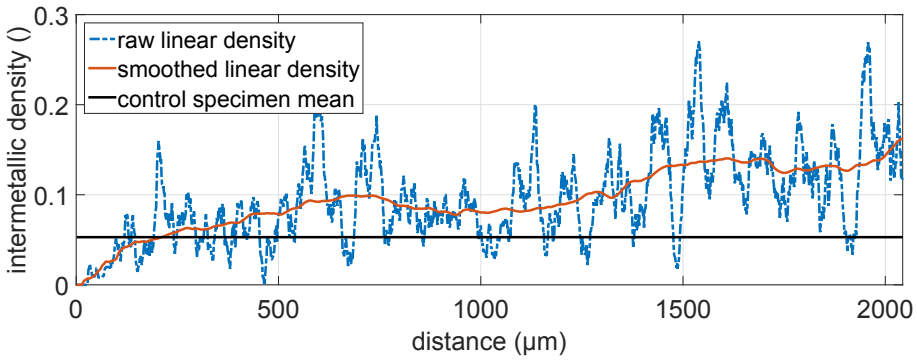

(c) SEM-BSE of analysed area

FIGURE 4.39 – Steady-crack propagation: intermetallic density analysis (Specimen 87T5: $\Delta\varepsilon/2 = \pm 0.3\%$, $R_\varepsilon = -1$, 20 °C, $N_f = 2904$ cycles)

While not representative of the 3D nature of the crack, surface observation clearly illustrates the aforementioned explanations and gives insights on steady crack propagation. Figure 4.40 shows SEM-BSE images of the crack:

— Figure 4.40a shows the image of the restitched crack, the initial specimen being completely fractured.

— Figure 4.40b displays the image after image processing: the colours are inverted to display the dendrites in the more usual white appearance, and the contrast increased to amplify the difference dendrite/eutectic zone.

The different phases of the steady-crack propagation can be seen in Figure 4.40b. The propagation through dendrite cells is associated with increased plasticity, causing a white halo. For the propagation through the eutectic zones, the plasticity is much more localized, and the crack appears precisely defined.

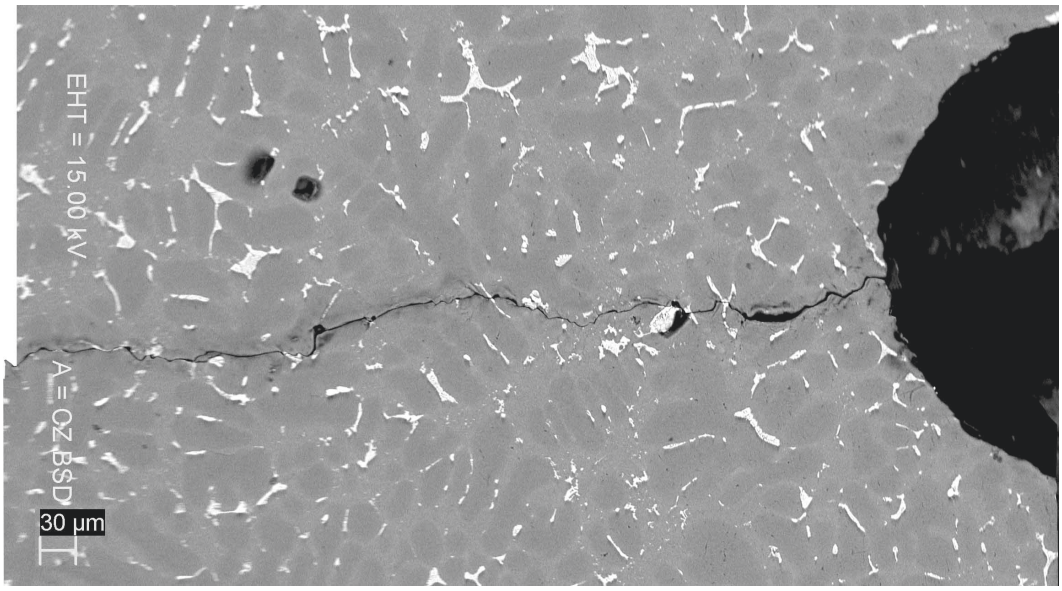

(a) SEM-BSE of crack on edge surface: raw image

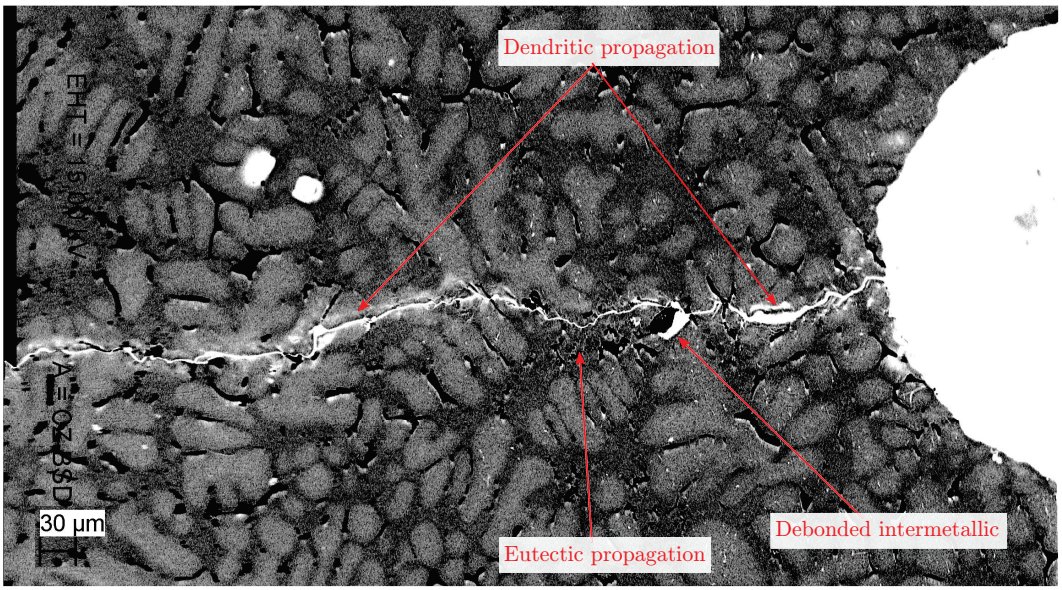

(b) SEM-BSE of crack on edge surface: inverted image and increased contrast

FIGURE 4.40 – Steady-crack propagation on artificially initiated crack (Specimen 20T5: $\Delta\varepsilon/2 = \pm 0.25\%$, $R_\varepsilon = -1$, 20 °C, $N_f = 4570$ cycles).

4.3.4 Steady-crack defect interaction: case study example

In order to understand the steady-crack propagation and defects interaction, specimen 67T5 ($\Delta\varepsilon/2 = \pm 0.3\%$, $R_\varepsilon = -1$, 200 °C, $N_f = 1567$) is studied. A general SEM and topography view is shown in Figure 4.41, while Figure 4.42 presents the zoomed area and a 3D view of the crack zone. Lastly, Figure 4.43 illustrates tomography slices of Figure 4.42b.

The initiating defects are illustrated in Figure 4.41:

— Defect (a): hemispherical gas defect right on the specimen edge, see Figure 4.41c

— Defect (b): gas defect, see Figure 4.41d

— Defect (c): shrinkage defect, see Figure 4.41d

The crack scenario can be conjectured following these observations and seen in Figure 4.42a:

1. Crack initiation on defect (a): this defect is the most harmful by his size and his proximity to the free edge (see Figure 4.41c), and therefore initiates a crack and propagates the farthest.
2. Crack initiation on defect (b): this defect, while larger than defect (a) (it has a Feret diameter of 250 against 130 µm for defect (a)), is farther from the free edge (100 µm) and therefore less harmful.
3. Crack interaction on defect (c): it is unclear if the shrinkage defect (c) has propagated to a small crack before interacting with the main crack. However, it clearly interacts with the main crack, as can be seen whith the shrinkage residue seen in Figure 4.43c. The Figure also displays a small topographical depression (below the local "mean" height of the surface of the crack) indicating the influence of the defect on the crack path.
4. Crack coalescence: given the elliptical shape of the cracks, the crack coalescence starts at the specimen edge by plastic strain accumulation (see further details in the next Section 4.3.5). However, as can be seen in Figure 4.42, and on the evolution of the coalescence front in Figure 4.43 (the crack coalescence initiating at the edge, the observation at the depth L can be seen as the evolution of the coalescence in time), the coalescence starts by plastic deformation close to the specimen surface, and transforms to a slant fracture. In the end, the slant fracture becomes smaller and the crack surface horizontal.

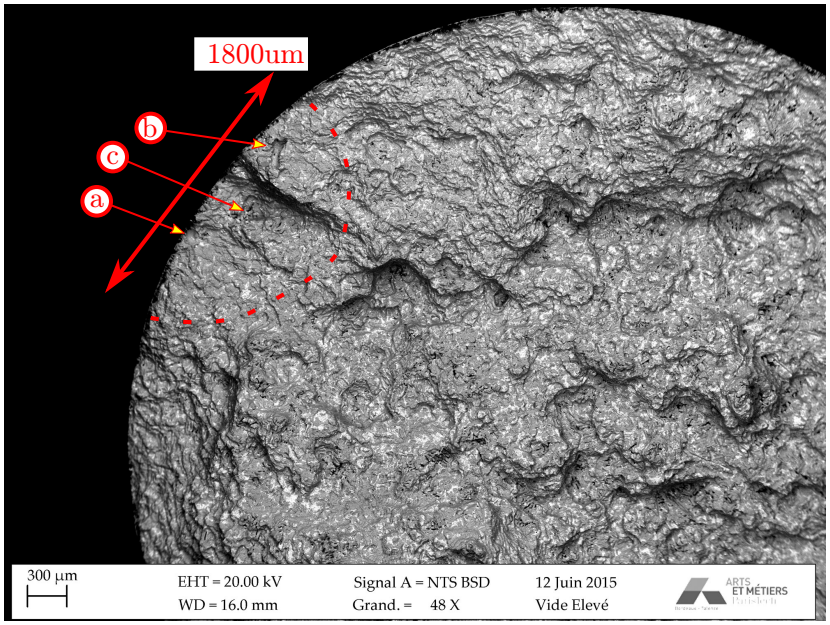

(a) SEM-BSE global observation

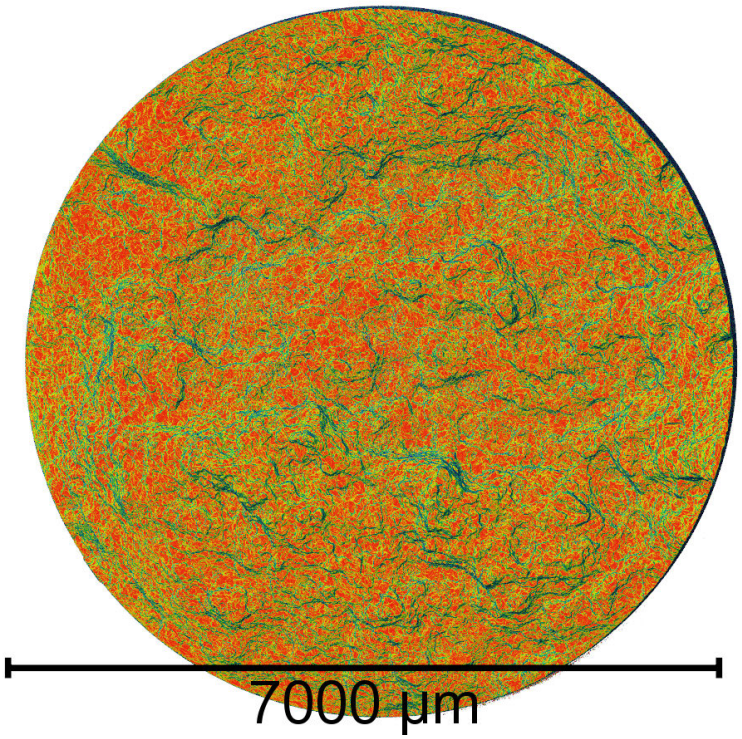

(b) Top view of surface topography by tomography reconstruction (same orientation as SEM image (a))

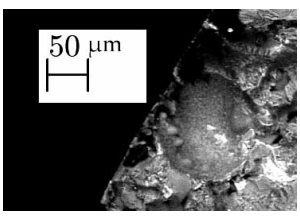

(c) Defect a

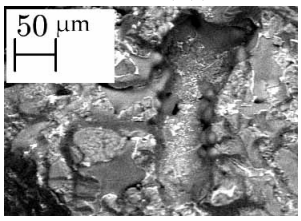

(d) Defect b

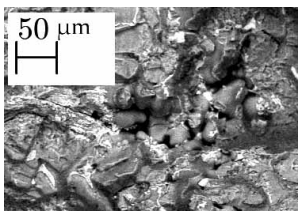

(e) Defect c

FIGURE 4.41 – Steady-crack propagation: defect interactions (Specimen 67T5: $\Delta\varepsilon/2 = \pm 0.3\%$, $R_\varepsilon = -1$, 200 °C, $N_f = 1567$)

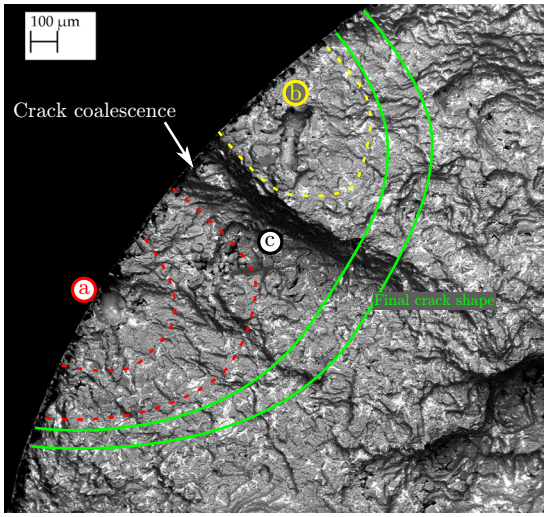

(a) SEM-BSE observation of steady-crack propagation: labels (a), (b) and(c) are three defects.

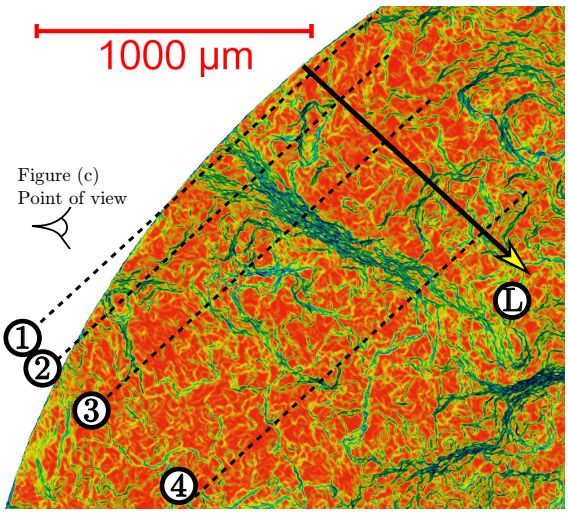

(b) Top view of topography of surface by tomography reconstruction, slice numbers of Figure 4.43 (same orientation as SEM image (a))

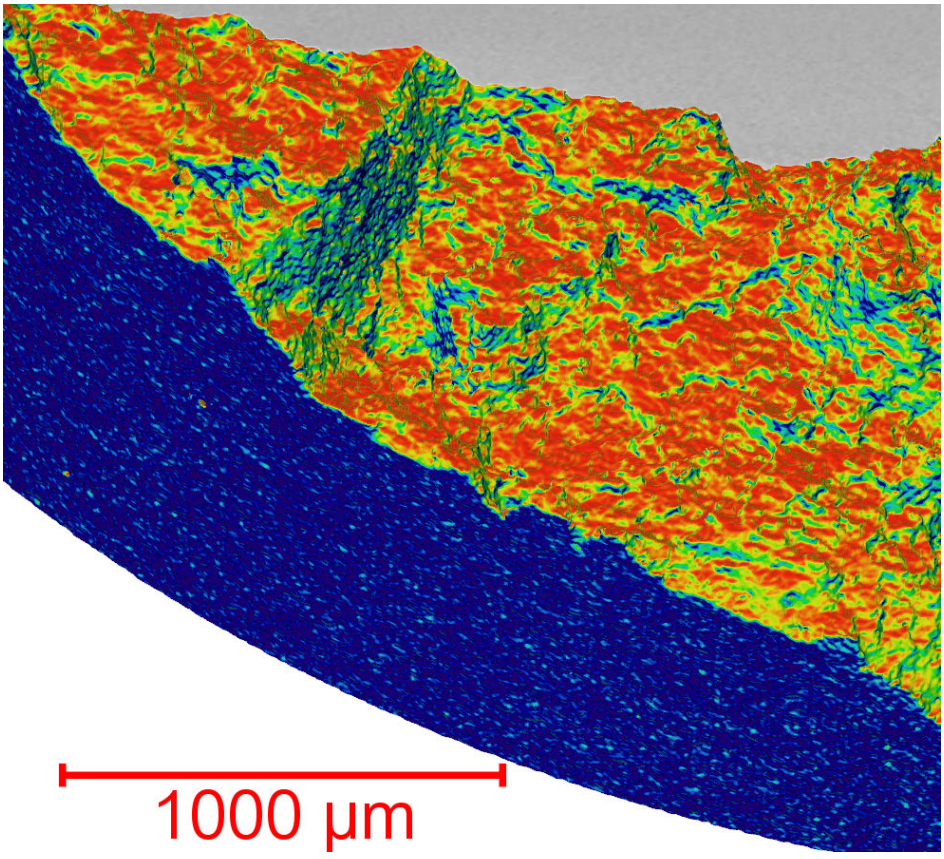

(c) 3D view of topography of surface by tomography reconstruction

FIGURE 4.42 – Steady-crack propagation: defect interactions (Specimen 67T5: $\Delta\varepsilon/2 = \pm 0.3\%$, $R_\varepsilon = -1$, 200 °C, $N_f = 1567$)

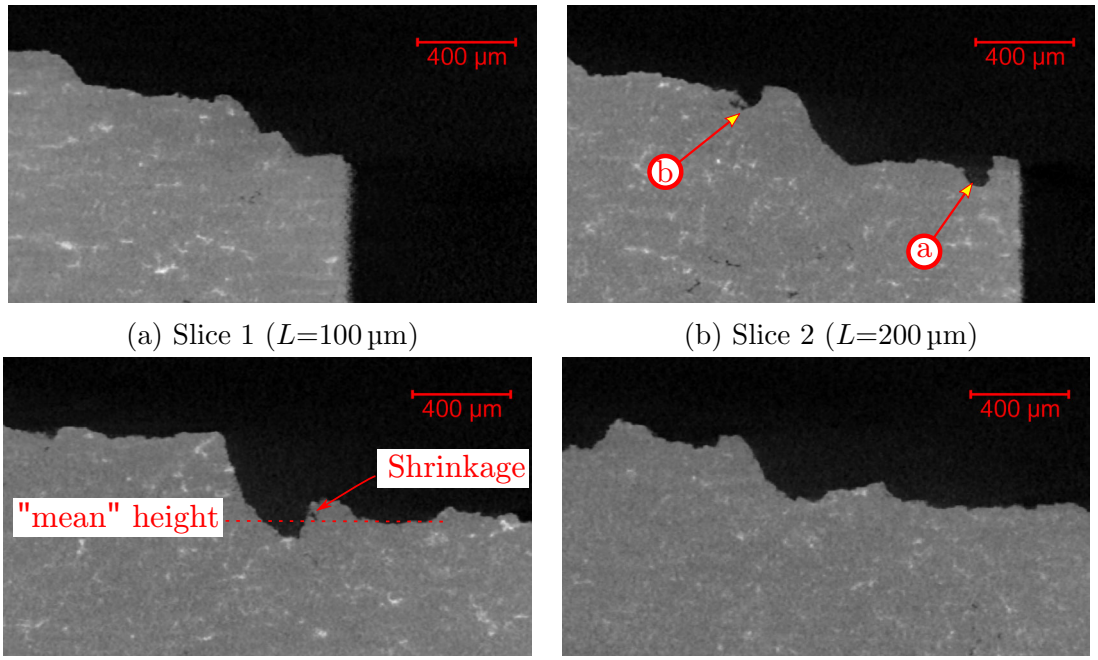

(a) Slice 1 (L=100 µm)

(b) Slice 2 (L=200 µm)

(c) Slice 3 (L=400 µm)

(d) Slice 4 (L=900 µm)

FIGURE 4.43 – Steady-crack propagation: evolution of the crack coalescence thread as a function of depth from free edge L (Specimen 67T5: $\Delta\varepsilon/2 = \pm 0.3\%$, $R_\varepsilon = -1$, 200 °C, $N_f = 1567$ cycles)

4.3.5 Effect of temperature on the crack propagation mechanisms

Steady crack propagation mechanisms

Differences are first studied by comparing general steady-crack propagation surface between two specimens:

— At ambient temperature (see Figure 4.44a), as previously described in Section 4.3.3, large areas of the fracture surface exhibit the propagation mechanisms in the aluminium dendrites.

— At higher temperatures (200 °C, see Figure 4.44b), the mechanisms are mainly identical. However, the comparison reveals a lower surface fraction of fractured dendrites, and higher fraction of rough eutectic zones. The flat surfaces of sliced aluminium dendrite cells are smaller.

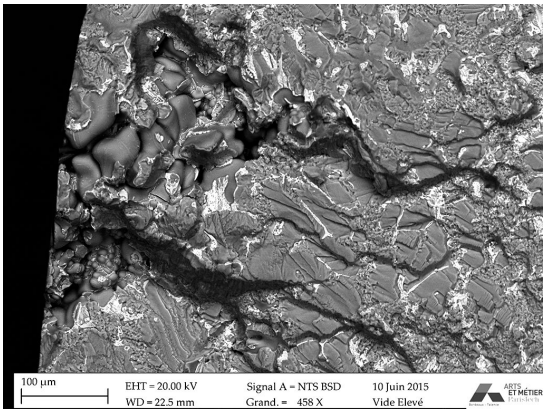

(a) SEM-BSE of fracture surface (Specimen 87T5: $\Delta\varepsilon/2 = \pm 0.3\%$, $R_\varepsilon = -1$, 20 °C, $N_f = 2904$ cycles)

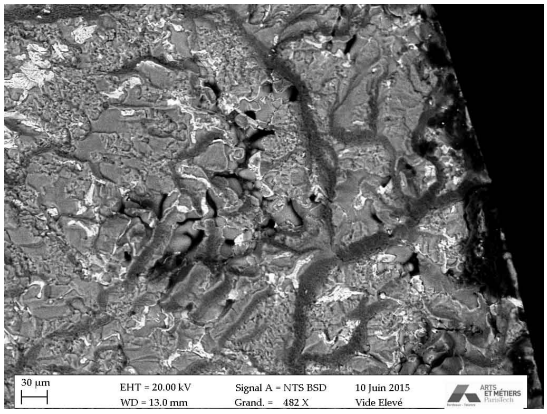

(b) SEM-BSE of fracture surface (Specimen 71T5: $\Delta\varepsilon/2 = \pm 0.3\%$, $R_\varepsilon = -1$, 200 °C, $N_f = 2622$ cycles)

FIGURE 4.44 – Effect of temperature on steady-crack propagation (same figure scales)

The same comparison can be emphasized in Figure 4.45. Crack in Figure (a), at ambient temperature, appears flatter than at higher temperature (crack in Figure (b)). It is worth noting despite the different mechanisms, the total fatigue life (N_f) only slightly decreases with temperature increase.

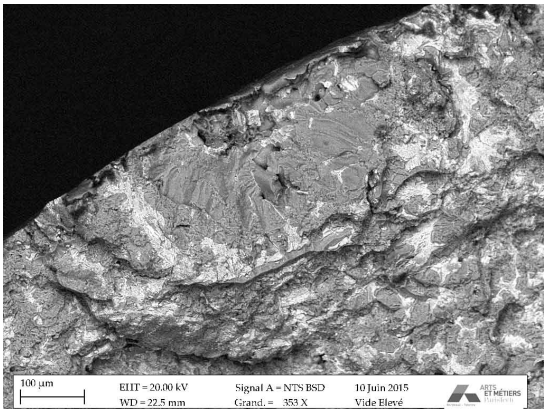

(a) SEM-BSE of fracture surface (Specimen 87T5: $\Delta\varepsilon/2 = \pm 0.3\%$, $R_\varepsilon = -1$, 20 °C, $N_f = 2904$ cycles)

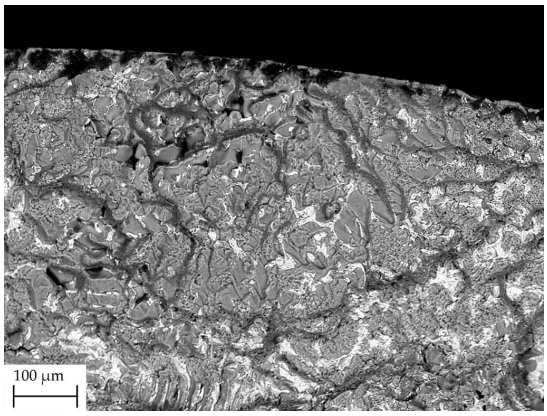

(b) SEM-BSE of fracture surface (Specimen 71T5: $\Delta\varepsilon/2 = \pm 0.3\%$, $R_\varepsilon = -1$, 200 °C, $N_f = 2622$ cycles)

FIGURE 4.45 – Effect of temperature on steady-crack propagation: small cracks (same figure scales)

Crack coalescence

Figure 4.46 shows the kinetic of crack interaction at ambient temperature (Specimen 76T5: $\Delta\varepsilon/2 = \pm 0.4\%$, $R_\varepsilon = -1$, 20 °C, $N_f = 734$). In Figure 4.46b, the main crack and a secondary crack can be seen. The two crack seem to start coalescing, and the crack tip branches to propagate through a ligament at 45° caused by the interaction of the crack tips generated stress fields. However, the mode I crack opening strength is higher, and the crack once again branches (see Figure 4.46c) and returns to a propagation normal to loading direction. Another possible explanation is the 3D aspect of the crack, which could drive the crack back to a normal to loading direction. Finally, Figure 4.46d shows the effect of final stages of main crack propagation: the secondary crack appears to close. Every image being taken at maximum cyclic imposed strain, this is the effect of local unloading due to main crack.

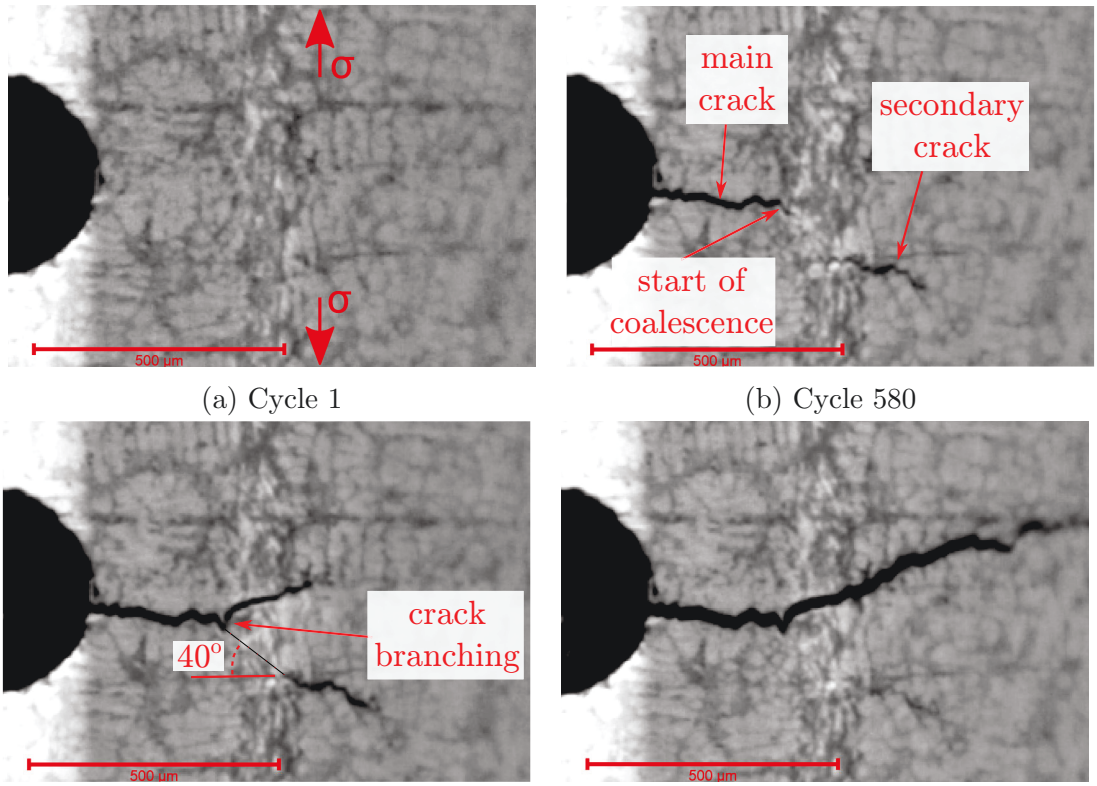

(a) Cycle 1 (b) Cycle 580

(c) Cycle 683 (d) Cycle 726

FIGURE 4.46 – Crack propagation monitoring: branching crack mechanism (Specimen 76T5: $\Delta\varepsilon/2 = \pm 0.4\%$, $R_\varepsilon = -1$, 20 °C, $N_f = 734$ cycles)

Figure 4.47 shows a similar initial configuration of both the main crack and the secondary one at high temperature (Specimen 89T5: $\Delta\varepsilon/2 = \pm 0.4\%$, $R_\varepsilon = -1$, 250 °C, $N_f = 701$). Figure 4.47b shows the two cracks configuration before coalescence. Like in the previous case at ambient temperature, interaction between the cracks starts when opposing crack tips are around 45° from the axial loading direction. However, with the higher plastic strain caused by the elevated temperature, the ligament cracks and both cracks coalesce.

This coalescence is further studied by analysing the crack post-mortem by SEM. Figure 4.48 displays the surface and the crack ligament. Specifically, in Figure 4.48b, label (a) shows an aluminium dendrite cell which displays intense plastic deformation due to the cracks interaction. For label (b) however, in the eutectic zone, the crack

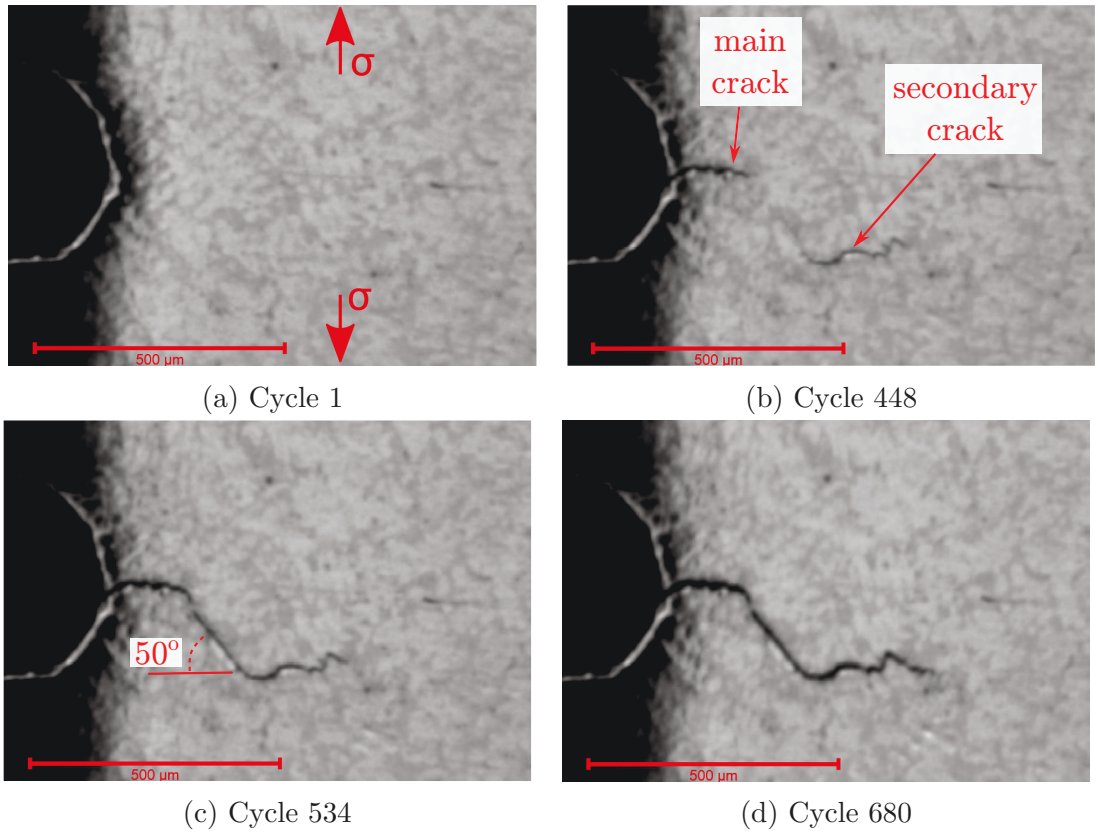

(a) Cycle 1 (b) Cycle 448

(c) Cycle 534 (d) Cycle 680

FIGURE 4.47 – Crack propagation monitoring: coalescence crack mechanism (Specimen 89T5: $\Delta\varepsilon/2 = \pm 0.4\%$, $R_\varepsilon = -1$, 250 °C, $N_f = 701$ cycles)

appears sharper with a higher surface fracture roughness. This is shown in details in Figure 4.49 by SEM-SE1 imaging. The different crack propagation regions have distinct features. The dendritic crack propagation appears blunt and the crack path linear, corresponding to high plastic strain accumulation. Propagation through the eutectic phase however, appears sharper (very little interaction with the neighbouring areas) and rough. The roughness features are in the order of magnitude of the Si particles, making them a probable cause of the surface aspect.

High temperature mechanisms and defect interaction

As can be seen in the previous Section, crack/defect interaction is crucial for the highest temperature (250 °C). This can be observed by analysing interrupted fatigue tests. While for lower temperatures, crack opening is rather small before final failure which occurs in a single cycle (thereby making tomography thresholding of the crack complicated), at high temperature, the more ductile final failure occurs in several cycles. This can be seen in Figure 4.50. For this specimen with an artificial defect, the crack leading to failure appeared elsewhere, and the crack monitoring test captures the final failure. Two cracks preceding the final failure can also be seen in Figure 4.50d, emphasizing the crack interaction with defects (the preceding cracks probably started on other defects).

By analysing a specimen interrupted before final failure by tomography, defect interaction with crack can be seen in Figure 4.51. The method applied is similar to that of Zhang et al. [2007]: the crack is thresholded and the crack opening displacement measured. In presence of defects, the measured displacement is the sum of displace-

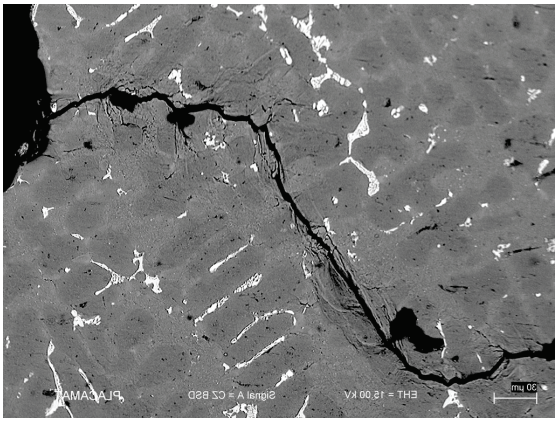

(a) SEM-BSE of crack on edge surface: raw image

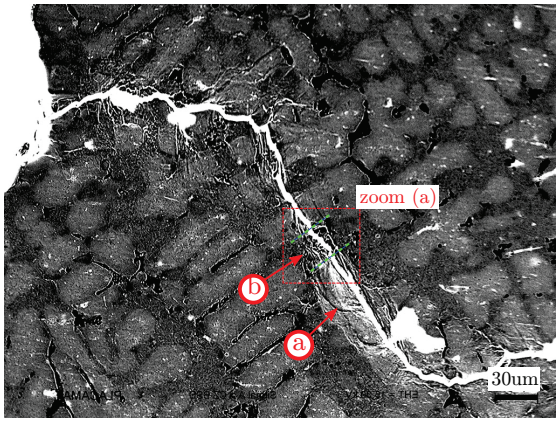

(b) SEM-BSE of crack on edge surface: inverted image and increased contrast

FIGURE 4.48 – Coalescence of cracks by propagation in ligament, zoom (a) is Figure 4.49 (Specimen 89T5: $\Delta\varepsilon/2 = \pm 0.4\%$, $R_\varepsilon = -1$, 250 °C, $N_f = 701$ cycles)

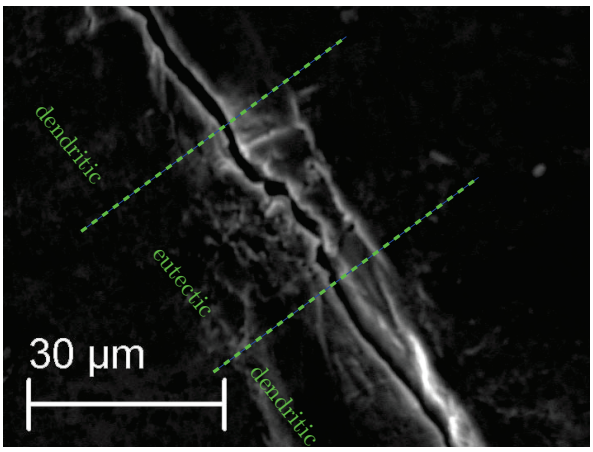

FIGURE 4.49 – SEM-SE1 image of crack coalescence (Specimen 89T5: $\Delta\varepsilon/2 = \pm 0.4\%$, $R_\varepsilon = -1$, 250 °C, $N_f = 701$ cycles)

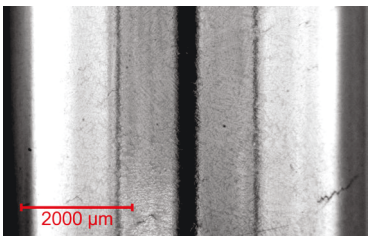

(a) Cycle 3800

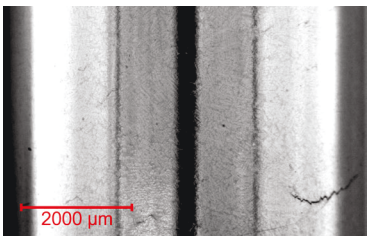

(b) Cycle 4000

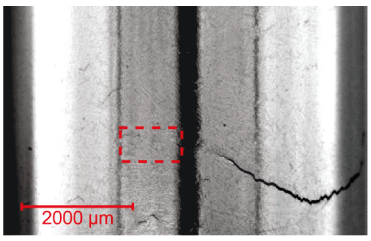

(c) Cycle 4120 (N_f)

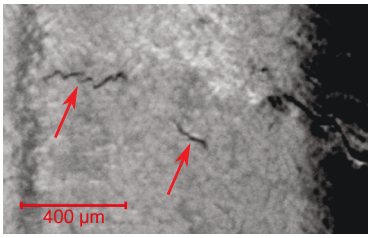

(d) Cycle 4120: zoom

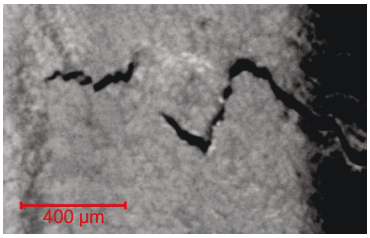

(e) Cycle 4130: zoom

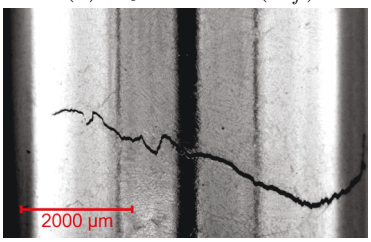

(f) Cycle 4180

FIGURE 4.50 – Final fatigue failure (Specimen 29T5: $\Delta\varepsilon/2 = \pm 0.25\%$, $R_\varepsilon = -1$, 250 °C, $N_f = 4100$ cycles)

ment and defect height, causing defects to appear red on the map. Several defects can be seen for all crack advances. Especially, for the latter stages of crack propagation, defects influence the crack path for larger scales ($\approx 1\,\mathrm{mm}$). This can be seen on the corresponding slice (see Figure 4.51b) which displays a defect (label (a) in Figure 4.51) which strongly influences the crack path.

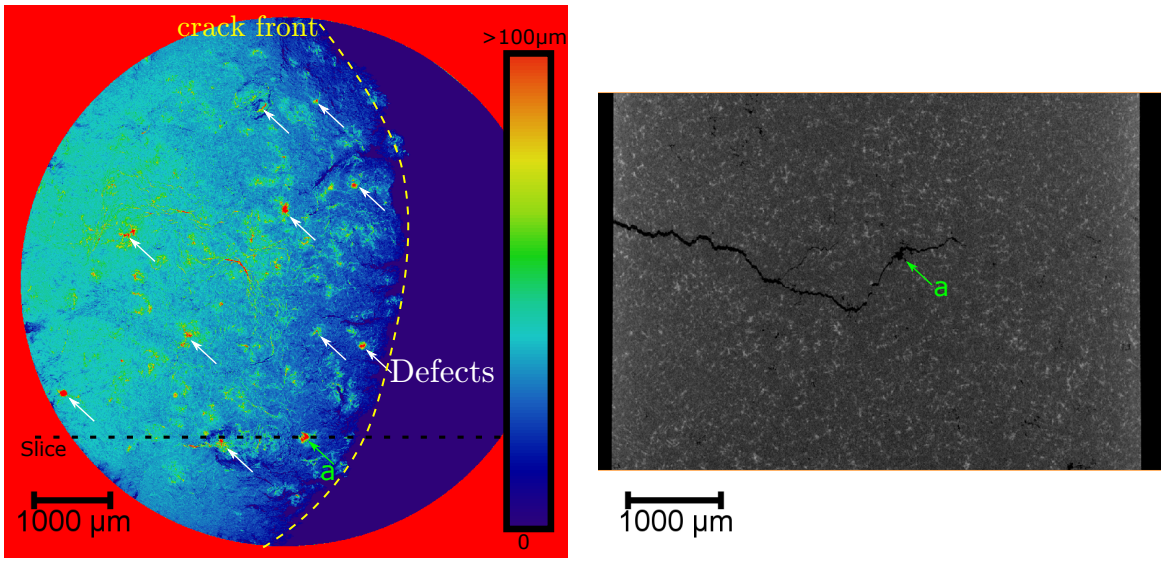

(a) Crack opening displacement

(b) Long distance defect interaction

FIGURE 4.51 – Crack opening displacement showing interactions of the main crack with defects. (specimen 62T5, $\Delta\varepsilon/2 = \pm 0.3\%$, $R_\varepsilon = -1$, $250\,^\circ\mathrm{C}$, $N_f = 2089$ cycles)

4.3.6 Conclusions and surface analysis

Fractured surface tomographies are shown in Figures 4.52, 4.53, 4.54 and 4.55 and summarize the different observations done, as well as the influence of temperature.

For $T = 20\,°C$, crack initiation can clearly be identified (indicated by (i) in Figure 4.52). The steady-state crack propagation area clearly appears smoother and flatter than the fast fracture region. For specimen 88T5 (see Figure 4.52a), the test displays low plasticity ($N_f = 10823$ and $\Delta\varepsilon_p/2 = 2.810^{-4}$), hence the very flat section of the steady-crack surface.

For $T = 150\,°C$, the crack initiation region can still be clearly identified (the exact initiation area noted (i) is done by SEM imaging). However, with the higher temperature, the boundary between steady crack and fast fracture is less obvious. Figure 4.53a also shows smaller cracks on the fractured surface (corresponding to (ii) and (iii)), that were discussed in Section 4.3.2. They initiate early in the fatigue life, and coalesce only at final failure. For the higher imposed strain amplitude (see Figure 4.53b), the transition from steady crack to final failure appears for a smaller crack size. This observation can be done for all the different temperatures (except for the highest temperature, where the separation of crack stages cannot be clearly identified).

For $T = 200\,°C$, defect interaction cannot be neglected before explaining the cracked surface. For an imposed strain amplitude of $\Delta\varepsilon/2 = \pm 0.30\%$ (Figure 4.54b, corresponding to the case study detailed in Section 4.3.4) two distinct initiation sites can be detected (sites (i) and (ii)). The first site (i) is a gas round porosity of 126 µm Feret diameter, right at the specimen edge. It has propagated further than the second initiation site (ii), which is also a gas porosity. While larger (233 µm of Feret diameter), this second defect (ii) is further from the surface, which concurs with the harmfulness of edge defect established in Section 4.2.4.

For $T = 250\,°C$, fractography analysis is more complex. Due to the high level of plasticity, the fractured surface of steady-state crack propagation is very rough and the clear scenario of crack propagation is hard to establish. Even by using SEM observation, clear distinction of steady crack and final failure cannot be identified. Although, in Figure 4.55a, a semi-circular initiation zone can be seen (area (i)), Section 4.3.5 has shown that the crack path strongly interacts with defects, causing the high surface roughness. Surface observations of the higher temperature crack propagation shown in Section 4.3.5 provide first insights on this interaction: plasticity ligament develops between neighbouring cracks and coalesce at acute angles. In future work, tomography analysis of interrupted tests could be used to analyse these mechanisms in 3D, or 3D in-situ tests such as Dezecot et al. [2016].

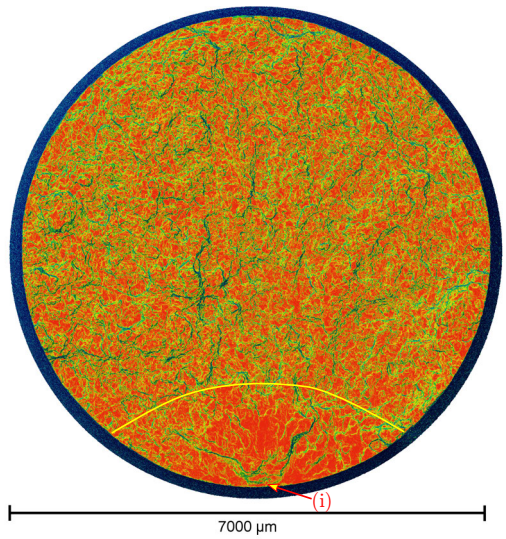

(a) specimen 88T5, $\Delta\varepsilon/2 = \pm 0.25\%$, $R_\varepsilon = -1$, 20 °C, $N_f = 10823$ cycles

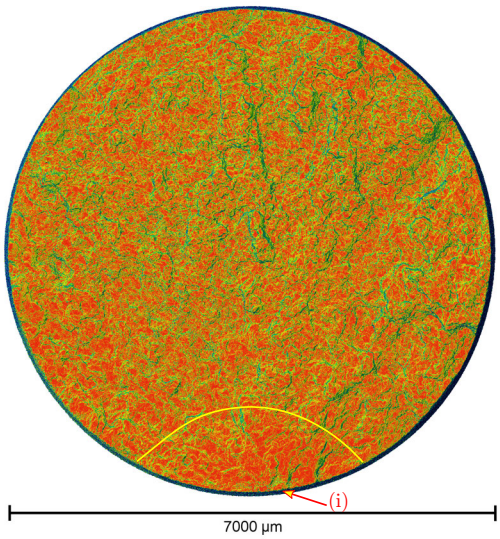

(b) specimen 87T5, $\Delta\varepsilon/2 = \pm 0.30\%$, $R_\varepsilon = -1$, 20 °C, $N_f = 2904$ cycles

FIGURE 4.52 – Tomography surface analysis for T=20 °C

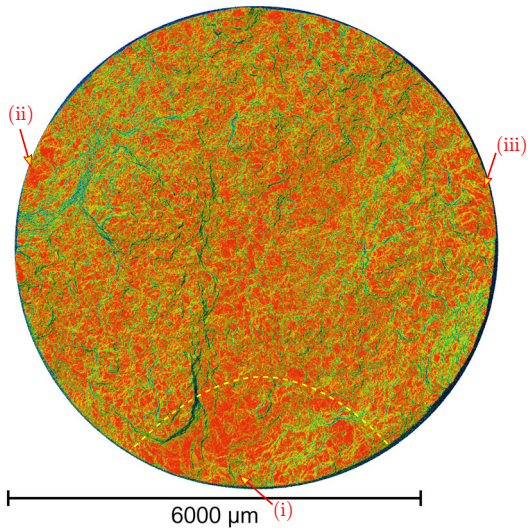

(a) specimen 14T5, $\Delta\varepsilon/2 = \pm 0.25\%$, $R_\varepsilon = -1$, 150 °C, $N_f = 6950$ cycles

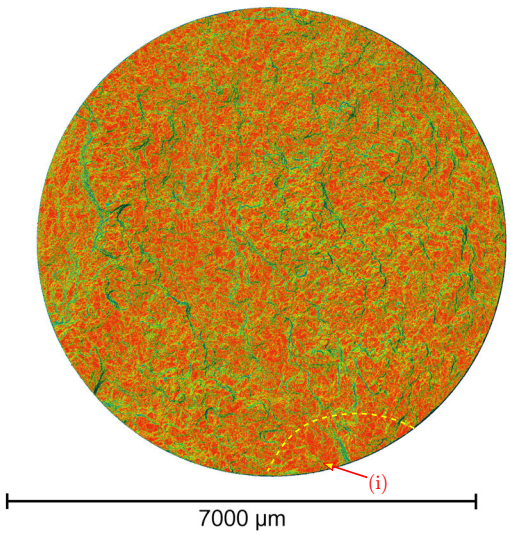

(b) specimen 28T5, $\Delta\varepsilon/2 = \pm 0.30\%$, $R_\varepsilon = -1$, 150 °C, $N_f = 2756$ cycles

FIGURE 4.53 – Tomography surface analysis for T=150 °C

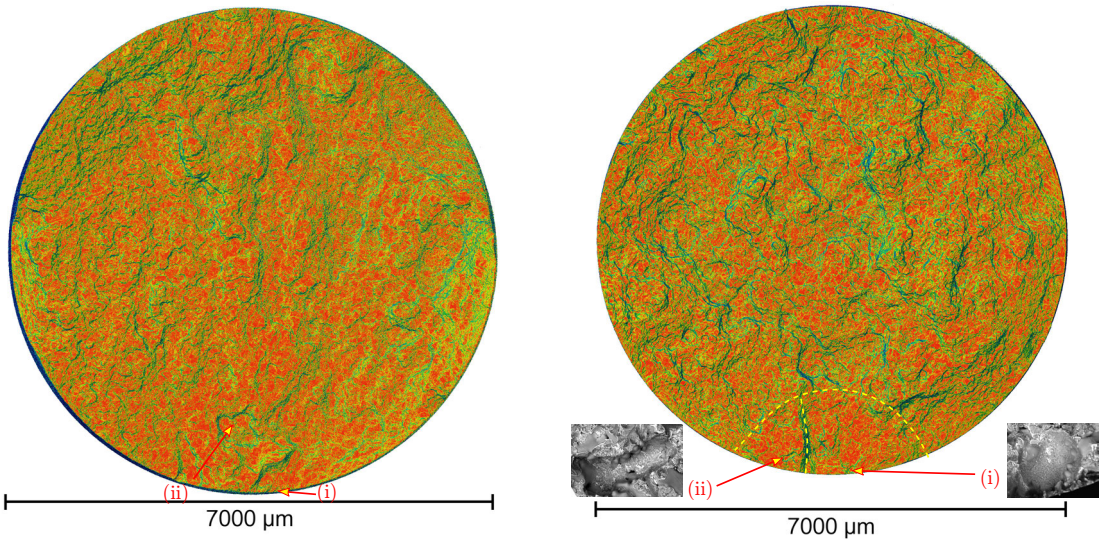

(a) specimen 49T5, $\Delta\varepsilon/2 = \pm 0.25\%$, $R_\varepsilon = -1$, 200 °C, $N_f = 3383$ cycles

(b) specimen 67T5, $\Delta\varepsilon/2 = \pm 0.30\%$, $R_\varepsilon = -1$, 200 °C, $N_f = 1560$ cycles

FIGURE 4.54 – Tomography surface analysis for T=200 °C

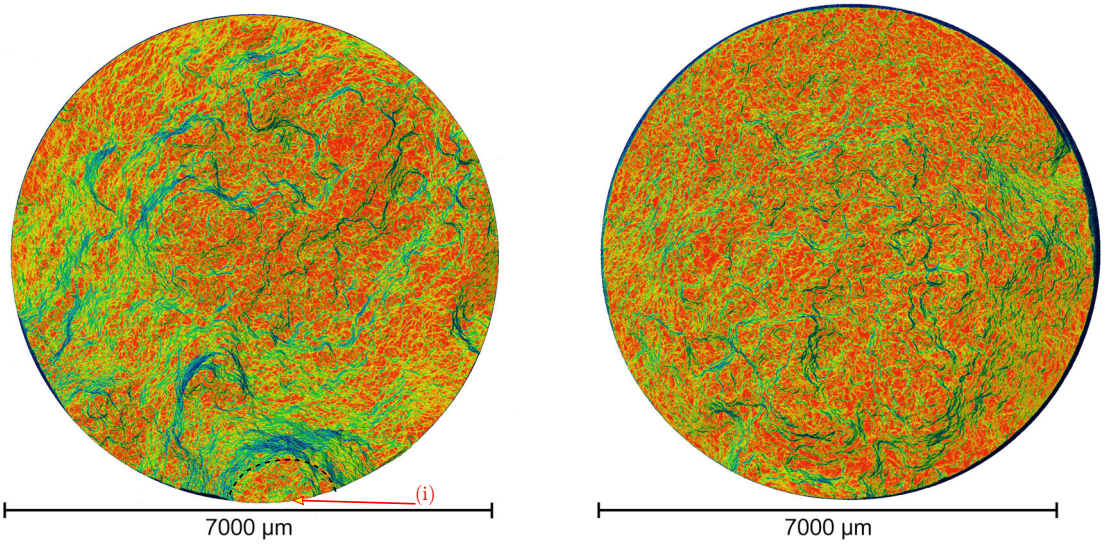

(a) specimen 133T5, $\Delta\varepsilon/2 = \pm 0.25\%$, $R_\varepsilon = -1$, 250 °C, $N_f = 3480$ cycles

(b) specimen 48T5, $\Delta\varepsilon/2 = \pm 0.30\%$, $R_\varepsilon = -1$, 250 °C, $N_f = 1511$ cycles

FIGURE 4.55 – Tomography surface analysis for T=250 °C

Chapitre 5

Numerical simulations

In this chapter, numerical specimens containing representative defect populations are generated to correlate with the observed critical defects. Study of the impact of volume size as well as the spatial statistics point process choice (Random or clustered defects) are conducted. Then, a crack propagation model is used to derive the fatigue life based on the observed defects, subsequently allowing for a virtual fatigue life estimation based on numerical defects.

5.1 Extreme value statistics

5.1.1 Theory of sample maxima

Let $X_1, X_2, ..., X_n$ be n independent and identically distributed random variables of probability distribution function (pdf) f_X and cumulative distribution function (cdf) F_X.

Let $M_n = \max\{X_1, ..., X_n\}$ be the maximum of the n random variables, the exact maximum distribution can be derived:

$$\Pr(M_n \leq y) = \Pr(X_1 \leq y, ..., X_n \leq y) = F_X(y)^n = G_X(y) \tag{5.1}$$

For the study of defects, f_{gpd} is the defect size distribution (i.e. the generalized Pareto distribution identified in Section 2.3.3, whose parameters are reminded in Table 5.1):

$$f_{gpd}(x) = \frac{1}{\sigma_{gpd}} \left(1 + \frac{\xi_{gpd}(x - \mu_{gpd})}{\sigma_{gpd}}\right)^{-\frac{1}{\xi_{gpd}}-1} \tag{5.2}$$

and F the corresponding cdf:

$$F_{gpd}(x) = 1 - \left(1 + \frac{\xi_{gpd}(x - \mu_{gpd})}{\sigma_{gpd}}\right)^{-\frac{1}{\xi_{gpd}}} \tag{5.3}$$

Supposing there is an identical number n of defects per specimen, the cdf of maximum defect size G_{gpd} is:

$$G_{gpd}(y) = F_{gpd}(y)^n = \left(1 - \left(1 + \frac{\xi_{gpd}(y - \mu_{gpd})}{\sigma_{gpd}}\right)^{-\frac{1}{\xi_{gpd}}}\right)^n \tag{5.4}$$

Table 5.1 – Parameters of the fitted generalized Pareto distribution filtered at 40 µm, the thresholding parameter μ_{gpd} is imposed while σ_{gpd} and ξ_{gpd} are obtained by maximum likelihood estimation.

parameter	value
σ_{gpd}	15.51
ξ_{gpd}	0.2159
μ_{gpd}	40

The number of defects per specimen is critical to derive the maximum size distribution G. This is shown in Figure 5.1. For $n = 1000$ defects to $n = 10000$, the median goes from 315 µm to 540 µm (as can also be seen in Figure 5.2), and the 95% percentile (i.e. the 5% of larger defects) from 575 µm to 960 µm.

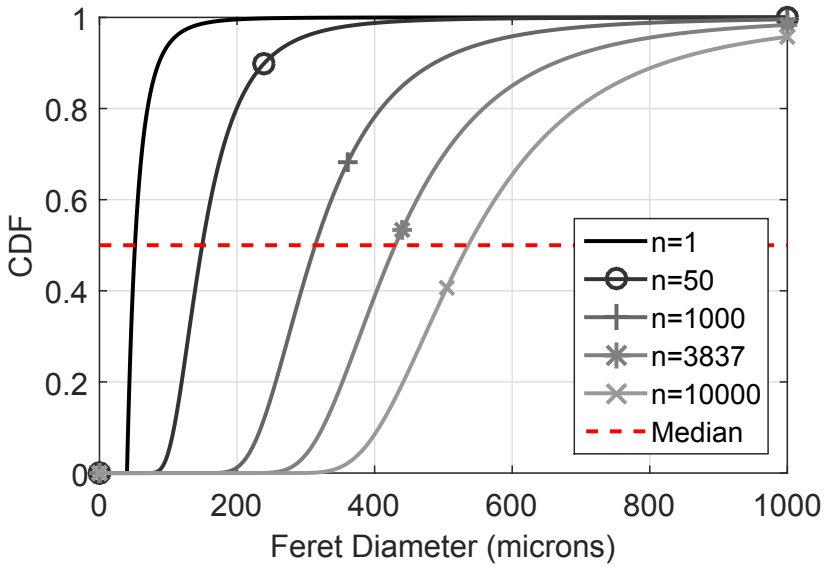

FIGURE 5.1 – Cumulative distribution function of maximum defect size G_{gpd} for different number of defects per specimen n. 3837 is the number of defects for the fatigue tested zone volume if considered proportional to the analysed volume.

5.1.2 Number of defects per sample

In order to study the number of defects per numerical sample, the spatial distributions fitted in Section 2.4 are used.

Cylindrical sample

Given a sample geometry of volume $|W|$ (corresponding to the cylindrical fatigue tested zone, $|W| = 461\,\mathrm{mm}^3$), the number of defects per sample depends on the spatial point process chosen:

— Homogeneous distribution (see Figure 5.3a): the deterministic number of defects n is proportional to the volume of the sample. The defect concentration is the same as the intensity λ identified in the point process statistics (see Section 2.4.4:

$$\lambda = 8.31\,\mathrm{mm}^{-3} \tag{5.5}$$

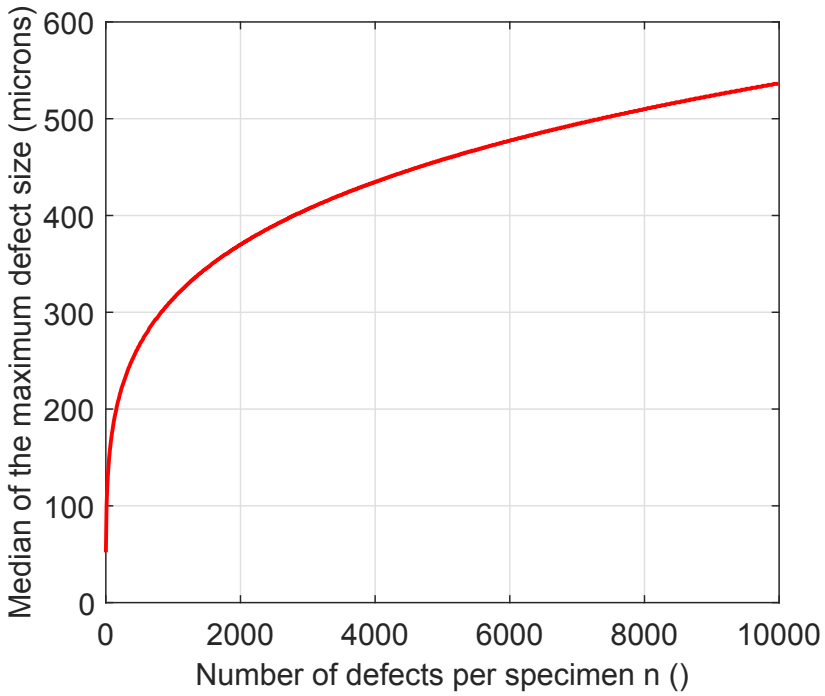

FIGURE 5.2 – Median size of maximum defect size as a function of number of defects per specimen n.

and the number of defects per sample is therefore:

$$n = \lambda |W| = 3837 \tag{5.6}$$

— Poisson distribution (see Figure 5.3b): the number of defects in a sample is the realization of a Poisson distribution. The variable n is therefore a random one:

$$n \sim \mathcal{P}(\lambda |W|) \tag{5.7}$$

where $\mathcal{P}$ is the Poison distribution, λ the process intensity ($\lambda = 8.31\,\mathrm{mm}^{-3}$) and $|W|$ the window volume

— Clustered point process (see Figure 5.3c): the number of defects per sample depends on the parameters of the point process and the geometrical shape of the sample. Each sample has to be numerically simulated, and the generated defects counted.

The different empirical cumulative distributions of number of defects are shown in Figure 5.4, and some characteristic statistical values in Table 5.2. The homogeneous and the Poisson point process provide analytical values, whereas for the clustered processes, the different distributions and values were obtained by simulating 10000 samples.

The deterministic homogeneous method and the Poisson process provide similar results, with only a slight variance for the Poisson process. Using the clustered point processes (Matérn or Thomas), the variance increases drastically. This increase can be explained by the variable number of parent points. For the Thomas point process, the parent point process intensity λ_p is:

$$\lambda_p = 0.0305\,\mathrm{mm}^{-3} \tag{5.8}$$

The Poisson distribution of the number of parents n_p is therefore of parameter $\bar{p}$:

$$\bar{p} = \lambda_p |W| = 14.1 \tag{5.9}$$

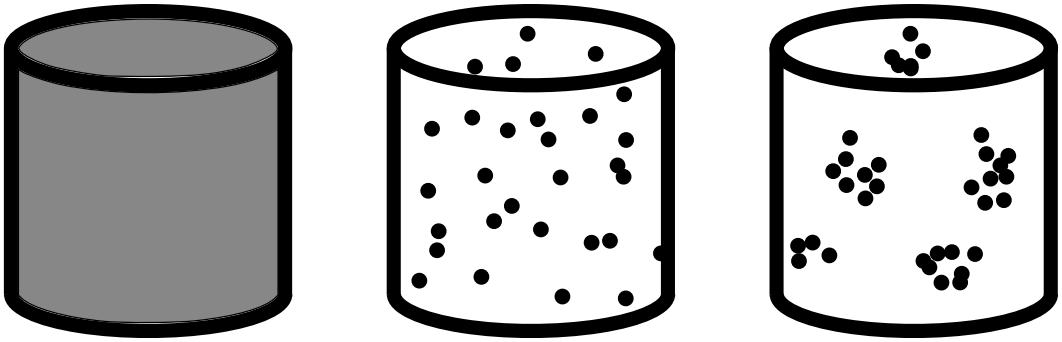

(a) Homogenous defect distribution: the number of defects per sample is deterministically proportional to the specimen volume.

(b) Poisson defect distribution: the number of defects per sample is a realization of a Poisson distribution.

(c) Clustered defect distribution: each sample has to be numerically simulated to account for the geometrical effect on the number of defects per sample.

FIGURE 5.3 – Methods of simulation of defect population.

i.e. there are 14.1 parents per sample in average. The standard deviation σ_{n_p} of the Poisson distribution can also be calculated:

$$\sigma_{n_p} = \sqrt{\lambda_p |W|} = 3.75 \tag{5.10}$$

The number of children per parent has a mean value $\bar{c} = 272.8$ and a standard deviation σ_c:

$$\sigma_c = \sqrt{\bar{c}} = 16.52 \tag{5.11}$$

The total number of points being the product of the number of parent points by the number of children (both random variables being independent), the standard deviation of the total number of points σ_n can be calculated by:

$$\sigma_n^2 = \sigma_{n_p}^2 \sigma_c^2 + \bar{p}^2 \sigma_c^2 + \bar{c}^2 \sigma_{n_p}^2 \tag{5.12}$$

Which numerically is:

$$\sigma_n = 1048.1 \tag{5.13}$$

The discrepancy with the observed value (950.3) can be explained by two factors. Firstly, for the simulations, parent points outside the sample could generate children points inside the sample (this is overcome by simulating a larger sample from which the sample of interest is taken). Secondly, some parent points generate children points outside the sample of interest which are not counted.

Similarly, for the Matérn point process, the calculated approximate variance 1020.8 is close to the descriptive statistic value of 894.3.

Ring sample

As was observed in Section 4.2.4, the initiating defects are all located at a distance lower than 263 µm from the specimen surface. To investigate this effect, ring numerical specimen are created (see Figure 5.5). In this thought experiment, the defects in the

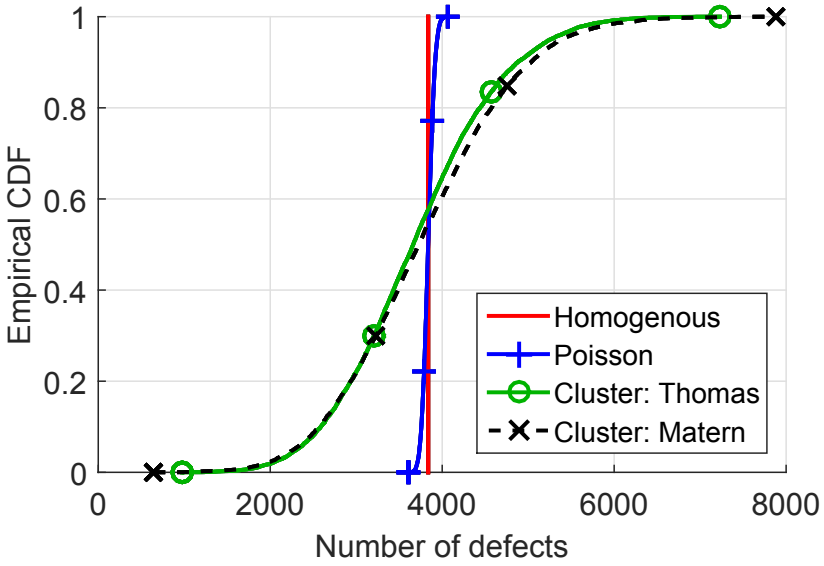

FIGURE 5.4 – Cylindrical sample: empirical cumulative distribution function (CDF) of number of defects per sample for different simulation methods. The estimates are based on 10000 simulated samples.

Table 5.2 – Cylindrical sample: descriptive statistics of the number of defects per sample.

Method	Mean $\bar{n}$	Standard deviation σ_n
Homogeneous	3837	0
Poisson	3836.5	62.1
Clustered: Matérn	3695	894.3
Clustered: Thomas	3735.7	950.3

center cylinder (of radius R_{min}) are omitted, and only the defects of the outside rim ($R_{min} < r < R$, with $R = 3.5\,\text{mm}$ the specimen radius) are considered.

For the numerical value of $R - R_{min}$, a value of $300\,\mu\text{m}$ is taken. The difference between the "distance to surface" parameter and $R - R_{min}$ is noteworthy: the distance to the surface is defined as the shortest distance from the defect contour to the specimen surface, while the distance $R - R_{min}$ encompasses the maximal distance from the specimen surface to the numerical defect center.

The sample volume $|W|$ is therefore:

$$|W| = \pi(R^2 - R_{min}^2).h = 75.8\,\text{mm}^3 \tag{5.14}$$

h being the height of the sample. The ring sample is approximately six times smaller than the cylindrical sample.

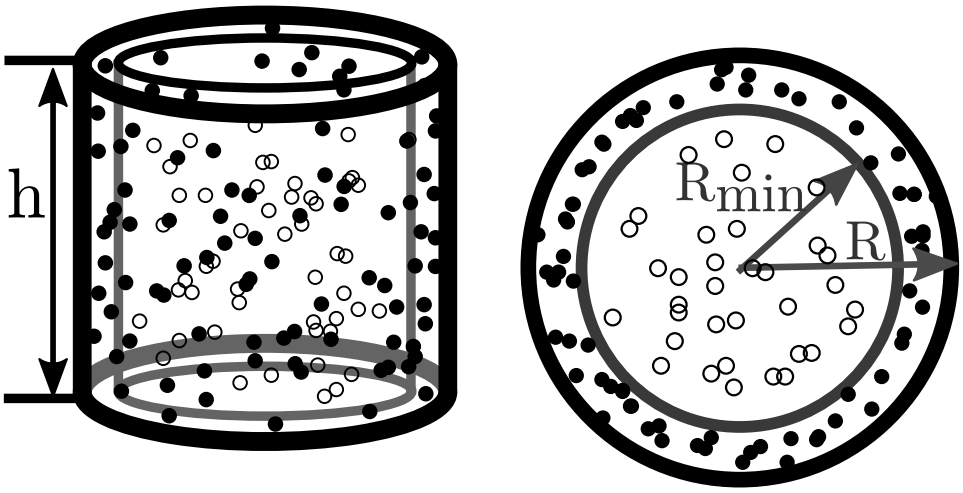

(a) 3D representation of the specimen (b) Top view of the specimen

FIGURE 5.5 – Ring sample: numerical defects are created in the cylindrical sample, but only the ones on the outside ring (•), and not in the center cylinder (o), are used.

As in the previous Section 5.1.2, four different simulation methods are used: homogeneous, Poisson, Matérn and Thomas. For the clustered processes, 10000 samples are simulated to derive the empirical CDF (see Figure 5.6), and the statistical values (see Table 5.3).

Similar conclusions to the ones observed for the cylindrical samples can be drawn: the clustered processes drastically increase the standard deviation while the mean value is only slightly modified.

Table 5.3 – Ring sample: descriptive statistics of the number of defects per sample.

Method	Mean $\bar{n}$	Standard deviation σ_n
Homogeneous	629	0
Poisson	629.3	25.6
Clustered: Matérn	617.6	220.7
Clustered: Thomas	607.1	153.1

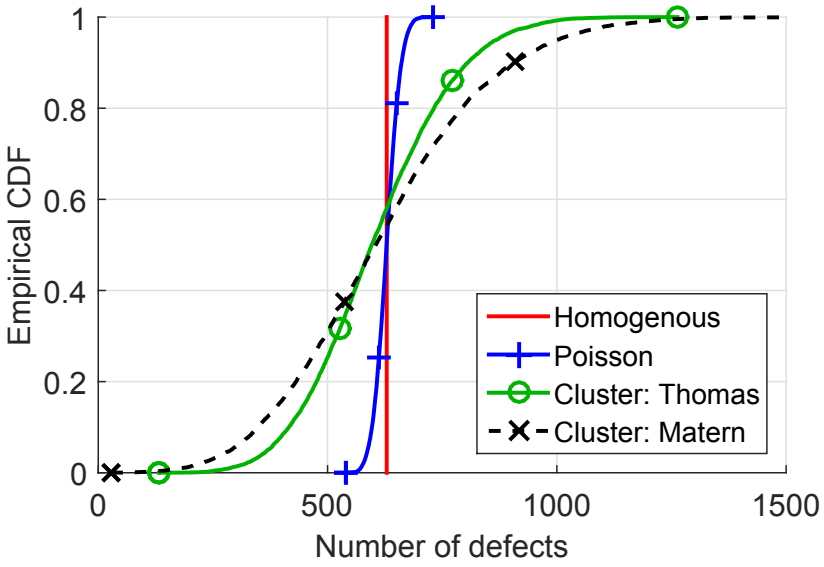

FIGURE 5.6 – Ring sample: empirical cumulative distribution function (CDF) of number of defects per sample for different simulation methods. The estimates are based on 10000 simulated samples.

5.1.3 Defect size sample maxima

Given the size distribution of defects per sample and the independence of the spatial distribution (see Section 2.4.5), the numerical method enables to simulate a maximum defect size for each sample. The goal being the comparison with the observed data, a conversion of the Feret diameter from 3D to 2D is done. Indeed, the simulated data is generated according to the tomographic data, in 3 dimensions. However, on the observed fractured specimens, only a 2D Feret diameter can be measured, and 3D defects are approximated by 2D defects:

Figure 5.7 shows an example of this conversion is done:

1. A 3D Feret diameter d_{3D} is numerically generated following the size distribution identified in Section 2.3.3 and corresponding to what could be measured by tomography.
2. Given the randomness of the 3D Feret diameter angle α, for each 3D Feret diameter, such a random angle is generated with respect to the plane (x, y), where z is the loading direction.
3. For each 3D Feret diameter d_{3D}, a corresponding 2D Feret diameter d_{2D} is generated:

$$d_{2D} = d_{3D}. \cos \alpha \tag{5.15}$$

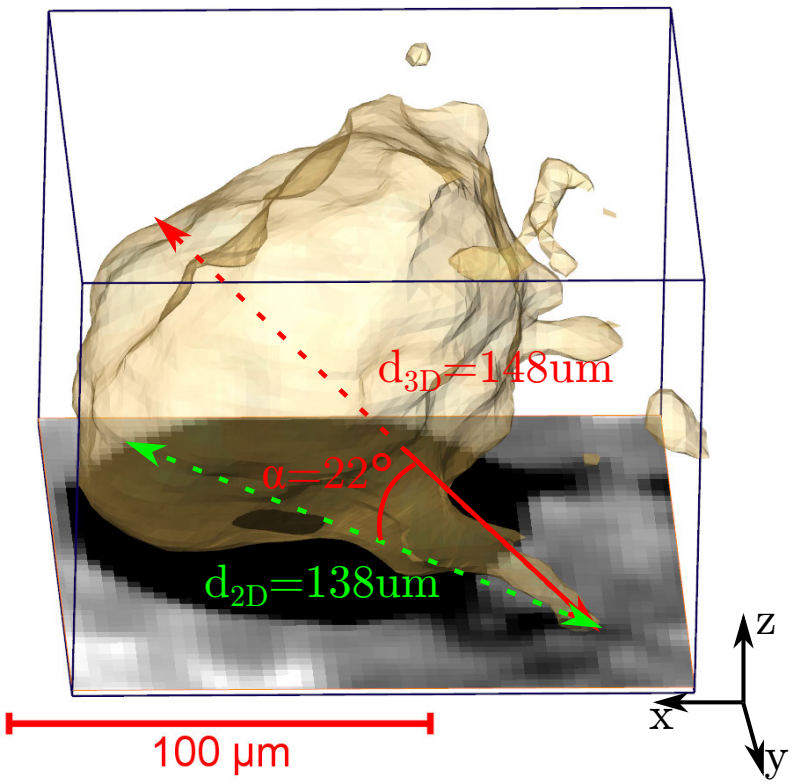

FIGURE 5.7 – Feret diameter conversion from 3D to 2D on real defect.

This method is applied to the cylindrical sample and the ring sample.

Cylindrical sample

Using the cylindrical sample defined in Section 5.1.2, the sample maxima distribution is generated for the different point processes (homogenous, poisson, Thomas and

Matérn). The results are shown in Figure 5.8. For the 4 different point processes used, the sample maxima distribution is almost identical. The higher standard deviation of the number of defects per numerical sample shown in the previous Section 5.1.2, has very little effect on the sample maxima distribution.

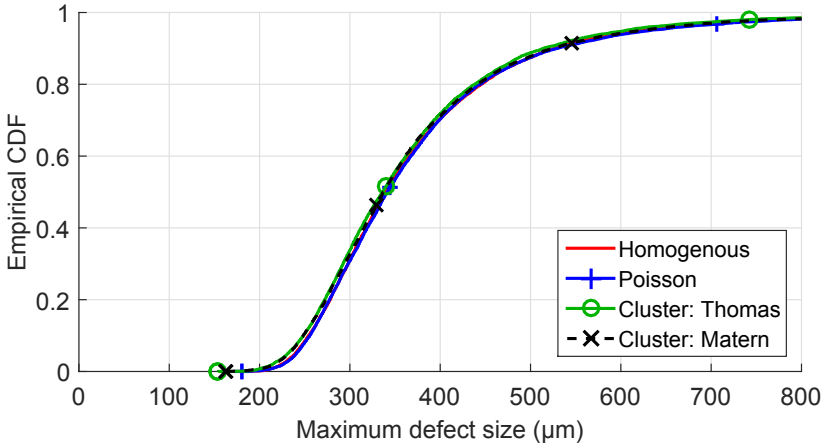

FIGURE 5.8 – Cylindrical sample: empirical Cumulative distribution function (CDF) of the largest defect per sample for different simulation methods. The estimates are based on 10000 simulated samples.

Ring sample

The sample maxima method is now applied to the ring sample defined in Section 5.1.2 for the different point processes (homogenous, Poisson, Thomas and Matérn). As for the cylindrical sample, the different point processes all provide the same results.

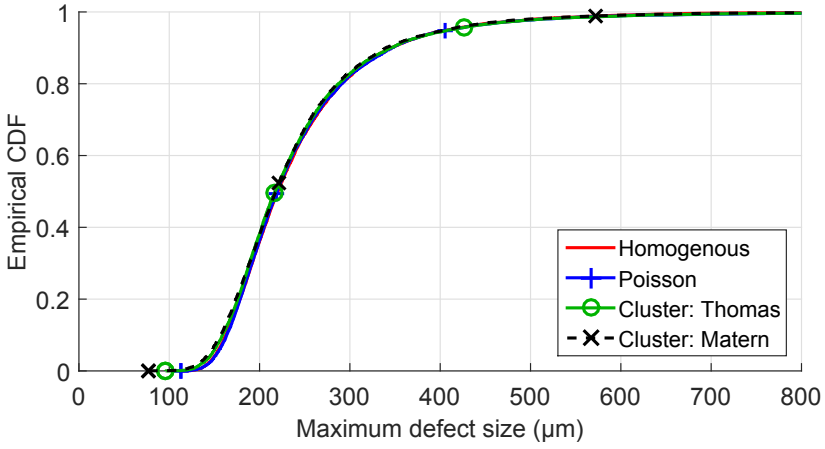

FIGURE 5.9 – Ring sample: empirical Cumulative distribution function (CDF) of the largest defect per sample for different simulation methods. The estimates are based on 10000 simulated samples.

5.1.4 Results

Using the results of the previous Section, the results on the cylindrical and ring samples are compared to the experimental results of the fatigue test results obtained in Section 4.2 (i.e. the critical defects measured on the fracture surfaces). The comparison

is shown in Figure 5.10. The differences between the simulation methods being very small, the different simulation methods are not differentiated (the reader can refer to the previous Figure 5.8 and Figure 5.9).

The cylindrical sample clearly overestimates the maximum defect size, meaning the simulated volume is too large, while the ring sample provides a good fit.

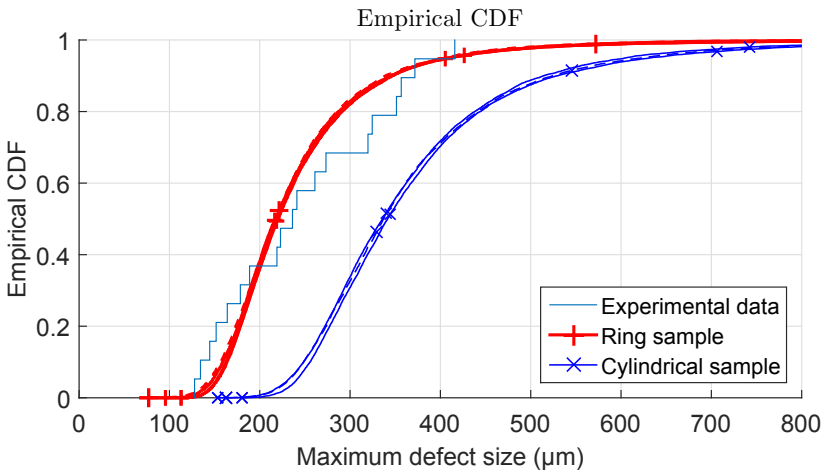

FIGURE 5.10 – Comparison of the ring and cylindrical samples sample maxima distribution to the experimentally observed defects.

In order to compare the different fittings, the different data sets are fitted with an Generalized Extreme Value distribution (GEV). An example of fitting for the homogenous process is shown in Figure 5.11. The GEV provides an excellent fit for both numerically generated samples (cylinder and ring). As is discussed in Section 4.2, given the sparse data, the GEV also provides a relatively good fit for the experimentally observed data.

The GEV obtained by fitting on the cylinder sample does not capture the experimental results, while the one obtained by the ring sample does.

For the higher values of maximum defect size (over 600 µm), further studies should be conducted in order to ascertain the tails of these extreme value distributions.

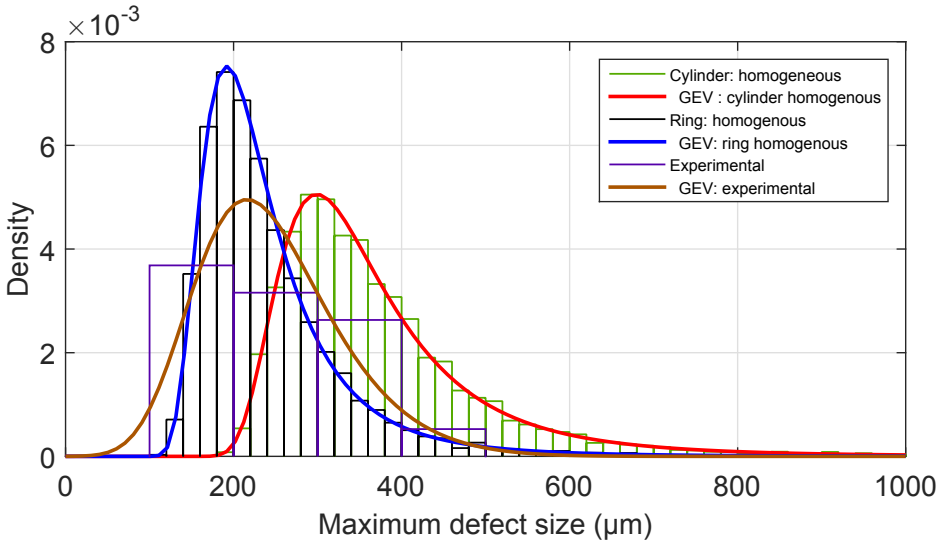

FIGURE 5.11 – GEV distribution fitting

The same distribution fitting method is applied to the other point processes. Table 5.4 shows the results of this distribution fitting. For each identified distribution, a Kolmogorov–Smirnov test hypothesis (KS-Test) is used with a 5% significance level [1].

For the ring sample, and all the point process methods, the location parameter μ is well captured, but the scale parameter σ is underestimated and the shape parameter ξ overestimated. However, given the small number of data, these parameters are estimated with a high uncertainty. For all the methods, the KS-Test fails to reject the null hypothesis, confirming the goodness of fit of the distributions.

For the cylindrical sample, all the point processes methods are rejected by the KS-Test. This demonstrates the cylindrical sample is not representative of the defect size population with respect to the crack initiation defect. While for some mechanisms, the larger the volume studied, the better the representativeness, the description of the largest defect in a sample requires an accurate estimate of the volume likely to contain a critical defect. Here, all the critical defects are close to the specimen surface, and the representative volume is the ring sample. This study also shows that the clustered aspect of defects plays only a small role in the size of the largest defect. This is due to the important size of the samples: even for the smaller ring sample, it contains in average around 600 defects. This high number of defects combined with the independence of the defect location within the sample weakens the impact of the clustering of defects compared to the random Poisson point process.

Table 5.4 – Generalized extreme value ditribution fitting of the numerical samples (cylindrical and ring specimen) and the experimentally observed defects. In parenthesis are the confidence intervals.

Data	Method	μ_{gev}	σ_{gev}	ξ_{gev}	KS-Test
Experimental		209 (±22.0)	74.5 (±17.5)	-0.0937 (±0.319)	
Ring sample					
	Homogenous	201.2	49.9	0.216	0
	Poisson	200.8	49.4	0.234	0
	Matérn	198.3	51.8	0.203	0
	Thomas	198.0	53.8	0.156	0
Cylinder sample					
	Homogenous	312.9	74.3	0.213	1
	Poisson	312.3	74.6	0.224	1
	Matérn	306.5	76.2	0.188	1
	Thomas	308.2	77.6	0.187	1

5.2 Crack propagation

In this Section, a crack propagation model is used to simulate the lifetime and to compare with the crack propagation monitored experiments. First the crack model is presented. Then, using the fatigue tests performed on smooth specimens, the model parameters are optimized. Thirdly, using the 4 crack monitored experiments, the crack model is tested. Lastly, using the sample maxima defect distribution identified in the previous Section 5.1, a probabilistic model is proposed to identify the observed scatter.

1. The test result is 1 if the test rejects the null hypothesis at the 5% significance level. The null hypothesis being that the Experimental Data comes from the distribution identified by simulation.

5.2.1 Fatigue crack growth model

The crack model is adapted from the model developed in Maurel et al. [2009] presented in Section 1.3. In this study, the energy definitions are slightly modified to be consistent with the fatigue criterion developed in chapter 3. The model uses the elastic energy ΔW_e and the plastic dissipated energy ΔW_p (defined in Section 3.3.2):

$$\Delta W_p = \int_{cycle} \underline{\underline{\sigma}} : \dot{\underline{\underline{\varepsilon}}}_p dt \tag{5.16}$$

$$\Delta W_e = \frac{1}{E}(\max_C(\mathrm{tr}\,\underline{\underline{\sigma}}))^2 \tag{5.17}$$

C being the considered cycle. The crack model propagation is:

$$\frac{1}{\lambda}\frac{da}{dN} = \left[\left(\beta_e \frac{\Delta W_e}{\gamma_e} a\right)^{m_e} + \left(\beta_p \frac{\Delta W_p}{\gamma_p} a\right)^{m_p}\right] \tag{5.18}$$

where λ is a geometric length used to rationalize the crack increment and can be linked, for example, to the grain diameter. For this study, this length normalized to $\lambda = 1\,\mathrm{m}$. Further investigations are needed to precisely evaluate this value.

In order to predict the fatigue life of the specimens, **the Feret diameter of defects measured on the fracture surfaces is considered as an initial crack length** a_0 (crack-like defect approach). The considered values of elastic energy ΔW_e and plastic dissipated energy ΔW_p are calculated at mid-life. While it is numerically possible to use all the measured cycles, using constant values for the energies allows for a rapid numerical integration of the ordinary differential equation, necessary for the parameter optimization. The fatigue life N_f of a smooth specimen can be therefore estimated by:

$$N_{f,sim} = \int_{a_0}^{a_f} \frac{da}{\frac{1}{\lambda}\frac{da}{dN}(\Delta W_e, \Delta W_p, a)} \tag{5.19}$$

where a_f is the final crack length. Given the different lengths of transition to the measured final fracture, a value of $a_f = 3\,\mathrm{mm}$ is chosen. It can be noted that the crack propagation having a exponential kinetic (see Figure 5.15), this final length has little impact on the final result.

Since all the test were done with a symmetric loading, no crack closure effect could be observed. However, for future work, this aspect could be taken into account by using only the positive part of the stress tensor.

5.2.2 Parameter optimisation

The parameters of the crack propagation model are optimized based solely on specimens where the natural crack initiating defect is measured (18 specimens). The parameters β_e (resp. β_p) and γ_e (resp. γ_p) represent the same degree of freedom for the optimisation procedure and therefore, the parameters β_e and β_p are set to 1.

The elastic part of the model can be related to the Paris Law as described in Maurel et al. [2009]:

$$\frac{da}{dN} = \left(\frac{\Delta W_e}{\gamma_e} a\right)^{m_e} \approx C\Delta K^m \approx C'(\sqrt{a})^m \approx C'(a)^{\frac{m}{2}} \tag{5.20}$$

Therefore, the elastic parameter β_e^{sur} for a semi-circular surface crack (see Broek [1986]) could also be used (consequently modifying the surface energy γ_e):

$$\beta_e^{sur} = \left(1.12\frac{2}{\pi}\right)^2 \times \pi \tag{5.21}$$

For metallic materials, the exponent m is often close to 4. To be consistent, the exponent m_e is set to 2.

In the end, the optimisation procedure aims at minimizing the cost function f:

$$f(\gamma_e, \gamma_p, m_p) = \sum_k \left(\frac{\log N_{f,sim}^k - \log N_{f,exp}^k}{\log N_{f,exp}}\right)^2 \tag{5.22}$$

where $N_{f,sim}^k$ is the simulated fatigue life of the k-th experiment and $N_{f,exp}^k$ the corresponding experimental value.

5.2.3 Results

The results are shown in Figure 5.12 and the optimised parameters in Table 5.5. All the results are in the fatigue scatter band of $N_{f,exp} \times 2$, $N_{f,exp}/2$.

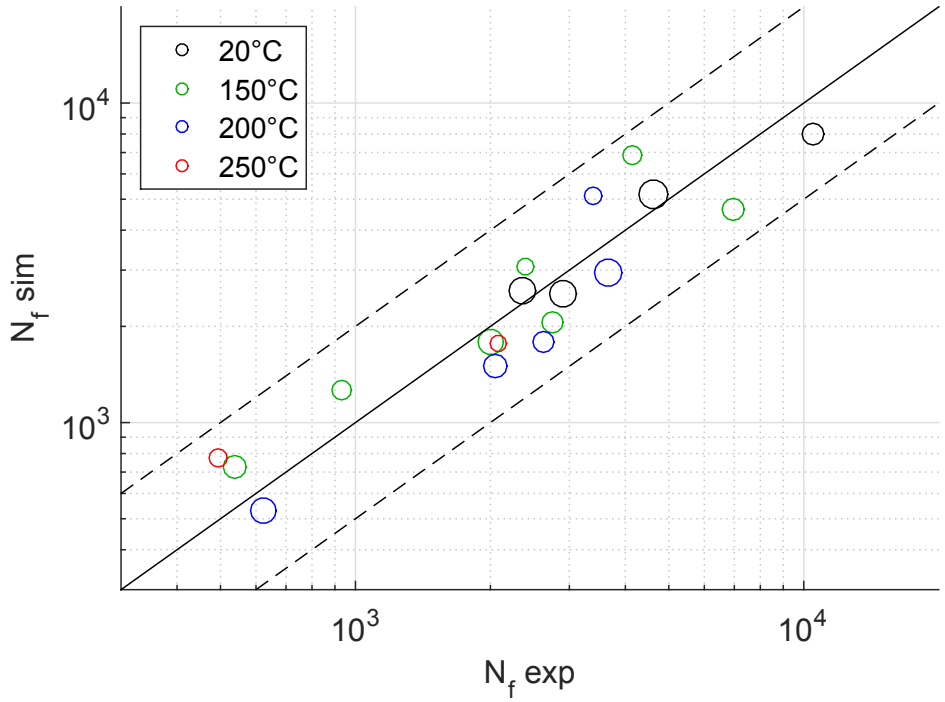

FIGURE 5.12 – Simulated versus experimental fatigue life for samples with measured defects. Marker area is proportional to Feret diameter, the marker in the legend corresponding to 100 µm.

The same parameters are used to numerically evaluate the fatigue specimen life where the crack initiating defect is not identified. In those cases, the initial crack length a_0 is taken as the median defect size a_{median} of the generalized extreme value distribution identified in Section 5.1.3 for the ring sample:

$$a_{median} = 209\,\mu\text{m} \tag{5.23}$$

Table 5.5 – Crack propagation model parameters

parameter	value
γ_e	1.08×10^6
m_e	2 (fixed)
γ_p	28.3×10^6
m_p	1.201

The results are presented in Figure 5.13. The model provides good fatigue life estimation for all the temperatures and imposed strains. However, for the highest temperature (250 °C), the model does not seem to capture the propagation kinetic and mechanism. This could be caused by the shift in propagation mechanism, with the increased plasticity effect, and the lack of measured defects. Indeed, as seen in Figure 5.12, only 2/18 sample initiating defects are identified for this high temperature, causing them to have small impact on the optimized parameters.

For most of the data points, the use of the median defect size allows for a conservative prediction of fatigue life.

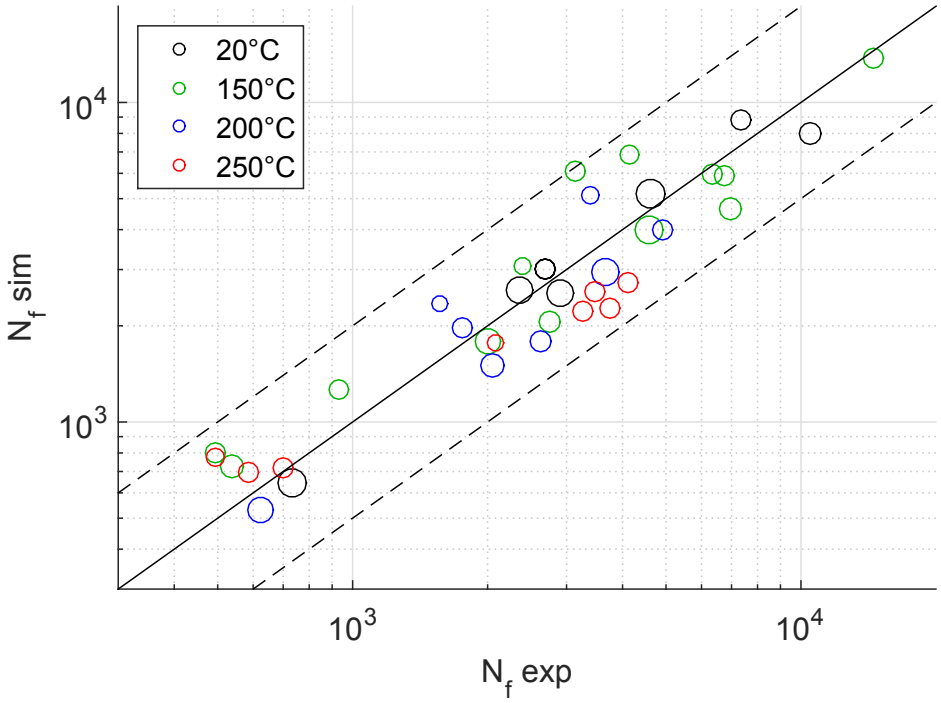

FIGURE 5.13 – Simulated versus experimental fatigue life for all samples. Marker area is proportional to Feret diameter, the marker in the legend corresponding to 100 µm.

Lastly, the results of the crack propagation monitoring experiments are compared to the model. Results are presented in Figure 5.14. As identified previously, high temperature (250 °C) crack propagation rate is overestimated by the model for the two specimens (89T5 and 29T5), but stills capture the right order of magnitude. For the two other specimens (76T5 and 20T5), the crack propagation rate is accurately predicted.

For the crack propagation experiments, the discrepancy for higher temperature could also be caused by the crack arrest: the monitored cracks do not cause final failure, and the main crack causes unloading in the specimen towards the end of the test.

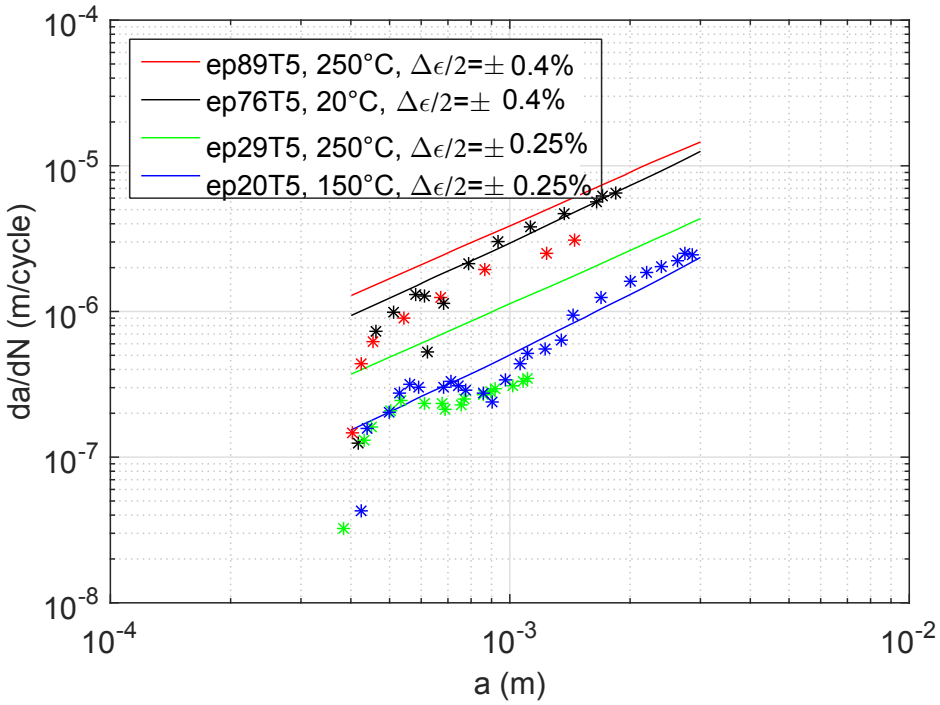

FIGURE 5.14 – Experimental (markers) and model (lines) crack propagation rates versus crack length.

Crack length simulation is shown in Figure 5.15. The initial defect length is taken as the measured hemispherical defect diameter (around 400 µm). The crack propagation model does not take into account the initiation period, and the experimental measured values of cycles to initiation N_{init} are therefore used for both simulated and experimental crack propagation data (i.e. the simulated crack propagation only starts at N_{init} in Figure 5.15). The simulated crack length are in good agreement with the observed data except for the high-temperature (250 °C) low strain ($\Delta\varepsilon_p$) experiment, which still remains conservative.

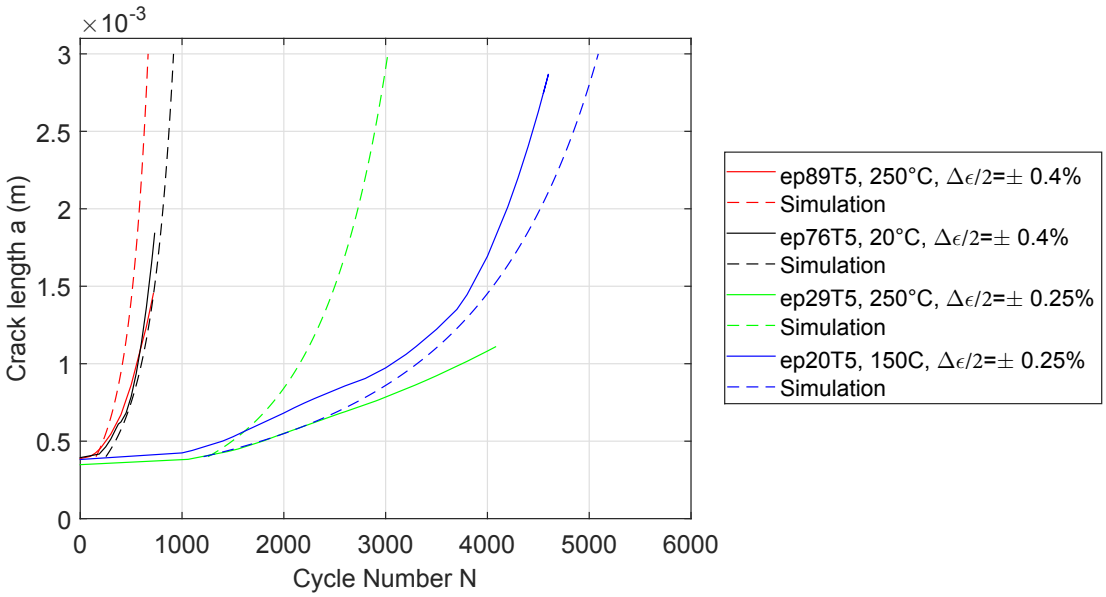

FIGURE 5.15 – Experimental (full line) and simulated (dashed line) crack length as a function of the number of cycles.

5.2.4 Probabilistic modelling

With the numerical model developed in Section 5.1, K samples containing each a defect population can be generated. From each sample, the largest 2D Feret is then determined. This largest defect is in turn used as the input for the crack propagation model, which gives a simulated number of cycles to failure N_f.

The variable N_f is then considered as a random variable, and for each condition, an estimated PDF can be calculated. Figure 5.16 shows the model results. On each PDF, the experimental values are indicated by markers enabling the comparison with the numerical simulation. For the lower temperatures ($\leq 200\,°C$), the numerical prediction provide satisfactory results. For the highest temperature ($250\,°C$), the results confirms the issues of the crack propagation model (see Figure 5.14): the crack propagation rate is overestimated, and life assessment too conservative.

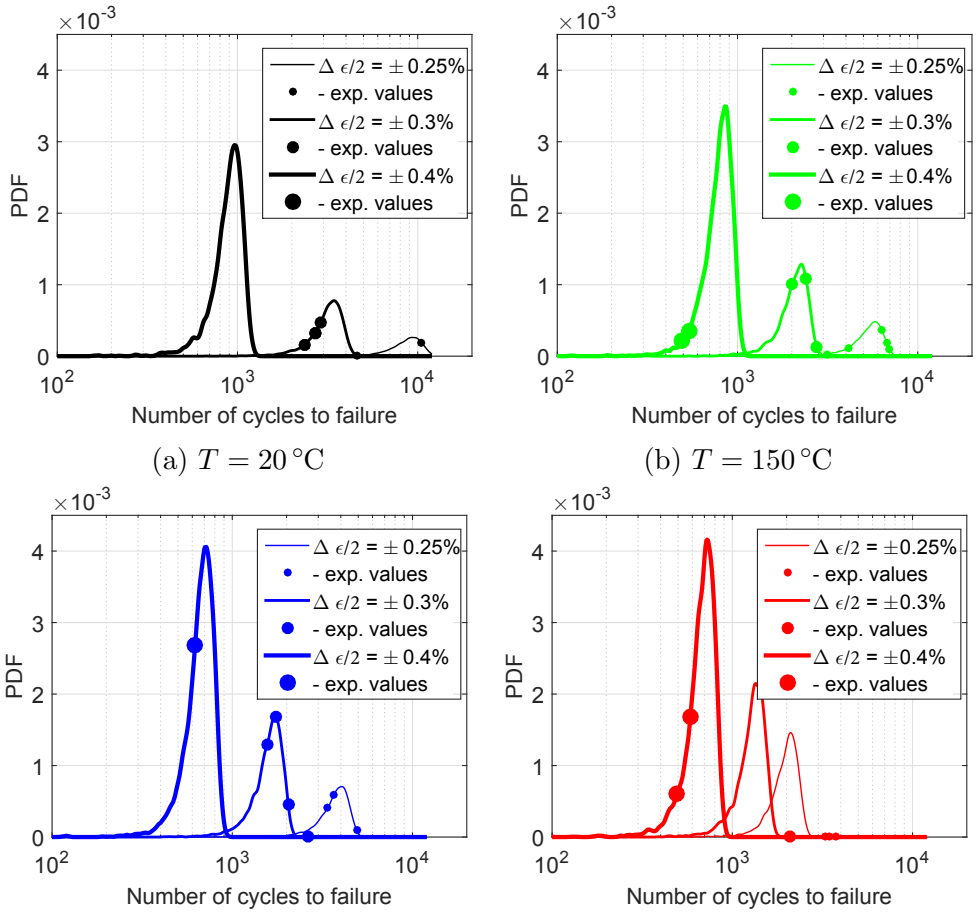

(a) $T = 20\,°C$ (b) $T = 150\,°C$

(c) $T = 200\,°C$ (d) $T = 250\,°C$

FIGURE 5.16 – Kernel density estimates of simulated number of cycles to failure for different test conditions, for each test, corresponding experimental (exp.) values.

5.3 Conclusions and prospects

Using the statistical models developed in chapter 2, numerical samples of defect population can be generated. Two types of samples are studied: cylindrical and tubular. For all simulation methods, the mean number of defects is very similar. However, the total number of defects for Clustered Point Processes (CPP) samples is more dispersed,

due to the small number of parent points per specimen. The defect size is considered independent of the defect location, which enables the generation of the defect size whatever the location. A conversion to a 2D measure of the Feret diameter finally enables a comparison with the experimental results of Section 4.2.1. The size of the observed defects on the crack surfaces is compared with the largest defect in the numerical specimen. **While the cylindrical sample clearly overestimates this defect size, the ring sample captures the distribution of the experimental results.** For this case, the clustering appears to have minimal effect: given the size distribution, the Poisson Point Process and the Clustered Point Process yield very similar results.

A fatigue crack growth model based on energy quantities is then introduced. Given the small number of crack propagation monitoring experiments, the parameters are optimized on the fatigue test series on smooth specimens for which the main defect could be identified. For the others tests, a median defect size is used. For all the test conditions, a good fatigue life assessment is achieved. The model is also applied to the crack monitoring experiments. It provides a very good fit for the lower temperatures, and an overestimated crack propagation rate for the higher temperatures.

Finally, the numerical samples are used to generate an artificial fatigue life dispersion: the numerically largest defects are considered as the initial crack size, producing variable fatigue lives. **In future works, study of the variability and sensitivity in crack propagation rates should be conducted. Indeed, it has been shown that crack propagation rate parameters can be considered random (Virkler et al. [1979]).**

Further works also imply generation of 3D meshed defects. Using the simulated defects location of a clustered Thomas point process and the generalized Pareto distribution, a 3D microstructure of the gauge length of simplified defects is generated (see Figure 5.17).

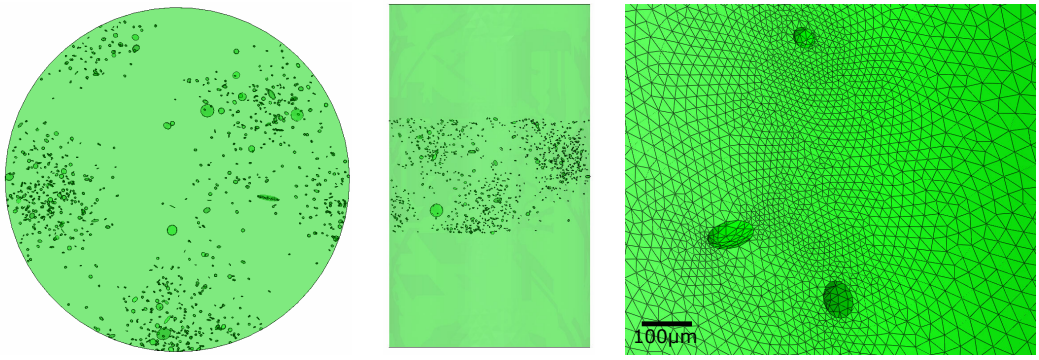

(a) Top view (b) Front view (c) Front view: surface mesh with intersecting defects

FIGURE 5.17 – Generation of 3D defects population and meshing.

Using the simulation parameters of the macroscopic model, finite element simulation of an imposed deformation (FEM) is carried out ($\Delta\varepsilon/2 = \pm 0.3\%$). Figure 5.18 shows the comparison of the cyclic elastic energy field for two different temperatures. Only a little number of defects are close enough to the surface for their effect on the fields to be seen. The maximum (seen on the top colour bar scale) for both cases shows unrealistic values. Due to the different length scales involved, high stress concentrators appear close to the defects, and local strain values can reach up to 5% (hence the unrealistic energy values). These strain values are clearly out of the scope of application of the

finite element simulation used (which supposes the infinitesimal strain theory), and further studies required to go deeper in the subject. These further studies could use finite strain and/or actual FEM modelling of the crack.

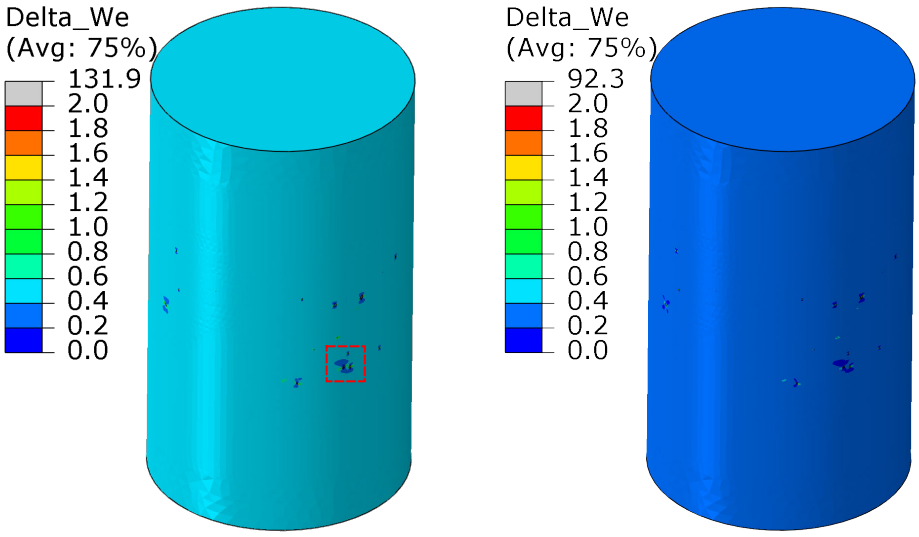

(a) $T = 20\,°C$ (b) $T = 250\,°C$

FIGURE 5.18 – FEM calculation: cyclic elastic energy.

Figure 5.19 shows a zoom of the window shown in Figure 5.18a. Due to the clustered point process, large defects ($\geq 100\,\mu m$) are located close to each other. The simulation allows observing the distribution of elastic and plastic dissipated distribution, and the interaction of two defects. For the room temperature, elastic energy is predominant and strong elastic energy appears between the two defects, which corroborates the observation of crack shielding caused by elastic interaction (see Section 4.3.5). For the higher temperature ($T = 250\,°C$), the main interaction is observed for the plastic dissipated energy too.

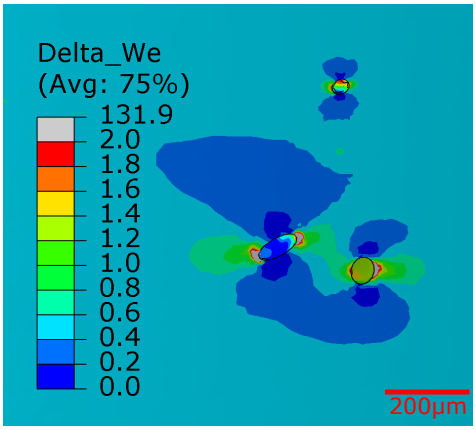

(a) ΔW_e, $T = 20\,°\mathrm{C}$

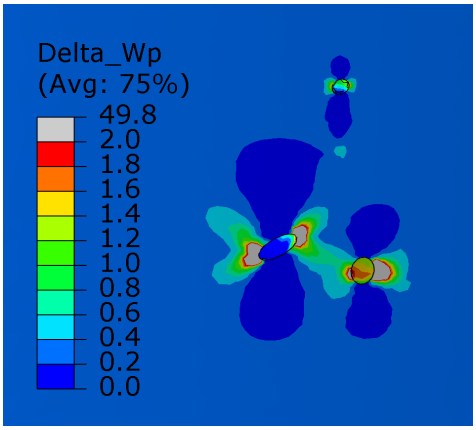

(b) ΔW_p, $T = 20\,°\mathrm{C}$

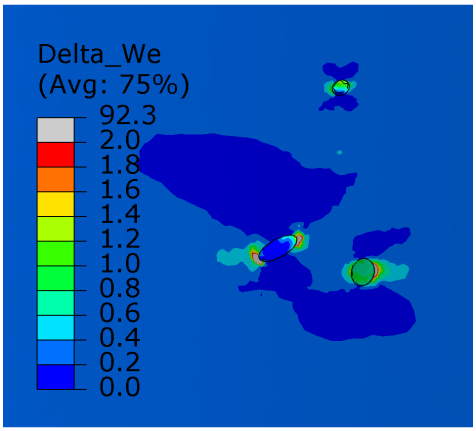

(c) ΔW_e, $T = 250\,°\mathrm{C}$

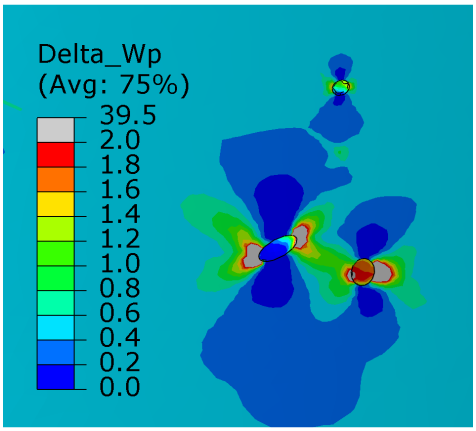

(d) ΔW_p, $T = 250\,°\mathrm{C}$

FIGURE 5.19 – FEM calculation of numerical microstructure, simulated energies for different temperatures ($\Delta\varepsilon/2 = \pm 0.3\%$).

Chapitre 6

Effect of defects on the LCF strength of notched specimens

A fatigue campaign on notched specimens has been carried out to study the impact of loaded volume size on the probability of finding a defect in the highly loaded volume. Indeed, for these specimens, only a small portion of the total volume is highly mechanically loaded, therefore containing much fewer defects. Mechanisms, similar to those observed on smooth specimens, are studied. Then, finite element simulation is used to asses the effect of this smaller highly loaded volume on the LCF life estimation and the impact of defect clustering.

6.1 Experimental

6.1.1 Test conditions and setup

Notched specimen has been defined in order for the stress gradient in the specimen to be close to that of the studied industrial component. The numerical results on the component are not shown for confidentiality reasons. Using Peterson's formula (Pilkey and Pilkey [2007]) for a tension bar of circular cross section with a U-shaped groove, with the dimensions indicated in Figure 6.1, the theoretical stress concentration factor in tension is:

$$K_t = 1.78 \tag{6.1}$$

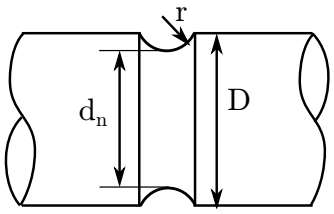

FIGURE 6.1 – Notch shape: $D = 7\,\text{mm}$, $d_n = 5.6\,\text{mm}$, $r = 1.2\,\text{mm}$

For the fatigue tests, a class 0.5 extensometer with a gauge length $l_0 = 12\,\text{mm}$ is used to perform strain controlled LCF tests. The notch is placed in the center of the extensometer gauge length. The loading is applied by an Instron 8500 servo-hydraulic fatigue testing machine equipped with a furnace (see 3.1.1 for further experimental details). Unlike for smooth specimens, the local strain cannot be directly imposed, and

the controlled parameter is solely the total extensometer gauge length l. The displacement d is further used in the graphics (the displacement d is the relative displacement $d = l - L_0$). In order to define the test frequency, a macroscopic strain ε_{macro} is defined:

$$\varepsilon_{macro} = \frac{l - L_0}{L_0} \tag{6.2}$$

and the frequency is chosen so that $\dot{\varepsilon} = 10^{-3}$ (which is the same strain rate used for the smooth specimens). The tests are done for 2 (3 for 20 °C) imposed displacements (see Table 6.1). The imposed signal waveform is triangular and symmetrical ($R = -1$). Tests are conducted under 3 different controlled temperatures: 20 (ambient), 150, 200 and 250 °C. Given some technical difficulties, all tests were not interrupted for the same stop conditions (load drop). However, for all tests, the specimen lifetime N_f is considered for a 10% load drop. For the SEM-BSE images, interrupted test specimens were opened at ambient temperature by a monotonously increasing tension load.

Table 6.1 – Design of experiment for notched specimens tests: number of tests per test condition. The tests are run at $L_0 \pm d$ (i.e. a d amplitude, or equivalently a $2d$ range), l_0 being the initial extensometer gauge length (12 mm).

T (°C)	$\Delta\varepsilon_{macro}/2$	20	150	200	250
$d = 0.016$ mm	±0.13%	1	1	1	1
$d = 0.020$ mm	±0.17%	2	0	3	1
$d = 0.025$ mm	±0.21%	1	0	0	0

As is shown in Section 3.1.3, temperature needs 30 min so stabilize. After this delay, the measured temperatures in the useful zone are in the tolerated values by the ASTM standard (ASTM [2004]). However, the 30 min stabilization time does not provide a totally stabilized temperature. This slight variation during the first ten minutes of the test was not critical for smooth specimens, but caused problem for notched specimens. This is shown in Figure 6.2: 30 min to test start (specimen 65T5) causes a deviation of mean load during the first 10 min, which leads to a non-negligible deviation of the mean load F_m during the test ($F_m \in [0N; 800N]$). By increasing the time to start to 40 min, the initial temperature is stable, and the mean load only slightly increases ($F_m \in [0N; 100N]$). No rigorous explanation are found for this problem which could be further investigated and only stable tests are showed and analysed in the following.

6.1.2 Results

Results are shown in Figures 6.3, 6.4, 6.5 and 6.6. For $T \leq 200$ °C, the tests are stable and material ageing has little to no effect on the cyclic behaviour. For $T = 250$ °C, see Figure 6.6, the load amplitude continuously decreases during the test making the distinction from crack initiation to crack propagation difficult.

Due to the limited number of specimens, repeatability is only tested for one condition ($d = 0.020$ mm and $T = 200$ °C) with 3 specimens. Results are shown in Figure 6.7. The lifetime has a mean value of 1662 cycles with a standard deviation of 212.2 cycles and for any given cycle, the load amplitude varies between tests in a 100 N range. The relatively low dispersion therefore allows conducting a meaningful fatigue analysis, despite the non-repeated test for other conditions.

The fatigue test results on notched specimens are presented in Table 6.2 and in Figure 6.8. Seemingly to the fatigue tests results on specimens in Section 3.3, temperatures decreases the fatigue lifetime for a given imposed displacement.

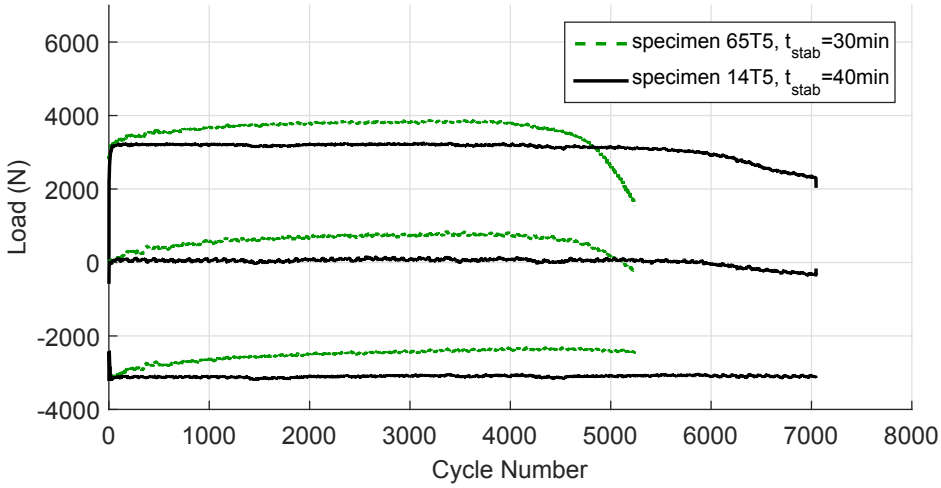

FIGURE 6.2 – Influence of stabilisation time: evolution of load minimum, mean and maximum value per cycle, test temperature $T = 200\,°C$ and displacement $d = 0.016\,mm$. For specimen 65T5 (resp. 14T5), the mechanical loading starts 30 min (resp. 40 min) after thermal loading. The total test time is approximetaly 5 h.

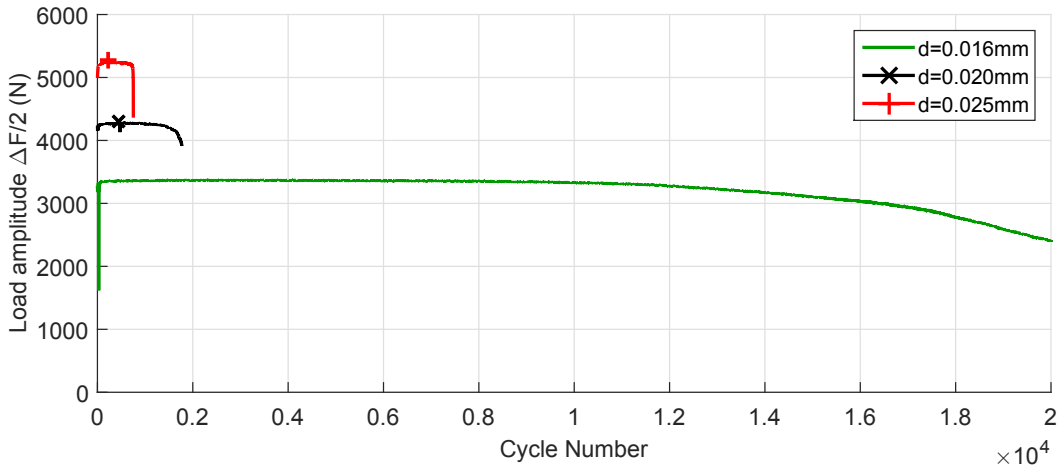

FIGURE 6.3 – Evolution of the load amplitude for $T = 20\,°C$, on notched specimen ($K_t = 1.78$).

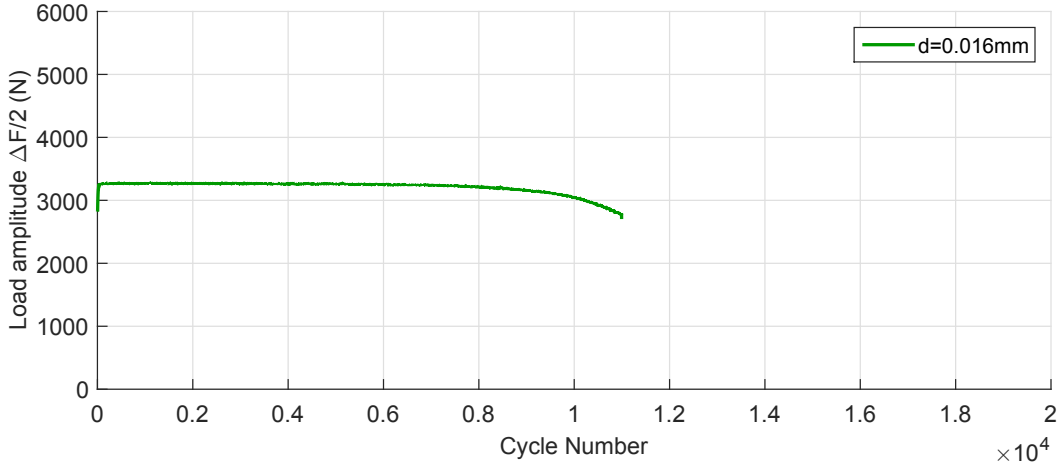

FIGURE 6.4 – Evolution of the load amplitude for $T = 150\,°C$, on notched specimen ($K_t = 1.78$).

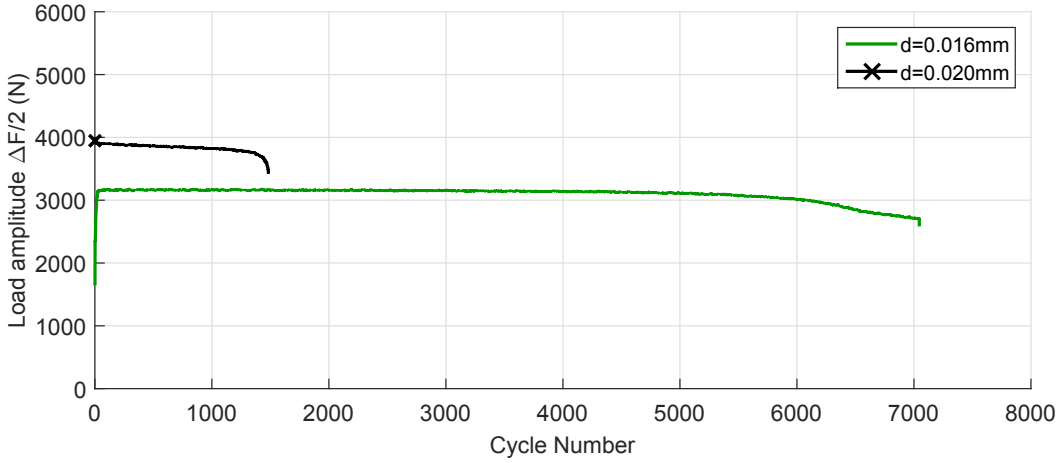

FIGURE 6.5 – Evolution of the load amplitude for $T = 200\,°C$, on notched specimen ($K_t = 1.78$).

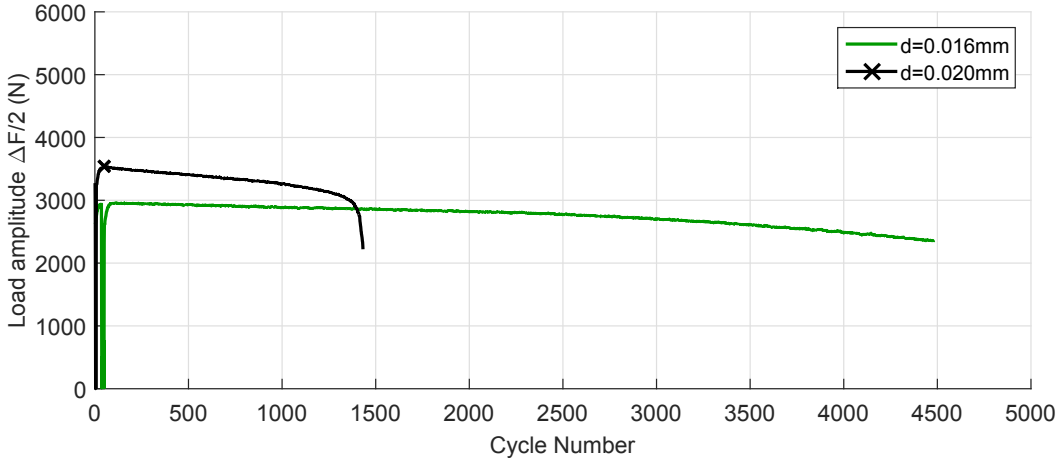

FIGURE 6.6 – Evolution of the load amplitude for $T = 250\,°C$, on notched specimen ($K_t = 1.78$).

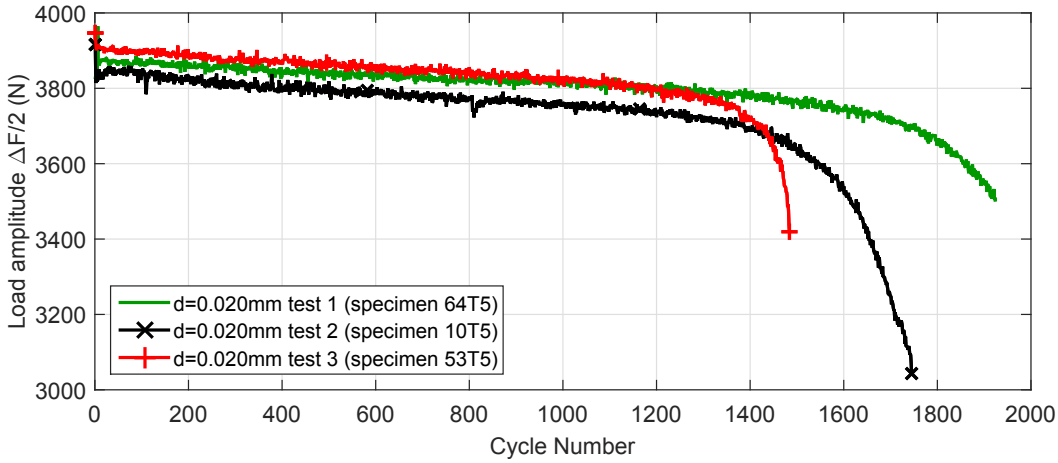

FIGURE 6.7 – Evolution of load amplitude for $T = 200\,°C$: test repeatability for 3 notched specimens ($K_t = 1.78$).

Table 6.2 – Fatigue test results on notched specimens ($K_t = 1.78$).

Specimen	d (mm)	Temperature (°C)	N_f (cycles)
41T5	0.016	20	11790
16T5	0.020	20	2376
75T5	0.020	20	1698
162T5	0.025	20	753
83T5	0.016	150	9924
17T5	0.016	200	6159
64T5	0.020	200	1880
10T5	0.020	200	1650
53T5	0.020	200	1456
38T5	0.016	250	3302
174T5	0.020	250	1358

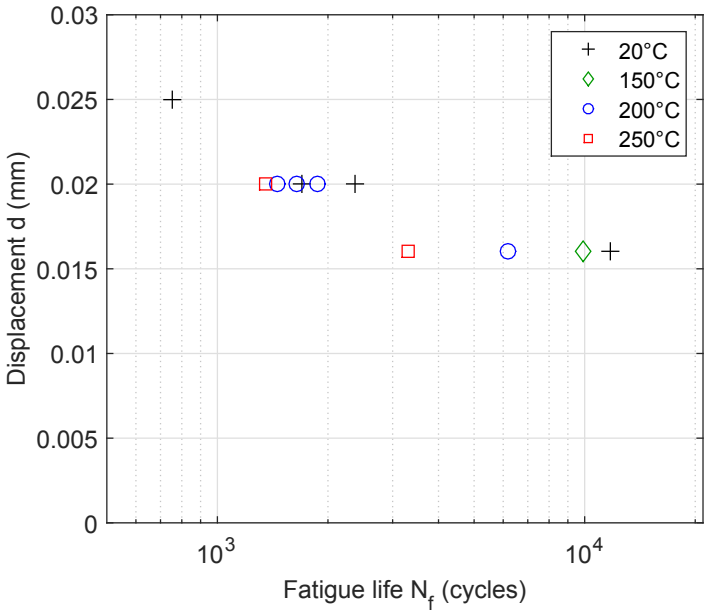

FIGURE 6.8 – Fatigue life for notched specimens ($K_t = 1.78$).

6.2 Fatigue mechanisms on notched specimens

Notched specimen fatigue mechanisms are described in this Section. For all the specimens, the fatigue crack initiated at the notch root. Figure 6.9 shows an example of a general fracture surface (at $T = 250\,°C$ and $d = 0.016\,mm$). As for crack mechanisms observed on smooth specimens in chapter 4, the main crack initiates on a shrinkage defect close to the specimen free surface. The steady crack propagation region, however, transforms in a more complex shape induced by the notch stress concentration. Figure 6.9 also shows a secondary crack with characteristic features, which has less propagated and exhibits a almond crack shape, similar to smooth specimen cracks. **Given the reduced number of tests and observations, the results are shown for specific imposed strains and temperatures. Further, more extensive, studies would be necessary to investigate the impact of temperature and imposed strain on the observed mechanisms as well as the sequencing of events.**

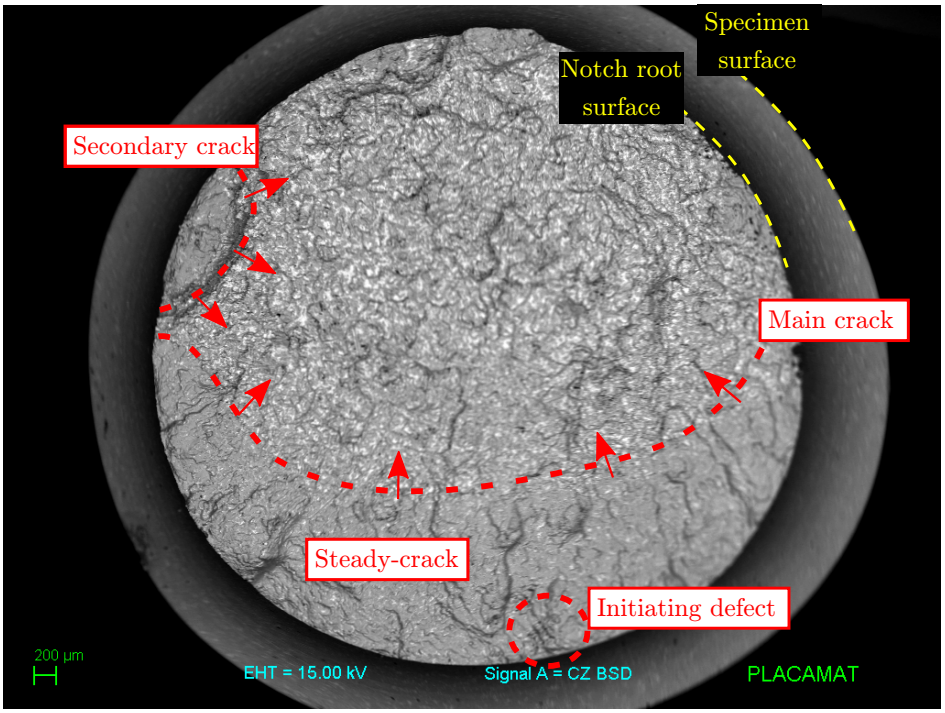

FIGURE 6.9 – General view of the fractured surface of a notched fatigue specimen (specimen 38T5, $d = 0.016\,mm, T = 250\,°C, N_f = 3302$ cycles.

6.2.1 Crack initiation

For 6/11 tests, crack initiation is clearly identified on a shrinkage defects at or very close to the edge. However, compared to smooth specimens, post-mortem observations of notched specimens do not clearly reveal a single main critical defect, and several crack initiating defects are identified. For the remaining tests, no clear initiation area could be identified, even though defects appear on the fracture surface close to the free edge.

Figure 6.10 shows a clearly identified initiation [1] location (at $T = 250\,°C$ and $d = 0.016\,mm$). The tortuous shape together with the smooth aspect of the dendrites (see

1. Further studies would be necessary to determine if this is indeed a crack initiating defect, and not a defect that has interacted with the main crack.

for example label (c)) reveals it is a shrinkage defect. It is however unclear if label (d) could identify the frontier between 2 very close defects coalescing. Considering it as a single defect, it has a large overall size (Feret diameter of 420 µm) and almost intersects the specimen free surface. As for smooth specimens, the crack initiates on the defect edges with particular microstructure. Label (b) shows eutectic zones: the brittle silicon particles together with their high Young modulus compared to Al (creating strain mismatches) are favourable to crack initiation. Label (a) corresponds to Fe-rich intermetallics: their highly convoluted shape and their brittle nature are also inclined to initiate fatigue crack.

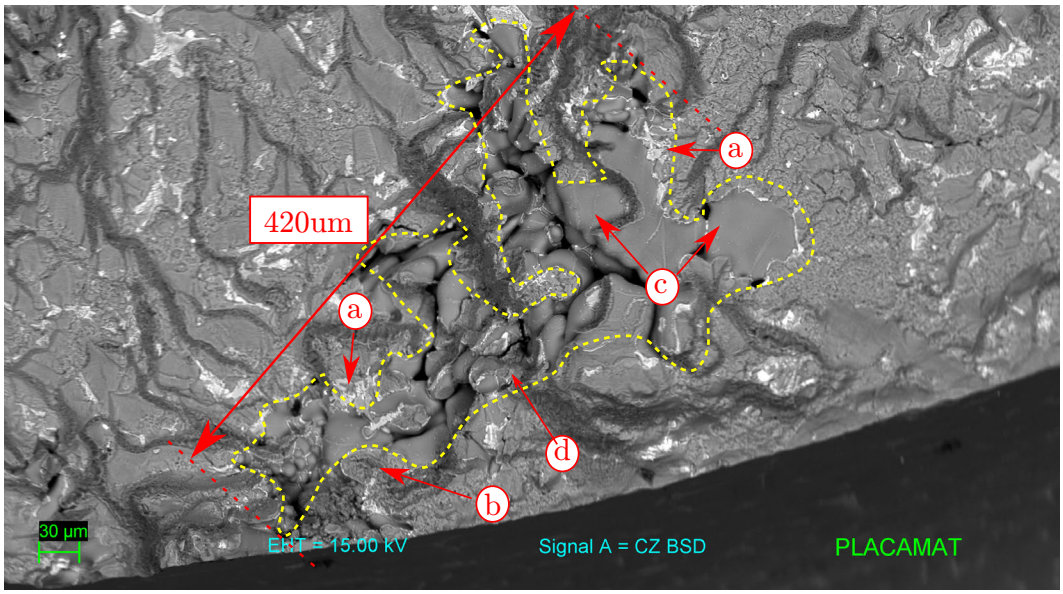

FIGURE 6.10 – Crack initiation on large shrinkage defect. Label (a) indicates initiation on intermetallics. Label (b) shows initiation on the eutectic zone. Label (c) displays the smooth surface aspect of dendrites inside the shrinkage defect (zoom of Initiating defect in Figure 6.9, specimen 38T5, $d = 0.016\,\text{mm}, T = 250\,°\text{C}, N_f = 3302$ cycles.

6.2.2 Crack propagation

Fractography analysis

Figure 6.11 shows the first stage of crack propagation (at $T = 200\,°\text{C}$ and $d = 0.020\,\text{mm}$). The crack initiates on a shrinkage defect (see image B) and three different morphological features can be seen (image C):

- Eutectic fracture zone: the small silicon particles cause a highly rough surface. The fractured and debonded Silicon particles form dimples. The ratio of crack versus debonded particles has not been quantified.
- The fractured dendrites: at low magnification (see Figure 6.11 image B) appear as smooth and flat surfaces. At higher magnifications (see image C), they reveal the presence of tire track marks, revealing the fatigue process.
- Intermetallics: amid the eutectic and the fracture dendrites, tangled white intermetallics are present.

Figure 6.12 shows the general aspect of the crack propagation for specimen 38T5 ($d = 0.016\,\text{mm}, T = 250\,°\text{C}, N_f = 3302$). The different labels allow distinguishing the crack propagation mechanisms and chronological phases:

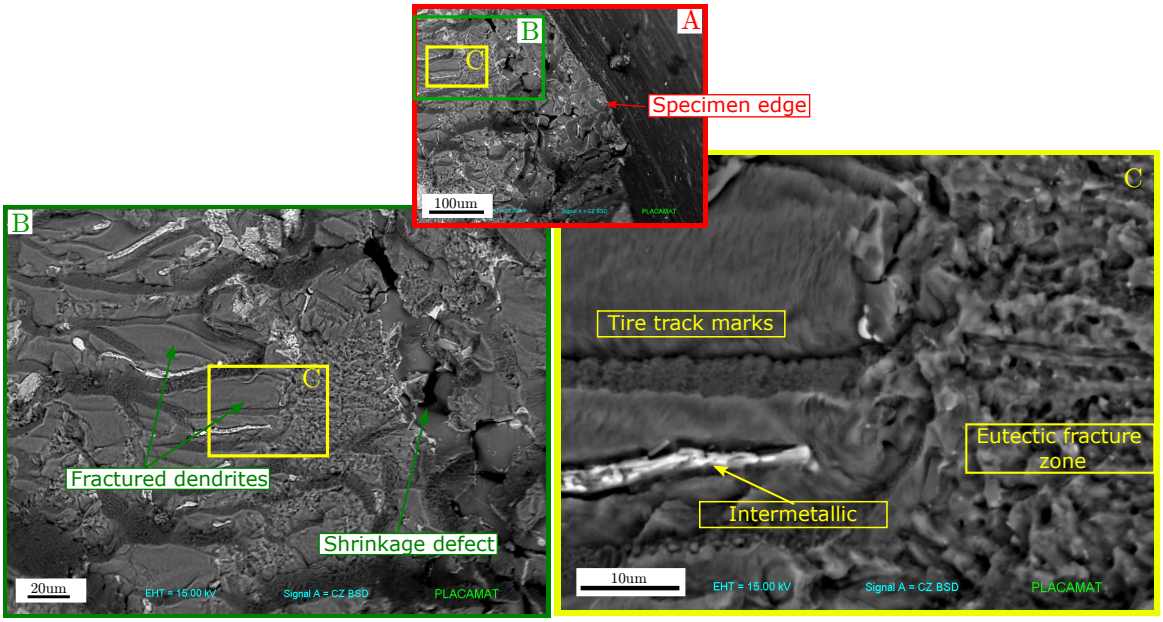

FIGURE 6.11 – Crack initiation and first stage propagation on an edge shrinkage defect (specimen 53T5, $d = 0.020\,\text{mm}, T = 200\,°\text{C}, N_f = 1456$ cycles)

— Label (I): This defect is the identified main critical defect (shown in Figure 6.10). It is considered as the critical defect, for it is roughly located at the center of the fatigue crack (see Figure 6.9). Moreover, this casting defect is the largest defect (Feret diameter 420 µm) on the steady crack path of the fracture surface.

— Label (c) and (c_i): these labels identify defects that interact with the main crack. Further observation are needed to understand if these secondary defects initiate secondary cracks before the main crack reaches them, or if the main crack path is deviated through these defects.

— Label (II): This appears to be a gas defect (Feret diameter of 280 µm) close to the specimen edge (54 µm) which has initiated a crack propagation.

— Label (III): The slant fracture visible indicates the location of crack I (the crack initiated by defect (I)) and crack II (initiated by defect (II)) coalescence. At coalescence, crack I has propagated 2200 µm whereas crack II only 550 µm, hence the definition of crack I as the main crack and defect (I) as the main critical defect.

Tomography analysis

To investigate crack propagation behaviour, specimen 53T5 is analysed using laboratory X-ray tomography. The fatigue test is stopped after crack initiation is detected [2] and the cracked sample scanned. A 5.1x5.1x5.1µm voxel is used, providing a 1450x1450x796 voxels tomography. The general 3D shape of the sample is shown in Figure 6.13a as well as a 2D slice of the center of the specimen in Figure 6.13b. The main crack appears at or very close to the notch root along the z direction: the crack is contained in a ±400 µm interval from the notch middle. For corresponding SEM-BSE images, the test specimens are opened by a tension test at ambient temperature.

2. The specimen 53T5 has a fatigue life N_f of 1456 (corresponding to a 10% load drop), but this test was carried until a 20% load drop was detected for 1484 cycles.

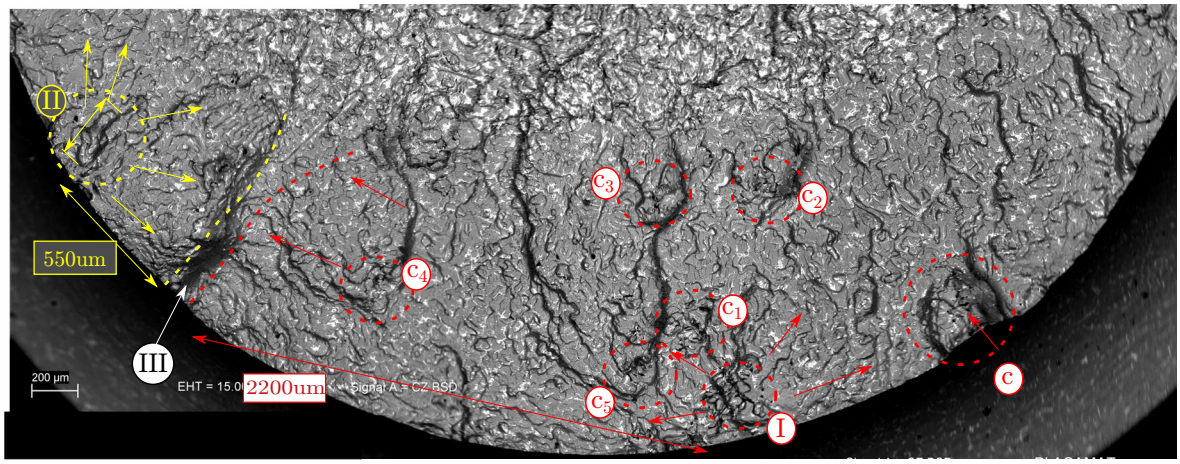

FIGURE 6.12 – Crack propagation and interacting defects, specimen 38T5, $d = 0.016\,\text{mm}, T = 250\,°\text{C}, N_f = 3302$ cycles

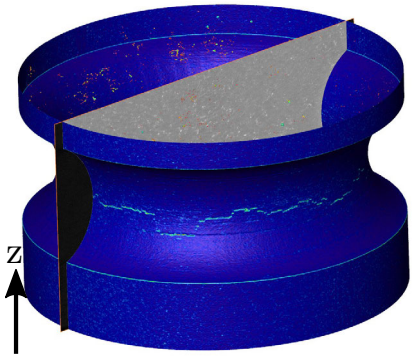

(a) 3D isosurface view of fatigue notched specimen analysed by tomography. The color indicates surface curvature, allowing to reveal the crack.

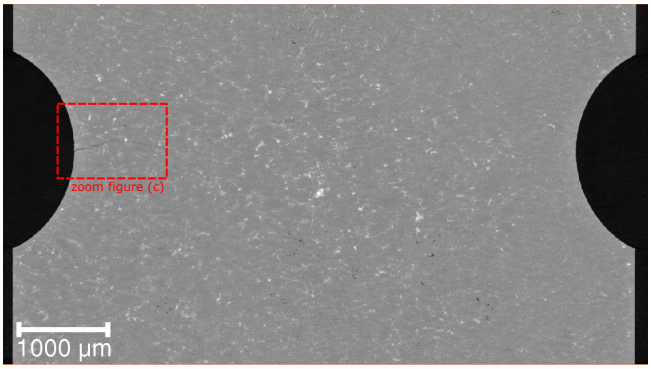

(b) 2D slice of specimen middle section.

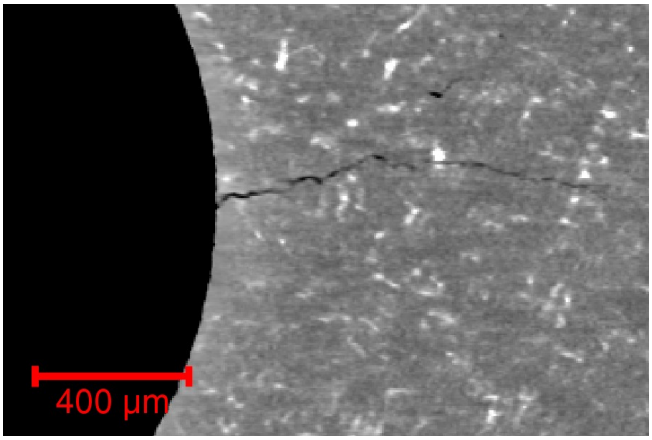

(c) 2D slice of specimen middle section: zoom.

FIGURE 6.13 – Tomography of notched fatigue specimen. (specimen 53T5, $d = 0.020\,\text{mm}, T = 200\,°\text{C}, N_f = 1456$ cycles)

Image correction described in Section 2.2 is applied to the sample in order to correctly differentiate the thin crack. Figure 6.14 compares SEM fractography image obtained after specimen opening with the reconstructed crack obtained by tomography on fatigue interrupted specimen. This comparison indicates that the fast crack propagation only occurs at the very end of the specimen lifetime. Indeed, the test is interrupted for a 20% load drop, and the crack has only propagated approximately 1 mm towards the specimen core, and the remaining load drop occurs rapidly. The tomography also clearly shows the shape of the crack: the stress concentration at notch root favours the crack propagation to a particular "sickle" or "crescent" shape (Lin [1999], Carpinteri et al. [2013]).

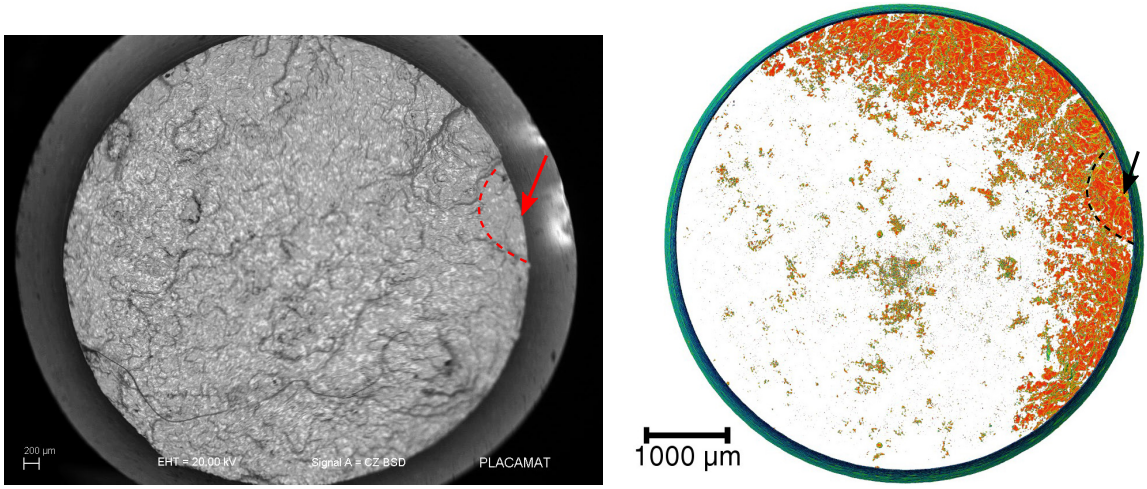

(a) SEM fractography of broken specimen. The contrast has purposely been increased to reveal crack features.

(b) 3D crack reconstruction by tomography before total failure.

FIGURE 6.14 – Use of different techniques to analyse crack shape (specimen 53T5, $d = 0.020\,\text{mm}, T = 200\,°\text{C}, N_f = 1456$ cycles).

Figure 6.15 displays what is identified as the main crack initiation. The initiating defect is highly spherical, suggesting a gas porosity defect of 80 µm. The initial shape of the crack corresponds to a classical almond shape centred on the identified defect. The steady crack appears roughly 1200 µm wide before it changes aspect.

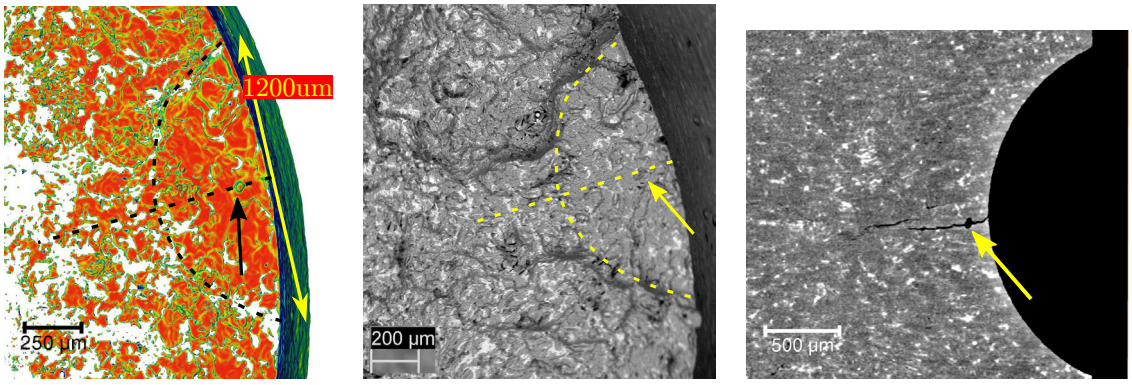

(a) Tomography reconstruction of crack.

(b) SEM view of fatigue crack after specimen opening

(c) Gas spherical defect: Feret Diameter 80 µm. The slice is perpendicular to images (a) and (b).

FIGURE 6.15 – Analysis of first stages of crack initiation and propagation on microstructural defect identified by the arrow (specimen 53T5, $d = 0.020\,\text{mm}, T = 200\,°\text{C}, N_f = 1456$ cycles)

6.2.3 Temperature effect

For notched specimens, similar features of temperature effects on smooth specimens (see chapter 4) can be found. Figure 6.16 displays the different surfaces observed by BSE-SEM. For the highest temperature combined with the highest imposed displacement (specimen 174T5, $d = 0.020\,\text{mm}, T = 250\,°\text{C}, N_f = 1358$, see Figure 6.16f), the crack appears to cause an extreme case of sickle shape: the crack propagates all around the notch root and caused a ring shape. For all the other cases, the crack shape resembles the one identified in Section 6.2.2: a sickle shape crack develops on the notch root before final failure. When identified, the cases in Figure 6.16 show the center of the crack sickle shape in the bottom of the Figure.

As for smooth specimens, higher temperature fatigue testing appears to increase the number of defects seen on the fracture surface. At the highest temperature (250 °C, see Figure 6.16e which is analysed in detail in the previous Figure 6.12, and 6.16f for the higher imposed deformation), many frontiers revealing crack interacting with another crack or with a defect can be seen. For ambient temperature, crack appear much flatter. The first Figure 6.16a must be taken with precaution, the contrast being accidentally set too high, it emphasises the crack roughness, especially with the low magnification. In the second Figure 6.16b, despite the high imposed mechanical loading, the crack surface appears relatively flat, confirming the crack interacting with other defects and secondary cracks is indeed due to the higher temperature. Further studies using roughness measurements could help quantify this effect.

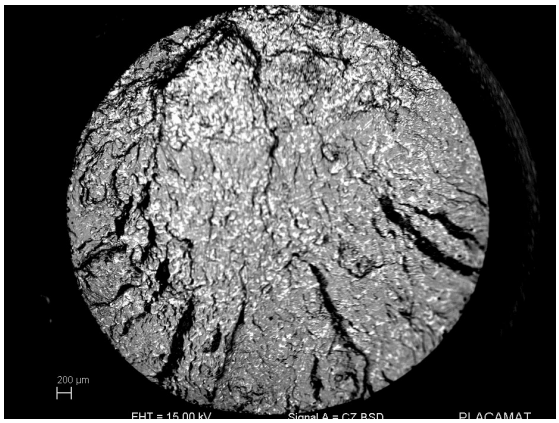

(a) Specimen 41T5, $d = 0.016\,\text{mm}, T = 20\,°\text{C}, N_f = 11790$

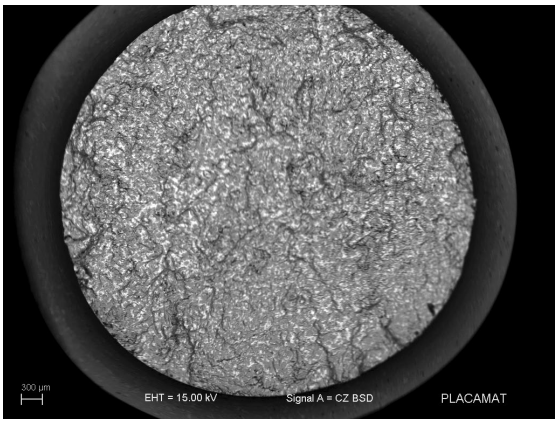

(b) Specimen 75T5, $d = 0.020\,\text{mm}, T = 20\,°\text{C}, N_f = 1698$

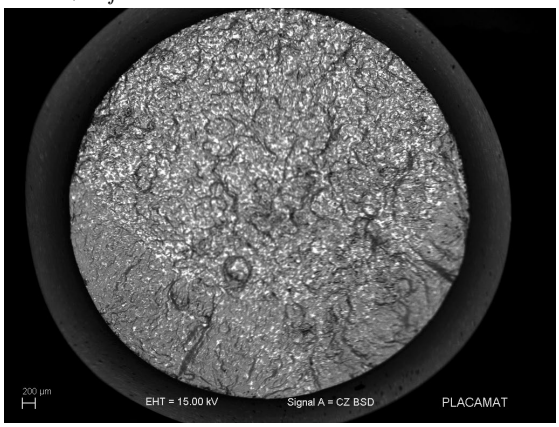

(c) Specimen 17T5, $d = 0.016\,\text{mm}, T = 200\,°\text{C}, N_f = 6159$

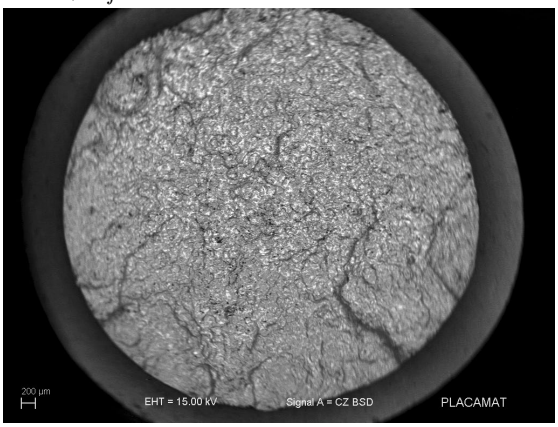

(d) Specimen 10T5, $d = 0.020\,\text{mm}, T = 200\,°\text{C}, N_f = 1650$

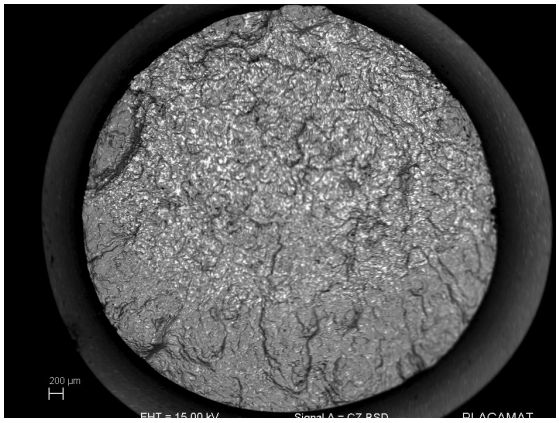

(e) Specimen 38T5, $d = 0.016\,\text{mm}, T = 250\,°\text{C}, N_f = 3302$

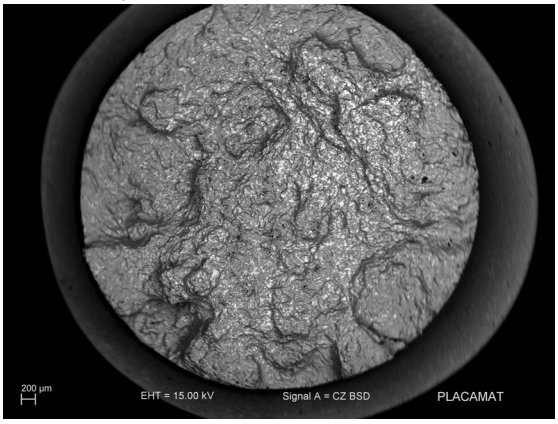

(f) Specimen 174T5, $d = 0.020\,\text{mm}, T = 250\,°\text{C}, N_f = 1358$

FIGURE 6.16 – Fracture surfaces of notched specimen fatigue tests ($K_t = 1.78$).

6.3 Numerical Simulation of Fatigue life

Given the test set-up, only macroscopic values can be experimentally measured (extensometer displacement and applied load). Of interest for fatigue life calculation are local quantities (stress, strain and energies) which require numerical simulations.

6.3.1 Numerical and mesh generation

In order to simulate notched specimens, Abaqus© finite element method (FEM) code and software simulation were used. Given the problem symmetry, a quarter of the specimen was simulated using axi-symmetric 2D CAX8R elements (see Figure 6.17).

The boundary conditions used are:

— Middle nodes (on line m): the vertical displacement (z) is set to 0, as to impose the model symmetry.

— Top nodes (on line t): the vertical displacement d_{sim} (along z) is imposed according to experimental conditions.

— node P: the z degree of freedom of all nodes on line t are linked to the z degree of freedom of node P.

Using this method, twice the z displacement of node P matches the measured displacement of the experimental extensometer, and the reaction force on node P corresponds to the experimental load. These are the values used in the following numerical study.

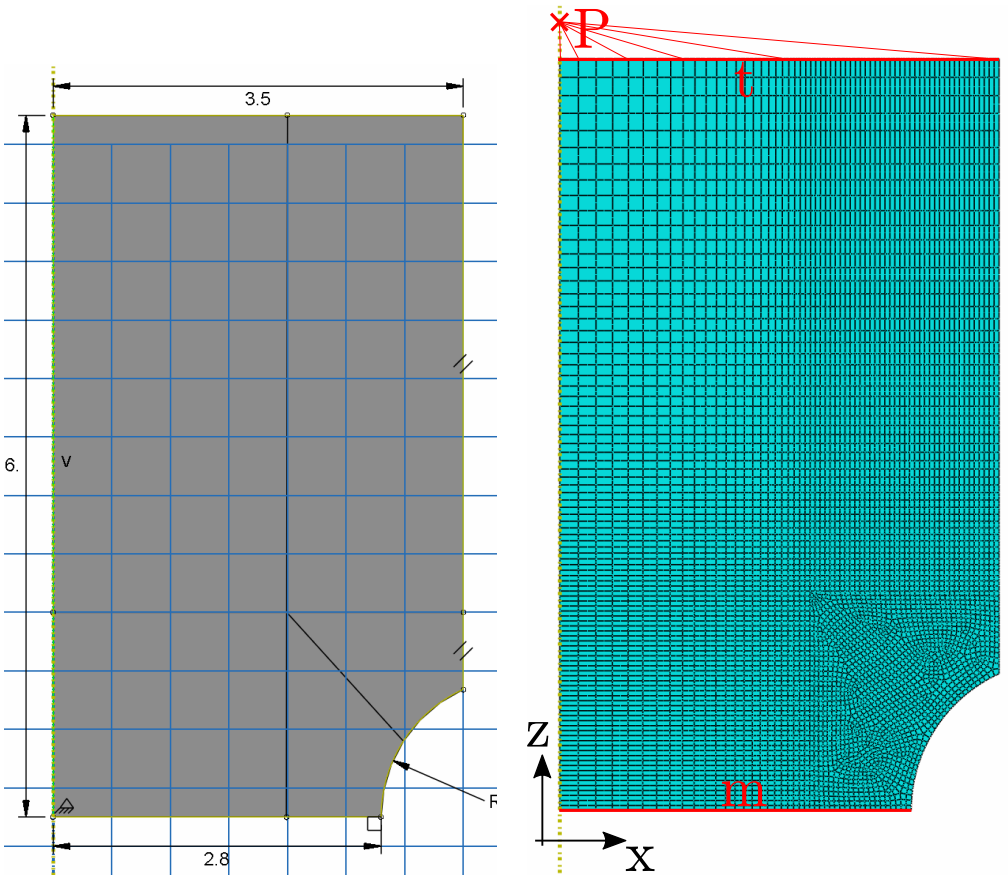

(a) Notch geometry used (b) Optimal mesh generation.

FIGURE 6.17 – Meshing the notched specimen

The numerical simulation not being computer intensive, only a short convergence study is done, and a fine mesh will be used. Figure 6.18a shows a typical result of normal to loading stress in the notched specimen. The more intense values are obtained in the region of interest of the notch ligament. The simulations are done for decreasing mesh size (h =500, 250, 50 µm), and for an optimized mesh (40 µm close to notch root, and 150 µm far, total of 5789 elements). As seen in Figure 6.18, the results rapidly converge for a mesh size of 50 µm, and the optimized also provides converged results. Therefore, the optimized mesh is used in the rest of this study.

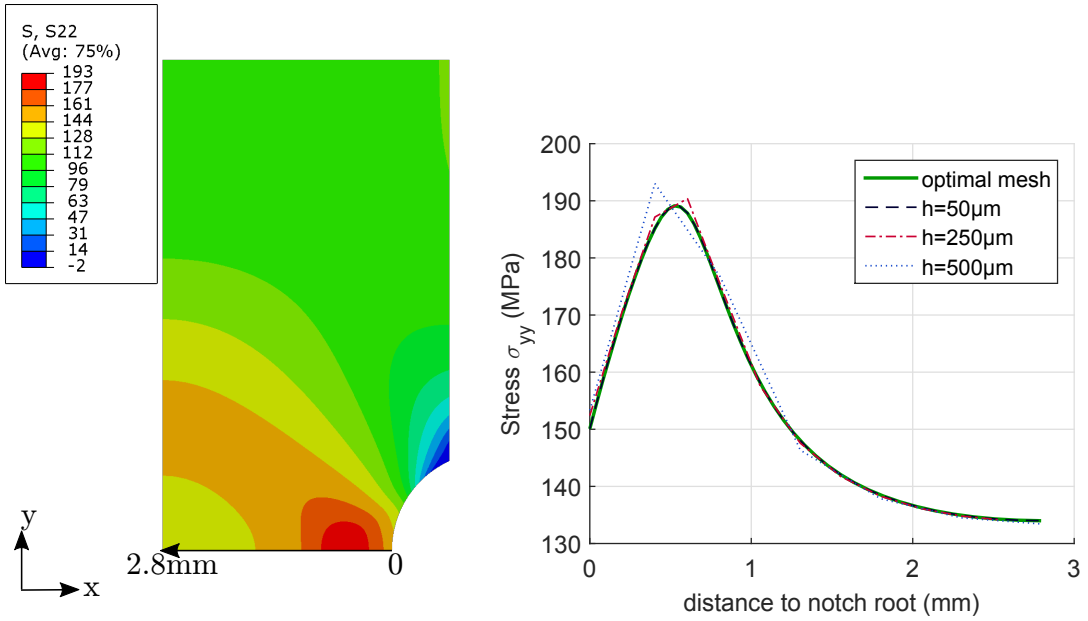

(a) FEM results (σ_{yy}) for d = 0.016 mm and T = 250 °C, at maximum imposed strain.

(b) Mesh size influence on normal to load stress (σ_{yy}) along the notch ligament

FIGURE 6.18 – FEM convergence study.

Given the cyclic nature of the simulation model used, numerical cyclic stabilization must also be ensured. However, with the mechanical model used (kinematic hardening and no isotropic hardening, see Section 3.2.3), the simulation model provides rapid cyclic convergence. Evolution of stress at notch root is shown in Figure 6.19. The maximum cyclic stress at the notch root in Table 6.3 confirm that only five cycles are necessary to provide cyclic stabilisation (the same method was used for the different stresses and deformation at notch root, and confirmed rapid stabilisation).

6.3.2 Simulation results

Figure 6.22 shows results for all the temperatures and imposed displacement. The simulations and experimental results are all shown for cycle N = 15, corresponding to initial stabilisation (material ageing for higher temperatures is not simulated). The global stiffness is well simulated for all the temperatures, as confirmed by comparison of the load amplitude in Figure 6.21a. The global plasticity is compared by calculating an equivalent plastic displacement d_p (illustrated in Figure 6.20), corresponding to the hysteresis loop width for zero load. Results shown in Figure 6.21b display good correlation between simulation and experimental results, especially when considering uncertainties (value measured are between 0.15 and 4 µm).

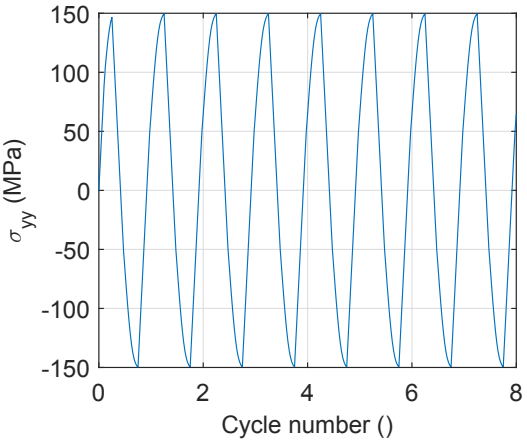

FIGURE 6.19 – Cyclic stabilization of stress (σ_{yy}) at the notch root.

Table 6.3 – Notch fatigue test results ($d = 0.016$ and $T = 250\,°C$)

Cycle number	Stress(σ_{yy}, MPa) at notch root
1	146.704
2	149.485
3	149.525
4	149.527
5 (stabilized)	149.527
6	149.527
7	149.527
8	149.527

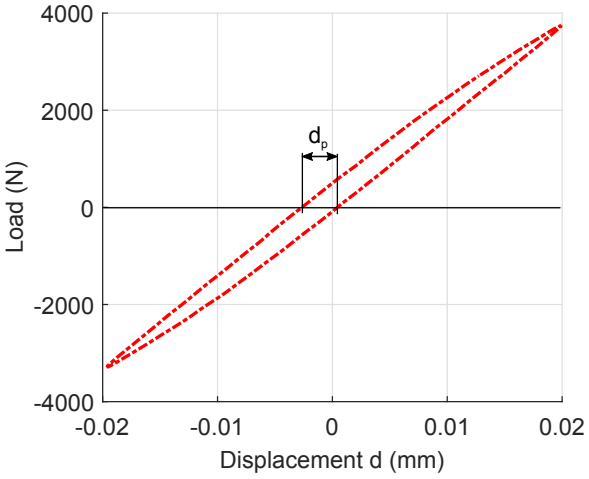

FIGURE 6.20 – Illustration of equivalent plastic displacement d_p.

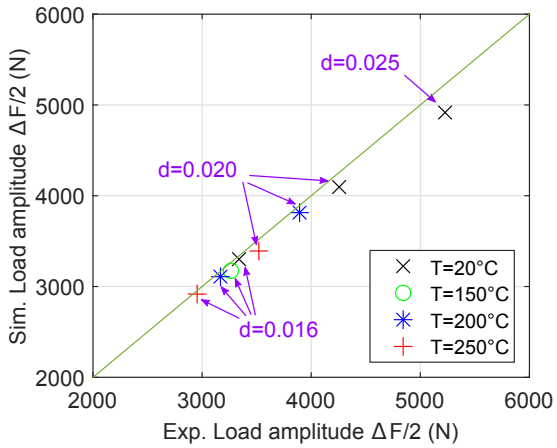

(a) Comparison of experimental and simulated load amplitude for different temperatures and imposed displacements d (indicated in mm).

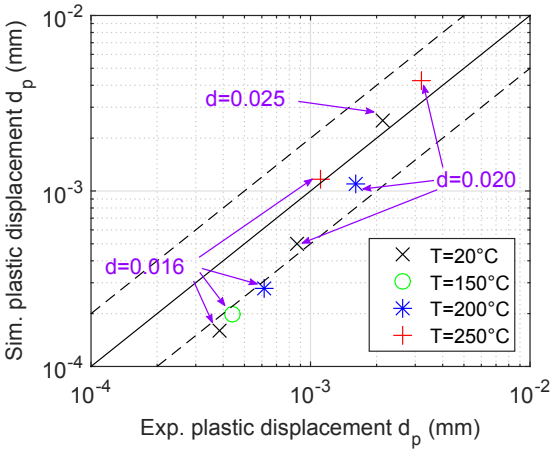

(b) Comparison of experimental and simulated equivalent plastic displacement amplitude for different temperatures and imposed displacements d (indicated in mm).

FIGURE 6.21 – Simulation for notched specimen ($K_t = 1.78$)

6.3.3 Fatigue life assessment using TCD (theory of critical distance)

In order to simulate the fatigue life, the values of the mechanical quantities along the notch ligament are extracted and the different energies are calculated (as defined in Section 3.3.2): plastic dissipated energy ΔW_p, elastic energy ΔW_e and total energy ΔW_T. Two examples are given in Figure 6.23 for ambient and high (250 °C) temperatures. While the plastic dissipated energy maximum is always located at the notch root, the maximum elastic energy can be at specimen subsurface (see Table 6.4).

Table 6.4 – Notch simulation: location of maximum elastic energy density.

Temperature (°C)	d (mm)	location of the maximum elastic energy (µm)
20	0.016	0
	0.020	84
	0.025	252
150	0.016	0
200	0.016	84
	0.020	196
250	0.016	168
	0.020	308

Fatigue life is then calculated using the fatigue criterion developed in Section 3.3.3:

$$N_f = B(\Delta W_T)^a \tag{6.3}$$

N_f being the number of cycles to failure, and B and a the material parameters identified on smooth specimens ($B = 284.15$ and $a = -1.86$, see Section 3.3.3). Defining x the distance to the notch root ($x = 0$ being the notch root and $x = 2.8$ mm the specimen center), and $\Delta W_T(x)$ the total equivalent energy at ligament location x, three different methods are used to derive the total equivalent energy (see Figure 6.24, and Section 1.4.2 for more details):

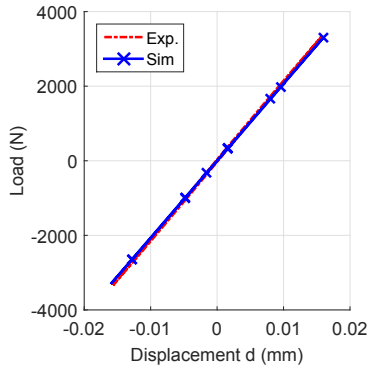

(a) $d = 0.016$mm and $T = 20\,°C$

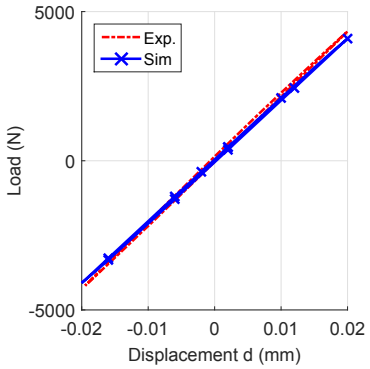

(b) $d = 0.020$mm and $T = 20\,°C$

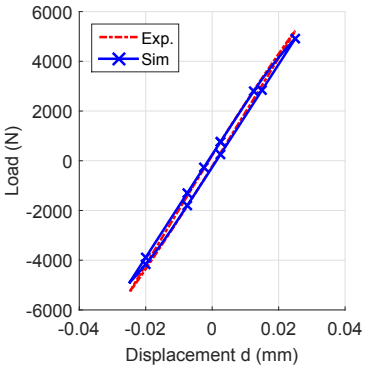

(c) $d = 0.025$mm and $T = 20\,°C$

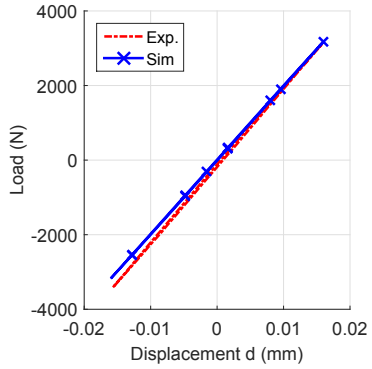

(d) $d = 0.016$mm and $T = 150\,°C$

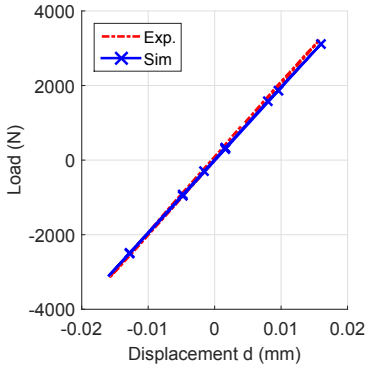

(e) $d = 0.016$mm and $T = 200\,°C$

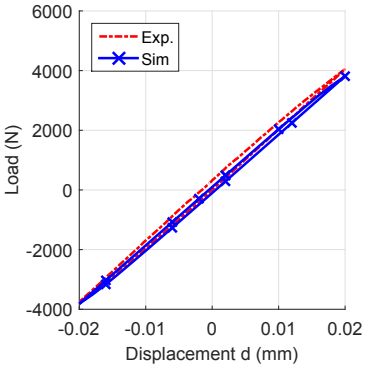

(f) $d = 0.020$mm and $T = 200\,°C$

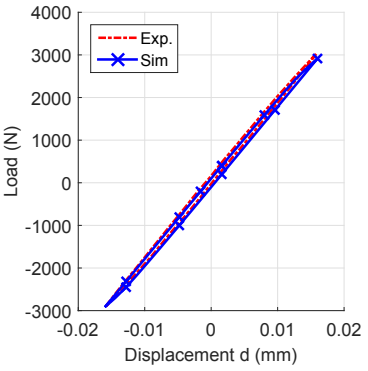

(g) $d = 0.016$mm and $T = 250\,°C$

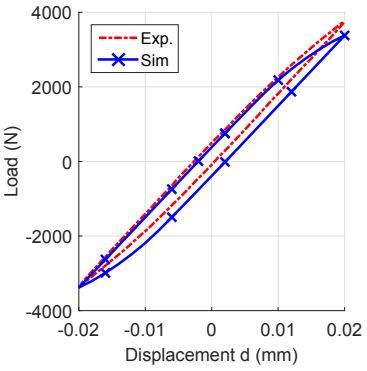

(h) $d = 0.020$mm and $T = 250\,°C$

FIGURE 6.22 – Simulation for notched specimens ($K_t = 1.78$) for cycle $N = 15$.

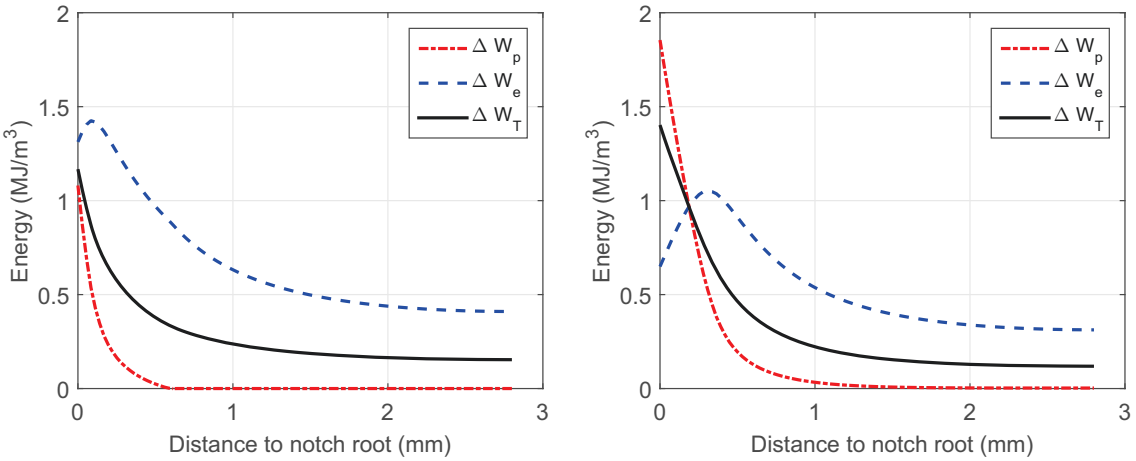

(a) $T = 20\,°C$ (b) $T = 250\,°C$

FIGURE 6.23 – Simulation of energy quantities in the notch ligament for $d = 0.020$mm at different temperatures.

— **Hot-spot approach.** The total equivalent energy ΔW_T^{HS} is defined as the value at the notch root:

$$\Delta W_T^{HS} = \Delta W_T(x = 0) \tag{6.4}$$

— **Point method** L_{PM}. Here, $\Delta W_T^{(L_{PM})}$ is defined as the total equivalent energy for a distance $L_{PM}/2$:

$$\Delta W_T^{(L_{PM})} = \Delta W_T(x = \frac{L_{PM}}{2}) \tag{6.5}$$

— **Line method** L_{LM}. The equivalent energy $\Delta W_T^{L_{LM}}$ is the average over a distance $2L_{LM}$:

$$\Delta W_T^{L_{LM}} = \frac{1}{2L_{LM}} \int_0^{2L_{LM}} \Delta W_T(x)dx \tag{6.6}$$

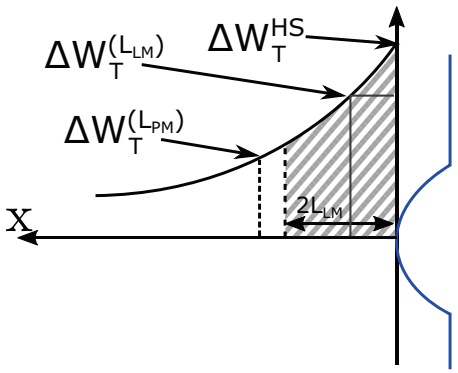

FIGURE 6.24 – Illustration of different methods to estimate fatigue life of notched specimens.

The results are shown in Figure 6.25a. Using the hot spot approach, fatigue life is clearly underestimated (roughly by a factor 10), similar to the results found in low cycle fatigue (see Bentachfine [1999], Adib and Pluvinage [2003]). For the given quantity (total equivalent energy), the maximum value is always located at the notch root.

Finding the critical distances L_{PM} and L_{LM} is done by optimizing[3] the life predic-

3. The critical distances are searched to optimize the accuracy of all the life prediction.

tion accordingly. The distances found are:

$$L_{PM} = 1120\,\mu m \tag{6.7}$$

$$L_{LM} = 910\,\mu m \tag{6.8}$$

The results are shown in Figure 6.25. Both the point and the line method provide a good fatigue life prediction, with very little differences between the two methods. The distances found are much higher than in the literature (L_{PM} between 100 and 500 µm, and L_{LM} between 50 and 400 µm in Susmel and Taylor [2010] with K_t between 1.27 and 3.24). However, the values in the literature correspond to the use of the Manson-Coffin or the so-called SWT parameter (described in Smith et al. [1970]) and were obtained only at ambient temperature.

Further investigations need to be done to confirm these statements. Especially, sharper notch geometries could help to evaluate the predictive capability of the proposed fatigue life calculation method.

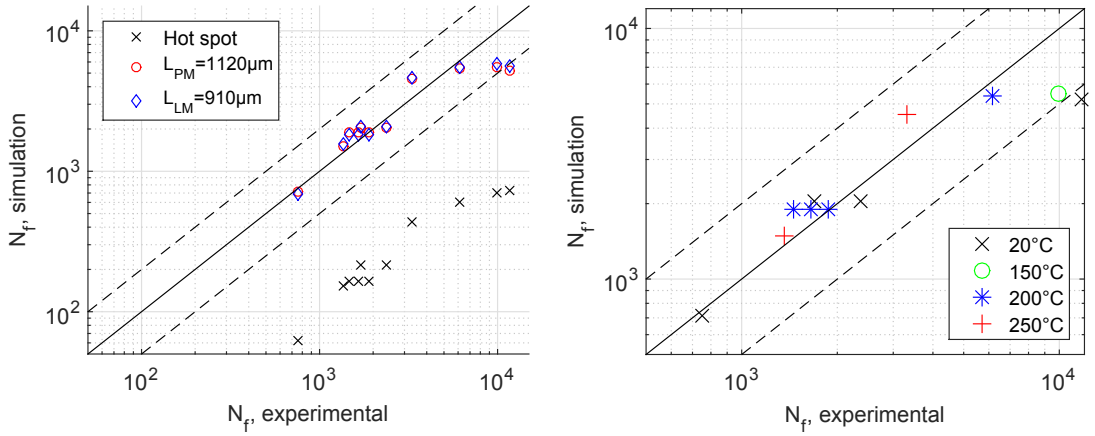

(a) Fatigue Life prediction of notched specimens using different methods.

(b) Point method (L_{PM}): zoom on simulation results and effect of temperature.

FIGURE 6.25 – Theory of Critical Distance: results of fatigue life prediction.

6.4 Fatigue life assessment of notched specimen with numerical defect generation

In this Section, a method similar to the proposal of Fjeldstad et al. [2008] is introduced. Numerical defects are generated according to spatial distribution (homogenous or clustered process), as well as each defect size. For each defect, considered individually, a life prediction can be made using the crack propagation model. The number of cycles to failure is then defined as the lowest simulated value. This critical value depends on the defect size, considered as the initial crack length, and the defect location, which modifies the mechanical values (plastic dissipated and elastic energies).

It must be noted the accurate life prediction of notched specimens would requires several steps:

1. Simulating the defect population
2. Mapping the defects location to the stress distribution of a defect free specimen (the FEM model could also take these defects into account, since they locally modify the stress distribution);
3. For each defect, estimate the crack growth. Especially, this step should use accurate stress intensity factors to take into account the particular shape (and its evolution) of the sickle shaped cracks (see Section 6.2).
4. Find the critical defect which leads to the smallest fatigue life.

Given the time allocated to the study, the crack propagation model will be identical as for smooth specimen (i.e. it will not take the modification of the crack geometry and the heterogeneous stress distribution into account).

6.4.1 Defect population generation

Firstly, a defect population is generated according to the method described in Section 5.1: defect location and the 2D Feret diameter equivalent are generated in a large window defined on $(x, y, z) \in [-5; 5]^3$. The defect location can be generated using a Poisson distribution, or a clustered one (as the one illustrated in Figure 6.26a). For this study, the clustered distribution is limited to the Thomas Point process. Each defect i is located by cylindrical coordinates (ρ_i, θ_i, z_i). For subsequent illustrations, all the defects are projected on the $\theta = 0$ cross section (see Figure 6.26b) and defects outside the virtual notched specimen are omitted.

6.4.2 FEM mapping and calculation method

Using the results of the FEM calculation in Section 6.3.2 without considering any defect, each defect can be mapped with a local value of elastic energy (see Figure 6.27a) and plastic strain energy (see Figure 6.27b). To obtain the mapping, FEM results are firstly extracted at calculation nodes and results linearly interpolated at defect location. Although the stress values are only approximate values at nodes, the fine mesh used in our FEM model allows neglecting the approximation.

After obtaining the energy values at each defect center, the crack propagation model defined in Section 5.2 is used to simulate the predicted life $N^i_{f,sim}$ of each defect:

$$N^i_{f,sim}(d_i) = \int_{d_i}^{a_f} \frac{da}{\frac{1}{\lambda}\frac{da}{dN}(\Delta W_e(\rho_i, z_i), \Delta W_p(\rho_i, z_i), a)} \tag{6.9}$$

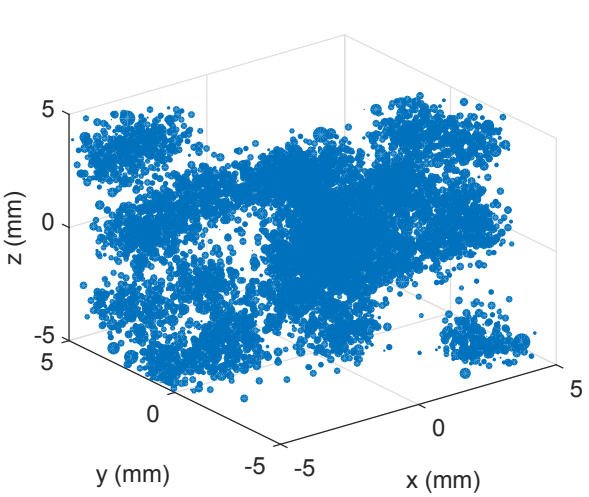

(a) 3D defect generation.

(b) 2D projection of defect position

FIGURE 6.26 – Defect population generation in a notched specimen. The diameter is proportional to the simulated 2D Feret diameter.

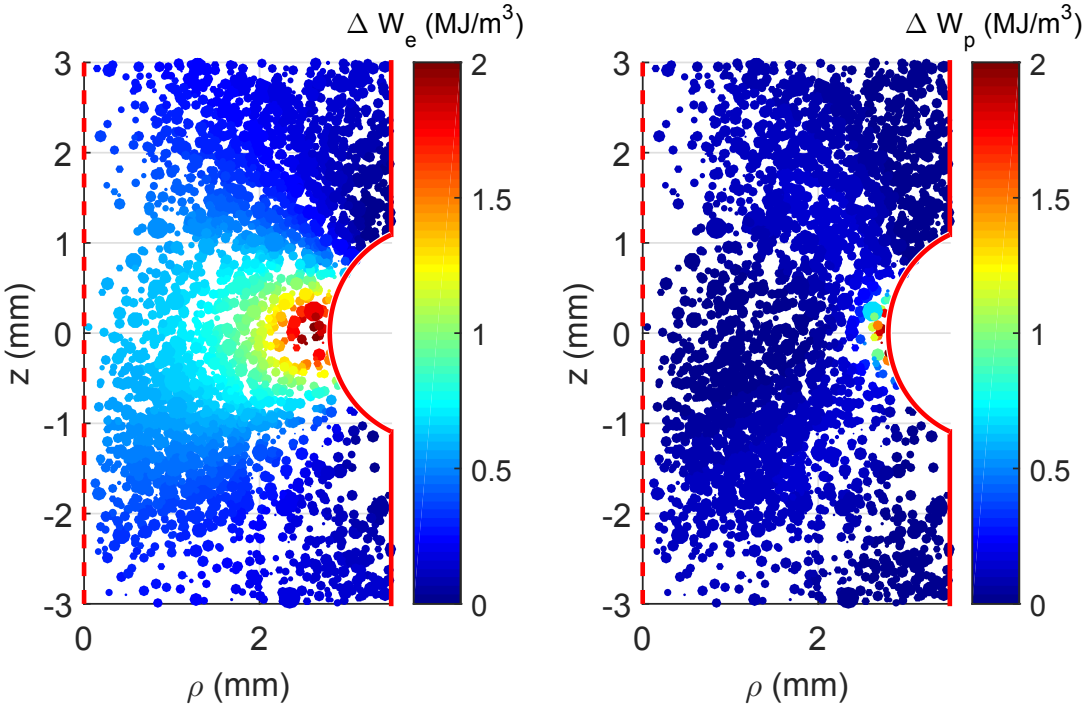

(a) Elastic energy ΔW_e

(b) Plastic dissipated energy ΔW_p

FIGURE 6.27 – Defect population generation in a notched specimen and FEM calculation mapping ($d = 0.025$mm and $T = 20\,^{\circ}$C).

where d_i is the $i-th$ defect 2D feret diameter of cylindrical coordinate (ρ_i, z_i). The angle coordinate θ is omitted given the revolution symmetry. The variable $\Delta W_e(\rho, z)$ (resp. $\Delta W_p(\rho, z)$) is the elastic energy field (resp. the plastic dissipation energy field). This calculation method is a first step towards micro structure sensitive fatigue simulation, and aims at quantifying the influence of clustering on fatigue life. Considering the notch effect, only a small volume is subjected to high loading. As observed, the damage occurs only in this highly stressed region, thereby creating a smaller representative volume element (RVE).

For a rigorous calculation, the β_e and β_p parameters should account for the notch geometry and the inhomogeneous mechanical field, as well as the change in crack front shape. Given the observed crack surfaces, the strong interaction between cracks and defects should also be taken into account to estimate fatigue lie. The results presented hereafter aim at emphasizing the effect of defect clustering on fatigue life.

Figure 6.28 shows the result of the fatigue life simulation for one specimen. Given the theoretical stress concentration at the notch root, all the shorter lives are found close to the root, even though some larger defects slightly further also predict a relatively low fatigue life.

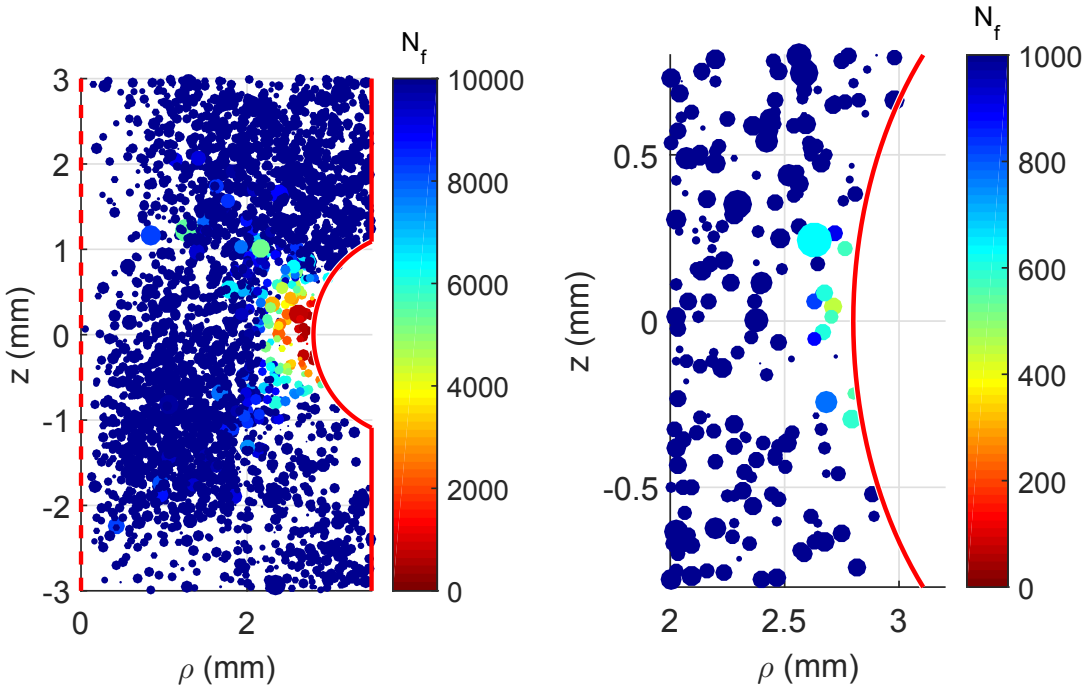

(a) Global view

(b) Zoom of notch region, notice the different in the scale of the color bar for N_f.

FIGURE 6.28 – Fatigue life simulation of number of cycles to failure (N_f) of notched specimen ($d = 0.025$mm and $T = 20\,°C$, $N_f = 753$).

Figure 6.29a presents the results in a different manner, showing the distance to the notch root is indeed a critical factor for fatigue life assessment. The critical defect, and the subsequent ones, are all located close to the notch root.

This information is useful to simulate a large number of specimens for a statistical study. The calculation time being rather important ($\approx 1\,$min for all the defects of a specimen), the number of crack propagation simulation per specimen has to be reduced. This is achieved by restraining the area for which calculation are done: only the defects closer than $r_c = 1\,$mm to the notch root are considered as critical and the corresponding

crack propagation simulation made (see Figure 6.29c).

6.4.3 Results

Figure 6.30 presents the kernel density estimate of the simulated fatigue life for $T = 200\,°C$ and $d = 0.020\,mm$ using 200 simulated specimens (using a Poisson point process). As for the round bar specimens (see Section 5.2.4), this method is able to estimate the fatigue life distribution. Due to the simulation hypothesis (the crack propagation model does not take into account the notch geometry and no interaction of the crack with other defects), the model is unable to estimate the fatigue life of the notched specimens, and the simulation clearly underestimates the observed fatigue lives. Consequently, comparisons with experimental fatigue life are only shown for illustration purposes, and focus is set on studying the effect of clustering for a small highly loaded volume.

The same method is used on all the experimental conditions. As was mentioned previously, the main interest is the influence of the numerical generation method: the spatially random process (Poisson) and the clustered one (limited here to the modified Thomas point process). This effect can be seen in Figure 6.31: the clustered point process tends to lower the value of the critical defect size.

Using this data, a mean value for each test condition can be calculated. The results follow the distribution of critical defects: for the clustered point process, the defects are slightly smaller thereby increasing the estimated number of cycles to failure (see Figure 6.32a). Furthermore, by using the 5% and 95% percentiles, the Poisson and clustered point processes simulations can be compared. The 5% percentile is strongly lowered by the clustering of defect, while the 95% percentile is only slightly affected.

While these conclusions might seem counter-intuitive, they can be explained by specific cases. Indeed, for most of the cases, there are a relatively high number of defects close to the notch root (more than 200 in the restricted area r_c): Poisson and clustered point processes, as for the smooth specimens, provide similar results. However, for some clustered point processes cases, there is a very low number of defect in the restricted area r_c. This is illustrated in Figure 6.33: the parents points of the clustered point process are all far from the notch root, causing a local low density of defects (52 in the restricted area r_c). Due to the low number of defects, the critical one is comparatively smaller (23 µm, compared to the mean values over all the specimens of 70 µm) and the estimated fatigue life higher (811 cycles, as opposed to the mean value 423).

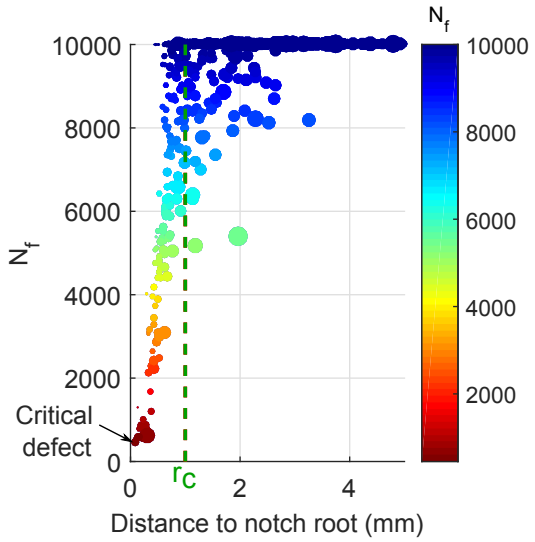

(a) Effect of distance to notch root on number of cycles to failure.

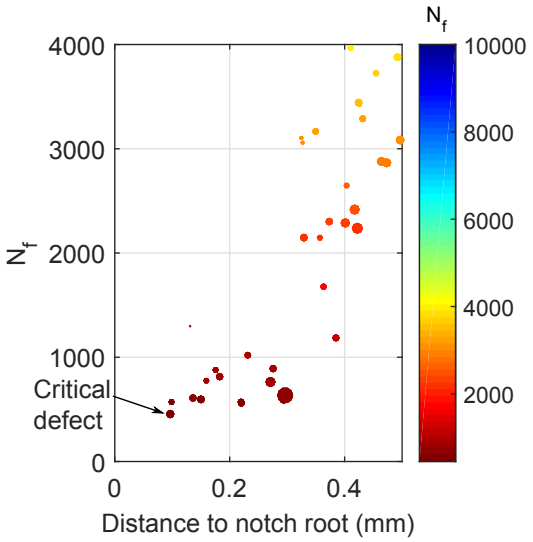

(b) Effect of distance to notch root on number of cycles to failure: zoom on the most critical defects.

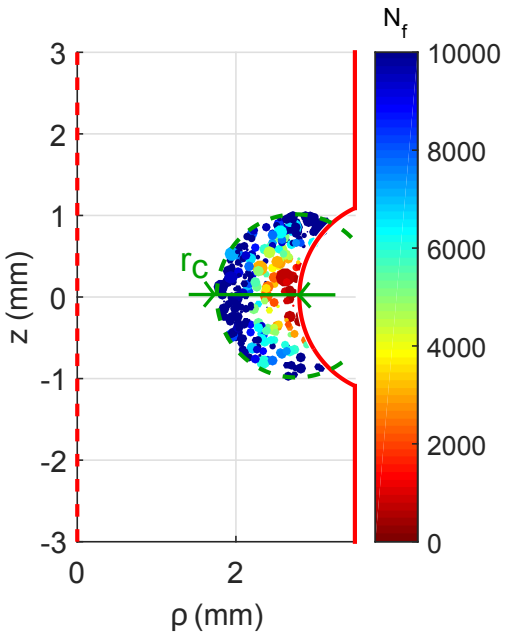

(c) Restriction of notch region: only the defects close to the notch root are simulated.

FIGURE 6.29 – Fatigue life simulation of number of cycles to failure (N_f) of notched specimen ($d = 0.025$mm and $T = 20\,°C$, $N_f = 753$).

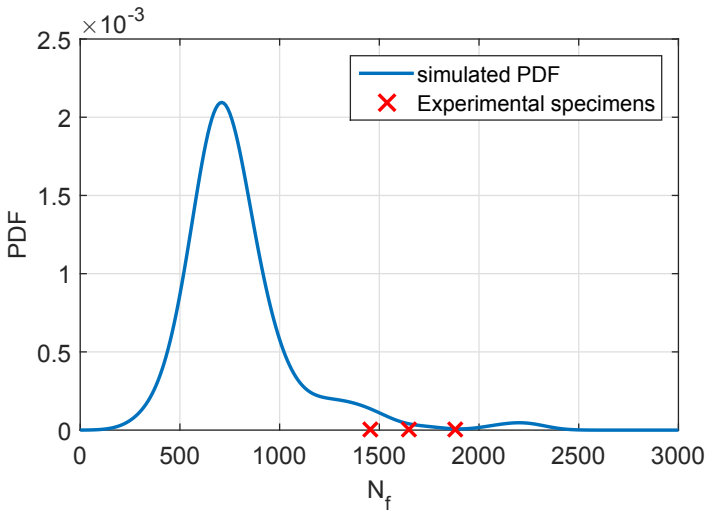

FIGURE 6.30 – Kernel density estimate of simulated fatigue life for $T = 200\,°\mathrm{C}$ and $d = 0.020\,\mathrm{mm}$ and experimental results. Numerical defects are generated by a modified Thomas Point process.

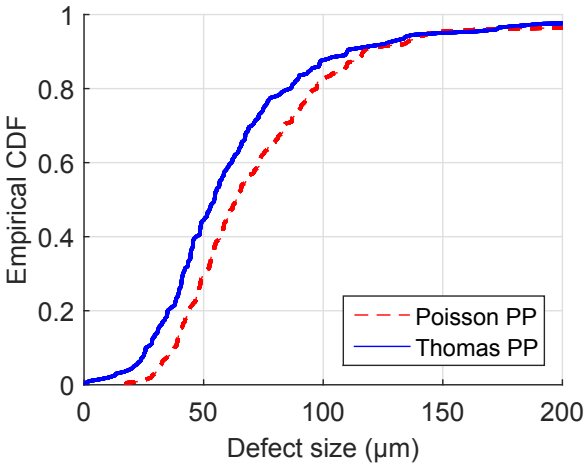

FIGURE 6.31 – Empirical cumulative distribution of simulated critical defects for Poisson point process and Thomas point process ($d = 0.016\,\mu\mathrm{m}$).

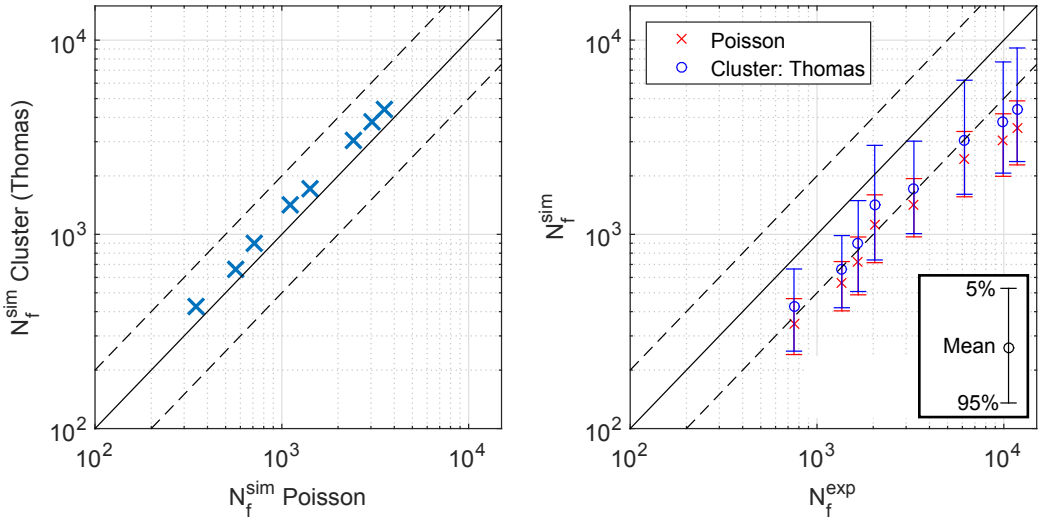

(a) Simulation of the mean number of cycles to failure: Poisson or Clustered (modified Thomas) point processes generated defects.

(b) Effect of clustering on the dispersion of fatigue life prediction, 5% and 95% percentiles are shown.

FIGURE 6.32 – Comparison of point process effect on fatigue life prediction.

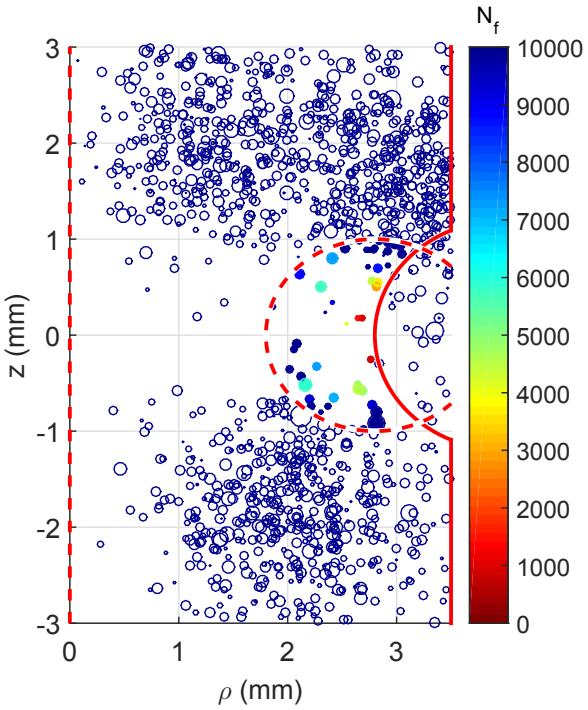

FIGURE 6.33 – Fatigue life simulation of the number of cycles to failure (N_f) of notched specimen with defects ($K_t = 1.78$, $d = 0.025$mm and $T = 20\,°C$, $N_f = 753$). Specific case of low number of defects close to the notch root. Only the fatigue lives of defects close to the notch root are calculated (full markers)

6.5 Conclusions

Notched specimens strongly modify the different mechanical fields, and damage localization appears. However, for the first stages of crack propagation, the mechanisms are similar to the ones observed on smooth specimens. Especially, there is a sufficient amount of defects for cracks to be located close to the highly loaded notch root, and crack initiation occurs on these defects. For the later stages of crack propagation, the crack shapes shifts from an elliptic shape to a sickle shape. The temperature effect on the crack mechanisms is once again similar to those observed for smooth specimens: the increase in temperature causes an intensification of the crack interaction with secondary defects.

Then, Finite Element Method (FEM) was used to simulate the behaviour of notched specimens. The macroscopic quantities simulated (load and displacement) show good agreement with the experimental results. Different fatigue damage parameters are applied, and while the Hot Spot approach provides highly conservative results, the theory of critical distance produces more accurate fatigue life estimation.

Lastly, numerical defect population (size and position) are generated and the crack propagation model applied. While the strong hypothesis (the crack shape is not taken into account) does not allow for a rigorous correlation with the experimental results, the model gives a first insight to the effect of clustering on the fatigue of notched specimens: clustering tends to lower the size of the critical defect. However, this has to be confirmed by additional study of the crack propagation model applied to notched specimens.

Conclusions and prospects

Aluminium alloys and fatigue have been studied for more than a century. The literature survey has showed us many parameters influence fatigue mechanisms. While some factors have been investigated for a long time (such as chemical composition, heat treatment, Secondary Dendrite Arm Spacing), only recently has precise porosity characterization and its relationship with fatigue been possible. Indeed, development of laboratory X-ray tomography has made this technology more accessible and precise, allowing for the scan of a cubic centimetre in a few hours, and the subsequent 3D detection of defects down to a few micrometers. Applied to tested specimens, tomography also allows for a better understanding of the fatigue mechanisms: defects and the interaction with crack can be visualized and quantified. However, the huge amount of data requires extensive numerical treatment and specific tools.

In the second chapter, after a brief presentation of the classical microstructural features (chemical composition, dendritic/eutectic phase and intermetallic characterization) focus is put on the 3D characterization of porosity. Statistical inference and sensitivity study allows for a robust characterization of the porosities. Since only the largest defects are of interest, the tail of the size distribution is studied. It is shown that the generalized Pareto distribution is the most adequate, and captures the most appropriate features of the distribution. Three specimens are studied demonstrating the considered fatigue specimens represent a statistical population with respect to porosity size, and that tomography image treatment is robust. The study of the sphericity and its correlation with size confirms the representativeness of the considered specimens. Lastly, the spatial distribution of defect is investigated. It is clearly shown the defects are not randomly distributed: they aggregate into clusters and can be modelled by adequate cluster point processes. Furthermore, the correlation of defect size with location is analysed by marked point processes and size and location appear uncorrelated. The clustering of defects slightly undermines the aforementioned representativeness: while a specimen contains several thousands of defects, the causal parent points (each virtual parent point generating hundreds of defects) are only in the tens, suggesting there are only a few clusters of defects per specimen.

In the third chapter, the fatigue test results are presented. Careful best practices are used to minimize the test dispersion: the measurement uncertainty are quantified and can indeed be neglected with respect to the standard uncertainties associated with low cycle fatigue. The tests are repeatable and the observed dispersion can undoubtedly be linked to the intrinsic random nature of fatigue. In order to be used in an industrial context, a first fatigue criterion is developed. While the Manson-Coffin criterion provides satisfactory results for the different temperatures, it does not provide unified parameters. Moreover, for the high temperatures, the quantities used to evaluate the Manson-Coffin criterion change during the test and their evaluation becomes an issue. By means of energies derivations, a stable equivalent energy is calculated and considered as representative of the fatigue life. Indeed, used together with a classical

power law, it provides an accurate empirical model for assessing the fatigue life of this aluminum alloy with temperature-independent parameters. An empirical model of the observed dispersion using a non-constant standard deviation improves the model fit and confirms the classical observation: the scatter diminishes together with the expected fatigue life.

The fourth chapter presents a detailed investigation of the fatigue mechanisms by several techniques (crack popagation monitoring, SEM and EDS analysis, X-ray tomography). Combined, they provide insights on crack initiation and propagation, and especially the influence of defects. As is observed in literature, cracks originate on defects close to the surface. These defects are observed and their features quantified: size, nature (gas or shrinkage) and location (noticeably the distance to the specimen surface). It is shown that size combined with location determines the harmfulness of a defect. In the specimen core, larger defects than the crack originating one exist. While some produce small cracks, especially for the higher temperatures, they do not cause final failure. The mechanisms of the crack are also unveiled. While a void defect provides the main cause for the crack, microstructural features such as intermetallics and eutectic phase at the defect frontier confer stress raiser, thereby assisting crack initiation. A specifically designed crack monitoring set-up with a digital camera provides crack length monitoring, as well as a large surface observation window. While the crack initiation on an artificial defect takes approximately 20% of the total fatigue life, some natural cracks initiate rapidly (less than 5% of the total fatigue life), thus validating the common hypotheses of a crack propagation driven total fatigue life (as opposed to an initiation, or initiation/propagation one). The crack propagation and the interaction with defects is then studied. The difference between the first steady-stage crack (which appears flat and smooth) and the final stages of propagation (much more uneven and rough) are observed. As the main crack propagates, it interacts with secondary cracks that have developed concomitantly on other defects. This interaction is amplified for the higher temperature where crack coalescence becomes predominant.

In the fifth chapter, numerical specimens containing a defect population are generated. The largest defects of these numerical specimens are compared to the critical defects which caused the main crack in low cycle fatigue tests. If the largest defect is considered for the whole specimen, the numerical representation overestimates the observed critical defects. However, results of the fourth chapter have shown only the defects close to the surface are prone to cause the main crack. Therefore a ring sample (i.e. a tube in 3D) is used: only the numerical defects close to the specimen surface (300 µm) are considered to be potentially harmful. Using this hypothesis, the numerical simulation allows a good estimate of the observed critical defects size. This also implies only the outer ring (namely around 15% of the whole volume) constitutes a representative volume of the defect population for the crack initiation mechanism. A crack propagation model is then used to estimate the crack propagation rate. Using the fatigue test series on smooth specimens, the parameters are identified, and the model predictions compared to the crack propagation monitoring experiments. The model is capable of correctly estimating the crack growth rate, considering the critical defect size as the initial crack length. Combined with the numerical simulation of defects size and position, this model can simulate the distribution of the number of cycles to failure for a given condition based on numerical defect size distribution.

Finally, in the sixth chapter, notched specimens are tested. While similar in the first stages, the mechanisms are slightly modified by the heterogeneous mechanical field. Especially, the crack front shape transforms into characteristic sickled shapes.

Finite element simulation is then used on the notched specimens and enables the use of the local fatigue criterion. It is shown that the local hot spot approach is unable to estimate the fatigue lives, while the line and point methods give a good estimate. However, further tests on different notch geometries are necessary to assure the non-local damage parameter validity. Lastly, the numerical defects are placed in the mechanical field created by the notch (and estimated by FEM without considering any defects). For each defect population generated, each single defect is located at a unique point in the specimen. Using the crack propagation model, and several hypotheses, a number of cycles to failure can be estimated for each defect, and the critical defect identified. Similarly to the previous chapter, this allows the simulation of the statistical distribution of fatigue lives based on the size and spatial distribution of the defects. It is shown that for most of the cases, Poisson and clustered point processes give similar results. However, some configuration specific to the clustered point processes (where only a few defects are located close to the notch root) result into smaller critical defects, thereby producing a higher estimation of the number of cycles to failure and showing the importance of spatial distribution of defects for the understanding of the fatigue damage mechanisms.

For future works, several aspects could be further studied:

— **Statistical features of defect populations**: the statistical methods developed could be applied to several specimens. Firstly, this could confirm the robustness of the method by comparing the extreme value statistics inferred and observed. Secondly, specimens from several batches of cast material (all the batches of this study were cast at once in identical conditions) could be studied, and the scatter between batches observed. The third aspect, which has already been started, aims at studying defect populations of specimens extracted from real component.

— **Fatigue damage mechanisms**: combination of different observations techniques show promising results to better understand the mechanisms. Recently, use of *in-situ* synchrotron tomography (Dezecot et al. [2016]) could help apprehending the intermediate states of the crack propagation. However, these experiments often use much smaller specimens and the help of the characterization of the defect population presented herein could help validate the representativeness of these experiments.

— **FEM simulation**: using the microstructure observed by tomography, FEM studies on simplified and real microstructures can be achieved. However, several barriers have to be overcome such as local material heterogeneities, convergence of simulations, crack geometry modelling. Recent studies (see for example Wang [2015], Limodin et al. [2014]) show these simulation can be combined with Digital Image correlation (in 2D and in 3D) in order to ascertain the accuracy of the simulations.

— **Crack growth simulation**: the simulation of crack propagation using the crack like defect (the defects are considered as initial cracks) approximation also shows promising results. Further studies are necessary to better take into account the defects morphology and location into the model. Especially, the model should be able to differentiate a defect at the specimen surface, from one located further inside the specimen.

Résumé

Introduction

L'étude présentée ici s'inscrit dans le cadre d'une thèse CIFRE, fruit de la collaboration entre Renault (DEA-TC, Guyancourt, France) et l'institut de recherche I2M (Institut de Mécanique et d'ingénierie, CNRS UMR 5295, Bordeaux, France). Prof. Bruno Sudret (BS Conseil) a également collaboré en apportant un support pour les études statistiques.

Les alliages d'aluminium sont utilisés dans l'industrie automobile depuis plusieurs années. De par leurs caractéristiques mécaniques spécifiques et leur excellente coulabilité, ils constituent un excellent choix pour des pièces fortement sollicitées, telles que les culasses automobiles qui sont soumises à de fortes contraintes mécaniques et thermomécaniques. De plus, les alliages d'aluminium constituent une bonne alternative pour les aspects de réduction de poids, critère crucial dans le cadre des réductions d'émission. Enfin, d'un point de vue industriel, les alliages d'aluminium sont présents mondialement pour des coûts faibles. En y ajoutant leur bonne propension au recyclage, ils sont souvent le meilleur choix pour la fabrication de culasses automobiles.

Plus précisément, la sollicitation qui fera l'objet de cette étude concerne l'influence de la température. En effet, certaines zones de la culasse peuvent être soumises à des températures élevées (jusqu'à 250 °C) qui, combinées à des contraintes liées à la structure, soumettent les pontets inter-soupapes à de la fatigue thermomécanique (fatigue TMF). Bien qu'il soit possible de reproduire ces conditions thermomécaniques, ces essais sont complexes et difficiles à interpréter. Ainsi, cette étude se focalisera sur la fatigue oligocyclique à chaud, dans le but de mieux comprendre l'influence des défauts sur les mécanismes de l'endommagement en fatigue. Certains aspects de la microstructure et du matériau (espacement interdendritique, intermetallique, traitement thermique) ont fait l'objet de nombreux articles scientifiques. Cependant, la littérature est moins complète concernant l'effet des porosités sur la tenue en fatigue. Cette étude des défauts de porosité constitue un des points clefs de ce travail. La population de ces défauts peut en effet être analysée en 2D (voir Murakami [1993]), voire en 3D par l'utilisation de tomographie (comme dans l'étude Buffière et al. [2002]), mais cette identification doit se faire en utilisant les outils statistiques appropriés.

Afin de mieux comprendre la tenue en fatigue de l'alliage d'aluminium considéré et de proposer un critère de fatigue approprié, les objectifs de la présente étude sont:

— Utiliser les outils statistiques disponibles afin de caractériser la population de défauts (en taille et en position) ;

— Observer les différents mécanismes d'endommagement en fatigue, et plus particulièrement en prenant en compte les défauts et les différentes interactions (entre défauts, mais aussi entre la fissure principale et les défauts secondaires) ;

— Étudier la taille du volume statistiquement représentatif utilisé pour la génération de microstructures (par le numérique et en combinaison avec des essais sur éprouvettes entaillées), et son impact sur les statistiques des valeurs extrêmes de défauts. Ceci afin de proposer un modèle prenant en compte ces défauts pour la simulation de la durée de vie en fatigue.

Le manuscrit est organisé en six chapitres.

Dans le premier chapitre, une revue bibliographique présente les alliages d'aluminium et leurs spécificités. La fatigue à température ambiante est ensuite étudiée, et les différents mécanismes observés, notamment avec les études traitant de l'influence des porosités sur la durée de vie en fatigue. Les modifications provoquées par l'augmentation de la température sur les essais en fatigue sont ensuite détaillées et plusieurs critères adaptés sont présentés. Un critère utilisant les différentes énergies de déformation semble se distinguer, car adapté aux essais présentant d'importantes déformations plastiques.

Dans le second chapitre, après une brève étude classique de la microstructure (déjà examinée en profondeur dans la littérature scientifique), la population de défauts est analysée (tailles et positions des défauts). À l'aide d'observations de tomographie de laboratoire, une inférence statistique robuste de la distribution en taille est faite, et il est montré que cette distribution est représentative. Par la suite, l'utilisation de processus ponctuels permet de caractériser de manière quantitative la distribution spatiale des défauts, et démontre que ceux-ci se présentent sous forme d'agrégats (*clusters*).

Dans le troisième chapitre, une campagne d'essais en fatigue oligocyclique classique sur éprouvettes cylindriques lisses est détaillée. Après avoir illustré les problèmes liés à l'utilisation du critère de Coffin-Manson, un critère énergétique est appliqué. Il permet de correctement prévoir la durée de vie des éprouvettes, tout en restant applicable dans un contexte industriel (facilité d'application et robustesse).

Le quatrième chapitre se focalise sur les mécanismes d'endommagement en fatigue oligocyclique. En utilisant diverses méthodes d'observation (Tomographie, Microscopie à Balayage Electronique, appareil photo numérique), l'impact fort des porosités sur les mécanismes d'initiation et de propagation de fissures est démontré. L'effet de l'augmentation de température sur les mécanismes est aussi mis en évidence.

Le cinquième chapitre combine les résultats des chapitres précédents et fait le lien entre la distribution de défauts observés sur les éprouvettes non testées, et la distribution de défauts critiques observés sur les faciès de rupture. Il est démontré que la position des défauts dans l'éprouvette ne peut être négligée pour la simulation des défauts critiques. Enfin, un modèle de propagation de fissure prenant en compte la taille des défauts critiques est présenté.

Enfin, dans le sixième chapitre, les essais sur éprouvettes entaillées sont présentés. Une série de 11 essais permet de faire une première étude sur l'impact de la concentration de contraintes sur la durée de vie en fatigue oligocyclique à chaud. Cette concentration de contraintes permet en effet de réduire le volume fortement sollicité mécaniquement, et donc de réduire le nombre de défauts soumis à un champ de contraintes sévère.

Chapitre 1 : étude bibliographique

Dans un premier temps, l'étude bibliographique présente les alliages d'aluminium et plus spécifiquement les alliages aluminium-silicium. En effet, ces alliages sont par-

ticulièrement utilisés dans l'industrie car ils présentent des propriétés mécaniques intéressantes. La solidification sous forme de dendrites, caractéristique de ces alliages, est détaillée. Les différents éléments d'addition, qu'ils soient intentionnels ou non, sont listés. Alors que l'addition de cuivre et/ou de magnésium provoquent un durcissement structural, les impuretés (notamment le fer, voir la figure 6.34) peuvent conduire à des composés nocifs à la tenue mécanique. Enfin, les procédés d'élaboration sont également listés.

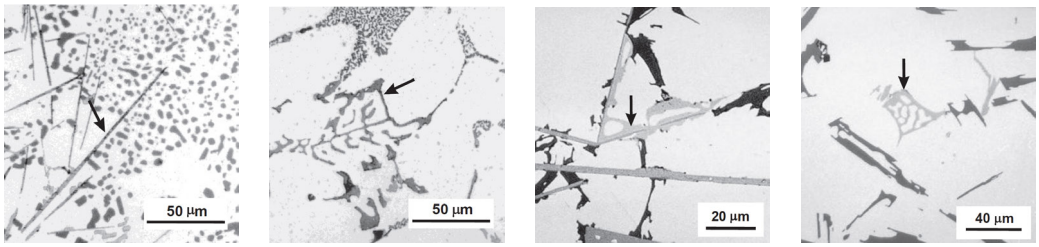

(a) (b) (c) (d)

FIGURE 6.34 – Exemples d'intermetalliques dans un alliage AS5U1G (Taylor [2012]) (a) plaquettes β-Al_5FeSi; (b) écritures chinoises α-$Al_8FeMg_3Si_6$; (c) phase π-$Al_8FeMg_3Si_6$; (d) phase π en écriture chinoises

Dans la deuxième partie de l'étude bibliographique, l'endommagement en fatigue à température ambiante est étudié. Bien que notre travail porte sur une microstructure spécifique avec un espacement interdendritique (SDAS) constant, il est intéressant d'observer en premier lieu l'influence du SDAS sur la tenue mécanique. En effet, ce paramètre est d'ordre un et conditionne la tenue en fatigue à composition chimique constante. Cependant, il faut noter qu'il est très difficile de décorréler la valeur du SDAS des autres composants microstructuraux et du taux de porosité. Par la suite, l'influence des porosités sur la durée de vie en fatigue est présentée. Pour la tenue en fatigue oligocyclique, la taille et la position par rapport à la surface des défauts apparaissent comme les facteurs critiques (voir tableau 6.5).

Dans la troisième partie de l'étude bibliographique, la fatigue oligocyclique à chaud est présentée. En remarquant que le critère de Coffin-Manson n'est pas le plus adapté dans une optique future de fatigue thermomécanique (ce qui sera démontré dans la partie 3.3.1), les critères énergétiques sont introduits. Contrairement au critère de Coffin-Manson, les critères énergétiques se montrent à même de prévoir la durée de vie en fatigue (voir figure 6.35), tout en utilisant des paramètres indépendants de la température. De manière plus microscopique, l'effet des porosités est illustré. Comme pour la fatigue oligocyclique à température ambiante, les porosités sont critiques pour la durée de vie et leur caractérisation précise nécessaire.

Dans la quatrième et dernière partie de l'étude bibliographique, l'effet des concentrations de contraintes sur éprouvettes est détaillé. Bien que notre travail se concentre sur la fatigue oligocyclique (dans notre cas en plasticité généralisée), l'effet d'entaille a le plus souvent été étudié en fatigue à grande durée de vie. Ainsi, les méthodes en élasticité linéaire sont présentées. L'approche dite du "point chaud" consiste à considérer le point le plus sévèrement sollicité mécaniquement comme le point représentatif du phénomène de fatigue. Il est alors montré dans la littérature que cette approche est bien trop sévérisante et qu'il faut tenir compte des champs mécaniques de manière plus globale. Par exemple, la théorie de la distance critique (TCD) suggère que le phénomène de fatigue nécessite un volume pour se développer. La contrainte effective utilisée

Table 6.5 – Rupture en fatigue d'un alliage A319 avec différentes amplitudes de déformation De-Feng et al. [2010]

Échantillon	Amplitude de déformation (%)	Durée de vie en fatigue(cycles)	Aire du pore (mm^2)	Distance du pore à la surface (μm)
1	0.2	24806	0.0930	10
2	0.2	78322	0.0237	25
3	0.2	51244	0.0256 0.0272	Coalescence de deux pores
4	0.2	38542	0.0841	10
5	0.2	51668	0.0441	0
6	0.25	11734	0.0247	80
7	0.25	13269	0.0437	0
8	0.25	8567	0.0600	30
9	0.25	6701	0.1521	0
10	0.3	3119	0.0812	0
11	0.3	4503	0.0635	50
12	0.3	1119	0.1406	0

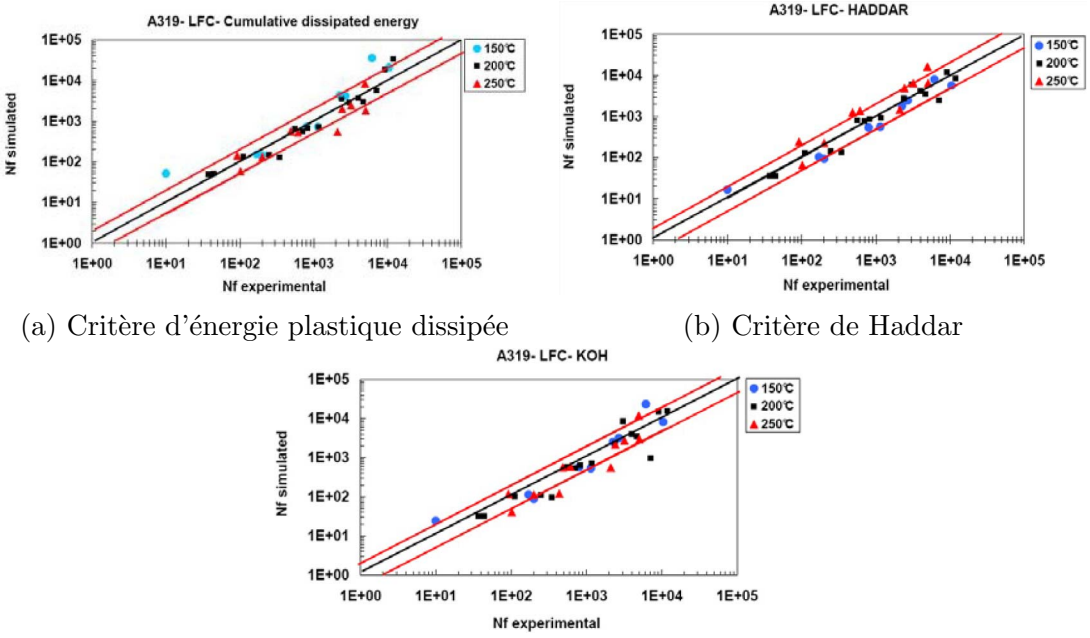

(a) Critère d'énergie plastique dissipée

(b) Critère de Haddar

(c) Critére de Koh

FIGURE 6.35 – Simulation des durées de vie en fatigue d'un alliage A319 en fatigue oligocyclique à chaud (T=150, 200 et 250 °C), Tabibian et al. [2010]

pour comparer la limite de fatigue avec celle sur éprouvette lisse peut être calculée de différentes manières :

— méthode du point : la contrainte effective est la contrainte prise à une distance spécifique du fond de l'entaille ;
— méthode de la ligne : la contrainte effective est la contrainte moyenne prise sur un segment :
— méthode de l'aire : la contrainte effective est la contrainte moyenne prise sur une surface.

Enfin, l'effet d'entaille en élasto-plasticité est présenté. Une méthode s'appuyant sur la théorie de la distance critique montre de bons résultats (voir figure 6.36). En lieu et place de la contrainte, cette méthode utilise une énergie de déformation effective, qui est la moyenne de l'énergie de déformation sur un volume donné.

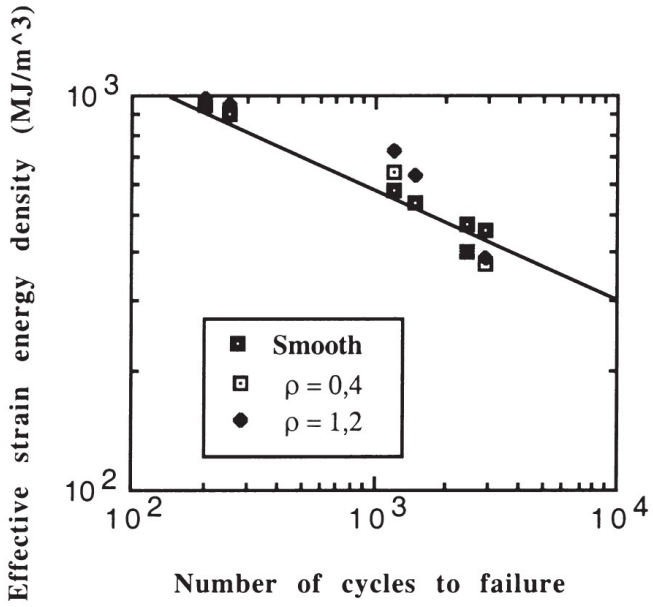

FIGURE 6.36 – Nombre de cycles à rupture en fonction de l'énergie de déformation plastique calculée (énergie effective dans les cas d'éprouvettes entaillées. Le trait plein correspond à la régression sur les essais sur éprouvettes lisses, Bentachfine [1999]

Chapitre 2 : étude microstructurale

Dans le chapitre 2, les méthodes classiques d'observation sont utilisées dans un premier temps pour caractériser le matériau. L'espacement interdendritique, les zones eutectiques et les intermétalliques sont étudiés. Par la suite, la tomographie rayons-X de laboratoire est présentée et appliquée à l'étude de la porosité dans le matériau. En effet, comme il sera plus tard démontré, les défauts (porosités dues au gaz et retassures) jouent un rôle essentiel dans les mécanismes de la fatigue oligocyclique, et il est nécessaire de caractériser la population de défauts.

Après avoir présenté les problématiques spécifiques liées à la tomographie (volume important de données, traitement d'images, méthodes d'analyse d'images), une inférence statistique de la distribution des défauts en taille (diamètre de Feret mesuré par tomographie) est présentée. Il est montré que la distribution généralisée de Pareto

permet de modéliser les défauts pertinents. En effet, la criticité des défauts est liée à leurs tailles, et seuls les plus gros défauts sont critiques. La distribution généralisée de Pareto se focalise sur les queues de distributions (ici les défauts supérieurs à 40 µm) en négligeant les plus petits défauts. La figure 6.37 présente les résultats de l'identification de la distribution de défauts avec les distributions empiriques observées, et démontre que chaque échantillon constitue un volume élémentaire représentatif de la distribution en taille des défauts.

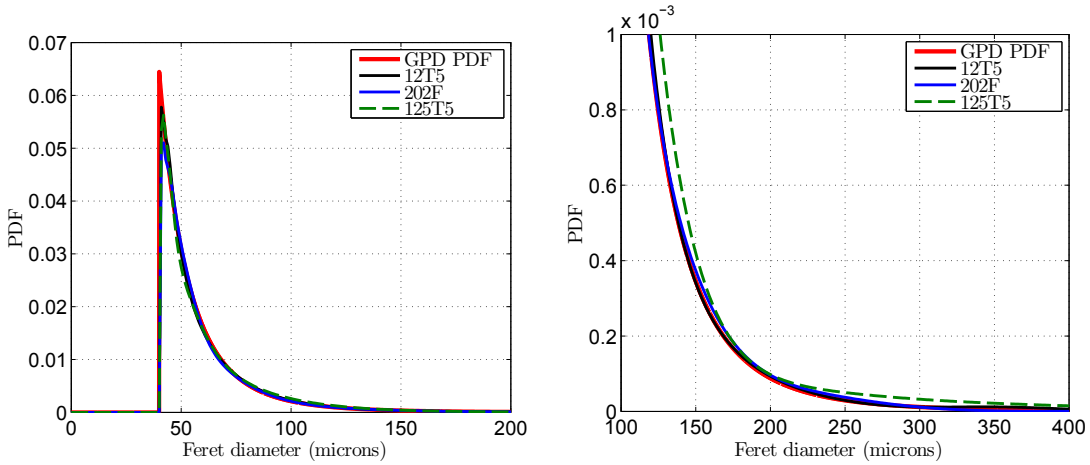

(a) Distribution globale (b) Queues de distributions

FIGURE 6.37 – Estimation par densité à noyaux de 3 échantillons et comparaison à la distribution généralisée de Pareto (GPD) identifiée sur l'échantillon 12T5.

Par la suite, l'attention est portée sur la distribution spatiale des défauts. Les processus ponctuels sont les modèles appropriés pour étudier ces distributions. En se basant sur les distances entre chaque défaut (ici considéré comme des points), il est possible de conclure quant à la nature de ces processus ponctuels: les points sont-ils distribués aléatoirement dans l'espace (processus de Poisson), ou sont-ils attirés (processus agrégés) les uns par les autres? La figure 6.38 présente les résultats de cette étude au travers de la fonction classiquement utilisée (fonction K de Ripley) pour l'étude des processus ponctuels. Ainsi, la répartition aléatoire, représentée par le processus ponctuel de Poisson, ne permet pas de corréler avec les observations expérimentales. Au contraire, après optimisation des paramètres, il est démontré que les processus ponctuels agrégés (ici de Thomas ou de Matérn) permettent de décrire les caractéristiques essentielles des distributions spatiales observées.

Enfin, les processus ponctuels marqués sont introduits. Ils font le lien entre une caractéristique (ici la taille des défauts) et leur position spatiale. Il est ainsi démontré qu'au premier ordre, la taille des défauts est indépendante de leur position dans l'éprouvette.

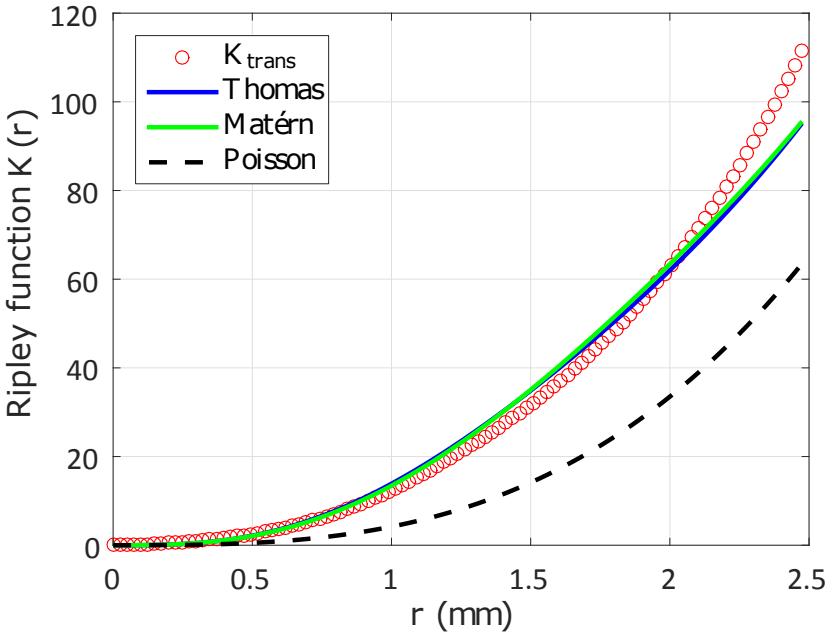

FIGURE 6.38 – Processus poncuels: fonction K_{trans} de Ripley estimée et comparaison avec les processus ponctuels agrégés (Thomas et Matérn) et totalement aléatoire (Poisson).

Chapitre 3 : Campagne d'essais de fatigue.

La campagne d'essai de fatigue oligocylique réalisée dans le cadre de travail sur éprouvettes lisses est présentée. Pour les essais à température inférieure ou égale à $T = 200\,°C$, le comportement mécanique cyclique de l'alliage étudié est stable dès les premiers cycles. Au contraire, à température élevée ($T = 250\,°C$), le matériau s'adoucit cycliquement. Ce mécanisme est analysé, et les observations en microscopie en transmission (TEM) confirment qu'il s'agit d'un mécanisme de vieillissement par croissance des précipités (voir figure 6.39).

Dans un premier temps, les résultats en fatigue sont analysés en utilisant le critère de Manson-Coffin. Celui-ci donne de bons résultats, mais ne permet pas une unification des résultats : les paramètres dépendent de la température. Une quantité énergétique équivalente ΔW_T, basée sur une combinaison linéaire de l'énergie de déformation élastique et de l'énergie de déformation plastique est alors introduite. Combinée à une loi puissance, elle permet de prévoir les durées de vie expérimentales (voir figure 6.40). Cette loi présente deux avantages: les paramètres (au nombre de trois) sont indépendants de la température et le calcul des énergies de déformation mises en jeu est peu sensible au choix du cycle.

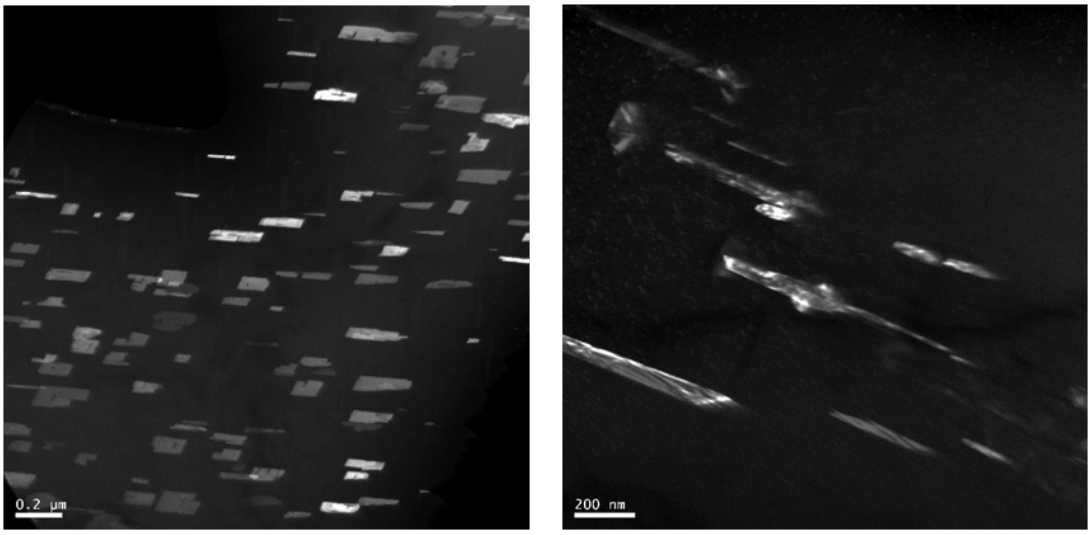

(a) TEM champ sombre: condition initiale

(b) TEM champ sombre: condition vieillie (72h à $T = 250\,°C$)

FIGURE 6.39 – Évolution des précipités Al_2Cu par vieillissement thermique, observation en microscopie en transmission.

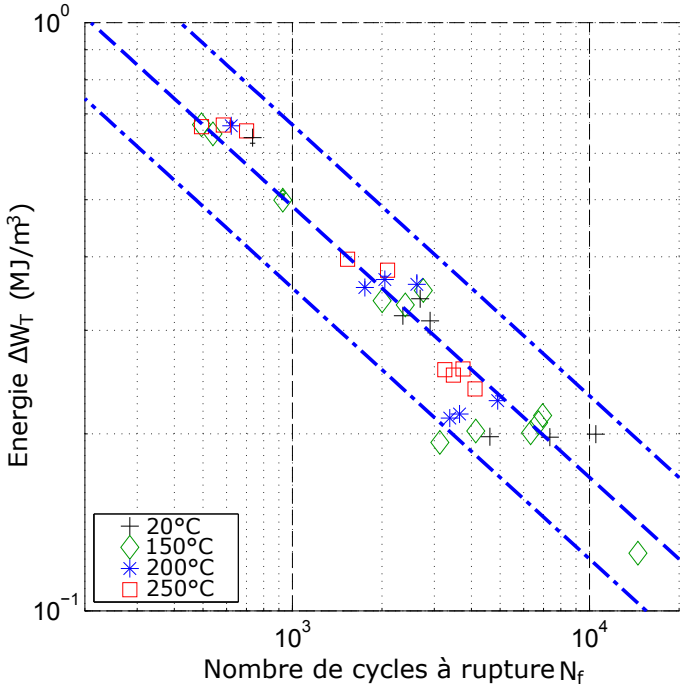

FIGURE 6.40 – Énergie équivalente totale en fonction du nombre de cycles à rupture.

Chapitre 4 : Mécanismes d'endommagement en fatigue oligocylique

L'objectif de ce chapitre est d'analyser en détail les mécanismes d'endommagement en fatigue oligocyclique à chaud de l'alliage d'aluminium étudié. En particulier, l'impact des défauts sur l'amorçage et la propagation de fissure sont observés. Dans un premier temps, une analyse systématique des faciès de rupture permet la compréhension des mécanismes d'amorçage. En effet, grâce à l'observation en microscopie électronique à balayage, il est montré que l'amorçage se produit sur des défauts de fonderie (porosités dues au gaz et retassures) localisées proches de la surface de l'éprouvette (voir figure 6.41). Complétée par une analyse dispersive en énergie, il est également montré que les intermétalliques et les précipités (type Al2Cu) situés à la frontière des défauts contribuent également à favoriser l'amorçage.

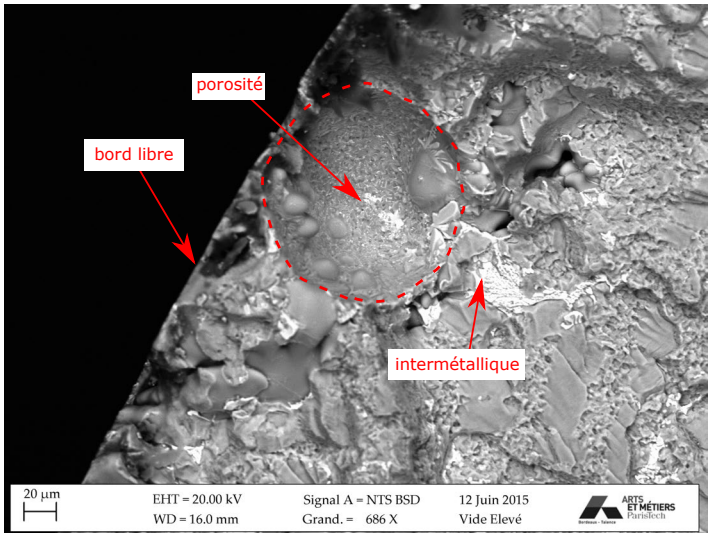

FIGURE 6.41 – Exemple de porosité due au gaz en bord d'éprouvette

Par la suite, les défauts clairement identifiés sont mesurés. Il est alors possible d'inférer une distribution statistique qui sera par la suite comparée aux valeurs simulées (voir figure 6.45). En complément, deux spécimens interrompus (quelques cycles avant la rupture finale) sont analysés par tomographie. Cette analyse montre l'importance de la localisation des défauts : alors que des défauts au diamètre de Feret plus important sont présents au cœur de l'éprouvette (de diamètre 250 à 300 µm), la fissure principale s'amorce sur un défaut plus petit (environ 150 µm), mais localisé en bord d'éprouvette, comme le montre la figure 6.42.

À l'aide d'un suivi de fissure par appareil photo numérique spécialement développé pour les éprouvettes cylindriques, l'initiation et la propagation de fissures sont observées. Grâce à la grande fenêtre d'observation (10×4 mm), de nombreux amorçages de fissures sont observés en plus de celui sur défaut artificiel. Ces fissures apparaissent rapidement pendant les essais et confirment que la durée de vie en fatigue oligocyclique est contrôlée par la propagation de fissures, comme le montre la figure 6.43. La distinction entre fissuration par fatigue et rupture finale est ensuite clairement établie, notamment à l'aide d'une reconstruction tridimensionnelle des faciès de rupture analysée par tomographie : la fissuration par fatigue se développe perpendiculairement au chargement (en mode I), avec peu d'interactions avec la microstructure, alors que la rupture finale se fait en suivant les zones eutectiques et en interagissant avec les défauts

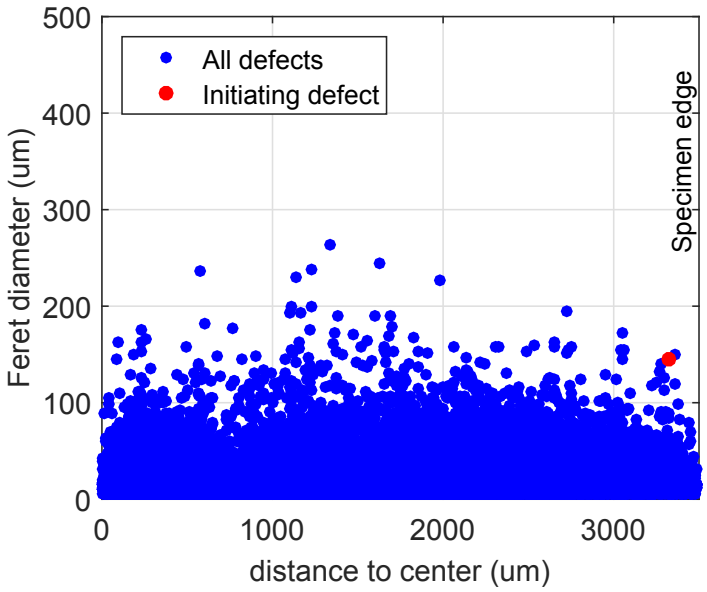

FIGURE 6.42 – Le défaut critique (Initiating Defect) est situé proche de la surface de l'éprouvette.

secondaires.

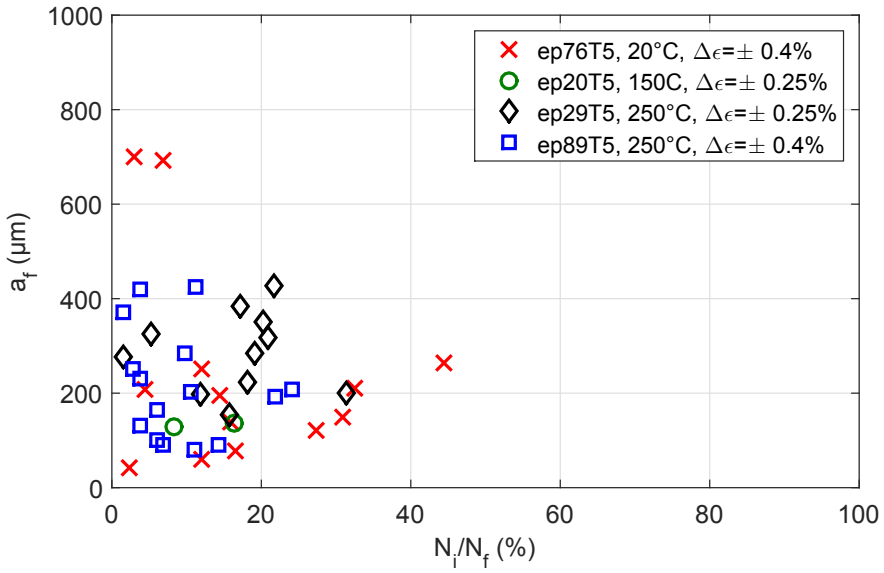

FIGURE 6.43 – Proportion de phase d'initiation (N_i) et de propagation (N_f) de la propagation de petites fissures, et longueur finale de fissure (a_f). Chaque marqueur représente une petite fissure avec sa longueur finale, et la fraction de durée de vie pour l'amorçage de cette même petite fissure.

Enfin l'effet de la température est étudié. Avec l'augmentation de la température, les surfaces de rupture montrent une rugosité plus importante, correspondant à une augmentation de la part de fissuration dans la zone eutectique. Il est également montré que la coalescence de fissures et l'interaction entre fissure et défauts sont favorisées par cette augmentation de température (voir figure 6.44).

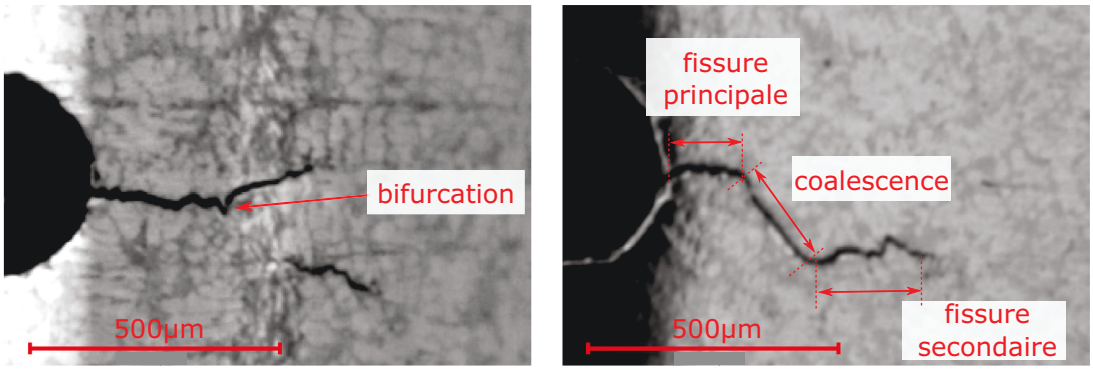

(a) $T = 20\,°C$: bifurcation de la fissure principale à l'approche d'une fissure secondaire

(b) $T = 250\,°C$: Coalescence de la fissure principale avec une fissure secondaire.

FIGURE 6.44 – Effet de la température sur l'interaction entres fissures

Chapitre 5 : Simulations numériques

À l'aide des distributions de défauts (en taille et en position), des éprouvettes numériques sont simulées. Compte tenu de la taille des éprouvettes, l'agrégation des défauts agit uniquement sur la variance du nombre de porosités, et seulement faiblement sur la taille extrême des défauts. Ainsi, la distribution des plus gros défauts est sensiblement identique, peu importe le processus ponctuel utilisé (de Poisson ou agrégé). À l'aide de cette distribution spatiale et du volume considéré, il est possible de simuler la taille des défauts critiques observés expérimentalement. En particulier, il est montré que les échantillons simulant la totalité de la zone utile surestiment fortement la taille des défauts critiques. Au contraire, en utilisant des échantillons virtuels ne contenant que le pourtour de l'éprouvette (formant un tube d'épaisseur 300 µm et de rayon externe égal à celui des éprouvettes testées), il est possible de reproduire numériquement la distribution des défauts critiques observés expérimentalement (voir figure 6.45).

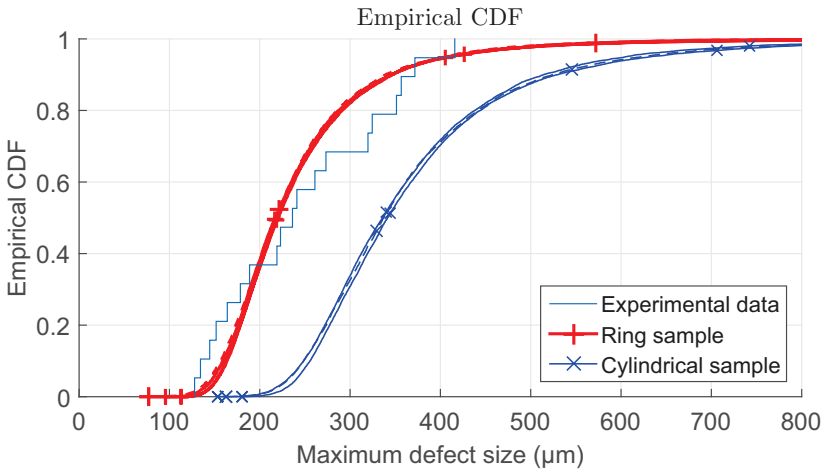

FIGURE 6.45 – Corrélation de la taille des défauts critiques observés (Experimental Data) avec les défauts simulés pour l'échantillon complet (cylindrical Sample) et pour l'échantillon en tube (Ring Sample).

Par la suite, la modélisation de la propagation de fissure est introduite. Les tailles des défauts critiques sont alors considérées comme des tailles de fissures initiales et permettent de prévoir la durée de vie des éprouvettes testées en fatigue (voir figure 6.46a).

La modélisation est ensuite appliquée aux essais de suivi de fissure, et donne également de bons résultats (voir figure 6.46b).

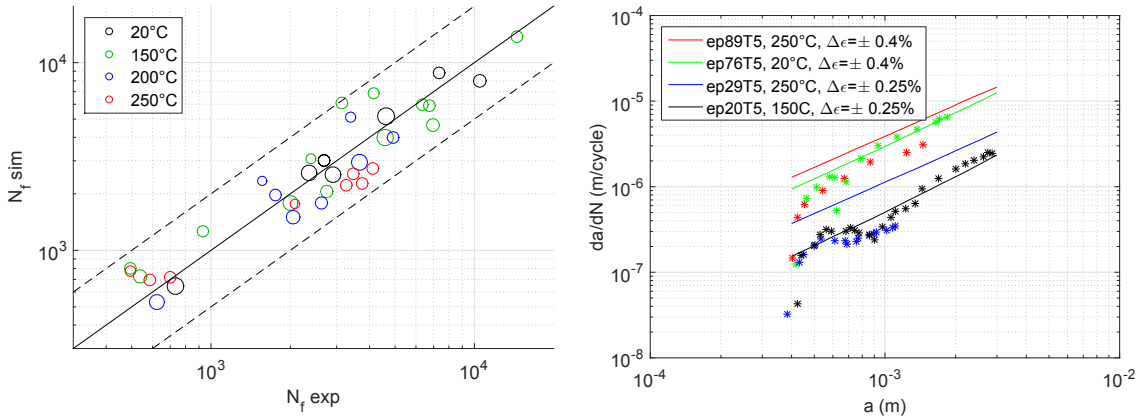

(a) Corrélation expérimentale de la durée de vie simulée et observée pour les éprouvettes sans défauts artificiels.

(b) Corrélation de la vitesse de propagation de fissure

FIGURE 6.46 – Modèle de propagation de fissure.

En dernier lieu, la modélisation de la propagation de fissure est combinée à la simulation numérique des défauts. En utilisant des échantillons virtuels, des défauts critiques sont générés. Ceux-ci sont alors considérés comme des tailles de fissures initiales, et permettent la simulation de la distribution en durée de vie.

Chapitre 6 : Effet des défauts sur la fatigue oligocyclique des éprouvettes entaillées.

Afin d'étudier la compétition entre taille des défauts extrêmes et volume sollicité, mais aussi l'impact de l'agrégation des défauts, des éprouvettes cylindriques entaillées, présentant un volume fortement sollicité faible, sont testées en fatigue (voir figure 6.47). Les mécanismes d'initiation de fissures (sur défaut proche de la surface, voir figure 6.48c) et les premiers stades de propagation de fissures (voir figure 6.48a et figure 6.48b) sont identiques à ceux observés sur éprouvette cylindrique. Cependant, comme observé dans la littérature, la distribution des contraintes en fond d'entaille favorise une croissance de la fissure en forme caractéristique de faucille et non, comme pour les éprouvettes lisses, en forme elliptique.

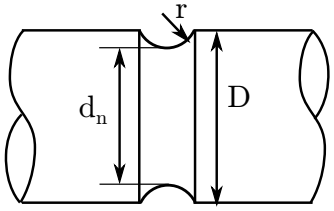

FIGURE 6.47 – Géométrie de l'éprouvette entaillée : $D = 7\,\text{mm}$, $d_n = 5.6\,\text{mm}$, $r = 1.2\,\text{mm}$, $K_t = 1.78$

Dans un dernier temps, la simulation par éléments finis est utilisée avec la génération de population de défauts. Pour chaque défaut, le champ de contrainte sans défaut est

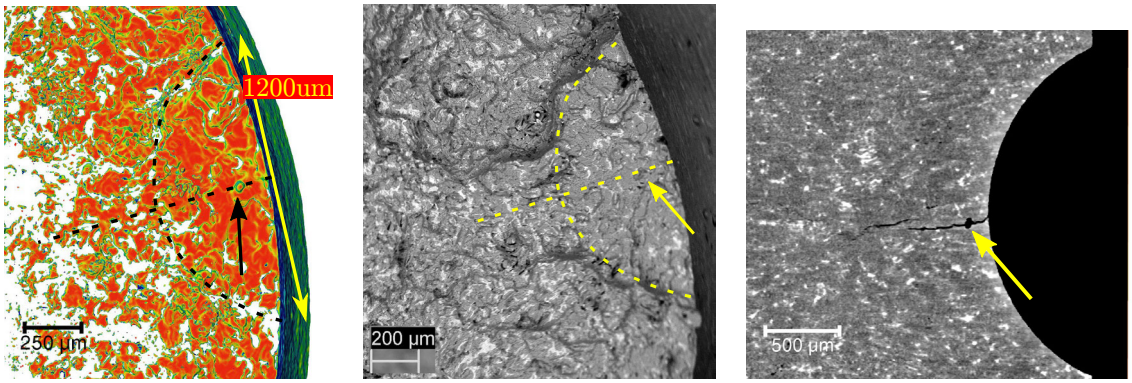

(a) Reconstruction de la fissure basée sur la tomographie.

(b) Observation MEB de la fissure.

(c) Défaut sphérique observé en coupe tomographique.

FIGURE 6.48 – Observation de l'initiation et des premiers stades de la propagation de fissure.

utilisé pour calculer une durée de vie (estimée à partir du modèle en propagation). Cela permet de classer la nocivité des défauts et de calculer une durée de vie en localisant le défaut critique (voir figure 6.49a).

Ainsi, en utilisant cette méthode, il est possible de générer un grand nombre d'éprouvettes numériques et leurs durées de vie correspondantes. Ces simulations ont pour principal but de comparer les différentes populations de défauts (agrégés ou non). Cela est illustré par la figure 6.49b. En comparaison de l'utilisation d'un processus "complètement" aléatoire de Poisson (*Complete Spatial Randomness* ou *CSR*), les processus agrégés tendent à produire des défauts plus petits dans un volume confiné. En effet, pour certaines configurations, les processus ponctuels agrégés génèrent un très faible nombre de défauts dans ce volume restreint. Compte tenu du faible nombre de défauts générés dans ce volume, le plus gros d'entre eux est alors statistiquement de plus faible taille (au sens des valeurs extrêmes), conduisant à une durée de vie plus élevée.

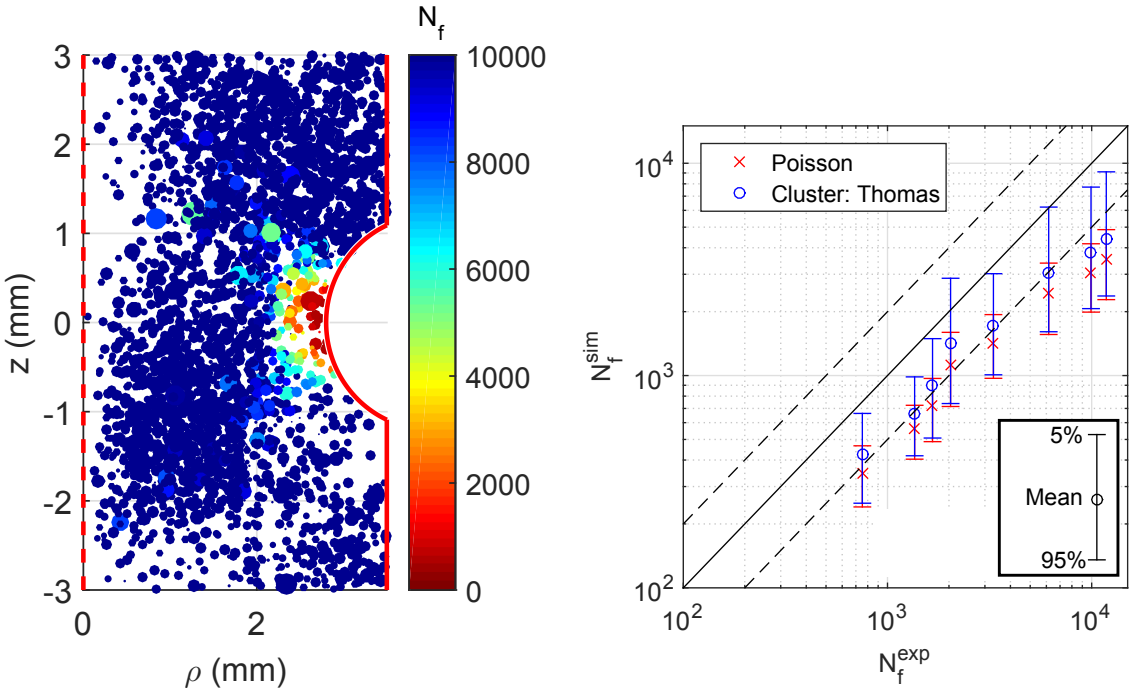

(a) Simulation de la durée de vie basée sur la taille de défaut et la localisation spatiale.

(b) Simulation de la durée de vie des éprouvettes entaillées pour différentes répartitions spatiales simulées des défauts.

FIGURE 6.49 – Éprouvette entaillée : simulation de la durée de vie avec prise en compte de la population de défauts.

Conclusions et perspectives

Les alliages d'aluminium et leur tenue en fatigue ont été étudiés depuis plus d'une centaine d'années. La littérature scientifique montre que plusieurs facteurs entrent en jeu dans les mécanismes de fatigue. Alors que certains sont étudiés depuis longtemps (composition chimique, traitement thermique, ou encore l'espacement des dendrites), la caractérisation précise des porosités en trois dimensions n'est possible que depuis quelques dizaines d'années grâce à la tomographie. En effet, les avancés récentes de la tomographie aux rayons-X de laboratoire ont permis de la rendre plus précise, mais surtout beaucoup plus accessible. Aujourd'hui, il est possible d'analyser en seulement quelques heures des volumes de l'ordre du centimètre cube, en préservant une résolution de quelques micromètres. En appliquant ces analyses à des éprouvettes issues d'essais interrompus, il est ainsi possible d'avoir accès à une information tridimensionnelle sur les mécanismes d'endommagement en fatigue par l'observation des fissures et de leurs interactions avec les défauts de matière. Cependant, les volumes de données mises en jeu (une tomographie peut contenir plusieurs milliards de points) nécessitent des outils numériques et mathématiques adaptés.

Après une étude matériau classique (composition chimique, phases eutectiques et dendritiques, caractérisation des intermétalliques), une étude plus poussée de la population de porosités présentes au sein du matériau est détaillée dans le second chapitre. Par le biais de l'inférence statistique et d'études de sensibilité, il est fait une analyse précise et robuste des porosités présentes. La finalité étant la caractérisation des plus grosses porosités (qui sont les plus critiques pour la tenue en fatigue), l'étude se concentre sur les queues de distribution. Il est ainsi démontré que la distribution généralisée de

Pareto est la plus à même de capturer ces aspects. En comparant trois éprouvettes, il est aussi montré que chacune d'entre elles représente une population statistiquement représentative vis-à-vis de la taille de défaut et que l'utilisation de la tomographie est un outil robuste pour l'analyse. En combinant l'étude statistique de la sphéricité, la représentativité de la population de défauts d'une éprouvette est confirmée. L'étude de la distribution spatiale des défauts tempère cette représentativité. En effet, à l'aide de la statistiques des processus ponctuels, il est possible de quantifier la distribution spatiale des défauts : ceux-ci apparaissent pendant la coulée de l'alliage sous forme d'agrégats. Ainsi, dans une éprouvette, la population de défauts peut atteindre plusieurs milliers, alors que les agrégats se limitent à seulement quelques dizaines. Il est alors plus difficile de considérer qu'une seule éprouvette est représentative. Par la suite, l'utilisation de processus ponctuels marqués révèle que taille et position de défauts semblent décorrélées, simplifiant les études développées par la suite.

Le troisième chapitre présente les résultats des essais de fatigue menés lors de cette étude. La méthodologie d'essai, et la quantification des incertitudes de mesures, permettent d'assurer que la suite du travail se focalise effectivement sur la dispersion due aux mécanismes d'endommagement en fatigue. Tout d'abord, le critère de Coffin-Manson est testé et montre qu'il permet de prévoir la durée de vie correctement. Cependant, son utilisation nécessite différents paramètres pour chaque température qui sont difficilement compatibles avec une perspective d'utilisation en fatigue thermomécanique. Au contraire, en utilisant les énergies de déformation, un critère énergétique permet d'unifier les courbes sous forme de loi puissance et de prévoir la durée de vie en fatigue pour toutes les températures étudiées. Enfin, une inférence statistique détaillée de la dispersion à l'aide d'un écart-type variable confirme les observations classiques de la littérature scientifique : la dispersion diminue avec la durée de vie en fatigue.

Dans le quatrième chapitre, plusieurs techniques d'observation combinées (suivi de fissure, analyses MEB et EDS, tomographie rayons-X) permettent d'observer les mécanismes mis en jeu, tout particulièrement l'influence des défauts. Comme il est observé dans la littérature scientifique, les fissures s'initient sur les défauts proches de la surface. Ces défauts sont étudiés et leurs caractéristiques quantifiées : taille de défaut, type (porosités dues au gaz ou retassures) et position par rapport à la surface. Il est démontré que la criticité d'un défaut est liée à sa taille, mais aussi à sa position par rapport à la surface. Ainsi, au cœur de l'éprouvette, des défauts plus gros que le défaut critique peuvent exister. Ces défauts peuvent initier des fissures, notamment pour les températures les plus élevées, mais ne sont pas responsables de la fissure principale. Les mécanismes de propagation de fissure sont également observés. La fissure principale est ainsi liée à un défaut critique, mais l'amorçage de fissure est également aidé par des composés microstructuraux tels les intermétalliques ou les zones eutectiques. Ces composés aux caractéristiques mécaniques différentes provoquent des hétérogénéités dans la distribution de contraintes et favorisent l'amorçage. En utilisant un dispositif d'observation spécifiquement développé (un appareil photo numérique et un éclairage diffus adapté), il est possible de suivre la propagation de fissure sur éprouvette cylindrique, mais aussi d'analyser une fenêtre d'observation plus large. L'amorçage de fissure sur des défauts artificiels est observé après environ 20% de la durée de vie totale, mais l'étude d'initiation naturelle de fissures montre que certaines d'entre elles apparaissent beaucoup plus tôt (moins de 5% de la durée de vie totale). De fait, l'hypothèse classique considérant que la durée de vie en fatigue oligocyclique est majoritairement liée à la propagation de fissures est confirmée. Par la suite, la propagation de fissure et son interaction avec les défauts en présence est détaillée. Les phases de propagations sont

clairement identifiées : après l'initiation, une première phase de propagation stable se développe de manière plane et relativement lisse, alors que la propagation au stade finale révèle une surface de rupture beaucoup plus accidentée (se rapprochant de celles observées en traction monotone). Pendant les différentes phases de propagation, la fissure interagit avec des fissures secondaires qui se sont elles-mêmes amorcées sur des défauts. Cette interaction est fonction de la température et beaucoup plus importante pour les températures les plus élevées.

Dans le cinquième chapitre, des éprouvettes numériques contenant une population de défauts virtuels sont simulées. Les défauts extrêmes (les plus gros) sont alors comparés à ceux observés sur les faciès de rupture. Il est alors montré que le plus gros défaut dans la totalité de l'éprouvette numérique (correspondant à la zone utile testée en fatigue) surestime la taille observée sur les faciès. Cependant, en prenant en compte les mécanismes observés (seuls les défauts proches de la surface libre sont susceptibles d'être critiques), il est possible de simuler une éprouvette virtuelle, contenant des défauts uniquement sur le pourtour. Ces éprouvettes numériques "tubulaires" comprennent les défauts uniquement à moins de 300 µm de la surface libre, correspondant à environ 15% du volume initial considéré. Les défauts extrêmes alors simulés sont alors de tailles similaires aux défauts critiques observés, démontrant que seul le pourtour de l'éprouvette constitue un volume représentatif du mécanisme d'amorçage. Par la suite, un modèle de propagation de fissure est utilisé pour modéliser la vitesse de propagation de fissure. Il est fait l'hypothèse que les défauts critiques sont équivalents à des fissures de même taille. Par intégration, la durée de vie peut alors être estimée. Les paramètres du modèle de propagation sont alors optimisés pour corréler avec les durées de vie expérimentalement observées. En utilisant des éprouvettes numériques (contenant une population de défauts simulés), le modèle permet alors de prévoir la distribution de durée de vie en fonction de la population de défauts.

Dans le sixième et dernier chapitre, des essais sur éprouvettes entaillées sont réalisés. Les mécanismes d'amorçages identifiés sont similaires à ceux observés sur éprouvettes lisses, mais le champ de contraintes hétérogène modifie la phase de propagation. Le front de fissure se développe ainsi en forme caractéristique de "faucille" (*sickle* en anglais). La simulation par la méthode des éléments finis est alors utilisée pour évaluer plusieurs critères locaux. Alors que le critère de type "point chaud" se révèle inefficace pour prévoir la durée de vie en fatigue, les critères issus de la théorie de la distance critique (méthode du point et de la ligne) donnent de bonnes estimations. Cependant, l'unicité de la géométrie d'entaille étudiée ne permet pas de conclure et des essais complémentaires sur différentes géométries seront nécessaires. Enfin, dans la dernière partie, une population de défauts numériques est placée dans le champ de contraintes issu de la simulation par la méthode des éléments finis de l'éprouvette entaillée (réalisée sur éprouvettes sans défauts). Pour chaque population de défauts simulée, les défauts individuels sont donc soumis à un champ de contraintes local. À l'aide du modèle de propagation de fissure et d'hypothèses de calcul, un nombre de cycles à rupture est alors associé à chaque défaut, permettant l'identification du défaut critique. Cette modélisation permet donc la simulation de la dispersion de la durée de vie en tenant compte de la population de défauts (en taille et en position). Il est alors montré que, pour la plupart des cas, l'utilisation d'un processus de Poisson ou d'un processus agrégé donne des résultats similaires. Les processus agrégés font néanmoins apparaître certaines différences : dans certains cas, peu d'agrégats sont proches de l'entaille et seuls des défauts de petites tailles se situent dans des zones fortement sollicitées mécaniquement. Les durées de vie estimées sont alors nettement plus élevées, démontrant l'importance de

la distribution spatiale pour la compréhension des mécanismes.

Pour les futurs travaux, plusieurs perspectives peuvent être envisagées :

— **Distribution spatiale des défauts** : les méthodes statistiques développées dans la présente étude pourraient être appliquées à plus d'éprouvettes. Cela permettrait de comparer les distributions de valeurs extrêmes observées et simulées. De plus, cette étude pourrait également être étendue à des éprouvettes provenant de différents lots matières afin de quantifier la dispersion inter-lots (tous les lots de cette étude ont été réalisés en même temps, donc dans des conditions très similaires). Enfin, il serait intéressant d'étendre l'étude à des éprouvettes extraites de pièces industrielles (cette étude a déjà débutée).

— **Mécanismes d'endommagement en fatigue** : la combinaison de différentes méthodes d'observation montre des résultats prometteurs pour la compréhension des mécanismes. Récemment, des expériences de tomographie *in-situ* (voir Dezecot et al. [2016]) réalisées au synchrotron démontrent la possibilité d'observer plus précisement les différents stade de la propagation de fissures. Cependant, ces expériences sont souvent réalisées en utilisant des éprouvettes de petite taille. Le travail présenté ici pourrait alors permettre de valider la représentativité de tels essais.

— **Simulation par la méthodes éléments finis** : en se basant sur la microstructure observée par tomographie, des simulations sur microstructures réelles ou simplifiées peuvent être faites. Néanmoins, plusieurs problématiques se posent : comment prendre en compte les hétérogénéités microstructurales ? Comment assurer la convergence des simulations ? Faut-il (et si oui comment) modéliser les fissures ? Des études récentes (voir Wang [2015] et Limodin et al. [2014]) montrent qu'il est possible de combiner ces modélisations avec des techniques de corrélation d'images numériques (en deux et trois dimensions) et ainsi de pouvoir valider les résultats de simulation.

— **Simulation de la propagation de fissure** : en utilisant des modèles de propagation de fissure et en émettant l'hypothèse que les défauts se comportent comme des fissures, il est possible de simuler la dispersion de la durée de vie. Cependant, des études complémentaires seront nécessaires afin de prendre en compte la morphologie des défauts et leur position par rapport à la surface. Le modèle devrait en particulier permettre de quantifier l'impact de la distance à la surface sur la durée de vie.

Bibliography

Bibliographie

A. Karolcsuk, T. P.-L. (2013). Modelling of stress gradient effect on fatigue life using Weibull based distribution function. *Journal of theoretical and applied mechanics*. 109

Adib, H. and Pluvinage, G. (2003). Theoretical and numerical aspects of the volumetric approach for fatigue life prediction in notched components. *International Journal of Fatigue*, 25(1):67–76. iii, 33, 197

Albonetti, R. (2000). Porosity and Intermetallic formation in lost foam casting of A356 Alloy. Master's thesis, The University of Western Ontario. 23

Armstrong, P. J. and Fredericks, C. O. (1966). A mathematical representation of the multiaxial baushinger effect. Rd/b/n731, Berkeley Nuclear Laboratory. 94

ASTM (2004). Standard Practice for Strain-Controlled Fatigue Testing. *ASTM E606-04*. 87, 180

Baddeley, A., Rubak, E., and turner, R. (2015). *Spatial Point Patterns: Methodology and Applications with R*. CRC Press. 73

Baddeley, A. J., Moyeed, R. A., Howard, C. V., and A., B. (1993). Analysis of a Three-Dimensional Point Pattern with Replication. *Appl. Statistics*, 42-4:641–668. stat spat. 73

Barlas, B. (2003). *Etude du comportement et de l'endommagement en fatigue d'alliages d'aluminium de fonderie*. PhD thesis, Ecole des Mines ParisTech. 94, 97

Barralis, J. and Maeder, G. (1997). *Précis de métallurgie : élaboration, structures-propriétés, normalisation*. AFNOR-Nathan. ii, 5

Bentachfine, S. (1999). Notch effect in low cycle fatigue. *International Journal of Fatigue*, 21(5):421–430. iii, x, 33, 35, 36, 197, 214

Besag, J. (1977). Contribution to the Discussion on Dr. Ripley's Paper. *Journals of the Royal Statistical Society, B39, 193-195*. 70

Bidouard, H. (2009). *Etude de l'effet de surcharges sur la tenue en fatigue à grande durée de vie d'un acier ferrito-bainitique sous chargement d'amplitude variable*. PhD thesis, Arts et Métiers ParisTech. iii, 27, 28

Boettinger, W. J., Warren, J. A., Beckermann, C., and Karma, A. (2002). Phase-Field Simulation and Solidification. *Annual Review of Materials Science*, 32:163–194. ii, 4

Brand, A. and Sutterlin, R. (1980). *Calcul des pièces à la fatigue*, chapter Méthode du gradient. France. 32, 33, 34

Broek, D. (1986). Elementary engineering fracture mechanics. 171

Buades, A., Coll, B., and Morel, J.-M. (2005). A Non-Local Algorithm for Image Denoising. *2005 IEEE Computer Society Conference on Computer Vision and Pattern Recognition (CVPR05)*. 114

Buffière, J.-Y., Savelli, S., Jouneau, P. H., Maire, E., and Fougères, R. (2002). Experimental study of porosity and its relation to fatigue mechanisms of model Al-Si7-Mg0.3 cast Al alloys. *Materials Science and Engineering*, A316:115–126. ii, 1, 13, 14, 16, 17, 18, 58, 210

Carpinteri, A., Ronchei, C., and Vantadori, S. (2013). Stress intensity factors and fatigue growth of surface cracks in notched shells and round bars: two decades of research work. *Fatigue Fract Engng Mater Struct*, 36(11):1164–1177. 188

Caton, M. J., Jones, J. W., and Allison, J. E. (2001). The influence of heat treatment and solidification time on the behavior of small-fatigue-cracks in a cast aluminum alloy. *Materials Science and Engineering*, A314:81–85. 8

Charkaluk, E., Bignonnet, A., Constantinescu, A., and Dang Van, K. (2002). Fatigue design of structures under thermomechanical loadings. *Fat Frac Eng Mat Struct*, 25(12):1199–1206. 109

Charkaluk, E., Constantinescu, A., Szmytka, F., and Tabibian, S. (2014). Probability density functions: From porosities to fatigue lifetime. *International Journal of Fatigue*. iii, 23, 24, 26

Charkaluk, E., Thomas, J. J., and Constantinescu, A. (2004). Numerical approach in thermomechanical fatigue. ii, 19, 20

Constantinescu, A., Charkaluk, E., Lederer, G., and Verger, L. (2004). A computational approach to thermomechanical fatigue. *International Journal of Fatigue*, 26:805–818. 19

Dahdah, N., Limodin, N., El Bartali, A., Witz, J. F., Seghir, R., Charkaluk, E., and Buffiere, J. Y. (2016). Damage Investigation in A319 Aluminium Alloy by X-ray Tomography and Digital Volume Correlation duringIn SituHigh-Temperature Fatigue Tests. *Strain*, 52(4):324–335. iii, 23, 24, 26

De-Feng, M., Guo-Qiua, H., Zheng-Feia, H., Xiao-Shana, L., and Wei-Huab, Z. (2010). Effect of microstructural features on fatigue behavior in A319-T6 aluminum alloy. *Materials Science and Engineering A*, 527:3420–3426. xii, xiii, 13, 14, 127, 213

Dezecot, S., Buffiere, J.-Y., Koster, A., Maurel, V., Szmytka, F., Charkaluk, E., Dahdah, N., El Bartali, A., Limodin, N., and Witz, J.-F. (2016). In situ 3D characterization of high temperature fatigue damage mechanisms in a cast aluminum alloy using synchrotron X-ray tomography. *Scripta Materialia*, 113:254–258. iii, 23, 25, 156, 209, 226

Dinnis, C. M., Taylor, J. A., and Dahle, A. K. (2006). Interactions between iron, manganese, and the Al-Si eutectic in hypoeutectic Al-Si alloys. *Metallurgical and Materials Transactions A*. 7

El Haddad, M. H., Smith, K. N., and Topper, T. H. (1979). Fatigue Crack Propagation of Short Cracks. *Journal of Engineering Materials and Technology*, 101(1):42. 29

Fang, H.-B., Fang, K.-T., and Kotz, S. (2002). The Meta-elliptical Distributions with Given Marginals. *Journal of Multivariate Analysis*, 82(1):1–16. 61

Fjeldstad, A., Wormsen, A., and Harkergard, G. (2008). Simulation of fatigue crack growth in components with random defects. *Engineering Fracture Mechanics*, 75(5):1184–1203. 199

Gall, Yang, Horstemeyer, McDowell, and Fan (2000). The influence of modified intermetallics and Si particles on fatigue crack paths in a cast A356 Al alloy. *Fat Frac Eng Mat Struct*, 23(2):159–172. 7, 139

Gao, Y. X., Yi, J. Z., Lee, P. D., and Lindley, T. C. (2004). The effect of porosity on the fatigue life of cast aluminium-silicon alloys. *Fatigue Fract Engng Mater Struct*, 27:559–570. xii, 13, 14, 15

Genest, C. and MacKay, R. J. (1986). Copules archimédiennes et familles de lois bidimensionnelles dont les marges sont données. *Statistical Society of Canada*. 62

González, R., Martínez, D. I., González, J. A., Talamantes, J., Valtierra, S., and Colás, R. (2011). Experimental investigation for fatigue strength of a cast aluminium alloy. *International Journal of Fatigue*, 33(2):273 – 278. 8

Guerchais, R., Saintier, N., Morel, F., and Robert, C. (2014). Micromechanical investigation of the influence of defects in high cycle fatigue. *International Journal of Fatigue*, 67:159â€“172. 16

Haddar, N. (2003). *Fatigue thermique d'un acier inoxydable austénitique 304L : simulation de l'amorçage et de la croissance des fissures courtes en fatigue isotherme et anisotherme*. PhD thesis, Ecole Nationale Supérieure des Mines de Paris. 23

Halford, G. (1966). The energy required for fatigue. *Journal of Materials*, 1:3–17. 34

Heywood, R. (1952). *Designing by Photoelasticity*. Chapman and Hall, London. 33

Illian, J., Penttinen, A., Stoyan, H., and Stoyan, D. (2007). Statistical Analysis and Modelling of Spatial Point Patterns. iv, xii, 68, 71, 72, 74, 81

Kandil, F. A. (2000). The Determination of Uncertainties in Low Cycle Fatigue Testing. 85

Kiskowski, M. A., Hancock, J. F., and Kenworthy, A. K. (2009). On the Use of Ripleys K-Function and Its Derivatives to Analyze Domain Size. *Biophysical Journal*, 97(4):1095–1103. 71

Kitagawa H, T. S. (1976). Applicability of fracture mechanics to very small cracks. In *In Proceedings of the Second International Conference on Mechanical Behavior of Materials*, pages 627–631. 15

Koh, S. K. (2002). Fatigue damage evaluation of a high pressure tube steel using cyclic strain energy density. *Pressure Vessels and Piping*, 79:791–798. iii, 20, 21, 102

Kruzic, J. J. and Ritchie, R. O. (2006). Kitagawa-Takahashi diagrams define the limiting conditions for cyclic fatigue failure in human dentin. *Journal of Biomedical Materials Research Part A*, (79(3)):747–51. ii, 15

Kuhn, P. and Hardraht, H. (1952). An engineering method for estimating notch size effect in fatigue tests on steel. *NACA Technical Note*, 2805. 34

Kumaraswamy, P. (1980). A generalized probability density function for double-bounded random processes. *Journal of Hydrology*, 46(1-2):79–88. 56

Lazzarin, P., Tovo, R., and Meneghetti, G. (1997). Fatigue crack initiation and propagation phases near notches in metals with low notch sensitivity. *International Journal of Fatigue*, 19(8-9):647–657. 30

Le, V.-D., Morel, F., Bellett, D., Saintier, N., and Osmond, P. (2016). Multiaxial high cycle fatigue damage mechanisms associated with the different microstructural heterogeneities of cast aluminium alloys. *Materials Science and Engineering: A*, 649:426–440. 16

Li, P., Lee, P., Maijer, D., and Lindley, T. (2009). Quantification of the interaction within defect populations on fatigue behavior in an aluminum alloy. *ActaMateriala*, 57:3539–3548. ii, 13, 14

Lieshout, M. N. M. and Baddeley, A. J. (1996). A nonparametric measure of spatial interaction in point patterns. *Statistica Neerlandica*, 50(3):344–361. 70

Limodin, N., El Bartali, A., Wang, L., Lachambre, J., Buffiere, J.-Y., and Charkaluk, E. (2014). Application of X-ray microtomography to study the influence of the casting microstructure upon the tensile behaviour of an Al???Si alloy. *Nuclear Instruments and Methods in Physics Research Section B: Beam Interactions with Materials and Atoms*, 324:57–62. Microtomo in situ tensile. 209, 226

Lin, X. (1999). Shape evolution of surface cracks in fatigued round bars with a semicircular circumferential notch. *International Journal of Fatigue*, 21(9):965–973. 188

Manson, S. S. (1965). Fatigue: A complex subject-Some simple approximations. *Experimental Mechanics*, 5(4):193–226. 100

Martinez, R., Russier, V., Couzinié, J., Guillot, I., and Cailletaud, G. (2013). Modeling of the influence of coarsening on viscoplastic behavior of a 319 foundry aluminum alloy. *Materials Science and Engineering: A*, 559:40–48. 93, 94, 97

Maurel, V., Rémy, L., Dahmen, F., and Haddar, N. (2009). An engineering model for low cycle fatigue life based on a partition of energy and micro-crack growth. *International Journal of Fatigue*, 31:952–961. iii, 21, 22, 170

McEvily, A. and Ishihara, S. (2001). On the dependence of the rate of fatigue crack growth on the $\sigma_a^n(2a)$ parameter. *International Journal of Fatigue*, 23(2):115–120. 17, 18

Merkus, H. G. (2009). Particle Size Measurements. *Particle Technology Series*. 41

Mondolfo, L. F. (1976). *Aluminium alloys, structure and propreties*. Butterworths. 3, 6, 7

Murakami, Y. (1993). *Metal fatigue : effects of small defects and non-metallic inclusions*. Yokendo Ltd. 1, 13, 15, 84, 127, 210

Nafisi, S., Ghomashchi, R., and Vali, H. (2008). Eutectic nucleation in hypoeutectic Al-Si alloys. *Materials Characterization*, 59(10):1466–1473. 39

Nelder, J. A. and Mead, R. (1965). A ssimple method for function minimization. *The Computer Journal*, 7:308–313. 96

Nelsen, R. B. (2006). *An Introduction to Copulas*. Springer New York. 60

Neuber, H. (1958). *Theory of notch stresses : principles for exact calculation of strength with reference to structural form and material*. Springer Verlag, 2ed edition. 29, 34

Neyman, J. and Scott, E. L. (1952). A Theory of the Spatial Distribution of Galaxies. *The Astrophysical Journal*, 116:144. 68

Odegard, J. A. and Pedersen, K. (1994). *Fatigue Properties of an A356 (AlSi7Mg) Aluminium Alloy for Automotive Applications - Fatigue Life Prediction*. Number 0. 13

Pascual, F. and Meeker, W. (1997). Analysis of fatigue data with runouts based on a model with non constant standard deviation and a fatigue limit parameter. *Journal of Testing and Evaluation*, 25:292–301. 107

Penttinen, A. and Stoyan, D. (2000). statistics. *Statist. Sci.*, 15(1):61â€“78. 71

Peterson, R. E. (1959). *Metal Fatigue*, chapter 13. Notch Sensitivity, pages 293–306. McGraw Hill. 29, 33, 34

Peterson, R. E. and Wahl, A. (1936). Two and Three-Dimensional Cases of Stress Concentration, and Comparison with Fatigue Tests. *Journal of Applied Mechanics*, A15. 29

Phragmen, G. (1950). *Inst Metal*, 77:489. 7

Pickands, J. (1975). Statistical Inference Using Extreme Order Statistics. *The Annals of Statistics*, 3(1):119–131. 52

Pilkey, W. D. and Pilkey, D. F. (2007). Peterson's Stress Concentration Factors. 179

Pineau, A., Ritchie, R. O., and Lankford, J. (1986). Small fatigue cracks. Proceedings of the 2nd International Conference on Small Fatigue Cracks, page 191. Warrendale. 14

Pommerening, A. and Stoyan, D. (2006). Edge-corrrection needs in estimating indices of spatial forest Structure. *Can J. For. Res.*, 36:1723–1739. 81

Qylafku, G. (1999). Application of a new model proposal for fatigue life prediction on notches and key-seats. *International Journal of Fatigue*, 21(8):753–760. xii, 32, 33, 34

Salvo, L., Cloetens, P., Maire, E., Zabler, S., Blandin, J., Buffiére, J., Ludwig, W., Boller, E., Bellet, D., and Josserond, C. (2003). X-ray micro-tomography an attractive characterisation technique in materials science. *Nuclear Instruments and Methods in Physics Research Section B: Beam Interactions with Materials and Atoms*, 200:273–286. 42

Schwarmann, L. (1986). *Material data of high-strength aluminium alloys for durability evaluation of structures: Fatigue strength, crack propagation, fracture toughness.* Aluminium-Verlag. 16

Shabestari, S. G. and Moemeni, H. (2004). Effect of copper and solidification conditions on the microstructure and mechanical properties of Al-Si-Mg alloys. *Journal of Materials Processing Technology*, 153-154:193–198. 39

Shankar, S., Riddle, Y. W., and Makhlouf, M. M. (2004). Nucleation mechanism of the eutectic phases in aluminum-silicon hypoeutectic alloys. *Acta Materialia*, 52(15):4447–4460. ii, 4, 5

Silverman, B. W. (1986). *Density Estimation for Statistics and Data Analysis*. Chapman and Hal. 50

Skelton, R. P., Rees, C. J., and Webster, G. A. (1996). Energy damage summation methods for crack initiation and growth during block loading in high-temperature low-cycle fatigue. *Fatigue & Fracture of Engineering Materials and Structures*, 19(2-3):287–297. 19

Smith, K. N., Watson, P., and Topper, T. H. (1970). A Stress-Strain Function for the Fatigue of Metal. *J. Mater*, 5:767–778. 198

Song, M., Kong, Y., Ran, M., and She, Y. (2011). Cyclic stress-strain behavior and low cycle fatigue life of cast A356 alloys. *International Journal of Fatigue*, 33(12):1600–1607. 139

Sternberg (1983). Biomedical Image Processing. *Computer*, 16(1):22–34. 43

Sudret, B. (2014). Rapport Technique R-2012-0601-002A : Traitement statistique des données géométriques de porosité. Technical report, BS Conseil. 48

Sudret, B. (2015a). Rapport Technique R-2012-0601-003A : Traitement statistique de la répartition spatiale de porosités par processus ponctuels. Technical report, BS Conseil. 66

Sudret, B. (2015b). Rapport Technique R-2012-0601-005A : Utilisation des processus ponctuels marqués pour l'analyse de porosités. Technical report, BS Conseil. 80

Susmel, L. (2008). The theory of critical distances: a review of its applications in fatigue. *Engineering Fracture Mechanics*, 75(7):1706–1724. iii, 30

Susmel, L. and Taylor, D. (2003). Fatigue design in the presence of stress concentrations. *The Journal of Strain Analysis for Engineering Design*, 38(5):443–452. iii, 31

Susmel, L. and Taylor, D. (2010). An Elasto-Plastic Reformulation of the Theory of Critical Distances to Estimate Lifetime of Notched Components Failing in the Low/Medium-Cycle Fatigue Regime. *Journal of Engineering Materials and Technology*, 132(2):021002. 198

Tabibian, S., Charkaluk, E., Constantinescu, A., Oudin, A., and Szmytka, F. (2010). Behavior, damage and fatigue life assessment of lost foam casting aluminum alloys under thermo-mechanical fatigue conditions. *Procedia Engineering*, 2:1145–1154. iii, x, 22, 23, 24, 213

Tabibian, S., Charkaluk, E., Constantinescu, A., Szmytka, F., and Oudin, A. (2012). TMF-LCF life assessment of a Lost Foam Casting A319 aluminum alloy. *International Journal of Fatigue*. 102, 109

Tanaka, K. (1983). Engineering formulae for fatigue strength reduction due to crack-like notches. *International Journal of Fracture*, 22(2):R39–R46. 30

Taylor, D. (1999). Geometrical effects in fatigue: a unifying theoretical model. *International Journal of Fatigue*, 21(5):413–420. 30, 31

Taylor, J. A. (2012). Iron-Containing Intermetallic Phases in Al-Si Based Casting Alloys. *Procedia Materials Science*, 1:19–33. ii, x, 7, 212

Timpel, M., Wanderka, N., Schlesiger, R., Yamamoto, T., Lazarev, N., Isheim, D., Schmitz, G., Matsumura, S., and Banhart, J. (2012). The role of strontium in modifying aluminium-silicon alloys. *Acta Materialia*, 60(9):3920–3928. 39

Virkler, D. A., Hillberry, B. M., and Goel, P. K. (1979). The Statistical Nature of Fatigue Crack Propagation. *Journal of Engineering Materials and Technology*, 101(2):148. 176

Waagepetersen, R. (2006). An estimating function approach to inference for inhomogeneous Neyman-Scott Processes. *Biometrics*, 63:252–258. 74

Wand, M. P. and Jones, M. C. (1995). *Kernel Smoothing*. Chapman & Hall. 50

Wang, L. (2015). *Etude de l'influence de la microstructure sur les mécanismes d'endommagement dans les alliages Al-Si de fonderie par des analyses in-situ 2D et 3D (English)*. PhD thesis, Ecole Centrale de Lille. 209, 226

Wang, L., Limodin, N., El Bartali, A., Witz, J.-F., Seghir, R., Buffiere, J.-Y., and Charkaluk, E. (2016). Influence of pores on crack initiation in monotonic tensile and cyclic loadings in lost foam casting A319 alloy by using 3D in-situ analysis. *Materials Science and Engineering: A*, 673:362â€“372. iii, 24, 25

Wang, Q. G., Apelian, D., and Lados, D. A. (2001a). Fatigue behavior of A356-T6 aluminum cast alloys. Part I. Effect of casting defects. *Journal of Light Metals*, 1:73–84. 9, 112, 133

Wang, Q. G., Apelian, D., and Lados, D. A. (2001b). Fatigue behavior of A356/357 aluminum cast alloys. Part II Effect of microstructural constituents. *Journal of Light Metals*, 1:85–97. ii, 9, 10, 11, 12

Wang, Q. G. and Cáceres, C. H. (1998). The fracture mode in Al - Si - Mg casting alloys. *Materials Science and Engineering*, A241:72–82. ii, 12

Weixing, Y. (1993). Stress field intensity approach for predicting fatigue life. *International Journal of Fatigue*, 15(3):243–246. 31

Yi, J. Z., Gao, Y. X., Lee, P. D., and Lindley, T. C. (2004). Effect of Fe-content on fatigue crack initiation and propagation in a cast aluminum–silicon alloy (A356–T6). *Materials Science and Engineering: A*. 135

Zhang, H., Toda, H., Hara, H., Kobayashi, M., Kobayashi, T., Sugiyama, D., Kuroda, N., and Uesugi, K. (2007). Three-Dimensional Visualization of the Interaction between Fatigue Crack and Micropores in an Aluminum Alloy Using Synchrotron X-Ray Microtomography. *Metallurgical and Materials Transactions A*, 38(8):1774–1785. 153

Zolotorevsky, V. S., Belov, N. A., and Glazoff, M. V. (2007). *Casting Alluminium Alloys*. Elsevier. ii, 6, 7

Statistical Inference of Defect Population for the Study and Simulation of the Low-Cycle Fatigue of a Cast Aluminium Alloy

Abstract: In a search for lightweight materials, cast aluminium alloys have become an efficient solution for the automotive industry. For cylinder heads, cast aluminium alloys (Aluminium-Silicon-Copper based) are often chosen for their mechanical performances combined with their good casting abilities. This study aims at better understanding the damage mechanisms of Low-Cycle Fatigue (LCF) to help define a suitable design criterion. This is achieved by combining experiments (LCF tests at ambient and high temperature), various observations (Scanning electron microscopy, laboratory 3D X-ray microtomography, crack propagation monitoring) and numerical techniques (Finite element method simulations and defect population generation). Specifically designed statistical tools allow clearly identifying the defect (casting defects) population: the defect size can be modelled by a generalized Pareto distribution and their positions by a clustered point process (thus showing the defect locations are not completely random). Using marked point processes, it is also shown that defect size and defect position are uncorrelated. Using this statistical information and by systematic observations, it is proven that only defects close to the surface are critical for the fatigue life. The different interactions between cracks and defects are also studied, especially with respect to temperature. A strain energy based fatigue criterion is introduced and allows estimating the fatigue life. Then, a crack propagation model provides a mean of taking the defect size into account, which combined with the statistics of defects, gives an estimate of the fatigue life dispersion. Finally, notched specimens tests and simulations show the study of the defect population is even more critical as the highly loaded volume becomes smaller.

Keywords: aluminium, low-cycle fatigue, cylinder head, defect, statistic, tomography

Inférence statistique de la population de défauts pour l'étude et la simulation de la fatigue oligocyclique d'un alliage d'aluminium de fonderie.

Résumé : Dans une optique d'allègement, les alliages d'aluminium de fonderie représentent une excellente solution technique. Ainsi, pour les culasses automobiles, les alliages d'aluminium Al-Si-Cu (Aluminium-Silicium-Cuivre) sont souvent choisis pour leurs performances mécaniques ainsi que leur bonne coulabilité. L'objectif de cette étude est d'améliorer la compréhension des mécanismes en fatigue oligocyclique pour définir un critère de fatigue adapté. Cet objectif est réalisé en combinant des essais (en fatigue oligocyclique à température ambiante et élevée), de nombreuses observations (microscopie à balayage électronique, microtomographie 3D rayons-X de laboratoire, suivi de fissure) et des simulations (génération de population de défauts et calculs éléments finis). À l'aide d'outils spécialement développés, la population de défauts (défauts de fonderie) est analysée en détails : la taille de défaut est modélisée par une distribution de Pareto généralisée et leurs positions par un processus ponctuel de type agrégé (démontrant que les défauts ne sont pas spatialement distribués de manière totalement aléatoire). Les processus ponctuels marqués permettent de montrer que tailles et positions de défauts ne sont pas corrélées. En utilisant ces informations statistiques, il est démontré que seuls les défauts proches de la surface sont critiques pour la fatigue oligocyclique. Un critère de fatigue basé sur l'énergie de déformation est utilisé pour prévoir la durée de vie en fatigue. Par la suite, un modèle de propagation de fissure permet de prendre en compte la taille de défaut dans la prévision de la durée de vie. Combiné à la statistique des défauts, ce modèle permet d'estimer la dispersion des essais. En dernier lieu, des essais et des simulations sur éprouvettes entaillées montrent que l'étude de la population de défauts est d'autant plus critique que le volume fortement sollicité mécaniquement devient plus faible.

Mots clefs : aluminium, fatigue oligocyclique, culasse, défaut, statistique, tomographie